UNIVERSITAT POLITÈCNICA DE VALÈNCIA

INSTITUTO UNIVERSITARIO MIXTO DE TECNOLOGÍA QUÍMICA

Hybrid Lead Perovskites as Photocatalysts and Materials for Photo- and Electrocatalytic N_2 Reduction

Doctoral Thesis

Presented by:

Yong Peng (彭勇)

Supervisor:

Prof. Hermenegildo García Gómez

Dr. Josep Albero Sancho

Valencia, April 2021

Dr. HERMENEGILDO GARCÍA GÓMEZ, Professor of the Universitat Politècnica de València and Dr. JOSEP ALBERO SANCHO, doctor at the Instituto de Tecnología Química (UPV-CSIC) as supervisors,

CERTIFY, that this doctoral thesis, entitled: "**Hybrid Lead Perovskites as Photocatalysts and Materials for Photo- and Electrocatalytic N_2 Reduction**", has been developed by Yong Peng, in the doctoral program in Sustainable Chemistry, at the Instituto de Tecnología Química (ITQ), Universitat Politècnica de València (UPV).

Prof. Hermenegildo García Gómez Dr. Josep Albero Sancho

Acknowledgements

It has taken me almost 6 years to achieve my target since the first time I had an aggressive thought to pursue a doctoral degree abroad. The process was tough and stressful, and on some occasions, I even doubted my ability. Fortunately, my wife always supported and encouraged me without hesitation when I was about to crumble. The support from my parents, parents-in-law and Prof. Zhang (my director in my master's stage), also endow me with the courage and confidence to proceed, thus enabling me to finally enter the gate of a new career.

I hereby express my deep acknowledgment to my supervisor Prof. Hermenegildo García Gómez, who has shaped my scientific research habit during my doctoral study. I met Prof. García in 2017, when I got an impression of his easy-going character, unlike my previous sophisticated concept that a worldwide famous professor should be rigid and unapproachable. What latter amazed me is his profound knowledge. His is like a dictionary of both inorganic chemistry and organic chemistry, that can always give answers to my doubts and come up with an idea regarding any of my problems. I was influenced by Prof. García and have tried my best to extend my knowledge in different research fields during the last three years. Besides the above all, I also thanks Prof García for his support on my personal life in Valencia. Living in a foreign country, especially with my wife accompanying, I had some problems occasionally, and Prof. García always ready to help. I still remember one word from his, 'The most important thing is that you are happy here'.

I thank my supervisor, Dr. Josep Albero Sancho. I received tremendous support from him from the moment I step on the earth of Spanish territory. As I said, settling down in a foreign country, especially when you have a language barrier with them, is very difficult. Thanks to Dr. Josep, all those things became easier with his help. He helped me with my accommodation and accompanied me to make all the official documents. Most importantly, I thank Dr. Josep for his guidance in my experiments. He was always willing to listen to my ideas, and

discuss with me my experimental results, thus timely corrected my research direction.

Prof. María Mercedes Toledo Aliaga and Mrs. Inmaculada Cubas Moreno, thank you very much for your assistance with my Ph.D. applications, and also thank you for helping me solve different kinds of issues in my family's life in Valencia.

Dr. Abdessamad Grirrane, a kind-hearted man and always willing to help. Thank you very much for solving lots of problems I had in my experiment in the last three years. Dr. Aicha Anouar, you are so helpful, and thank you very much for being a translator whenever I asked.

Esther Domínguez Torres and Amparo Forneli Rubio, two elder sisters in the lab, can always offer me the experimental instruments that I asked for. Also, thank you for giving me lots of help and advice about taking care of the baby.

It is of a great fortune to meet and work with you all, parters from ITQ (Dr. Ana Maria Primo Arnau, Dr. Hermenegildo Garcia Baldovi, Dr. Diego Mateo, Dr. Sonia Remiro Buenamañana Dr. Jinbao He, Lu Peng, Alejandra Rendón Patiño, Ana Garcia Mulero, Ruben Ramirez Grau, Horatiu Szalad, Alberto Garcia Baldovi, Jiajun Hu, Xiangze Du), parters from the chemistry department (Prof. Sergio Navalón, Dr. Belén Ferrer, María Cabrero-Antonino, Arianna Melillo, Cristina García Vallés) and partners from CPI (Prof. Pedro Atienzar Corvillo, Rocío García Aboal and Elena Segura Sanchis).Because of help from all of you, my life in Valencia and my laboratory work became easier.

I would like to express my thanks to the technicians from the characterization center (Rosa, Marta Puche, Dolo, Adelina, Amparo, Maribel, Patricia, Jose Miguel, Cristina, Maria Jesus, Fani, Estrella, Miguel, etc) and the microscopy center (Merche, Manolo, Jose Luis, Alicia and Ximo**)** for help me to acquire nice images for my research. I also need to thank the workshop (Oscar, Álvaro, Javier Pérez, etc), especially Oscar, for the equipment maintenance and reactor modification.

I also want to express my appreciation to the administrative staff and security guards in ITQ, for that you ensure a good research environment for us.

Lastly, I would like to give my thanks to my wife and little daughter for you bring me motivation to strive and offer me a harbor to rest. I love you all.

Valencia, 15th June, 2021

Abbreviations

HRTEM	High-Resolution Transmission Electron Microscopy
HAADF	High-Angle Field Image Detector
SEM	Scanning Electron Microscopy
XRD	X-Ray Powder Diffraction
EDX	Energy-Dispersive X-ray Spectroscopy
ICP-OES	Inductively Coupled Plasma Optical Emission Spectroscopy
EA	Combustion Elemental Analysis
XPS	X-Ray Photoemission Spectroscopy
DRS	Diffuse Reflectance UV-Vis Spectroscopy
FTIR	Fourier-Transform Infrared Spectroscopy
XRF	X-Ray Fluorescence Spectroscopy
HPLC-MS	Ultra-performance Liquid Chromatography
GC	Gas Chromatography
NMR	Nuclear Magnetic Resonance Spectroscopy
TG	Thermal Gravimetry
µm	Micrometer
µmol	Micromole
µg	Microgram
µs	Microsecond
nm	Nanometer
mg	Milligram
mW	Milliwatt
HI	Hydroiodic Acid
HCl	Hydrochloric Acid
Ar	Argon
O_2	Oxygen
N_2	Nitrogen
H_2	Hydrogen
τ	Half Life Time
H_2SO_4	Sulfuric Acid
Cs_2CO_3	Cesium Carbonate

PbI_2	Lead Iodide
DMF	Dimethylformamide
$RuCl_3$	Ruthenium Chloride
KI	Potassium Iodide
$PbBr_2$	Lead Bromide
NaClO	Sodium Hypochlorite
MA	Methylammonium
BDA	Di-cation of 1,4-diaminobutane
BZ	Benzidine
BZI	Benzidinium Diiodide
BHP	Benzidinium lead iodide hybrid perovskite
BZN	Benzidinium Dications
ODTMS	Trimethoxy(octadecyl)silane
TEOS	Tetraethyl Orthosilacate
FTS	Triethoxy Perfluorodecyl Silane
SHP	Surface-silynated Hybrid Perovskite
SA	Styryl Ammonium Iodide
PHP	Surface-polymerized Hybrid Perovskite
STO	Strontium Titanate
tpzB	Tris(pyrazolyl) Borate Anion
CV	Cyclic Voltammetry
CA	Chronoamperometry
Fc	Ferrocene
ACN	Acetonitrile
THF	Tetrahydrofuran
ORTEP	Oak Ridge Thermal Ellipsoid Plot
LSPR	Localized Surface Plasmon Resonance
NP	Nanoparticles
UV	Ultraviolet
Vis	Visible
NIR	Near-Infrared

Table of Contents

Chapter 1 General Introduction

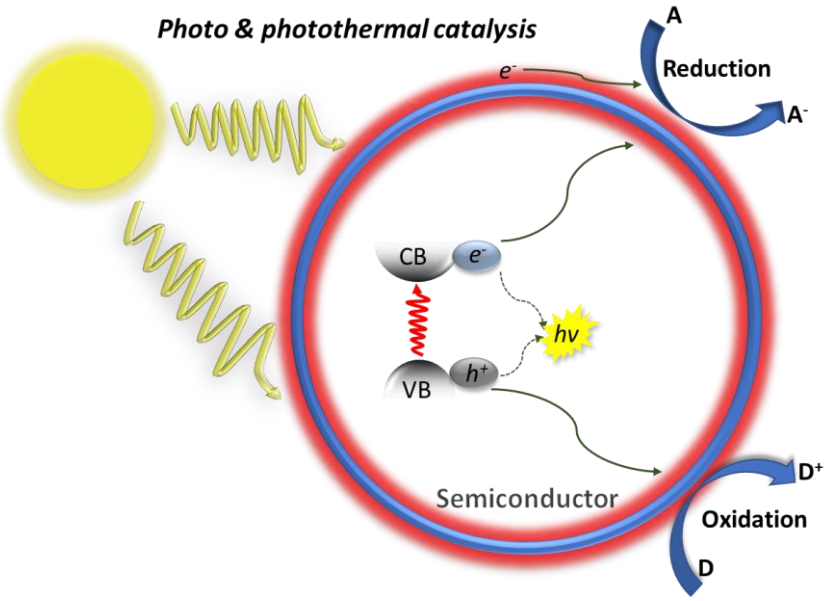

1.1 Natural Photosynthesis

Life on Earth is based on the energy of the Sun and the photosynthetic activity of bacteria, algae and green plants. Photosynthetic living organisms use the photons energy reaching the Earth's surface from the Sun to reduce CO_2 by the action of H_2O to form glucose. The process is indicated in eq. 1.1 and is extremely endergonic.[1]

$$CO_2 + H_2O \rightarrow C_6H_{12}O_6 + O_2 \qquad \textbf{Equation 1.1}$$

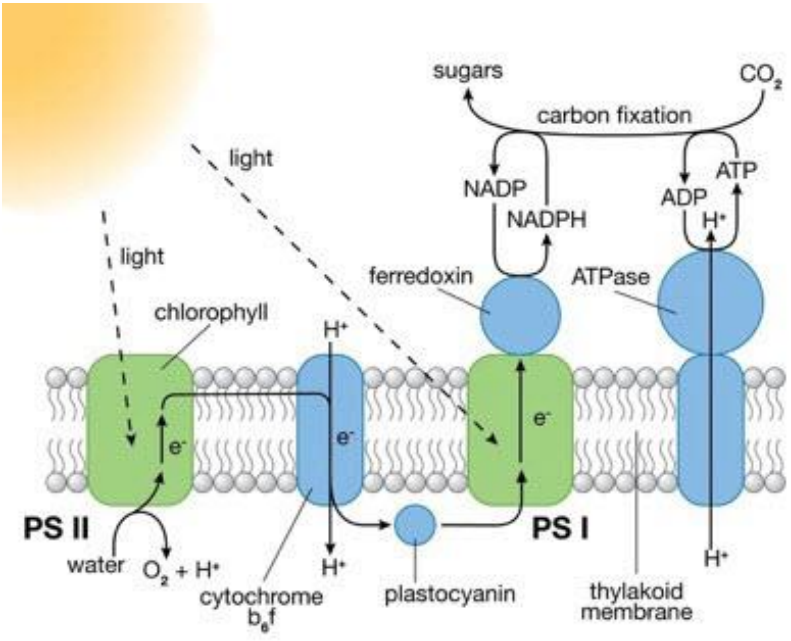

Scheme 1.1 Schematic illustration of the natural photosynthetic process.

Natural photosynthesis in green plants takes place in the thylakoid membrane where a complex and delicate array of embedded proteins are spatially ordered in contact with light harvesting centers, electron relays and catalytic sites. The photosynthetic center is split in two main parts, photosynthetic system I (PSI) and II (PSII) and connecting quinonic and cyanine moieties to transfer electrons and protons (H^+). The membrane ensures the location of all the components in a spatial

arrangement that enhances the rates of electron transfer and an enhancement of H^+ concentration inside the thylakoid, being this higher than on the lumen, and fueling the operation of the ATP synthesis through the complex ATPase motor.[2] Scheme 1,1 illustrates some of the features of the natural photosynthetic system.

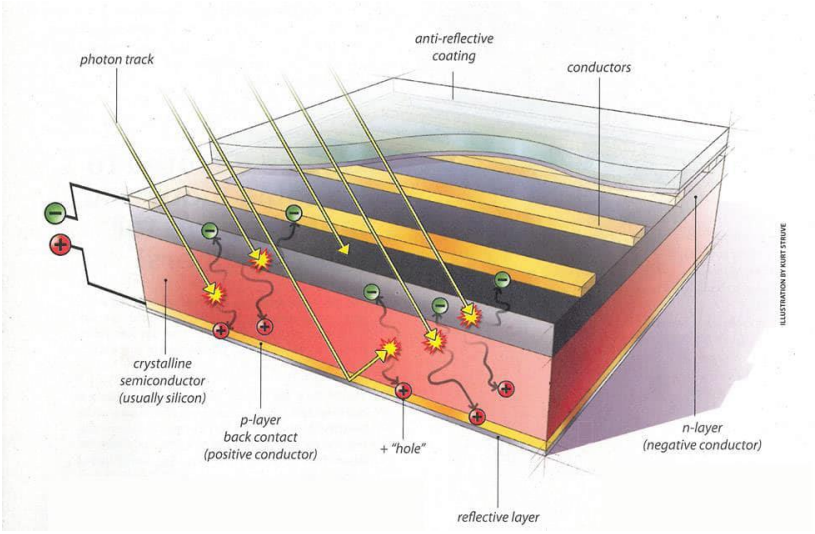

Scheme 1.2 Diagram of a typical crystalline silicon solar cell and the operation mechanism.

1.2 Artificial Photocatalysis

1.2.1 Methods of Solar energy conversion

Considering the vast amount of Solar energy reaching the Earth surface, there is an obvious interest in making use of this clean and inextinguishable energy. Besides indirect ways of taking advantage of Solar energy, like using wind to move turbines, marine streams and others, the direct use of sunlight as primary energy source has attracted considerable attention in the last decades, in this regard, photovoltaics is a mature technology that has reached commercial application. In photovoltaics, the energy of a solar photon is absorbed by a semiconductor or a junction of semiconductors, generating charge separation with the promotion of one electron from the valence to the

conduction band. The conduction band electron migrates to the electrical circuit causing a voltage difference.[3] The most commonly used photovoltaic devices are based on silicon, either crystalline or amorphous. Scheme 1.2 illustrates the operation mechanism of semiconductor photovoltaics and the structure of a silicon solar cell.

1.2.2 Solar light capture and electron/hole pairs generation

While photovoltaics convert solar energy into electricity with an efficiency above 20 %,[4] there is a certain interest in the conversion of solar energy directly into chemicals, mimicking in natural photosynthesis. The general advantage of the sunlight-to-chemicals process is that chemicals can store massive amounts of energy in chemical bonds that can be released on demand. After all, this is the concept of fossil fuels and hydrocarbons as energy source that has been powering the modern societies since 19th Century. In contrast, electricity storage requires of additional electrical devices that have to be connected to the power grid and make complicate decentralization and energy production in remote geographical places.

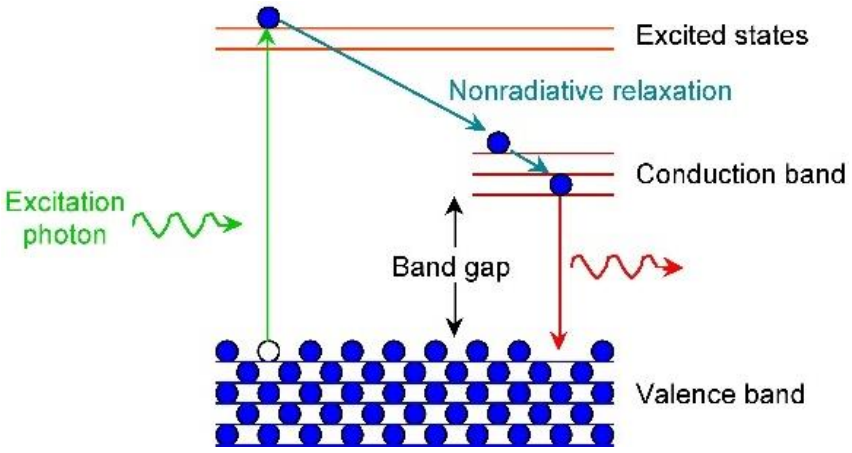

Scheme 1.3 illustration of the elemental steps in photoactive materials upon light absorption, including photogeneration of electrons and holes, and subsequent radiative and non-radiative deactivation.

Thus, although photovoltaics has achieved a considerable degree of efficiency and maturity, there are still opportunities for developing alternative processes based on sunlight as primary energy source. One of these methods that meets the research area of the present Doctoral Thesis is photocatalysis. In photocatalysis, a material absorbs photons having energy higher than the energy gap between the frontier occupied and empty electronic states and promotes an electron jump from the ground to a transient state.[5, 6] Scheme 1.3 illustrates the elementary steps that can occur upon photon absorption in a photoresponsive particle.

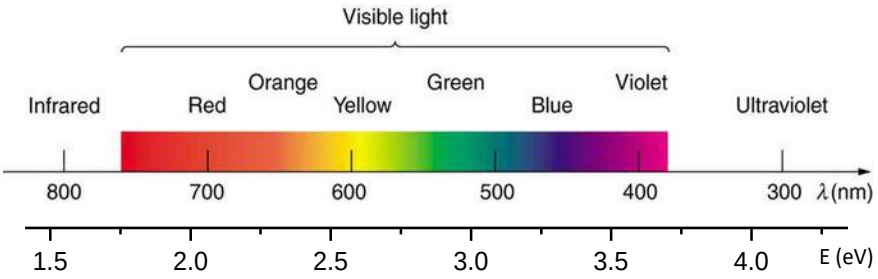

Fig. 1.1 Relationship between the semiconductor bandgap value (eV) and the corresponding band wavelength of the onset UV-vis absorption.

Typical photocatalysts are semiconducting materials, in which it is possible to promote one electron from the occupied valence (localized) band to an electronically excited partially or totally empty state that is denoted as conduction band. The term semiconductor alludes to the fact that the electrical conductivity of this material can increase orders of magnitude when the conduction band is somehow populated, as for instance, electrochemically or upon irradiation. In this way, the material has two states with contrasting electrical properties. The difference in energy between the valence and the conduction band is denoted as “bandgap” (Scheme 1.3). The semiconductors can be classified as wide or narrow bandgap depending on whether the bandgap energy is higher or lower than 2.5 eV. The possibility of the electronic transition from the valence to the conduction band by photon absorption is reflected in the UV-Vis absorption spectrum of the semiconductor by

the appearance of an absorption band. If the semiconductor is wide bandgap, then, the absorption band in the optical spectrum should appear in the UV range. In contrast if the semiconductor is a narrow bandgap material, the absorption should have a wavelength maximum in the visible and even in the near-infrared region. Figure 1.1 illustrates the relationship between the semiconductor bandgap and the position of the absorption band in the UV-Vis-NIR spectrum.

Upon absorption and electron promotion, a transient excited state is produced in the semiconductor. This excited state is generally denoted in semiconductors as charge separation state. The most general way to deactivate this excited state is by electron recombination by returning to the valence band. The deactivation can occur in a non-radiative way by passing the electronic energy to the lattice of the material (electron-phonon coupling) and producing the heating of the material (light to heat conversion) or the electron can return to the ground state in a radiative mode by emitting a photon of longer wavelength than the wavelength of the photon absorbed. Typically, the radiative mode (photoluminescence) is a minor deactivation pathway and this can be assessed by measuring the number of photons emitted by the semiconductor in comparison to the number of photons absorbed. These photons emitted vs. photons absorbed is denoted as photoluminescence quantum yield and, even though they are difficult to determine accurately in solid due to the uncertainty in photon absorption vs. scattering, they are typically very low in the range of 0.1%. However, since it is possible to detect spectroscopically even a single photon, photoluminescence is a routine technique typically used to characterize semiconductor materials. Scheme 1.4 illustrates the ways of electron deactivation and the typical detection system of photoluminescence in semiconductors.

As indicated above, the transient state is denoted as a charge separated state. The reason for this term is that a third possible pathway towards electron deactivation in a semiconductor is by electron or hole migration. In this way the distance between the promoted electron and the local position where light absorption

occurred increases and, consequently electron deactivation become much more difficult. Scheme 1.5 depicts the process of charge (electron or hole) migration and the *random walk* until other charge recombination event occurs.

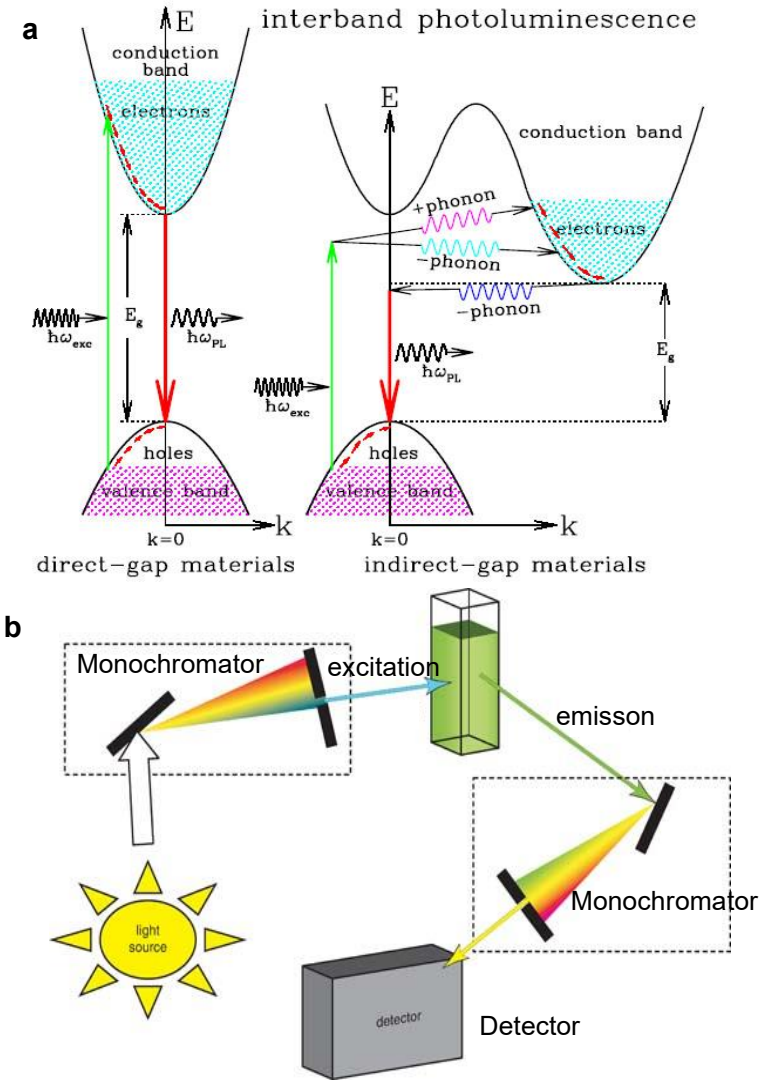

Scheme 1.4 (a) Band diagrams for the photoluminescence processes in a direct gap material (*left*) and an indirect gap material (*right*). (b) a representative fluorescence spectrometer and the detection process.

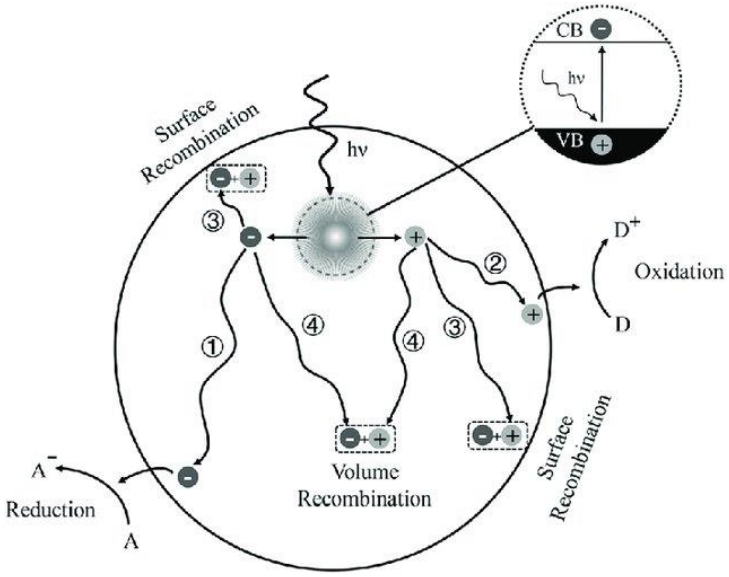

Scheme 1.5 Depiction of photoinduced generation of an electron-hole pair in a semiconductor with possible decay paths. A = electron acceptor, D = electron donor.[7] Copyright 2013, Wiley-VCH.

Depending on whether electrons in the conduction band or holes in the valence band are the species that migrates faster, the semiconductor is denoted as "*n*" or "*p*" semiconductor. It is generally indicated that electrons migrate faster in n-type semiconductors, while in contrast, the positive holes undergo faster delocalization in p-type semiconductors. In any case, when there is a charge (electron or positive hole) migration, the process of photoexcitation results in a long-lived state of charge separation. Electron and hole recombination becomes much slower when any of the two charge carriers migrate fast from the site where light was absorbed. A quantitative number to determine the efficiency of charge migration is the charge migration length that is the average length travelled by the charge carriers without undergoing recombination. [8-11]

Typically, "geminate" charge recombination (recombination of electrons with the holes that were created in the same event) occur in the time scale of picoseconds to nanoseconds. In contrast if the event

of migration of any of the charge carriers occur, then, the life time increases by six orders of magnitude extending to the microsecond or even longer time scale. Scheme 1.6 shows kinetic information related to charge migration processes.

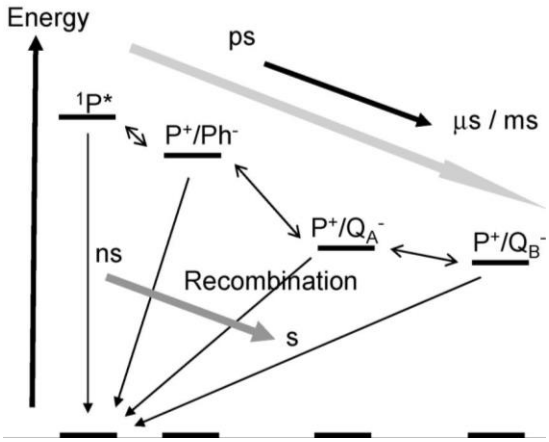

Scheme 1.6 Illustration of the energetics and kinetics of charge separation in semiconductors. [12] Copyright 2010 American Chemical Society.s

1.2.2 Photocatalytic chemical reactions.

Semiconductor materials can have special structural sites in which charge carriers can be trapped. They are sites in which the energy of the electron or hole decreases and, therefore, they stop or make even slower, the charge migration. The binding energy of the charge carriers and the trapping agents can be determined based on the influence of the temperature on the photoluminescence[13] or by transient absorption spectroscopy (TAS).[14] Typically, values for charge carrier binding energies are in the range of tens of J/mol. The existence of trapping sites in the material increases the life time of the charge carriers, since their migration is slow.[11] Thus, one quantitative number that is important in photocatalysis is the efficiency of charge separation and this can be calculated by determining the percentage of electron excitation events that result in electrons surviving in the µs time scale. Scheme 1.7 illustrates some of the quantitative terms that serve to determine the electronic properties of a semiconductor.

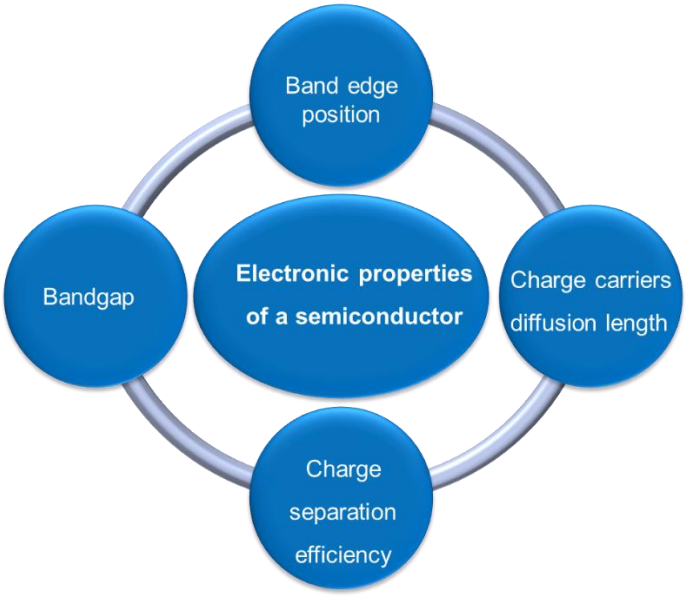

Scheme 1.7 List of the quantitative terms that serve to determine the electronic properties of a semiconductor.

Surface of materials are places where structural defects are generally more abundant. Thus, particularly for particulate semiconductors, if the charge carrier migration length is longer than the particle size, at least one of the charge carriers has had the opportunity of explore the particle and, probably reach the external surface. The defects of the external surface and the terminal groups present there would act as trapping sites, holding the charge carriers there. Once on the external surface, electrons and holes are available to promote chemical reactions. As many compounds can participate in redox type reactions, the electrons and holes on the surface of an illuminated semiconductor can promote reduction (by surface electrons) and oxidation by surface holes of substrates that could be adsorbed or in contact with the material. The conduction band electrons, after migration and trapped on the surface sites exhibit a reduction potential. Similarly, valence band holes after generation and migration to the surface, located at their corresponding trapping sites will have an oxidation potential that depends on the semiconductor. Therefore,

another important parameter of the semiconductor is the energies of the photogenerated electrons and holes.

Since most of the photocatalytic reactions by semiconductors are carried out in contact with the atmosphere, the most reducible chemical always present in contact with the semiconductor is molecular oxygen. Molecular oxygen can be easily reduced by surface electrons forming initially superoxide ($O_2^{\cdot-}$). Upon protonation, superoxide forms hydroperoxyl radicals (HOO·). Subsequent reduction forms hydroperoxide that upon a second protonation gives rise to hydrogen peroxide. The process can continue forming numerous oxygenated species that are denoted as *reactive oxygen species.* Scheme 1.8 indicates the processes that can occur upon reduction of ambient O_2.

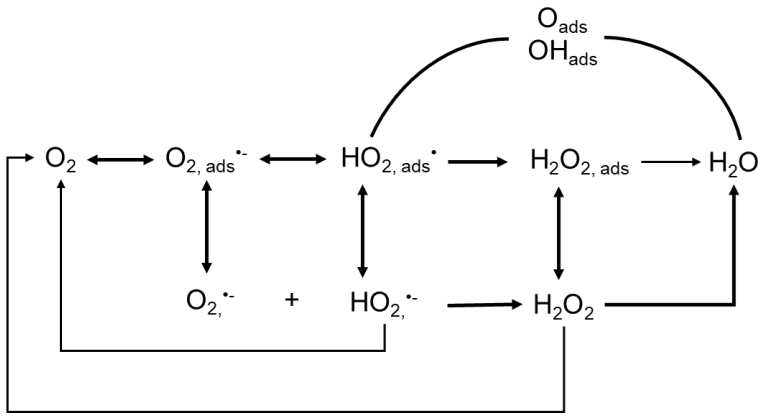

Scheme 1.8 Simplified reaction mechanism connecting some of the reversible reaction oxygen species. Reproduced from ref 15. Copyright 2018 Science Direct.

The positive holes can promote oxidation. In contact to the Earth atmosphere the most oxidizable chemical is water. Upon oxidation, H_2O forms hydroxyl radical (HO·) releasing a proton. Hydroxyl radicals are very aggressive species and would react with many organic and inorganic compounds, but in the absence of other chemical it would dimerize to form hydrogen peroxide. H_2O_2 can form hydroperoxyl and

superoxide as previously indicate. Scheme 1.8 also includes the processes derived from H_2O oxidation.

1.3 Photothermal Catalysis

Heterogeneous catalysis is one of the most important types of catalysis. Industrial processes such as those reactions involving the formation of ammonia from Haber-Bosch process,[16, 17] hydrocarbons from Fischer-Tropsch reactions[18, 19] and hydrogen from methanol reforming[20, 21] or methane reforming[22, 23], all being heterogeneous catalytic process, requiring extremely high temperatures and pressures. Accordingly, these processes are energy-intensive and unavoidably produce a massive amount of CO_2, sulfur dioxide and oxynitrides, causing environmental problems like global warm and air pollution. In this context, photocatalysis was pushed to the center stage among the research fields. However, despite massive works have been reported on artificial photosynthesis since the first report in 1972,[24] targeting at converting the clean solar energy directly to chemical fuels through water splitting or CO_2 reduction with water,[5, 25-28] the energy conversion efficiency is still too low for any practical application, especially at industrial scale.

The practical demand of massive chemical fuels to sustain human daily activities determines that in spite of it is deemed that the artificial photosynthesis would be the ultimate solution to energy crisis, global warm and environmental pollutions, other forms of solar energy utilization should be developed to complement the traditional efficient heterogeneous catalytic process. Thus, it inspired the concept of photothermal catalysis, by which the solar energy is converted into heat and thereafter synergistically drive the heterogeneous catalytic reactions through a thermal reaction mechanism.

1.3.1 Solar thermal heating

In photothermal catalysis, one key point is to efficiently convert the solar energy to heat. The direct conversion of light to heat can be carried out through traditional solar thermal heating, in which black

materials absorb photons, inducing, subsequently, phonon vibrations, and consequently elevating the materials temperature. Other possible way to convert solar light into heat is indirect by converting through recombination of hot electron/holes. Specifically, for semiconductors, the light absorption will induce the generation of electrons and holes pairs, the process of that is the same as the one mentioned in the photocatalytic process. But instead of migrating to the reaction site, the charge carriers must recombine through non-radiative processes and the released energy would thereafter be transferred to the phonons, contributing eventually to the heat generation.[29]

1.3.2 Local surface plasmonic resonance effects

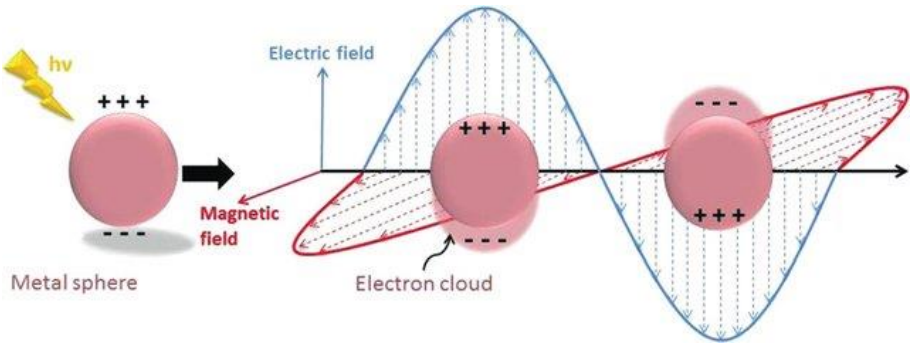

Scheme 1.9 Depiction of the localized surface plasmon resonance effect.

Local surface plasmonic resonance (LSPR) effect appears to be another form to carry out photothermal catalysis. The LSPR can be explained as the light-excited collective oscillation of electrons confined in metallic nanoparticles (NPs) and this oscillation can in turn causes dramatic light absorption at certain wavelengths in the visible or NIR range, (as schematically illustrated in Scheme 1.9). Consequentially, the local electromagnetic field in the vicinity of the particle surface is amplified, and thus can also facilitate the electron/hole pairs separation in a semiconductor in close contact with the plasmonic metal NPs.[30, 31] Besides, this conducting electron oscillation can generate hot electrons in an athermal way, that can thereafter activate the reactant in photothermal reactions.[32-34] Although the mechanism of LSPR

photothermal catalysis is not very clear yet, a large number of research works have proposed several possible mechanisms, which are summarized in Scheme 1.10.[35, 36]

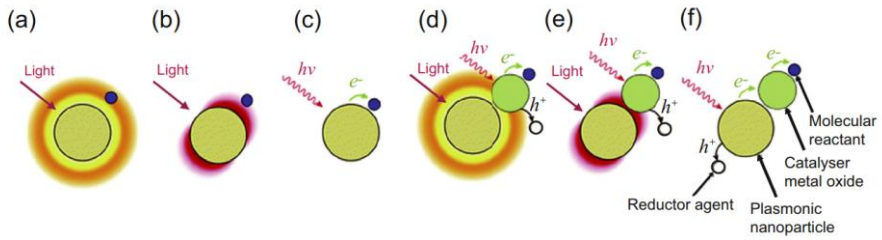

Scheme 1.10 Possible mechanisms for LSPR catalysis: (a) LSPR induced local temperature increase and transfer to the adsorbed reactant; (b) adsorbed reactant experiencing an increase in incident photon rate; (c) LSPR induced hot electron injection to the reactant; (d) increased local temperature facilitate the generation of electron and holes of the vicinity semiconductor; (e) near field optical enhancement experienced by semiconductor, leading to enhanced electron-hole generation; and (f) hot electron injection into the neighbouring semiconductor, which is then transferred into a reactant molecule nearby.[35]

The above discussion serves to illustrate that photocatalysis or photothermal catalysis can serve to promote chemical reactions, by converting a fraction of the photons absorbed into reactive surface electrons and holes at high redox potential or by converting the photon energy into local heat at the nanometric scale. In the present Doctoral Thesis, light involved catalysis (including photocatalysis and photothermal catalysis) will be used to promote chemical reactions such as the room-temperature *cis-trans* isomerization of *cis*-stilbene or N_2 reduction to ammonia.

1.4 The Development of Photocatalyst

1.4.1 Development of TiO_2 photocatalyst

TiO_2 is by far the most studied photocatalyst. About half of the papers on photocatalysis involve TiO_2 somehow. The reason for this TiO_2 prevalence is a combination of positive features, including

availability, high stability, lack of toxicity and a remarkable performance under UV irradiation.[37] TiO_2, like most transition metal oxides, is a wide bandgap semiconductor. Depending on the crystal phase, the bandgap ranges between 3.0 to 3.2 eV, and this means that the absorption band onset of TiO_2 is located about 380 to 400 nm.

While the photocatalytic activity of TiO_2 under artificial UV light of wavelengths shorter than 380 nm can be very high with apparent quantum efficiencies reported in the range of 30-40 %,[38] the lack of absorption in the visible region has determined the lack of TiO_2 photoresponse upon natural solar light illumination. Although it has been generally found that the rutile phase has lower photocatalytic activity than the anatase phase, the combination of some rutile (about 30 % or less) with a prevalent anatase phase, as it occurs on the commercial Evonics TiO_2 sample denoted as P25, renders one of the benchmarks TiO_2 materials exhibiting the highest efficiency. It has been proposed that the combination of rutile and anatase with a strong interaction due to the pyrolytic synthesis of P25 forms a heterojunction that favors charge transfer.[39] However, still P25 is not photoresponsive under solar light or visible light irradiation.

The solar radiation reaching the Earth's atmosphere undergoes filtration of the deep UV light by the ozone layer and other components at the atmosphere. Figure 1.2 presents the solar spectrum at the surface level. As it can be seen there, most of the energy of the solar photons correspond to the IR with about 52 % of the total solar energy. The energy of the photons corresponding to the visible region is about 44 %. Thus, the energy of the UV photons from the sunlight is very minor, about 4 %. Consequently, in order to promote sunlight photoresponse in TiO_2, various strategies have been developed, including photosensitization with dyes,[40, 41] doping with metal[42, 43] and non-metallic elements[44, 45] and surface amorphisation.[46] Fig. 1.3 illustrates the various strategies that have been followed to expand the TiO_2 photoresponse towards the visible region.

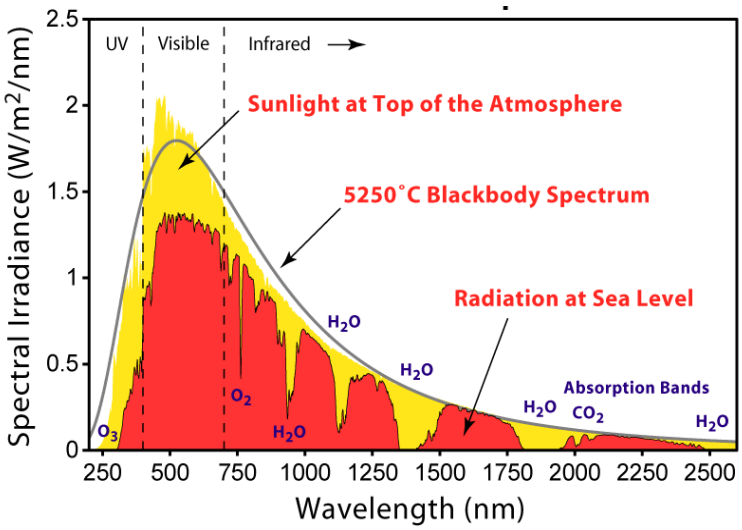

Fig. 1.2 Solar radiation spectrum

While there has been some progress to implement visible-light photoresponse in TiO_2, the current state of the art is still unsatisfactory. On one hand, the photoresponse has only been shifted an insufficient range, as for instance with N-doping.[47] On the other hand, the high photocatalytic activity observed for TiO_2 under irradiation on appropriate UV wavelengths becomes considerably diminished.[47] This deterioration of the photocatalytic activity upon TiO_2 modification derives in a large extent from the requirement of high crystallinity that is generally rule out in semiconductors and also particularly in TiO_2. It has been observed under UV light that the photocatalytic activity of amorphous TiO_2 samples is poor compared to highly crystalline samples. This fact has been interpreted considering that due to the presence of defects in amorphous samples, the defect sites act as charge carrier trap centers, decreasing charge carrier mobility and promoting charge carrier recombination.[48]

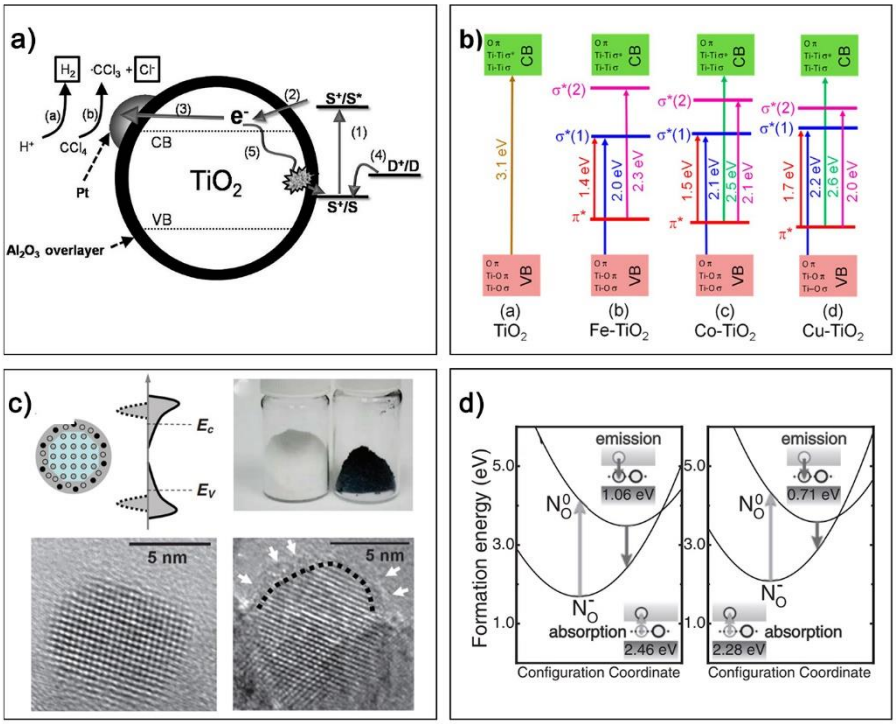

Fig. 1.3 Examples illustrating TiO_2 bandgap engineering strategies to expand the range of visible light response, including a) dye sensitization [40], b) metal doping [49], c) surface amorphous[46] and d) nitrogen doping [44].

Besides, the most widely accepted explanation for low efficiency from the doping strategy is the dual role of dopants as light harvesting centers by introduction of intra bandgap states and the role as charge carrier recombination points. These opposite effects generally meet a compromise, there being an optimal dopant concentration. [50] Lower or higher dopant percentages results in lesser photocatalytic efficiency due to either low light absorption or high charge recombination.

Regarding charge recombination, it has been recently disclosed in well crystallized samples with defined crystallographic facets, that electrons and holes migrate to different facets. Thus, charge recombination can be in some extent disfavored by preparing samples in which the required facets are well developed.[51, 52] Crystallization of

these TiO_2 can be performed using fluorides or other ligands that bind strongly to certain facets, thwarting their growth as the crystal is being formed (Scheme 1.11).

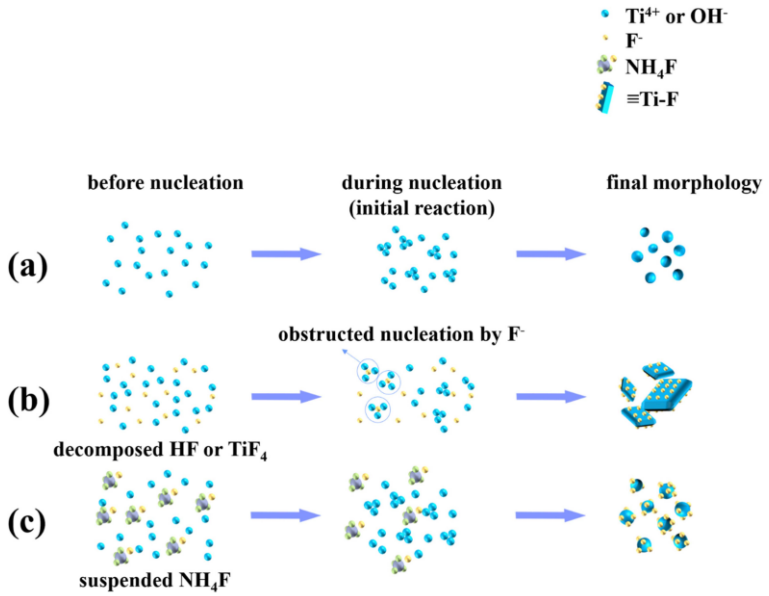

Scheme 1.11 Schematic illustration of the suggested growth behaviors with ligand treatment: (a) pure, (b) HF or TiF_4, (c) NH_4F.[53] Copyright 2016 IOP Publishing Ltd.

Dye sensitization has been proven to be useful in the design of dye-sensitized solar cells based on nanoparticulate TiO_2 with certified efficiencies over 10 %. However, it has led to unsatisfactory results in photocatalysis. [54, 55] one of the reasons of the little success of this approach has been attributed to the degradation of the expensive dyes used in the photosensitization under the operation conditions of the photocatalytic reactions.[56, 57]

1.4.2 Other metal oxide photocatalysts

There has been a considerable effort trying to implement other semiconductor materials, besides TiO_2, in photocatalysis. Other metal oxides like ZnO,[58] Cu_2O,[59] Fe_2O_3,[60] WO_3,[61] CeO_2[62] and ZrO_2[63] have also been reported as photocatalysts. The photocatalytic activity of

ZnO is very similar to that of TiO_2, except that ZnO is not chemically stable and dissolves in acid aqueous media. Similar corrosion of photocorrosion occurs for Cu_2O[64] and Fe_2O_3[65]. Thus, either these other metal oxides do not enjoy the remarkable chemical stability of TiO_2, or they do not again absorb visible light (CeO_2 is a pale-yellow material absorbing at 400 nm[66]) or the photocatalytic efficiency is low due to charge recombination. Thus, no advantage is apparent.

Besides metal oxides, metal oxide salts such as titanates, or mixed metal oxide salts, like strontium titanate or bismuth vanadate, have also been studied as photocatalyst.[67-70] The area has expanded with other hybrid organic-inorganic materials, like metal-organic frameworks, and metal-free photocatalysts like graphitic carbon nitride and doped graphenes.[71-74] Figure 1.4 illustrates various types of photocatalysts showing the width of possible materials.

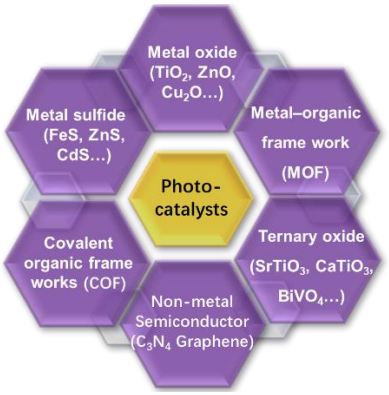

Fig. 1.4 Summary of various types of reported photocatalyst.

1.4.3 ABO_3 type perovskites

Among them, those having a crystal structure of perovskites have shown high photocatalytic activity. Perovskites having a general formula of ABO_3 are characterized by having two metal ions of very different ionic radii due to the different charge. The smallest cation occupies the center of an octahedral of O^{2-} ions forming BO_6 units. The oxide anions are, on the other hand at the center of each of the six faces of a cube. Then the larger A cation is located at the corners of

this cube. Fig. 1.5 illustrates the unit cell of a perovskite. The first found mineral with perovskite structure was $CaTiO_3$ in the Urals. However, there is a wide range of combinations of metal ions that can form oxides with perovskite structure. Among them, one that is relevant in the present Doctoral Thesis is $SrTiO_3$ that would be the support of active ruthenium metal NPs that would be studied in Chapter 6 as photocatalyst for N_2 hydrogenation. While some titanates of alkali metals are layered solids, the perovskite structure exhibits a considerable structural stability, a prerequisite that is needed for the use of the material in photocatalysis.

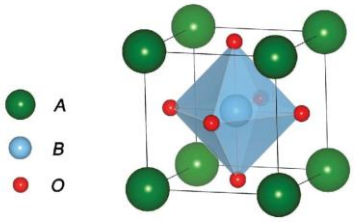

Fig. 1.5 A unit cell of ABO_3 perovskite structure.

Strontium titanate doped with Al and having co-catalysts was reported by Domen and coworkers as one of the most active materials to promote the photocatalytic overall water splitting into the corresponding stoichiometric amounts of hydrogen and oxygen.[75] Our group has shown that ruthenium NPs supported on $SrTiO_3$ is one of the most efficient photocatalysts for photocatalytic CO_2 hydrogenation to methane (eq. 1.2).[76] It was found that the mechanism for this reaction is photothermal, meaning that light is converted into local heat on the Ru NP producing a temperature increase on the NP. The role of $SrTiO_3$ is as heat insulator avoiding dissipation of the heat localized on Ru towards the support. Thus, the low thermal conductivity of $SrTiO_3$ plays a key role on the process.

$$\boldsymbol{CO_2 + 4H_2 \xrightarrow{catalyst} 2CH_4 + 2H_2O} \qquad \textbf{Equation 1.2}$$

From the comments on the photocatalytic activity of TiO_2 and the efforts that have been made so far, it can be concluded that there is still a considerable room for improvement of the photocatalytic efficiency and exploration of the performance of new materials is necessary.

1.4.4 Hybrid organic metal perovskite as photocatalysts

In this context, it was reported by Miyasaka and coworkers in 2009 that hybrid organic lead perovskites exhibit a considerable photovoltaic performance by incorporating as addictive to TiO_2.[77] Among the possible hybrid perovskite, the one that was first reported with $MAPbI_3$ perovskite in which MA corresponds to methylammonium cation and the anion is iodide. Figure 1.6 shows the structure of $MAPbI_3$ perovskite together with a scheme of a solar cell based on this hybrid material. In contrast to the slow progress achieved in dye-sensitized TiO_2 solar cells in which upon a massive research an efficiency slight over 10 % of solar light into electricity conversion has been achieved in about four decades, hybrid organic lead perovskites have reached in only a few years a certified solar light conversion efficiency over 20 %,[78] in the range of the value that can be considered for commercialization.

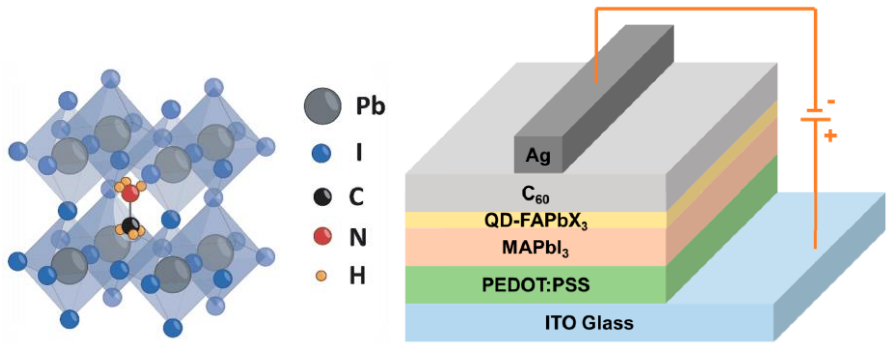

Fig. 1.6 Methylammonium lead iodide perovskite ($MAPbI_3$) structure and the scheme of a solar cell based on this material.

Among the various reasons for this remarkably high efficiency, those three that are considered as the most important in the case of hybrid organic lead perovskites are:

i) an extended light harvesting and photon adsorption through the whole visible zone, with onset at about 750 nm.[79] This light absorption is a reflection of the narrow bandgap as compared to other perovskites and metal oxide semiconductors.

ii) a high electron mobility and diffusion length that facilitates the charge separation after the process of light absorption.[80] Calculations have indicated that over 50 % of the events of photon absorption result in charge separation.[81] This contrast with the much lower charge separation efficiency of TiO_2, and

iii) low binding energy of trapping sites, allowing an easy charge carrier detrapping.[82] Trapping sites act frequently as recombination centers, since by immobilizing one of the carriers impedes charge carrier diffusion.

Besides $MAPbI_3$, also $MAPbBr_3$ and $MAPbCl_3$ have been similarly reported.[83, 84] These materials are easily synthesized by dissolving separately MAX (X: I, Br and Cl) and PbX_2 in DMSO, DMF or other solvents and observing the slow crystallization of the resulting hybrid perovskite. MAX is, in turn, obtained by protonation of methylamine by the corresponding hydrohalic acid, such as HI. Eq. 1.3 illustrates the synthesis of these materials.

$$CH_3NH_2 + PbX_2 + HX \xrightarrow{DMF} CH_3NH_3PbX_3 \text{ in } DMF \xrightarrow[\text{or adding anti-solvent}]{\text{Solvent evaporation}} \text{Hybrid Perovksite} \qquad \textbf{Equation 1.3}$$

One of the main differences among the three possible halides is the bandgap and the associated visible-light absorption band wavelength that moves gradually to the blue from I to Br to Cl, the latter having an absorption onset at 450 nm.[85, 86] In addition of a single halide, there is the possibility to prepare hybrid methylammonium perovskites of a

mixture of two halides in a wide range of various proportions. These mixed-halide hybrid lead perovskites exhibit intermediate absorption and optoelectronic properties between the two extreme pure lead halide perovskites. Figure 1.7 shows the corresponding diffuse reflectance UV-Vis absorption spectrum of $MAPbX_3$ as a function of the nature of the X anion.

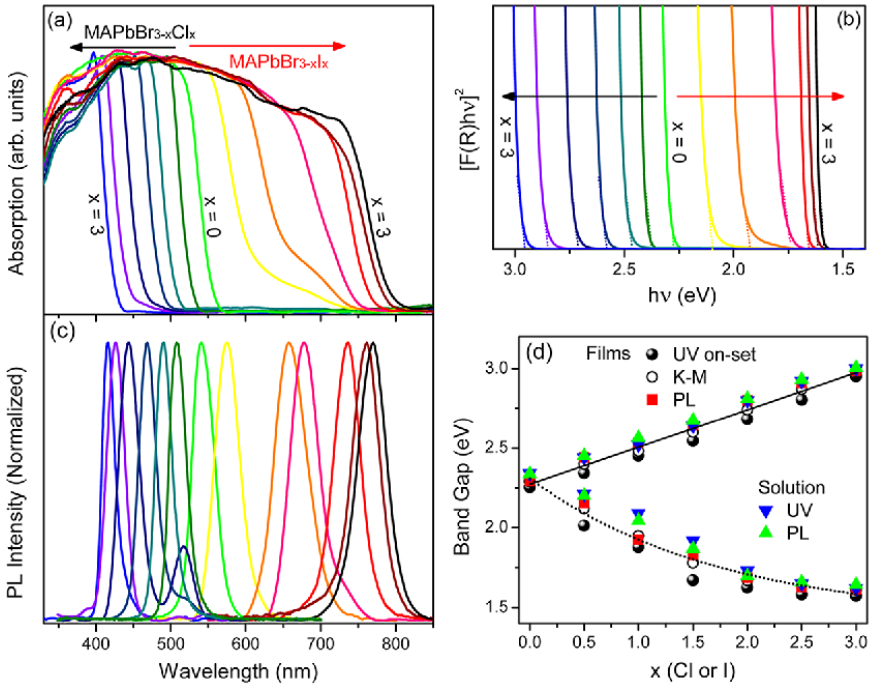

Fig. 1.7 (a) UV-vis diffuse reflectance spectra, (b) the corresponding Tauc plot, (c) photoluminescence spectra and (d) the band gap values of $MAPbBr_{3-x}Cl_x$ and $MAPbBr_{3-x}I_x$ materials, which demonstrate the relationship between the optical properties of the resulted perovskite and the nature of halides [87] Copyright 2015 American Chemical Society.

Besides halides, there have been attempts to find replacement for lead in the composition of the hybrid organic halide perovskite. This motivation derives in a large extent from the toxicity of lead that can cause *saturnism* and other mental disorders in humans. However, although organic hybrid perovskites of other transition and post-

transition metals such as Sn and Cu have been reported,[88, 89] the photovoltaic response of these alternative hybrid perovskites without lead is considerably much worst. As an example, the photovoltaic response of $MASnI_3$ is presented in Figure 1.8. It seems that these negative results derive from the correct balance between ionic and covalent bonding in the case of Pb that does not coincide exactly with those of other metals.

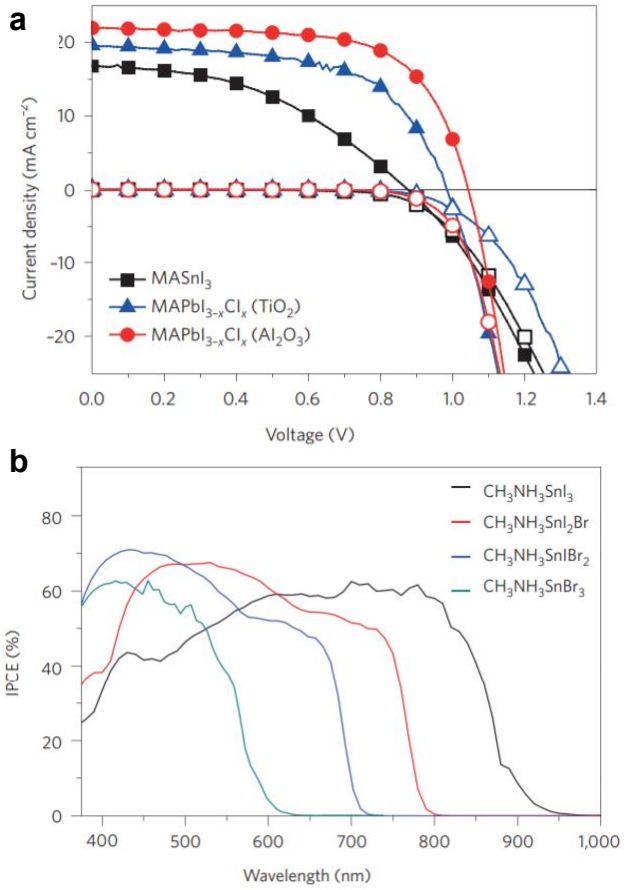

Fig. 1.8 (a) Current–voltage curves of Sn-based (on mesoporous TiO_2) and Pb-based (on either mesoporous TiO_2 or Al_2O_3) devices measured under AM1.5 simulated sunlight (100 mW cm^{-2})[90]. The lines denoted with hollow symbols are dark current–voltage curves. (b) Incident photon-to-converted-

electron (IPCE) fraction for the Sn-based perovskite solar cells with a range of different halides to tune the bandgap.[91, 92] Copyright 2019 Nature.

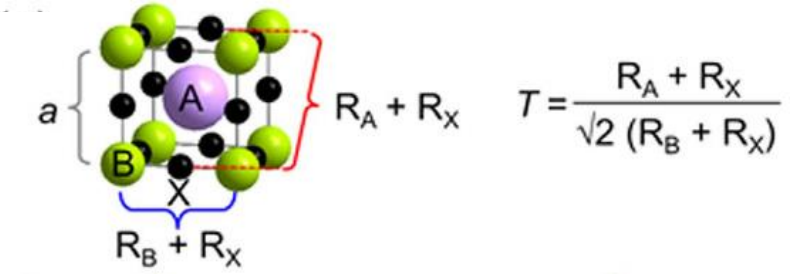

Fig. 1.9 The Goldschmidt tolerance factor and the corresponding model.[93] Copyright 2016 Nature.

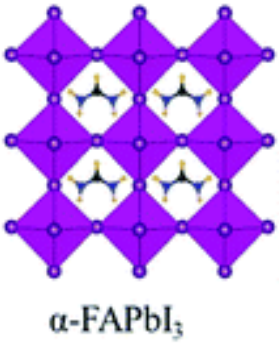

Fig. 1.10 The structure of Formamidinium lead iodide perovskite[94] Copyright 2019 Royal Society of Chemistry.

There have also been attempts to replace MA by other organic cations. However, the requirement of small size is a prerequisite to maintain the 3D crystal structure, since this organic cation has to fit within the voids of the surrounding halides. As the size of the cation increases, the PbI_6 octahedra start to distort from the cubic arrangement moving towards layered (2D) or even 1D structures. The Goldschmidt tolerance factor indicated in Figure 1.9 correlating the ionic radius of the elements involved is a simple rule to determine the feasibility of a 3D perovskite structure. Thus, so far, the only stable hybrid organic 3D perovskites besides those of MA are those having formamidinium cation (Figure 1.10).

Larger organic cations require larger space to be accommodated and, as consequence a change in the 3D to 2D structure occurs. For example, in the case of phenylethyl ammonium lead iodide ($(PEA)_2PbI_4$), the hybrid perovskite exhibits a 2D layered structure that in this way allows to accommodate the larger dimensions of the phenyl in comparison of the methyl group.[95] Figure 1.11 presents the structure of $(PEA)_2PbI_4$ as determined by single crystal XRD. The change in structure has significant consequences in the optoelectronic properties of the hybrid perovskite that losses most of the ideal properties of the 3D hybrid materials. First, the change from 3D to 2D is reflected in a notable blue shift of the onset of the absorption band, therefore, losing photoresponse in most of the visible range. Second, the charge separation efficiency and charge migration length become diminished due to the change in the structure.[96, 97] The variation of all these optoelectronic parameters has been responsible for the lesser interest in 2D perovskites respect to the 3D ones, in spite that the choice of organic ammonium ions in 3D is very limited.

Fig. 1.11 Illustration of the $(PEA)_2PbI_4$ hybrid perovskite structure.

In this regard, it would be of interest to explore the possibility to accommodate organic ammonium cations and even dications of chromophoric groups with well-known photochemical properties. The leading concept is to exploit the large flexibility that organic chemistry

offers regarding the structure of organic compounds to convert the 2D hybrid perovskites again into highly active photoresponsive materials. In other words, it appears evident that organic ammonium salts larger that MA cannot be accommodated in conventional 3D perovskites that have shown to be highly efficient in photovoltaics, but then the question is if it is possible to obtain highly efficient 2D hybrid perovskites by using appropriate (large) ammonium or diammonium salts.

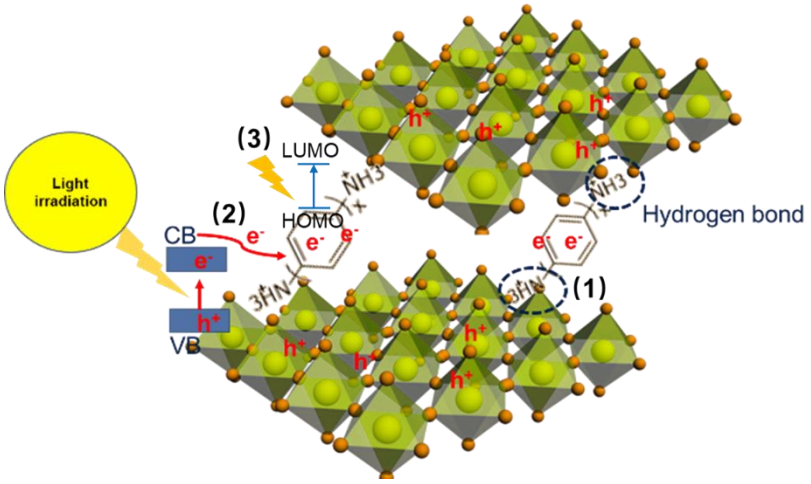

Scheme 1.12 Schematic illustration of the advantages of adopting aromatic diammonium cation for the fabrication of hybrid perovskite, (1) organic ligand can conjunct the adjacent 2D inorganic layers and thus form a 3D matrix (2) The aromatic rings are expected to accept photogenerated electrons and thus facilitate the electron/hole pairs separation and (3) the chromophoric ligands can also capture the incident light and generate charge carriers.

In this context, it can be envisioned that organic diammonium salts can act as bridge between two adjacent perovskite layers and in this way the 2D layered perovskite could exhibit some properties of the 3D materials. In addition, since charge separation efficiency decreases when comparing 3D with 2D perovskites, it is also reasonable to propose that charge separation can be enhanced in 2D perovskites by using suitable electron donor (or acceptor) organic ammonium ions. Other possibilities include the use of chromophores for more efficient

light harvesting. Scheme 1.12 illustrates this strategy that is one of the objectives of the present Doctoral Thesis.

On the other hand, one of the general objectives of the present Doctoral thesis is explore the potential that hybrid organic lead perovskites offer as photocatalysts. It has been commented that photocatalysis share with photovoltaics several common elementary steps including light absorption, charge separation and charge migration. The main difference is the efficient interparticle or particle-electrolyte electron transfer in photovoltaics *vs.* chemical oxidation and/or reduction of substrates in photocatalysis, as can be seen in Scheme 1.13. Therefore, considering that hybrid organic lead perovskites have revolutionized the field of solar photovoltaics it can be expected that the positive three main optoelectronic properties of these materials previously commented would also be reflected in a high photocatalytic activity.

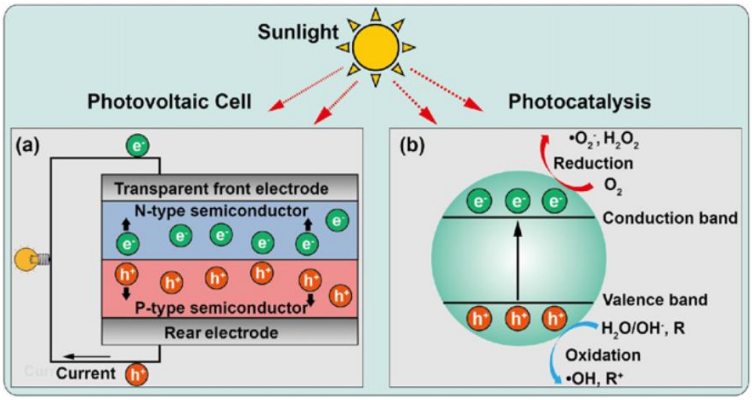

Scheme 1.13 Similarities and differences between photovoltaics and photocatalysis.[98] Copyright 2014 IOP Publishing Ltd.

However, towards the possible application of hybrid organic perovskites in photocatalysis the major drawback that has to be overcomes is the high structural instability. In fact, the main limitation of methylammonium lead iodide perovskite that has impeded so far its commercialization is its remarkable deactivation due to the negative

effect of moisture.[99] To understand the detrimental effect of moisture on the photovoltaic efficiency, even at low concentrations, it has been proposed that water molecules become adsorbed on the surface of the $MAPbI_3$ crystallites and increases the electrical resistance to electron migration. In other studies, it has been proposed that H_2O reacts with surface iodide forming Pb-OH bonds and evolving HI.[100] In any case, it is experimentally observed that the efficiency of $MAPbI_3$ cells decreases considerably after a few minutes' operation.

Besides moisture, $MAPbI_3$ is instable in many solvents. $MAPbI_3$ dissolves in water and also in other polar solvents. This structural instability impedes many applications in photocatalysis. It should be considered that one of the main areas of photocatalysis is wastewater treatment and that moisture is present in many photocatalytic reactions, including photocatalytic hydrogen generation and artificial photosynthesis, two key reactions for solar fuels production.

However, even though very challenging, the reward of having a photocatalyst with similar properties as those of $MAPBI_3$ would be very large. In this context, three experimental Chapters of the present Doctoral Thesis are aimed at exploring the photocatalytic activity of hybrid organic lead perovskites as indicated in Scheme 1.14. Chapter 3 will study the synthesis and properties of 4,4'-biphenylene diammonium as organic ammonium cation. The purpose is to determine whether diammonium cation can enhance charge separation by having in the structure of the organic part a biphenyl unit, which is well-known in classical molecular photoinduced electron transfer studies to act as electron relay by an easy electron transfer forming a long-lived radical ion. In addition, the presence of two positive charges in a layered hybrid perovskite can serve to increase the electrical connectivity among the layers by having one ammonium electrostatically connected to one layer and the other in the adjacent one. In this way the 2D perovskite could become a kind of 3D structure by strong interconnection among the layers.

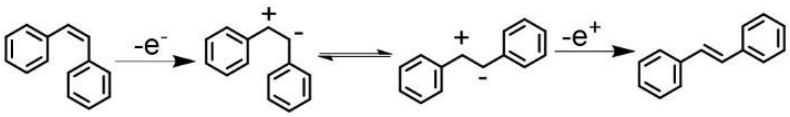

Scheme 1.14 Photoinduced electron transfer cis-to-trans stilbene isomerization reaction that will be explored in this Thesis using hybrid perovskites as the photocatalysts.

Chapters 4 and 5 of the present Doctoral Thesis are targeting the poor structural stability of hybrid organic lead perovskites against water and moisture. Chapter 4 will attempt protection against moisture by surface silanation with different silylating agents of different chain length and hydrophobicity. Besides surface silanation, other possibility is to coat the crystal surface with an organic polymer, like polystyrene. This idea will be explored in Chapter 5 by using 4-styryl ammonium as organic cation of the hybrid lead perovskite. After the synthesis of the material, the double C=C bond can subsequently be used to coat the surface and to promote cross polymerization with styrene as co-monomer.

1.5 N_2 Fixation.

Besides implementation of purposely-designed hybrid perovskites as photocatalysts, other two Chapters of the present Doctoral Thesis are aimed at exploring the photocatalytic N_2 hydrogenation. Considering the remarkably high activity of $Ru/SrTiO_3$ to promote the Sabatier reaction, as previously commented, a logical extension of these studies would be the evaluation of the photocatalytic activity of $Ru/SrTiO_3$ for related photocatalytic hydrogenations and in particular for N_2 fixation (eq. 1.4).

$$N_2 + 3H_2 \xrightarrow{\Delta/P} 2NH_3 \qquad \textbf{Equation 1.4}$$

N_2 hydrogenation to ammonia is a key industrial process performed at massive scale to produce fertilizers. The process (Haber-Bosch process) is currently carried out catalytically using heat to accelerate the reaction rate. The production volume of the reaction is so large and

consumes such a vast amount of energy that this process is responsible for 1-2 % of the total global CO_2 emissions.

Like CO_2, N_2 is one of the most inert molecules from the chemical point of view. N_2 hydrogenation to NH_3 is an exothermic process and from the thermodynamic point of view it should be performed at low temperature. However, from the kinetic point of view the N_2 hydrogenation is so slow that requires of high temperatures and H_2 pressures as well as efficient catalysts. Typical N_2 hydrogenation temperatures are about 400 ^oC and H_2 pressures above 100 bars. Regarding the catalyst, Haber was initially the chemist who working for BASF in Germany found that Fe was a suitable catalyst for this reaction. The catalyst was later improved by Bosch altering the surface of Fe metal. The current industrial Haber-Bosch catalyst contains also some Ru to enhance the activity of fritted Fe particles.[16]

Thus, in contrast to CO_2 hydrogenation that is not currently an industrial process, N_2 fixation is performed nowadays and, therefore, it would be important to extend the previous studies of the group on photo-assisted hydrogenations to the reaction of N_2 fixation. A search of the current state of the art indicates that N_2 hydrogenation is a more demanding process from the thermodynamic and kinetic viewpoints and implementation of a photocatalytic process would have a larger impact. Chapter 6 of the present Doctoral Thesis will be focused on the study of the performance of modified $Ru/SrTiO_3$ on N_2 hydrogenation.

Interestingly, as far as we know, the photocatalytic N_2 hydrogenation remains unexplored and there are not in the chemical literature any data about its possible feasibility. In contrast, even though extremely endothermic, there are some reports regarding N_2 reduction to NH_3 using H_2O as source of electrons and protons. The process is extremely ambitious and would avoid the need of H_2 generation, combining in a single photocatalytic process water oxidation to molecular O_2 and N_2 reduction to NH_3. In addition, it would be performed at near ambient temperature and pressure. The chemical process is depicted by eq. 1.5.

$$N_2 + 3H_2O \xrightarrow[photocatalysis]{} 2NH_3 + 3/2O_2 \qquad \textbf{Equation 1.5}$$

N_2 fixation by H_2O can be performed through two alternative ways to provide the required energy, either electrochemically or photocatalytically.[101, 102] Table 1.1 summarizes the current state of the art for the electrochemical N_2 reduction to NH_3, including production rates and electrochemical conditions. Analogously Table 1.2 gathers reports on the photocatalytic reduction of N_2 by H_2O.

Table 1.1 Summary of the state-of-the-art electrochemical nitrogen reduction to ammonia electrocatalysis.

Catalyst	NH_3 Yield	FE (%)	E (V vs RHE)	Ref.
$W_{18}O_{49}$	24.71 μg h^{-1} mg_{cat}^{-1}	20.0	-0.15	[103]
CB[7]–K2[B12H12]@A	41.69 μg h^{-1} mg_{cat}^{-1}	29.53	-0.4	[104]
Ru/ZrO2/NC	3.0 μg h^{-1} mg_{cat}^{-1}	12.21	-0.21	[105]
Ru/NC	4.6 μg h^{-1} mg_{cat}^{-1}	6.51	-0.21	[105]
TA-Au–TiO_2	21.4 μg h^{-1} mg_{cat}^{-1}	6.64	-0.2	[106]
Bi NCs	3406 μg h^{-1} mg_{cat}^{-1}	65.09	-0.6	[107]
Nb_2O_5 nanofibers	43.6 μg h^{-1} mg_{cat}^{-1}	6.1	-0.55	[108]
VN nanosheet	3.6 μg h^{-1} mg_{cat}^{-1}	1.52	-0.5	[109]
MoN nanosheets	78.4 μg h^{-1} mg_{cat}^{-1}	3.45	-0.3	[110]
SA-Mo/NPC	34.0 μg h^{-1} mg_{cat}^{-1}	0.79	-0.3	[111]

Table 1.2 Summary of the state-of-the-art photocatalytic nitrogen fixation.

Photocatalyst	Light source	scavenger	NH_3 yielding	Ref.
Rutile TiO_2	λ > 240 nm	2-PrOH	2.5 μM h^{-1}	112
Bi_5O_7I	280-800 nm	Methanol	223 μmol g_{cat}^{-1} h^{-1}	113
CuCr-LDH	λ > 400 nm	-	57 μmol g_{cat}^{-1} h^{-1}	114
Bi_5O_7Br	λ > 400 nm	-	1380 μM h^{-1}	115
$Au/(BiO)_2CO_3$	1 sun irradiation	-	38.2 μmol g_{cat}^{-1} h^{-1}	116
graphdiyne	λ > 400 nm	-	1762.35 μmol h^{-1} g_{cat}^{-1}	117
ZnAl - LDH	UV-Vis	-	110 μmol g^{-1} h^{-1}	118

As it can be seen in these Tables (1.1 and 1.2), there is considerable room for improvement with specific rates of N_2 reduction to NH_3 in the range of hundreds of micromoles of NH_3 per gram of catalyst per hour. Yet, the competing reaction of proton reduction to H_2 have rarely been commented in photocatalytic nitrogen reduction system and the average faradic efficiencies for electrolytic nitrogen reduction were less than 20 % even after careful control of the applied potential. So, it can be envisioned that H_2 is actually the dominating product, mainly because the N_2 was weakly activated and it is much harder to be reduced compared with proton. In contrast, in the case of natural nitrogen fixation process, the selectivity is extremely high. Thus, inspired by the structure of natural nitrogenase enzyme, researchers have recently developed promising metal-complexes as the homogeneous catalyst for nitrogen activation and reduction, with an impressive selectivity towards NH_3 over 90%.[119] In this regard, Chapter 7 of the present Thesis will deal with the use of a ligand to complex

transition metal ions to promote the electrochemical N_2 reduction, reaching production values that are in the range of those reported in the literature.

1.6 Outline of the Experimental Chapters.

In view of the above precedents, the present Doctoral Thesis has two main objectives. On one hand, the Thesis is aimed at preparing and studying the photocatalytic activity of hybrid organic lead perovskites. Due to their extremely moisture-sensitive photoresponse and the poor structural stability, hybrid organic perovskites have not been studied yet as photocatalysts. In addition, the photovoltaic responses are mostly limited to methylammonium and formamidinium organic ammonium cations. Thus, Chapters 3 and 4 will prepare and study the photocatalytic activity of hybrid perovskites of biphenylene diammonium cation without or after surface silanation. Chapter 5 will explore coating of a 2D hybrid perovskite with a polymeric shell as a method for surface protection against moisture.

In another tone, Chapters 6 and 7 are directed to study the photocatalytic N_2 fixation, one of the most important photocatalytic processes. In Chapter 6, the photocatalytic activity of modified **Ru-STO** will be tested for the N_2 hydrogenation, hoping that the excellent activity of this photocatalyst in CO_2 hydrogenation can also be applied for N_2 fixation. Finally, Chapter 7 will present the results obtained so far on the use of molecular complexes of tris-(3,5-disubstituted-pyrazolyl) borate with first and second raw transition metal cations as catalysts for the electrochemical production of ammonia from N_2 in the liquid phase. Scheme 1.15 provides a quick overview of the structure of the present Doctoral Thesis.

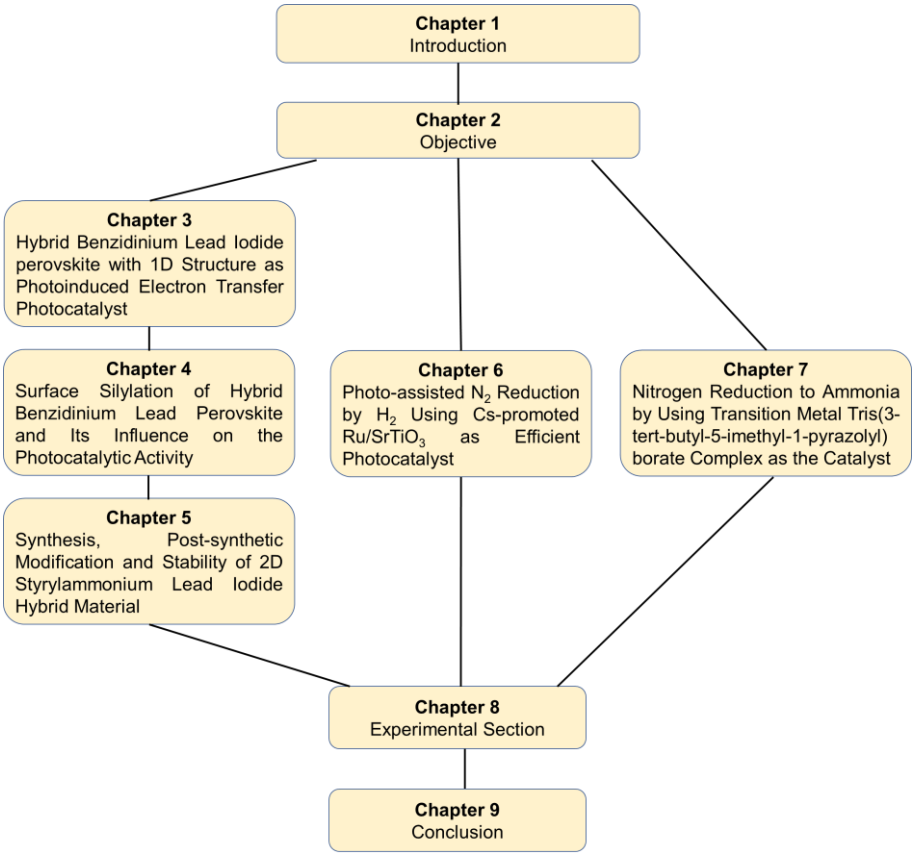

Scheme 1.15 An overview of the Chapters of the present Doctoral Thesis.

1.7 References

1. Hervás, M.; Navarro, J. A.; De la Rosa, M. A., Electron Transfer between Membrane Complexes and Soluble Proteins in Photosynthesis. *Acc. Chem. Res.* **2003,** *36*, 798-805.

2. Barber, J., Photosynthetic energy conversion: natural and artificial. *Chem. Soc. Rev.* **2009,** *38*, 185-196.

3. Parida, B.; Iniyan, S.; Goic, R., A review of solar photovoltaic technologies. *Renew. Sustain. Energy Rev.* **2011,** *15*, 1625-1636.

4. Rawat, R.; Lamba, R.; Kaushik, S. C., Thermodynamic study of

solar photovoltaic energy conversion: An overview. *Renew. Sustain. Energy Rev.* **2017,** *71*, 630-638.

5. Moniz, S. J. A.; Shevlin, S. A.; Martin, D. J.; Guo, Z.-X.; Tang, J., Visible-light driven heterojunction photocatalysts for water splitting – a critical review. *Energy Environ. Sci.* **2015,** *8*, 731-759.

6. Albero, J.; Peng, Y.; García, H., Photocatalytic CO_2 Reduction to C2+ Products. *ACS Catal.* **2020,** *10*, 5734-5749.

7. Habisreutinger, S. N.; Schmidt-Mende, L.; Stolarczyk, J. K., Photocatalytic Reduction of CO_2 on TiO_2 and Other Semiconductors. *Angew. Chem. Int. Ed.* **2013,** *52*, 7372-7408.

8. Zhitomirsky, D.; Voznyy, O.; Hoogland, S.; Sargent, E. H., Measuring Charge Carrier Diffusion in Coupled Colloidal Quantum Dot Solids. *ACS Nano* **2013,** *7*, 5282-5290.

9. Stranks, S. D.; Eperon, G. E.; Grancini, G.; Menelaou, C.; Alcocer, M. J. P.; Leijtens, T.; Herz, L. M.; Petrozza, A.; Snaith, H. J., Electron-Hole Diffusion Lengths Exceeding 1 Micrometer in an Organometal Trihalide Perovskite Absorber. *Science* **2013,** *342*, 341-344.

10. Mikhnenko, O. V.; Kuik, M.; Lin, J.; van der Kaap, N.; Nguyen, T.-Q.; Blom, P. W. M., Trap-Limited Exciton Diffusion in Organic Semiconductors. *Adv. Mater.* **2014,** *26*, 1912-1917.

11. Johnston, M. B.; Herz, L. M., Hybrid Perovskites for Photovoltaics: Charge-Carrier Recombination, Diffusion, and Radiative Efficiencies. *Acc. Chem. Res.* **2016,** *49*, 146-154.

12. Clarke, T. M.; Durrant, J. R., Charge Photogeneration in Organic Solar Cells. *Chem. Rev.* **2010,** *110*, 6736-6767.

13. Gaponenko, M. S.; Lutich, A. A.; Tolstik, N. A.; Onushchenko, A. A.; Malyarevich, A. M.; Petrov, E. P.; Yumashev, K. V.,

Temperature-dependent photoluminescence of PbS quantum dots in glass: Evidence of exciton state splitting and carrier trapping. *Phys. Rev. B* **2010,** *82*, 125320.

14. Berera, R.; van Grondelle, R.; Kennis, J. T. M., Ultrafast transient absorption spectroscopy: principles and application to photosynthetic systems. *Photosynth. Res.* **2009,** *101*, 105-118.

15. Gómez–Marín, A. M.; Ticianelli, E. A., A reviewed vision of the oxygen reduction reaction mechanism on Pt-based catalysts. *Curr. Opin. Electrochem.* **2018,** *9*, 129-136.

16. Kandemir, T.; Schuster, M. E.; Senyshyn, A.; Behrens, M.; Schlögl, R., The Haber–Bosch Process Revisited: On the Real Structure and Stability of “Ammonia Iron” under Working Conditions. *Angew. Chem. Int. Ed.* **2013,** *52*, 12723-12726.

17. Erisman, J. W.; Sutton, M. A.; Galloway, J.; Klimont, Z.; Winiwarter, W., How a century of ammonia synthesis changed the world. *Nat. Geosci.* **2008,** *1*, 636-639.

18. Masters, C., The Fischer-Tropsch Reaction. In *Adv. Organomet. Chem.*, Stone, F. G. A.; West, R., Eds. Academic Press: 1979; Vol. 17, pp 61-103.

19. Adesina, A. A., Hydrocarbon synthesis via Fischer-Tropsch reaction: travails and triumphs. *Appl. Catal. A-GEN* **1996,** *138*, 345-367.

20. Palo, D. R.; Dagle, R. A.; Holladay, J. D., Methanol Steam Reforming for Hydrogen Production. *Chem. Rev.* **2007,** *107*, 3992-4021.

21. Iulianelli, A.; Ribeirinha, P.; Mendes, A.; Basile, A., Methanol steam reforming for hydrogen generation via conventional and membrane reactors: A review. *Renew. Sustain. Energy Rev.* **2014,** *29*, 355-368.

22. Simpson, A. P.; Lutz, A. E., Exergy analysis of hydrogen production via steam methane reforming. *Int. J. Hydrogen Energy* **2007,** *32*, 4811-4820.

23. Carapellucci, R.; Giordano, L., Steam, dry and autothermal methane reforming for hydrogen production: A thermodynamic equilibrium analysis. *J. Power Sources* **2020,** *469*, 228391.

24. Fujishima, A.; Honda, K., Electrochemical Photolysis of Water at a Semiconductor Electrode. *Nature* **1972,** *238*, 37-38.

25. Wang, Z.; Li, C.; Domen, K., Recent developments in heterogeneous photocatalysts for solar-driven overall water splitting. *Chem. Soc. Rev.* **2019,** *48*, 2109-2125.

26. Chen, S.; Takata, T.; Domen, K., Particulate photocatalysts for overall water splitting. *Nat. Rev. Mater.* **2017,** *2*, 17050.

27. Li, K.; An, X.; Park, K. H.; Khraisheh, M.; Tang, J., A critical review of CO_2 photoconversion: Catalysts and reactors. *Catal. Today* **2014,** *224*, 3-12.

28. Nguyen, V.-H.; Nguyen, B.-S.; Jin, Z.; Shokouhimehr, M.; Jang, H. W.; Hu, C.; Singh, P.; Raizada, P.; Peng, W.; Shiung Lam, S.; Xia, C.; Nguyen, C. C.; Kim, S. Y.; Le, Q. V., Towards artificial photosynthesis: Sustainable hydrogen utilization for photocatalytic reduction of CO_2 to high-value renewable fuels. *Chem. Eng. J.* **2020,** *402*, 126184.

29. Kawakami, Y.; Inoue, K.; Kaneta, A.; Okamoto, K.; Funato, M., Quantification of the internal quantum efficiency in GaN via analysis of the heat generated by non-radiative recombination processes. *J. Appl. Phys.* **2015,** *117*, 105702.

30. Bian, Z.; Tachikawa, T.; Zhang, P.; Fujitsuka, M.; Majima, T., Au/TiO_2 Superstructure-Based Plasmonic Photocatalysts Exhibiting

Efficient Charge Separation and Unprecedented Activity. *J. Am. Chem. Soc.* **2014,** *136*, 458-465.

31. Tatsuma, T.; Nishi, H.; Ishida, T., Plasmon-induced charge separation: chemistry and wide applications. *Chem. Sci.* **2017,** *8*, 3325-3337.

32. Zou, J.; Si, Z.; Cao, Y.; Ran, R.; Wu, X.; Weng, D., Localized Surface Plasmon Resonance Assisted Photothermal Catalysis of CO and Toluene Oxidation over Pd–CeO2 Catalyst under Visible Light Irradiation. *J. Phys. Chem. C* **2016,** *120*, 29116-29125.

33. Li, J.; Ye, Y.; Ye, L.; Su, F.; Ma, Z.; Huang, J.; Xie, H.; Doronkin, D. E.; Zimina, A.; Grunwaldt, J.-D.; Zhou, Y., Sunlight induced photo-thermal synergistic catalytic CO_2 conversion via localized surface plasmon resonance of MoO_3−x. *J. Mater. Chem. A* **2019,** *7*, 2821-2830.

34. Boltersdorf, J.; Forcherio, G. T.; McClure, J. P.; Baker, D. R.; Leff, A. C.; Lundgren, C., Visible Light-Promoted Plasmon Resonance to Induce “Hot” Hole Transfer and Photothermal Conversion for Catalytic Oxidation. *J. Phys. Chem. C* **2018,** *122*, 28934-28948.

35. Kho, E. T.; Tan, T. H.; Lovell, E.; Wong, R. J.; Scott, J.; Amal, R., A review on photo-thermal catalytic conversion of carbon dioxide. *Green Energy Environ.* **2017,** *2*, 204-217.

36. Baffou, G.; Quidant, R., Nanoplasmonics for chemistry. *Chem. Soc. Rev.* **2014,** *43*, 3898-3907.

37. Luo, C.; Ren, X.; Dai, Z.; Zhang, Y.; Qi, X.; Pan, C., Present Perspectives of Advanced Characterization Techniques in TiO_2-Based Photocatalysts. *ACS Appl. Mater. Interfaces* **2017,** *9*, 23265-23286.

38. Amano, F.; Nakata, M.; Yamamoto, A.; Tanaka, T., Rutile titanium dioxide prepared by hydrogen reduction of Degussa P25 for

highly efficient photocatalytic hydrogen evolution. *Catal. Sci. Technol.* **2016,** *6*, 5693-5699.

39. Hurum, D. C.; Agrios, A. G.; Gray, K. A.; Rajh, T.; Thurnauer, M. C., Explaining the Enhanced Photocatalytic Activity of Degussa P25 Mixed-Phase TiO_2 Using EPR. *J. Phys. Chem. B* **2003,** *107*, 4545-4549.

40. Peng, T.; Dai, K.; Yi, H.; Ke, D.; Cai, P.; Zan, L., Photosensitization of different ruthenium(II) complex dyes on TiO_2 for photocatalytic H_2 evolution under visible-light. *Chem. Phys. Lett.* **2008,** *460*, 216-219.

41. Jin, E. M.; Park, K.-H.; Jin, B.; Yun, J.-J.; Gu, H.-B., Photosensitization of nanoporous TiO2films with natural dye. *Phys. Scr.* **2010,** *T139*, 014006.

42. Nguyen, V. N.; Nguyen, N. K. T.; Nguyen, P. H., Hydrothermal synthesis of Fe-doped TiO_2 nanostructure photocatalyst. *Adv. Nat. Sci.-NanoSci.* **2011,** *2*, 035014.

43. Liu, B.; Chen, H. M.; Liu, C.; Andrews, S. C.; Hahn, C.; Yang, P., Large-Scale Synthesis of Transition-Metal-Doped TiO_2 Nanowires with Controllable Overpotential. *J. Am. Chem. Soc.* **2013,** *135*, 9995-9998.

44. Burda, C.; Lou, Y.; Chen, X.; Samia, A. C. S.; Stout, J.; Gole, J. L., Enhanced Nitrogen Doping in TiO_2 Nanoparticles. *Nano Lett.* **2003,** *3*, 1049-1051.

45. Chen, Y.; Cao, X.; Lin, B.; Gao, B., Origin of the visible-light photoactivity of NH_3-treated TiO_2: Effect of nitrogen doping and oxygen vacancies. *Appl. Surf. Sci.* **2013,** *264*, 845-852.

46. Chen, X.; Liu, L.; Yu, P. Y.; Mao, S. S., Increasing Solar Absorption for Photocatalysis with Black Hydrogenated Titanium Dioxide Nanocrystals. *Science* **2011,** *331*, 746-750.

47. Wang, J.; Tafen, D. N.; Lewis, J. P.; Hong, Z.; Manivannan, A.; Zhi, M.; Li, M.; Wu, N., Origin of Photocatalytic Activity of Nitrogen-Doped TiO_2 Nanobelts. *J. Am. Chem. Soc.* **2009,** *131*, 12290-12297.

48. Ohtani, B.; Ogawa, Y.; Nishimoto, S.-i., Photocatalytic Activity of Amorphous−Anatase Mixture of Titanium(IV) Oxide Particles Suspended in Aqueous Solutions. *J. Phys. Chem. B* **1997,** *101*, 3746-3752.

49. Roy, N.; Sohn, Y.; Leung, K. T.; Pradhan, D., Engineered Electronic States of Transition Metal Doped TiO_2 Nanocrystals for Low Overpotential Oxygen Evolution Reaction. *J. Phys. Chem. C* **2014,** *118*, 29499-29506.

50. Katoh, R.; Furube, A.; Yamanaka, K.-i.; Morikawa, T., Charge Separation and Trapping in N-Doped TiO_2 Photocatalysts: A Time-Resolved Microwave Conductivity Study. *J. Phys. Chem. Lett.* **2010,** *1*, 3261-3265.

51. Takata, T.; Jiang, J.; Sakata, Y.; Nakabayashi, M.; Shibata, N.; Nandal, V.; Seki, K.; Hisatomi, T.; Domen, K., Photocatalytic water splitting with a quantum efficiency of almost unity. *Nature* **2020,** *581*, 411-414.

52. Liu, T.; Zhou, X.; Dupuis, M.; Li, C., The nature of photogenerated charge separation among different crystal facets of BiVO4 studied by density functional theory. *PCCP* **2015,** *17*, 23503-23510.

53. Lee, S. M.; Park, G. C.; Seo, T. Y.; Jung, S.-B.; Lee, J. H.; Kim, Y. D.; Choi, D. H.; Lim, J. H.; Joo, J., Facet-controlled anatase TiO_2 nanoparticles through various fluorine sources for superior photocatalytic activity. *Nanotechnology* **2016,** *27*, 395604.

54. Zhang, X.; Veikko, U.; Mao, J.; Cai, P.; Peng, T., Visible-Light-Induced Photocatalytic Hydrogen Production over Binuclear RuII–Bipyridyl Dye-Sensitized TiO_2 without Noble Metal Loading. *Chem. Eur. J.* **2012,** *18*, 12103-12111.

55. Jin, Z.; Zhang, X.; Lu, G.; Li, S., Improved quantum yield for photocatalytic hydrogen generation under visible light irradiation over eosin sensitized TiO_2—Investigation of different noble metal loading. *J. Mol. Catal. A: Chem.* **2006,** *259*, 275-280.

56. Nour-Mohhamadi, F.; Nguyen, S. D.; Boschloo, G.; Hagfeldt, A.; Lund, T., Determination of the Light-Induced Degradation Rate of the Solar Cell Sensitizer N719 on TiO_2 Nanocrystalline Particles. *J. Phys. Chem. B* **2005,** *109*, 22413-22419.

57. Kato, N.; Takeda, Y.; Higuchi, K.; Takeichi, A.; Sudo, E.; Tanaka, H.; Motohiro, T.; Sano, T.; Toyoda, T., Degradation analysis of dye-sensitized solar cell module after long-term stability test under outdoor working condition. *Sol. Energy Mater. Sol. Cells* **2009,** *93*, 893-897.

58. Ong, C. B.; Ng, L. Y.; Mohammad, A. W., A review of ZnO nanoparticles as solar photocatalysts: Synthesis, mechanisms and applications. *Renew. Sustain. Energy Rev.* **2018,** *81*, 536-551.

59. Zheng, Z.; Huang, B.; Wang, Z.; Guo, M.; Qin, X.; Zhang, X.; Wang, P.; Dai, Y., Crystal Faces of Cu_2O and Their Stabilities in Photocatalytic Reactions. *J. Phys. Chem. C* **2009,** *113*, 14448-14453.

60. Mishra, M.; Chun, D.-M., α-Fe_2O_3 as a photocatalytic material: A review. *Appl. Catal. A-GEN* **2015,** *498*, 126-141.

61. Sayama, K.; Hayashi, H.; Arai, T.; Yanagida, M.; Gunji, T.; Sugihara, H., Highly active WO_3 semiconductor photocatalyst prepared from amorphous peroxo-tungstic acid for the degradation of various

organic compounds. *Appl. Catal. B* **2010,** *94*, 150-157.

62. Ma, R.; Zhang, S.; Wen, T.; Gu, P.; Li, L.; Zhao, G.; Niu, F.; Huang, Q.; Tang, Z.; Wang, X., A critical review on visible-light-response CeO_2-based photocatalysts with enhanced photooxidation of organic pollutants. *Catal. Today* **2019,** *335*, 20-30.

63. Kambur, A.; Pozan, G. S.; Boz, I., Preparation, characterization and photocatalytic activity of TiO_2–ZrO_2 binary oxide nanoparticles. *Appl. Catal. B* **2012,** *115-116*, 149-158.

64. Toe, C. Y.; Zheng, Z.; Wu, H.; Scott, J.; Amal, R.; Ng, Y. H., Photocorrosion of Cuprous Oxide in Hydrogen Production: Rationalising Self-Oxidation or Self-Reduction. *Angew. Chem. Int. Ed.* **2018,** *57*, 13613-13617.

65. Krýsa, J.; Němečková, A.; Zlámal, M.; Kotrla, T.; Baudys, M.; Kment, Š.; Hubička, Z.; Neumann-Spallart, M., α-Fe_2O_3/TiO_2 stratified photoanodes. *J. Photochem. Photobiol. A* **2018,** *366*, 12-17.

66. Sayyed, S. A. A. R.; Beedri, N. I.; Kadam, V. S.; Pathan, H. M., Rose Bengal sensitized bilayered photoanode of nano-crystalline TiO_2–CeO_2 for dye-sensitized solar cell application. *Applied Nanoscience* **2016,** *6*, 875-881.

67. Townsend, T. K.; Browning, N. D.; Osterloh, F. E., Nanoscale Strontium Titanate Photocatalysts for Overall Water Splitting. *ACS Nano* **2012,** *6*, 7420-7426.

68. Mateo, D.; García-Mulero, A.; Albero, J.; García, H., N-doped defective graphene decorated by strontium titanate as efficient photocatalyst for overall water splitting. *Appl. Catal. B* **2019,** *252*, 111-119.

69. Wang, X.; Wang, Y.; Gao, M.; Shen, J.; Pu, X.; Zhang, Z.; Lin, H.; Wang, X., BiVO4 /Bi4Ti3O12 heterojunction enabling efficient

photocatalytic reduction of CO_2 with H_2O to CH_3OH and CO. *Appl. Catal. B* **2020,** *270*, 118876.

70. Obregón, S.; Caballero, A.; Colón, G., Hydrothermal synthesis of BiVO4: Structural and morphological influence on the photocatalytic activity. *Appl. Catal. B* **2012,** *117-118*, 59-66.

71. Lerma-Berlanga, B.; R. Ganivet, C.; Almora-Barrios, N.; Tatay, S.; Peng, Y.; Albero, J.; Fabelo, O.; González-Platas, J.; García, H.; M. Padial, N.; Martí-Gastaldo, C., Effect of Linker Distribution in the Photocatalytic Activity of Multivariate Mesoporous Crystals. *J. Am. Chem. Soc.* **2021,** *143*, 1798-1806.

72. Dhakshinamoorthy, A.; Asiri, A. M.; García, H., Metal–Organic Framework (MOF) Compounds: Photocatalysts for Redox Reactions and Solar Fuel Production. *Angew. Chem. Int. Ed.* **2016,** *55*, 5414-5445.

73. Fu, J.; Yu, J.; Jiang, C.; Cheng, B., g-C_3N_4-Based Heterostructured Photocatalysts. *Adv. Energy Mater.* **2018,** *8*, 1701503.

74. Lavorato, C.; Primo, A.; Molinari, R.; Garcia, H., N-Doped Graphene Derived from Biomass as a Visible-Light Photocatalyst for Hydrogen Generation from Water/Methanol Mixtures. *Chem. Eur. J.* **2014,** *20*, 187-194.

75. Lyu, H.; Hisatomi, T.; Goto, Y.; Yoshida, M.; Higashi, T.; Katayama, M.; Takata, T.; Minegishi, T.; Nishiyama, H.; Yamada, T.; Sakata, Y.; Asakura, K.; Domen, K., An Al-doped $SrTiO_3$ photocatalyst maintaining sunlight-driven overall water splitting activity for over 1000 h of constant illumination. *Chem. Sci.* **2019,** *10*, 3196-3201.

76. Mateo, D.; Albero, J.; García, H., Titanium-Perovskite-Supported RuO_2 Nanoparticles for Photocatalytic CO_2 Methanation. *Joule* **2019,** *3*, 1949-1962.

77. Kojima, A.; Teshima, K.; Shirai, Y.; Miyasaka, T., Organometal Halide Perovskites as Visible-Light Sensitizers for Photovoltaic Cells. *J. Am. Chem. Soc.* **2009,** *131*, 6050-6051.

78. Zhao, D.; Wang, C.; Song, Z.; Yu, Y.; Chen, C.; Zhao, X.; Zhu, K.; Yan, Y., Four-Terminal All-Perovskite Tandem Solar Cells Achieving Power Conversion Efficiencies Exceeding 23%. *ACS Energy Lett.* **2018,** *3*, 305-306.

79. Frolova, L. A.; Davlethanov, A. I.; Dremova, N. N.; Zhidkov, I.; Akbulatov, A. F.; Kurmaev, E. Z.; Aldoshin, S. M.; Stevenson, K. J.; Troshin, P. A., Efficient and Stable $MAPbI_3$-Based Perovskite Solar Cells Using Polyvinylcarbazole Passivation. *J. Phys. Chem. Lett.* **2020,** *11*, 6772-6778.

80. Zhao, Y.; Nardes, A. M.; Zhu, K., Solid-State Mesostructured Perovskite $CH_3NH_3PbI_3$ Solar Cells: Charge Transport, Recombination, and Diffusion Length. *J. Phys. Chem. Lett.* **2014,** *5*, 490-494.

81. Uratani, H.; Yamashita, K., Inorganic Lattice Fluctuation Induces Charge Separation in Lead Iodide Perovskites: Theoretical Insights. *J. Phys. Chem. C* **2017,** *121*, 26648-26654.

82. Righetto, M.; Lim, S. S.; Giovanni, D.; Lim, J. W. M.; Zhang, Q.; Ramesh, S.; Tay, Y. K. E.; Sum, T. C., Hot carriers perspective on the nature of traps in perovskites. *Nat. Commun.* **2020,** *11*, 2712.

83. Reyna, Y.; Salado, M.; Kazim, S.; Pérez-Tomas, A.; Ahmad, S.; Lira-Cantu, M., Performance and stability of mixed $FAPbI_3(0.85)MAPbBr_3(0.15)$ halide perovskite solar cells under outdoor conditions and the effect of low light irradiation. *Nano Energy* **2016,** *30*, 570-579.

84. Lu, H.; Zhang, H.; Yuan, S.; Wang, J.; Zhan, Y.; Zheng, L., An optical dynamic study of $MAPbBr_3$ single crystals passivated with

$MAPbCl_3/I_3$-$MAPbBr_3$ heterojunctions. *PCCP* **2017,** *19*, 4516-4521.

85. Hwang, B.; Gu, C.; Lee, D.; Lee, J.-S., Effect of halide-mixing on the switching behaviors of organic-inorganic hybrid perovskite memory. *Sci. Rep.* **2017,** *7*, 43794.

86. Park, B.-w.; Jain, S. M.; Zhang, X.; Hagfeldt, A.; Boschloo, G.; Edvinsson, T., Resonance Raman and Excitation Energy Dependent Charge Transfer Mechanism in Halide-Substituted Hybrid Perovskite Solar Cells. *ACS Nano* **2015,** *9*, 2088-2101.

87. Jang, D. M.; Park, K.; Kim, D. H.; Park, J.; Shojaei, F.; Kang, H. S.; Ahn, J.-P.; Lee, J. W.; Song, J. K., Reversible Halide Exchange Reaction of Organometal Trihalide Perovskite Colloidal Nanocrystals for Full-Range Band Gap Tuning. *Nano Lett.* **2015,** *15*, 5191-5199.

88. Liu, X.; Yan, K.; Tan, D.; Liang, X.; Zhang, H.; Huang, W., Solvent Engineering Improves Efficiency of Lead-Free Tin-Based Hybrid Perovskite Solar Cells beyond 9%. *ACS Energy Lett.* **2018,** *3*, 2701-2707.

89. Elseman, A. M.; Shalan, A. E.; Sajid, S.; Rashad, M. M.; Hassan, A. M.; Li, M., Copper-Substituted Lead Perovskite Materials Constructed with Different Halides for Working $(CH_3NH_3)_2CuX_4$-Based Perovskite Solar Cells from Experimental and Theoretical View. *ACS Appl. Mater. Interfaces* **2018,** *10*, 11699-11707.

90. Noel, N. K.; Stranks, S. D.; Abate, A.; Wehrenfennig, C.; Guarnera, S.; Haghighirad, A.-A.; Sadhanala, A.; Eperon, G. E.; Pathak, S. K.; Johnston, M. B.; Petrozza, A.; Herz, L. M.; Snaith, H. J., Lead-free organic–inorganic tin halide perovskites for photovoltaic applications. *Energy Environ. Sci.* **2014,** *7*, 3061-3068.

91. Hao, F.; Stoumpos, C. C.; Cao, D. H.; Chang, R. P. H.;

Kanatzidis, M. G., Lead-free solid-state organic–inorganic halide perovskite solar cells. *Nat. Photonics* **2014,** *8*, 489-494.

92. Stranks, S. D.; Snaith, H. J., Metal-halide perovskites for photovoltaic and light-emitting devices. *Nat. Nanotechnol.* **2015,** *10*, 391-402.

93. Sato, T.; Takagi, S.; Deledda, S.; Hauback, B. C.; Orimo, S.-i., Extending the applicability of the Goldschmidt tolerance factor to arbitrary ionic compounds. *Sci. Rep.* **2016,** *6*, 23592.

94. Jana, A.; Ba, Q.; Nissimagoudar, A. S.; Kim, K. S., Formation of a photoactive quasi-2D formamidinium lead iodide perovskite in water. *J. Mater. Chem. A* **2019,** *7*, 25785-25790.

95. Li, M.-H.; Yeh, H.-H.; Chiang, Y.-H.; Jeng, U.-S.; Su, C.-J.; Shiu, H.-W.; Hsu, Y.-J.; Kosugi, N.; Ohigashi, T.; Chen, Y.-A.; Shen, P.-S.; Chen, P.; Guo, T.-F., Highly Efficient 2D/3D Hybrid Perovskite Solar Cells via Low-Pressure Vapor-Assisted Solution Process. *Adv. Mater.* **2018,** *30*, 1801401.

96. Kamminga, M. E.; Fang, H.-H.; Filip, M. R.; Giustino, F.; Baas, J.; Blake, G. R.; Loi, M. A.; Palstra, T. T. M., Confinement Effects in Low-Dimensional Lead Iodide Perovskite Hybrids. *Chem. Mater.* **2016,** *28*, 4554-4562.

97. Febriansyah, B.; Koh, T. M.; John, R. A.; Ganguly, R.; Li, Y.; Bruno, A.; Mhaisalkar, S. G.; England, J., Inducing Panchromatic Absorption and Photoconductivity in Polycrystalline Molecular 1D Lead-Iodide Perovskites through π-Stacked Viologens. *Chem. Mater.* **2018,** *30*, 5827-5830.

98. Yang, W.; Li, X.; Chi, D.; Zhang, H.; Liu, X., Lanthanide-doped upconversion materials: emerging applications for photovoltaics and photocatalysis. *Nanotechnology* **2014,** *25*, 482001.

99. Park, B.-w.; Seok, S. I., Intrinsic Instability of Inorganic–Organic Hybrid Halide Perovskite Materials. *Adv. Mater.* **2019,** *31*, 1805337.

100. Niu, G.; Guo, X.; Wang, L., Review of recent progress in chemical stability of perovskite solar cells. *J. Mater. Chem. A* **2015,** *3*, 8970-8980.

101. Chen, X.; Li, N.; Kong, Z.; Ong, W.-J.; Zhao, X., Photocatalytic fixation of nitrogen to ammonia: state-of-the-art advancements and future prospects. *Mater. Horiz.* **2018,** *5*, 9-27.

102. Cui, X.; Tang, C.; Zhang, Q., A Review of Electrocatalytic Reduction of Dinitrogen to Ammonia under Ambient Conditions. *Adv. Energy Mater.* **2018,** *8*, 1800369.

103. Tong, Y.; Guo, H.; Liu, D.; Yan, X.; Su, P.; Liang, J.; Zhou, S.; Liu, J.; Lu, G. Q.; Dou, S. X., Vacancy Engineering of Iron-Doped $W_{18}O_{49}$ Nanoreactors for Low-Barrier Electrochemical Nitrogen Reduction. *Angew. Chem. Int. Ed.* **2020,** *59*, 7356-7361.

104. Zhao, X.; Yang, Z.; Kuklin, A. V.; Baryshnikov, G. V.; Ågren, H.; Wang, W.; Zhou, X.; Zhang, H., Potassium ions promote electrochemical nitrogen reduction on nano-Au catalysts triggered by bifunctional boron supramolecular assembly. *J. Mater. Chem. A* **2020,** *8*, 13086-13094.

105. Tao, H.; Choi, C.; Ding, L.-X.; Jiang, Z.; Han, Z.; Jia, M.; Fan, Q.; Gao, Y.; Wang, H.; Robertson, A. W.; Hong, S.; Jung, Y.; Liu, S.; Sun, Z., Nitrogen Fixation by Ru Single-Atom Electrocatalytic Reduction. *Chem* **2019,** *5*, 204-214.

106. Shi, M.-M.; Bao, D.; Wulan, B.-R.; Li, Y.-H.; Zhang, Y.-F.; Yan, J.-M.; Jiang, Q., Au Sub-Nanoclusters on TiO_2 toward Highly Efficient and Selective Electrocatalyst for N_2 Conversion to NH_3 at Ambient Conditions. *Adv. Mater.* **2017,** *29*, 1606550.

107. Hao, Y.-C.; Guo, Y.; Chen, L.-W.; Shu, M.; Wang, X.-Y.; Bu, T.-A.; Gao, W.-Y.; Zhang, N.; Su, X.; Feng, X.; Zhou, J.-W.; Wang, B.; Hu, C.-W.; Yin, A.-X.; Si, R.; Zhang, Y.-W.; Yan, C.-H., Promoting nitrogen electroreduction to ammonia with bismuth nanocrystals and potassium cations in water. *Nat. Catal.* **2019,** *2*, 448-456.

108. Han, J.; Liu, Z.; Ma, Y.; Cui, G.; Xie, F.; Wang, F.; Wu, Y.; Gao, S.; Xu, Y.; Sun, X., Ambient N_2 fixation to NH_3 at ambient conditions: Using Nb_2O_5 nanofiber as a high-performance electrocatalyst. *Nano Energy* **2018,** *52*, 264-270.

109. Zhang, R.; Zhang, Y.; Ren, X.; Cui, G.; Asiri, A. M.; Zheng, B.; Sun, X., High-Efficiency Electrosynthesis of Ammonia with High Selectivity under Ambient Conditions Enabled by VN Nanosheet Array. *ACS Sustain. Chem. Eng.* **2018,** *6*, 9545-9549.

110. Zhang, L.; Ji, X.; Ren, X.; Luo, Y.; Shi, X.; Asiri, A. M.; Zheng, B.; Sun, X., Efficient Electrochemical N_2 Reduction to NH_3 on MoN Nanosheets Array under Ambient Conditions. *ACS Sustain. Chem. Eng.* **2018,** *6*, 9550-9554.

111. Cheng, H.; Ding, L.-X.; Chen, G.-F.; Zhang, L.; Xue, J.; Wang, H., Nitrogen Reduction Reaction: Molybdenum Carbide Nanodots Enable Efficient Electrocatalytic Nitrogen Fixation under Ambient Conditions. *Adv. Mater.* **2018,** *30*, 1870350.

112. Hirakawa, H.; Hashimoto, M.; Shiraishi, Y.; Hirai, T., Photocatalytic Conversion of Nitrogen to Ammonia with Water on Surface Oxygen Vacancies of Titanium Dioxide. *J. Am. Chem. Soc.* **2017,** *139*, 10929-10936.

113. Bai, Y.; Ye, L.; Chen, T.; Wang, L.; Shi, X.; Zhang, X.; Chen, D., Facet-Dependent Photocatalytic N_2 Fixation of Bismuth-Rich

Bi_5O_7I Nanosheets. *ACS Appl. Mater. Interfaces* **2016,** *8*, 27661-27668.
114.Zhao, Y.; Zhao, Y.; Waterhouse, G. I. N.; Zheng, L.; Cao, X.; Teng, F.; Wu, L.-Z.; Tung, C.-H.; O'Hare, D.; Zhang, T., Layered-Double-Hydroxide Nanosheets as Efficient Visible-Light-Driven Photocatalysts for Dinitrogen Fixation. *Adv. Mater.* **2017,** *29*, 1703828.
115.Wang, S.; Hai, X.; Ding, X.; Chang, K.; Xiang, Y.; Meng, X.; Yang, Z.; Chen, H.; Ye, J., Light-Switchable Oxygen Vacancies in Ultrafine Bi5O7Br Nanotubes for Boosting Solar-Driven Nitrogen Fixation in Pure Water. *Adv. Mater.* **2017,** *29*, 1701774.
116.Xiao, C.; Hu, H.; Zhang, X.; MacFarlane, D. R., Nanostructured Gold/Bismutite Hybrid Heterocatalysts for Plasmon-Enhanced Photosynthesis of Ammonia. *ACS Sustain. Chem. Eng.* **2018,** *6*, 2806-2806.
117.Fang, Y.; Xue, Y.; Hui, L.; Yu, H.; Li, Y., Graphdiyne@Janus Magnetite for Photocatalytic Nitrogen Fixation. *Angew. Chem. Int. Ed.* **2021,** *60*, 3170-3174.
118.Zhang, S.; Zhao, Y.; Shi, R.; Zhou, C.; Waterhouse, G. I. N.; Wu, L.-Z.; Tung, C.-H.; Zhang, T., Efficient Photocatalytic Nitrogen Fixation over $Cu^{\delta+}$-Modified Defective ZnAl-Layered Double Hydroxide Nanosheets. *Adv. Energy Mater.* **2020,** *10*, 1901973.
119.Tanabe, Y.; Nishibayashi, Y., Comprehensive insights into synthetic nitrogen fixation assisted by molecular catalysts under ambient or mild conditions. *Chem. Soc. Rev.* **2021**.

Chapter 2 Objectives

It has been presented the current opportunity that solar photocatalysis offers to convert the abundant, ubiquitous and inextinguishable solar energy into chemicals that can be used as fuels or intermediates for the chemical industry.

The present Doctoral Thesis is aimed to contribute to this area in two different ways. On one hand, some of the experimental work will try to determine the possibility to synthesize hybrid organic lead perovskites in which the organic ammonium cation has some functionality, either to promote charge separation or to increase the stability of the hybrid material. It is clear that accommodation of organic ammonium ions larger than the methyl ammonium will produce a structural shift from 3D to 2D perovskite and that the current knowledge predicts that the optoelectronic properties of the 2D in terms of absorption band onset and charge separation are far from the optimal values found for the 3D materials, but the functionality of the organic ligand can possibly influence favorably some of these properties. Thus, to enhance charge separation the ammonium cation can have a biphenyl moiety that is known to form long-lived radical cations. On the other hand, stability against moisture can be improved if the crystallite surface is protected by a hydrophobic overcoat of silica or an organic polymer. Three Chapters of the present document will report on the results achieved in tuning the properties of hybrid organic lead perovskites.

In a second part of the Thesis the target will be to explore photo- and electrocatalytic methods for N_2 fixation, a challenging reaction that as it has been commented is key in the current chemical industry. Following the lead of CO_2, we want to explore the possibility to develop the so far unreported photocatalytic N_2 hydrogenation by using one of the most active materials reported for the photocatalytic CO_2 hydrogenation. The preliminary results on the use of transition metal complexes to promote the electrochemical N_2 reduction, targeting to understand the possibility of using metal complexes for the electro and photocatalytic N_2 reduction in the future works, will also be reported.

Thus, the specific objectives of the present Thesis are the following:

1. Synthesis and evaluation of the photocatalytic activity of hybrid organic lead perovskite with the 4,4'-biphenylene diammonium dication as the organic ligand. It is expected that due to the large molecular size, the structure of this so far unreported hybrid perovskite would be layered. If this is the case, the linear arrangement of the two ammonium cations could serve to establish a strong Coulombic interaction between two adjacent layers that could, somehow, lead to a 3D structure. In addition, the biphenylene moiety of the diammonium cation could promote the efficiency of charge separation upon photoexcitation of the material. The photoactivity of this new hybrid perovskite as photocatalyst will be evaluated for the *cis*- to *trans*-stilbene isomerization, a photochemical process that is known to involve the intermediacy of the corresponding radical cation.
2. Surface silanation of the previous hybrid benzidinium lead perovskite with different silylating agents and determination of the influence of the organosilica layer on the hydrophobic and photocatalytic properties of the resulting coated perovskite. It is of interest to determine the feasibility of photocatalytic *cis*- to *trans*-stilbene isomerization involving electron transfer as a function of the thickness of the silica overcoat.
3. Synthesis of the corresponding hybrid lead perovskite for styryl ammonium cation. After the synthesis the material will be submitted to post-synthetic radical polymerization without or with additional styrene co-monomer in order to create a protective polymeric layer on the surface of the perovskite crystallites. The resulting material will be tested regarding its photostability in order to determine the feasibility of photocatalysts based on this approach.
4. Use of ruthenium nanoparticles supported on strontium titanate as photocatalyst for hydrogenation of N_2 to NH_3. To enhance the photocatalytic activity, the possibility to introduce promoters, such as Cs, on the Ru photocatalyst will also be explored.
5. Screening of the electrocatalytic activity of transition metal complexes of 3,5-disubstituted tris(pyrazolyl)borates. It has been

reported that N_2 forms a stable complex with the Co^+ complex of tris-(3-methyl-5-tertbutylpyrazolyl)borate that has been characterized by single crystal XRD. It would be important to determine if the ability to bind N_2 of Co^+ and possibly other transition metals can be exploited to develop a photo/electrocatalytic system for N_2 reduction to NH_3.

In case that these general and specific objectives are achieved, the present Thesis would represent a significant step forward by showing the applicability as visible-light photocatalysts of hybrid lead perovskites and also to promote photo- and electrocatalytic reactions of N_2 fixation.

Chapter 3 Hybrid Benzidinium Lead Iodide Perovskite with 1D Structure as Photoinduced Electron Transfer Photocatalyst

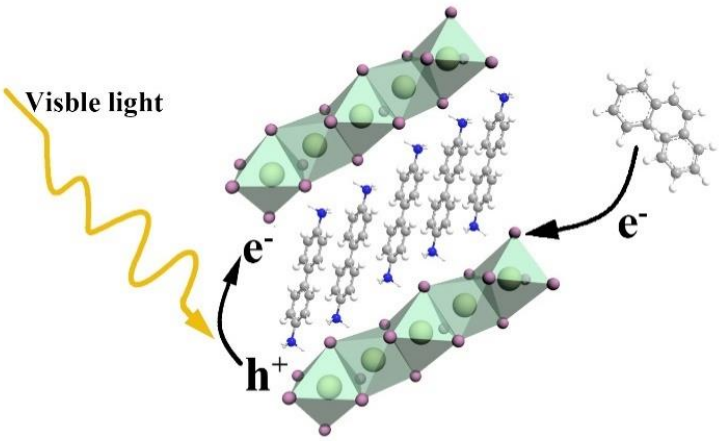

3.1 Introduction

As commented in the Chapter 1 (General Introduction) of this Doctoral Thesis, hybrid methylammonium lead iodide perovskite exhibits upon light excitation a high efficiency of charge separation and a large charge mobility that is responsible for the high efficiency of the solar cells based on this type of perovskite as photoactive material.[1, 2] Solar photon-to-current efficiencies over 20 % have been certified for some of these photovoltaic devices based on methylammonium lead iodide perovskite.[3, 4] Besides light absorption in the whole UV-vis spectral range, one of the key features for the excellent photo response is the low exciton binding energy that is responsible for a very efficient charge separation.[5]

One of the leading hypotheses of the present Doctoral Thesis is that many of the optoelectronic properties of hybrid lead iodide perovskites that are relevant in photovoltaic devices are also wanted in photocatalysis. However, up to now, the number of reports on the use of hybrid perovskites in photocatalysis is very limited,[6, 7] probably due to the lack of stability of hybrid perovskites in most of the media typically used in photocatalysis, particularly in water and polar solutions.

Regarding application in photocatalysis, other aspect to be considered for the potential application of hybrid perovskites beyond photovoltaics is the possibility to modify their chemical composition, introducing other organic ammonium cations that could play a specific role promoting charge separation.[8, 9]

Aimed at exploring the possibilities that hybrid organic lead iodides offer in photocatalysis, the present Chapter deals with the preparation of the hybrid lead iodide perovskite of the benzidine di-protonated salt. It will be presented that the resulting hybrid perovskite exhibits photocatalytic activity for the photoinduced electron transfer cis-to-trans isomerization of stilbene. Benzidine

diammonium was selected as organic cation in the composition of hybrid lead perovskite due to the well-known ability of biphenyls in molecular organic photochemistry to increase the efficiency of photoinduced electron transfer processes by enhancing charge separation.[10, 11] The long lifetime of biphenyl radical ions in the microsecond time scale allows their reaction with substrates promoting electron transfer processes.

3.2 Results and Discussion

3.2.1 Material preparation and characterization

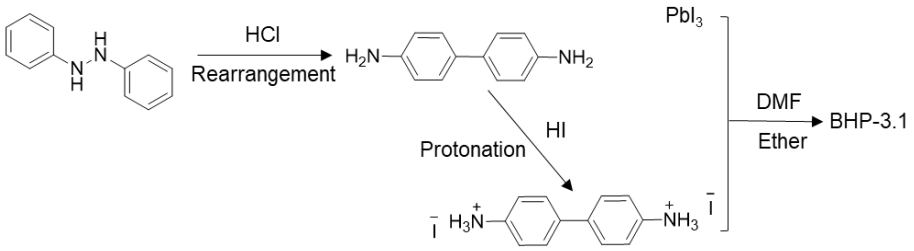

Scheme 3.1 Process for the preparation of the hybrid perovskite.

Scheme 3.1 summarized the preparation procedure of hybrid benzidinium lead iodide perovskite in present Chapter. The diammonium salt of benzidine was prepared in two steps starting from commercial hydrazobenzene by acid-catalyzed rearrangement to benzidine (**BZ-3.1**), followed by careful protonation of **BZ-3.1** with an excess of concentrated aqueous HI acid. The structure of product **BZ-3.1** was confirmed by ^{1}H NMR and IR spectroscopy (see Fig. 3.1 and 3.2). Particularly, remarkable changes in the symmetry and chemical shifts of the aromatic protons respect to parent hydrazobenzene were recorded in ^{1}H NMR spectroscopy of compound **BZ-3.1**. Specifically, **BZ-3.1** exhibits two doublets in the aromatic region corresponding to an A_2M_2 system appearing at 6.77 and 7.27 ppm corresponding to the aromatic protons at *ortho* and *meta* position of the amino groups. In IR spectroscopy **BZ-3.1** exhibits two

vibration peaks at 3400 and 3250 cm^{-1} attributed to a primary amine.[12]

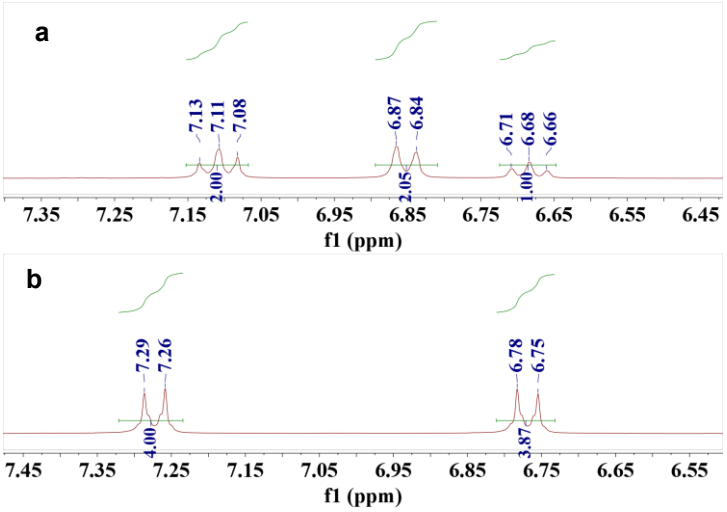

Fig. 3.1 ^{1}H NMR results of (a) hydrazobenzene and (b) **BZ-3.1**.

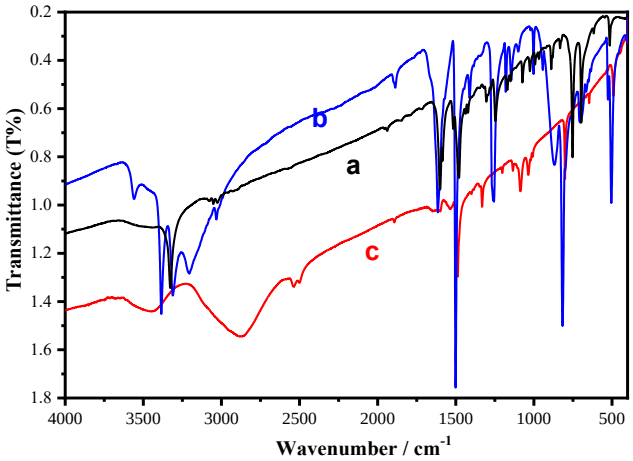

Fig. 3.2 Infrared spectra of (a) hydrazobenzene, (b) **BZ-3.1**, and (c) **BZI-3.1.**

The resulting salt benzidinium diiodide (**BZI-3.1**) was characterized by elemental combustion analysis (Table 3.1) and by IR spectroscopy. A good match between elemental composition determined by combustion analysis and the

theoretical value based on the molecular formula corresponding to the disalt **BZI-3.1**, combined with the broad peak near 3000 cm^{-1} and the disappearance of the double peak around 3500 ~ 3200 cm^{-1} in IR spectrum of **BZI-3.1** indicate the formation of benzidinium diiodide.

Table 3.1 Combustion Elemental analysis results and theoretic proportion of **BZI-3.1**

Type	N %	C %	H %	Rest %
Experimental proportion	6.483	33.038	3.298	57.181
Theoretic proportion	6.360	32.709	3.180	57.696

The wanted benzidinium lead iodide perovskite (**BHP-3.1**) was, then, obtained by mixing in DMF, the corresponding amount of lead iodide (PbI_2) and **BZI-3.1**. Precipitation of the solid perovskite **BHP-3.1** as a fine powder can be achieved by addition of toluene. Single crystals of the same hybrid perovskite **BHP-3.1** suitable for XRD structural characterization could be obtained by slow diffusion of toluene vapors into the DMF solution of PbI_2 and **BZI-3.1**, allowing the slow precipitation of fine yellow needle-like crystals to occur during one day.

Chemical analysis of **BHP-3.1** was carried out combining combustion elemental analysis for C, H and N elements with ICP-OES analysis of Pb (Table 3.2) and assuming that the residual percentage is due to the sum of I and O. It was also considered that a **BHP-3.1** perovskite unit formula contains 0.5 molecules of benzidinium cations (**BZN-3.1**, $^{+}NH_3$-$C_{12}H_8$-NH_3^{+}) to maintain neutrality. Then, the analytical data lead to the experimental formula PbI_3(**BZN-3.1**)$_{0.5}$$(DMF)_{0.3}$, indicating that the present material can be reasonably considered as a defective hybrid

perovskite. A detailed description of how the molecular formula was deduced is presented in the section 8.4 of Chapter 8. The proposed PbI_3(**BZN-3.1**)$_{0.5}$(DMF)$_{0.3}$ formula for perovskite **BHP-3.1** is within the accepted error for experimental analytical data of ± 0.4 %.

Table 3.2 ESI-MS and Combustion Elemental analysis results of hybrid perovskite **BHP-3.1**.

Element	Combustion Elemental analysis				ESI-MS
	N (wt%)	C (wt%)	H (wt%)	Rest (wt%) (Pb, I, O)	Pb(wt%)
Proportion	2.574	11.366	1.453	84.607	28.4 %

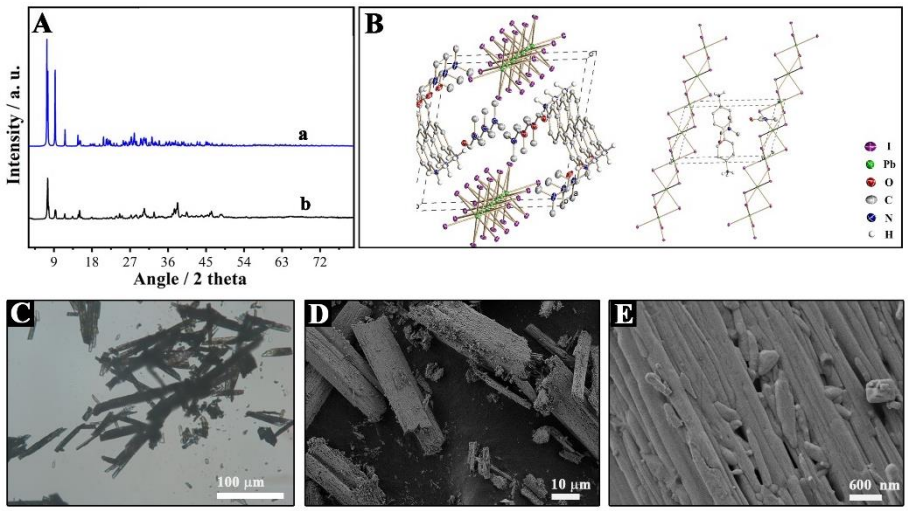

Fig. 3.3 (A) XRD patterns of **BHP-3.1** fine powder. (B) Two views (ORTEP representation) of crystal structure of PbI_3(**BZN-3.1**)$_{0.5}$ determined by single crystal-XRD with thermal ellipsoids set at a 30 % probability level. The hydrogen atoms and one part of modelling of a disordered DMF solvent molecule are omitted for clarity (CCDC 1902819). (C) Optical microscopy image of perovskite **BHP-3.1**crystals. and (D)-(E) SEM image of material **BHP-3.1**.

Single crystal XRD indicates that the structure of **BHP-3.1** is constituted by parallel chains of PbI_6 octahedra sharing the faces aligned along the long axis of the crystal that are coordinated to dications **BZN-3.1** that interact by Coulombic forces and hydrogen bonding with the PbI_6 octahedra. **BZN-3.1** ions establish van der Waals forces among them due to π-π stacking of the aromatic rings. The PbI_6 and dication **BZN-3.1** chains define channels that are occupied by DMF molecules that interact through hydrogen bonds with PbI_6 and dications **BZN-3.1**. Fig. 3.3 presents two views of the structure corresponding to material **BHP-3.1** prepared in this study. The crystal data, structure refining, crystal drawing of different views and partial packing diagram can be found in Table 8.1, Fig. 8.3 and Fig. 8.4, respectively, in Chapter 8.

Overall, the structure for PbI_3(**BZN-3.1**)$_{0.5}$ corresponds to a 1D hybrid perovskite. It is well established in the field of hybrid perovskites that the size of the organic cation determines the structure of the perovskite according to the Goldschmidt tolerance factor .[13] Only methylammonium and formamidinium, the smallest organic ammonium ions, are able to form hybrid perovskites with 3D structure. These structures are transformed into 2D or 1D when the size of the organic cation becomes larger. In particular, it has been reported that phenylammonium lead iodide is a 2D perovskite,[14] while in the present case the structure of solid **BHP-3.1** corresponds to a 1D material.

The **BHP-3.1** perovskite is sensitive to the temperature above 70 ºC (Fig. 3.4) and also depending on the nature of the solvent it shows a limited stability in solution (Fig. 3.5). However, it was found that the **BHP-3.1** perovskite is indefinitely stable in hexane and also can stand toluene for a few hours, In contrast, **BHP-3.1** dissolves partially in H_2O and acetonitrile. Therefore, although limited, there is a range of conditions and solvents in which the **BHP-3.1** perovskite can be employed.

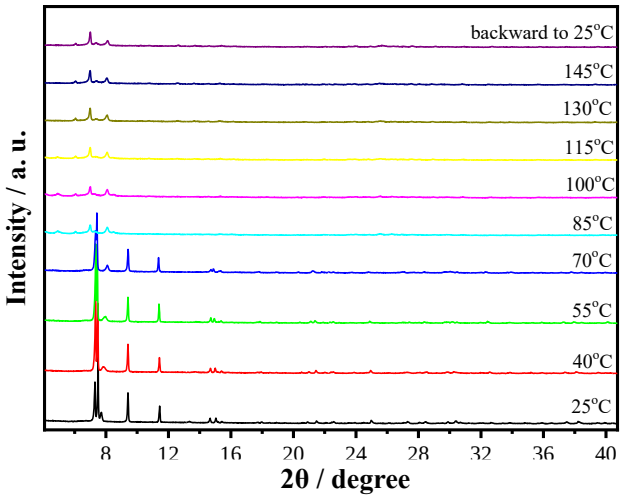

Fig. 3.4 Thermo-stability results of **BHP-3.1** perovskite by in-situ XRD monitoring.

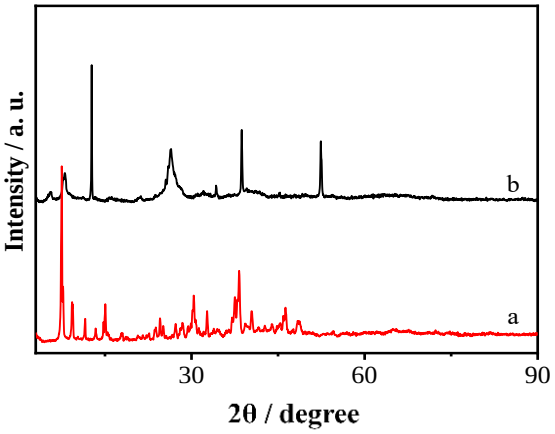

Fig. 3.5 XRD patterns of **BHP-3.1** perovskite (a) before, and (b) after disperse in acetonitrile for 3 h.

The 1D structure of **BHP-3.1** perovskite is reflected in the morphology of the crystals. According to optical microscopy, the solid **BHP-3.1** perovskite is constituted by needles and rods of millimetric dimensions and high aspect ratio (Fig. 3.3). SEM images show that the rods are constituted by the agglomeration

of thin needles of about 200 nm width and very long length about 50 µm. Much smaller debris due to the breakage of the needles can also be observed in the images. Besides optical microscopy, Fig. 3.3 also shows some representative SEM images of **BHP-3.1**.

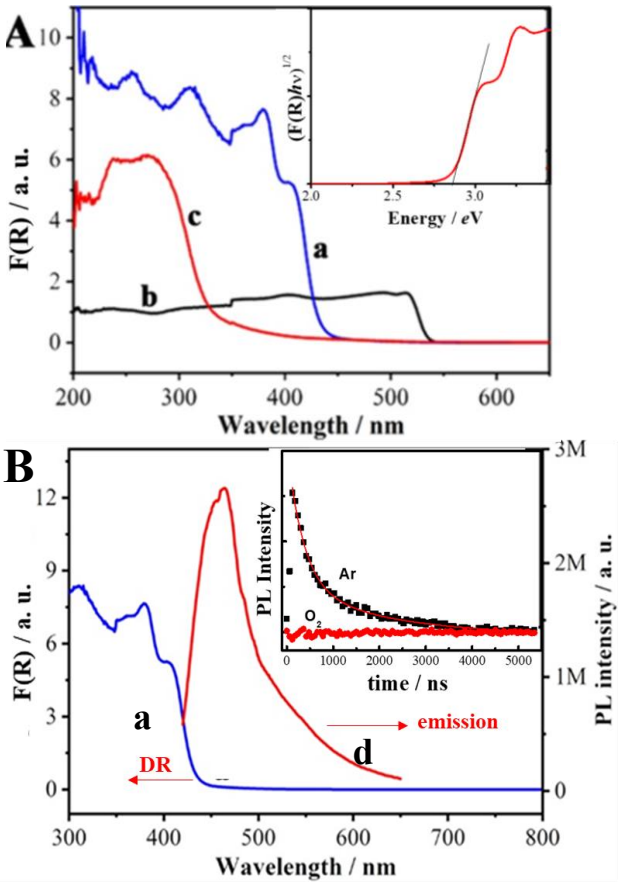

Fig. 3.6 (A) Diffuse reflectance UV-Vis spectra of **BHP-3.1** (a), PbI_2 (b), and **BZI-3.1** (c). Inset: Tauc plot corresponding to the **BHP-3.1** absorption spectrum. (B) Diffuse reflectance absorption (a) and emission (d) spectra of **BHP-3.1** perovskite upon excitation at 390 nm. Inset: temporal emission profile of **BHP-3.1** perovskite monitored at 465 nm under Ar atmosphere (black dots) and in the presence of O_2 (blue dots). The red line corresponds to bi-exponential fitting.

The 1D structure of **BHP-3.1** perovskite is also reflected in the optical absorption spectrum of the material. 3D Perovskites exhibit a continuous absorption band in most of the visible range. In contrast, the onset of the 1D and 2D hybrid perovskite occurs in the visible region. The diffuse reflectance UV-Vis spectrum of the **BHP-3.1** is presented in Fig. 3.6. As can be seen there, the onset of the absorption spectrum of the hybrid perovskite is about 450 nm, the corresponding Tauc plot indicates that the bandgap of **BHP-3.1** is 2.86 eV. It is well-known in the state of the art that a change in the structure of the hybrid perovskite from 3D to lower dimensionality originates an increase in the bandgap.[15] Thus, typical 3D $MAPbI_3$ perovskite exhibits a 1.51 eV band gap, while 2D $BDAPbI_3$ (BDA: di-cation of 1,4- diaminobutane) perovskite has reported a bandgap value of 2.37 eV.[16, 17]

BHP-3.1 exhibits a strong photoluminescence with partially resolved fine structure and an emission maximum at 463 nm, when the material is excited at 390 nm (Fig. 3.6). The temporal profile of the emission under argon can be fitted to a biexponential decay with a short-lived component with τ_1 = 344 ns, contributing about 15 % to the total emission intensity and a much longer-lived component with τ_2 = 1974 ns with a contribution of 85 %. This emission is totally quenched in the presence of O_2, and accordingly it can be assumed that it derives from excited electrons transferring to O_2.[18] In this regard, the biexponential kinetics can be rationalized considering that charge carriers responsible for the long-lived emission are those located in trap sites, thus prolonging their life.

3.2.2. Photocatalytic activity

As indicated in Chapter 1 of the present Doctoral Thesis, the purpose of the study was to explore the possible application of the optoelectronic properties of hybrid perovskites in photocatalysis. Since **BHP-3.1** should exhibit photoinduced charge separation through photoexcitation, it was selected as photocatalyst for a process that can be considered as a model

reaction for photoinduced electron transfer, namely, cis-to-trans stilbene photoisomerization.[19] This geometrical isomerization of stilbene was extensively studied in the context of photoinduced electron transfer processes promoted by organic photosensitizers, there being extensive literature describing the reaction mechanism.[20-22]

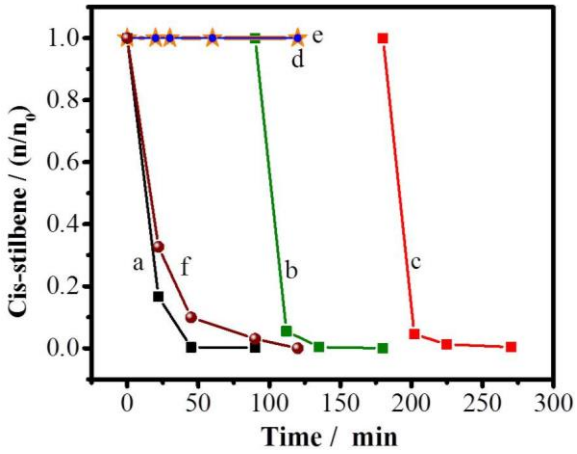

Fig. 3.7 Cis-to-trans stilbene isomerization promoted by visible light (λ > 450 nm) in the presence of **BHP-3.1** acting as photocatalyst (a). Plots b and c correspond to consecutive reuses of the photocatalyst. Control experiments carried out under the same conditions but in the absence of **BHP-3.1** (d), in the dark in the presence of **BHP-3.1** (e) or in the presence of MAPbI perovskite instead of **BHP-3.1** (f).

Preliminary blank controls by long-wavelength irradiation of cis-stilbene with visible light (λ > 450 nm) show that no cis-to-trans isomerization occurs in the absence of **BHP-3.1**. Also, control experiments in the dark, but in the presence of **BHP-3.1** show no cis-to-trans isomerization (Fig. 3.7 (d) and (e)).

In contrast, upon visible light irradiation of a solution of cis-stilbene in hexane in the presence of **BHP-3.1** (0.25 mmol/mL) a complete cis-to-trans isomerization was observed after 1 h irradiation. To put the photocatalytic activity of **BHP-3.1** into context, the well-known $MAPbI_3$ was also evaluated as

photocatalyst to promote the cis-to-trans stilbene isomerization under identical conditions as those employed in the case of **BHP-3.1**. As can be seen in Fig. 3.7 (f), although complete cis-to-trans isomerization was also achieved using $MAPbI_3$ as photocatalyst, the reaction kinetics was slower in this case as compared to **BHP-3.1**. This shows the benefits of the benzidine diammonium unit in the photocatalytic activity of the resulting hybrid perovskite.

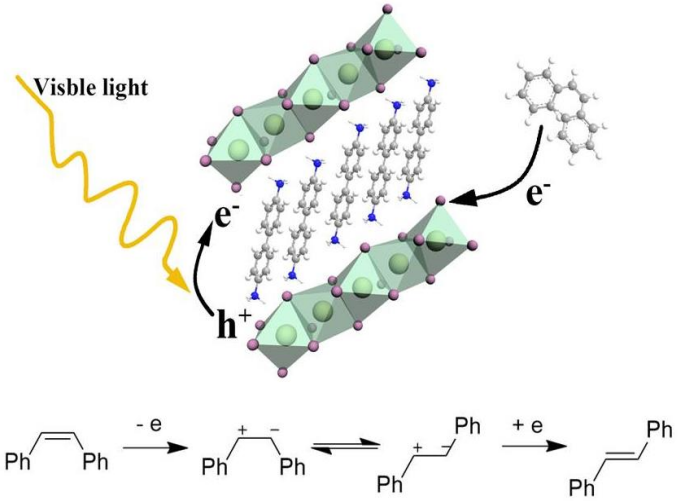

Scheme 3.2 Schematic illustration of the photoinduced cis-to-trans stilbene isomerization process photocatalyzed by **BHP-3.1** and the proposed mechanism.

Regarding the reaction mechanism, it is proposed that upon selective irradiation of **BHP-3.1**, photoinduced electron-hole separation should occur. Holes on the perovskite would abstract one electron from cis-stilbene, leading to the generation of the corresponding stilbene radical cation that would undergo isomerization to the trans-stilbene radical cation. Back electron transfer from hybrid perovskite to the photocatalyst would complete the reaction. The key mechanistic step is the cis-trans equilibrium of stilbene radical cation as a consequence of the lower bond order. The process is illustrated in the Scheme 3.2.

After the reaction, the **BHP-3.1** sample was used as photocatalyst was characterized by XRD and SEM (Fig. 3.8). XRD reveals changes in the diffraction pattern, although crystallinity was maintained. Unfortunately, the used **BHP-3.1** sample was not suitable for single-crystal diffraction. SEM images show that during the reaction a remarkable change in the morphology of the particles occurs. It seems that the rods constituted by agglomeration of thin needles initially present in the fresh sample have undergone extensive deaggregation during photochemical reaction. It is worth commenting that analogous deaggregation under irradiation has also been observed in carbon nanotubes and attributed to the Coulombic repulsion between photoexcited tubes due to their Coulombic charges of the same sign.[23]

In spite of the morphological changes in the **BHP-3.1** during reaction, the photocatalytic activity of this material remained unchanged, as it can be deduced from the three consecutive resues that were carried out without significant activity reduction, as can be seen in Fig. 3.7 (b) and (c).

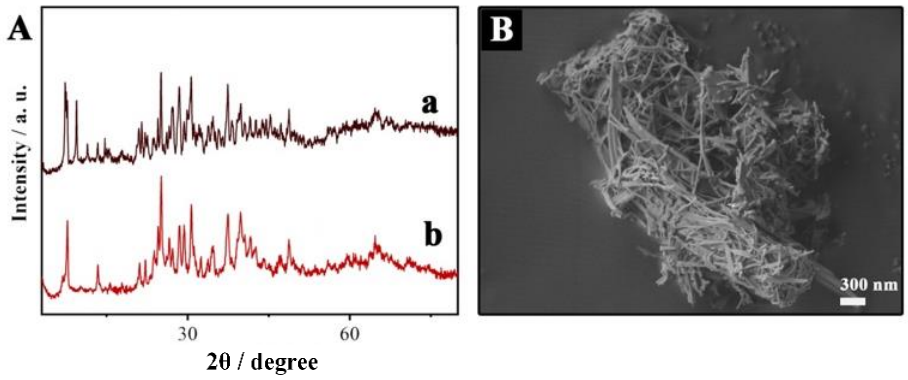

Fig. 3.8 (A) XRD patterns of **BHP-3.1** before (a) and (b) after photoinduced isomerization reaction. (B) SEM image of the sample of **BHP-3.1** after photoinduced isomerization reaction.

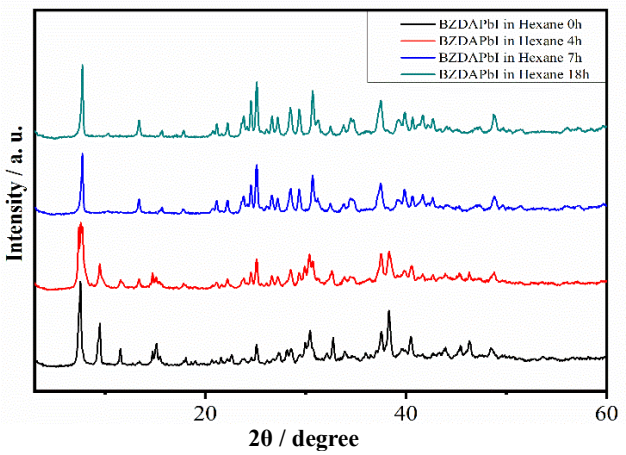

Fig. 3.9 XRD Patterns of **BHP-3.1** after dispersing the solid in hexane for different time.

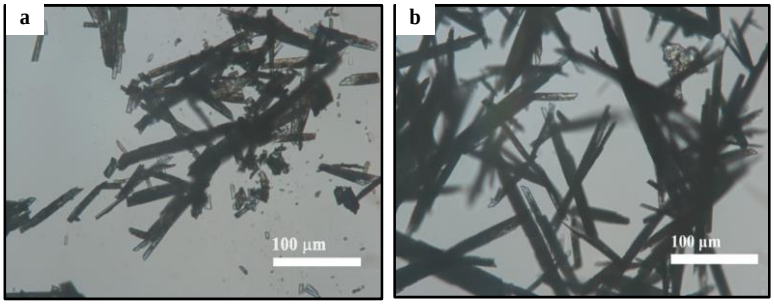

Fig. 3.10 Optical microscopy Images of **BHP-3.1** before dispersion in hexane (a), and after being dispersed in hexane for 18 h (b).

To further investigate the reason of the XRD pattern change, **BHP-3.1** was dispersed in hexane and then XRD patterns were recorded in the course of time (Fig. 3.9). Surprisingly, the peaks at 2θ = 7.36° and 7.56°, which belong to the (001) and (010) crystal plane of material gradually disappeared, while the peak at 2θ = 7.75° became more intense, indicating that without stirring or light irradiation, **BHP-3.1** suffered a structural change just when exposed in hexane. However, no obvious change in the morphology after dispersed in hexane was observed, as

confirmed by optical microscopy (Fig. 3.10). It should also be noted that the **BHP-3.1** XRD patterns after immersing in hexane for 20 h are coincident with the **BHP-3.1** patterns after its use in the photoinduced isomerization reaction, which demonstrated that the structural change during the photoinduced isomerization is due to exposure to the solvent.

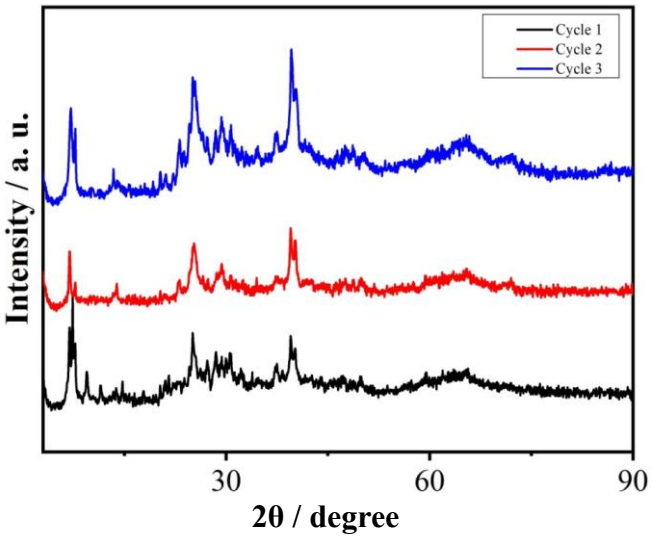

Fig. 3.11 XRD patterns of **BHP-3.1** after each use as photocatalyst for cis-to-trans stilbene isomerization reaction.

The XRD patterns of photocatalyst **BHP-3.1** after each reuse are shown in Fig. 3.11. As can be seen, no significant changes were found after the first use of **BHP-3.1** photocatalyst, and even, the XRD patterns of it after the second and third use were very similar.

In order to gain some information about the reasons for the change in the XRD pattern and particularly if it is caused by the removal of DMF in the structure, **BHP-3.1** was submitted to vacuum at 50 ºC for 30 h, without observing noticeable changes in the XRD pattern as shown in Fig. 3.12. It was expected that this treatment could remove DMF from the structure, but the lack of

changes in the XRD pattern seems to rule out the wanted DMF removal. This is indicating that the most probable reason for structural change is due to the action of hexane or light or the combination of both.

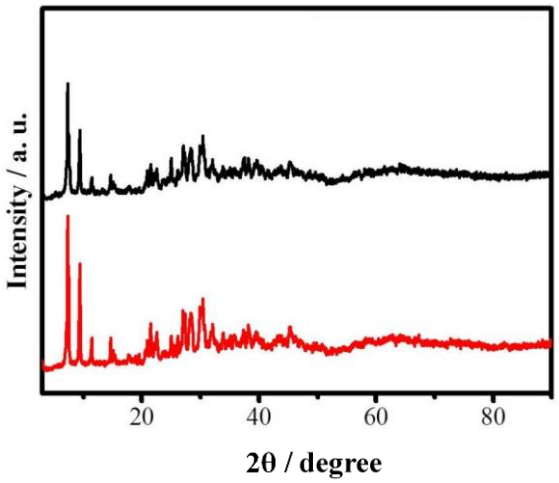

Fig. 3.12 XRD patterns of **BHP-3.1** before and (red) after treatment (black) under vacuum at 50 °C for 30 h.

In order to further advance in the understanding of the change of the XRD pattern, combustion and ICP analyses were carried out after stirring **BHP-3.1** in the dark in hexane for 7 h and submitting to reaction conditions (see Table 3.3). The results show a decrease in the N-Pb ratio from 1.34 in the fresh sample to 1.17 after hexane stirring in the dark and to 0.92 after photocatalytic reaction. Considering that the theoretical N-Pb ratio in **BHP-3.1** in the absence of DMF should be 1, it can be concluded that **BHP-3.1** exposed to hexane suffers a partial loss of DMF molecules, while under reaction conditions the DMF molecules in the structure are completely removed.

Table 3.3 Inductively Coupled Plasma – Optical Emission Spectroscopy (ICP-OES) and Combustion Elemental analyze (EA) data of **BHP-3.1**, after hexane exposure and after photocatalytic reaction.

Element	EA			ICP-ES
	N (wt%)	C (wt%)	H (wt%)	Pb (wt%)
Before in Hexane	2.574	11.366	1.453	28.400
After in Hexane	2.510	12.500	1.520	31.800
After the reaction	2.070	11.960	1.320	33.390

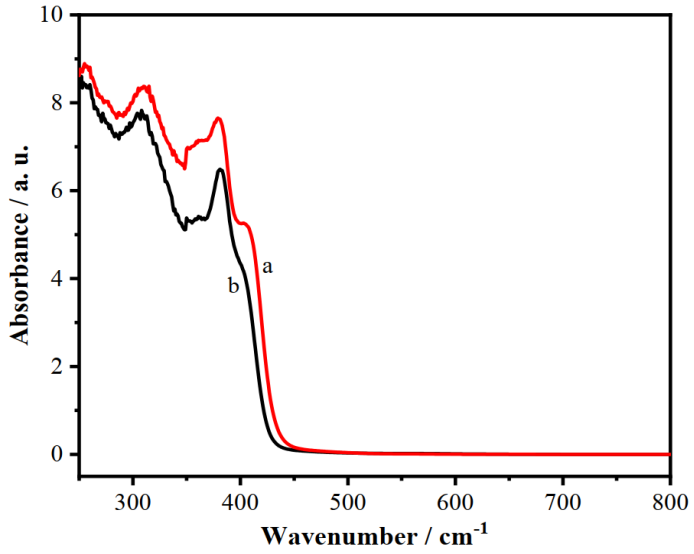

Fig. 3.13 Diffuse reflectance spectrum of **BHP-3.1** before dispersion in hexane (a), and after disperse in hexane for 18 h (b).

Worth noticing is that, in addition, the diffuse reflectance UV-Vis spectrum of **BHP-3.1** after being dispersed in hexane also exhibited a typical perovskite absorption spectrum with a

solvatochromic ~ 10 nm blue shift compared with the parent **BHP-3.1** as solid (Fig. 3.13).

Based on the small shift in the absorption spectrum and the structure of the single crystal of perovskite, it is reasonable to propose that the changes in the observed XRD pattern after dispersion in hexane are due to the removal of the DMF molecules from the void of crystalline **BHP-3.1** upon exposure to the hexane solvent. As consequence, it is suggested that the XRD pattern changes after photoinduced isomerization reaction are the result of the loss of DMF molecules located in the void of **BHP-3.1** crystal during the course of photocatalytic reaction.

3.3 Conclusions

The present Chapter has shown the possibility to prepare hybrid lead iodide perovskite with benzidinium dication as organic moiety. The resulting perovskite has the specific formula PbI_3(**BZN-3.1**)$_{0.5}DMF_{0.3}$ including some DMF molecules from the synthesis in the structure. The hybrid material corresponds to 1D perovskite. This **BHP-3.1**, although it loses some DMF crystallization molecules, is stable in hexane and in this solvent can promote the photoinduced electron transfer cis-to-trans isomerization of stilbene. Although the material undergoes changes in the particle morphology and the XRD pattern during the photochemical reaction, it is proposed that these changes are the result of the loss of intracrystalline DMF molecules. Moreover, these changes do not affect the photocatalytic activity of this photocatalyst.

Overall, this Chapter shows the potential of hybrid lead perovskites beyond the realm of solar cells and indicates that it should be possible to extend the application of this type of semiconducting materials as photocatalysts under conditions compatible with the structure.

3.4 References

1. Kojima, A.; Teshima, K.; Shirai, Y.; Miyasaka, T., Organometal halide perovskites as visible-light sensitizers for photovoltaic cells. *J. Am. Chem. Soc.* **2009,** *131*, 6050-1.

2. Ponseca, C. S.; Savenije, T. J.; Abdellah, M.; Zheng, K.; Yartsev, A.; Pascher, T.; Harlang, T.; Chabera, P.; Pullerits, T.; Stepanov, A.; Wolf, J.-P.; Sundström, V., Organometal Halide Perovskite Solar Cell Materials Rationalized: Ultrafast Charge Generation, High and Microsecond-Long Balanced Mobilities, and Slow Recombination. *J. Am. Chem. Soc.* **2014,** *136*, 5189-5192.

3. Saliba, M.; Orlandi, S.; Matsui, T.; Aghazada, S.; Cavazzini, M.; Correa-Baena, J.-P.; Gao, P.; Scopelliti, R.; Mosconi, E.; Dahmen, K.-H.; De Angelis, F.; Abate, A.; Hagfeldt, A.; Pozzi, G.; Graetzel, M.; Nazeeruddin, M. K., A molecularly engineered hole-transporting material for efficient perovskite solar cells. *Nat. Energy* **2016,** *1*, 15017.

4. Zhao, D.; Wang, C.; Song, Z.; Yu, Y.; Chen, C.; Zhao, X.; Zhu, K.; Yan, Y., Four-Terminal All-Perovskite Tandem Solar Cells Achieving Power Conversion Efficiencies Exceeding 23%. *ACS Energy Lett.* **2018,** *3*, 305-306.

5. Brenner, T. M.; Egger, D. A.; Kronik, L.; Hodes, G.; Cahen, D., Hybrid organic—inorganic perovskites: low-cost semiconductors with intriguing charge-transport properties. *Nat. Rev. Mater.* **2016,** *1*, 15007.

6. Park, S.; Chang, W. J.; Lee, C. W.; Park, S.; Ahn, H.-Y.; Nam, K. T., Photocatalytic hydrogen generation from hydriodic acid using methylammonium lead iodide in dynamic equilibrium with aqueous solution. *Nat. Energy* **2016,** *2*, 16185.

7. Zhu, X.; Lin, Y.; Sun, Y.; Beard, M. C.; Yan, Y., Lead-Halide

Perovskites for Photocatalytic alpha-Alkylation of Aldehydes. *J. Am. Chem. Soc.* **2019**.

8. Febriansyah, B.; Koh, T. M.; John, R. A.; Ganguly, R.; Li, Y.; Bruno, A.; Mhaisalkar, S. G.; England, J., Inducing Panchromatic Absorption and Photoconductivity in Polycrystalline Molecular 1D Lead-Iodide Perovskites through π-Stacked Viologens. *Chem. Mater.* **2018,** *30*, 5827-5830.

9. Hu, H.; Meier, F.; Zhao, D.; Abe, Y.; Gao, Y.; Chen, B.; Salim, T.; Chia, E. E. M.; Qiao, X.; Deibel, C.; Lam, Y. M., Efficient Room-Temperature Phosphorescence from Organic–Inorganic Hybrid Perovskites by Molecular Engineering. *Adv. Mater.* **2018,** *30*, 1707621.

10. Merkel, P. B.; Luo, P.; Dinnocenzo, J. P.; Farid, S., Accurate oxidation potentials of benzene and biphenyl derivatives via electron-transfer equilibria and transient kinetics. *J. Org. Chem.* **2009,** *74*, 5163-5173.

11. Meggers, E.; Steckhan, E.; Blechert, S., Radical C C Bond Formation by Photoinduced Electron Transfer Addition of α‐Silyl Carbamates to Acceptor‐Substituted Alkenes. *Angew. Chem. Int. Ed. Engl.* **1995,** *34*, 2137-2139.

12. Heacock, R. A.; Marion, L., The Infrared Spectra of Secondary Amines and Their Salts. *Can. J. Chem.* **1956,** *32*, 1782-1795.

13. Albero, J.; Asiri, A. M.; García, H., Influence of the composition of hybrid perovskites on their performance in solar cells. *J. Mater. Chem. A* **2016,** *4*, 4353-4364.

14. Gao, P.; Bin Mohd Yusoff, A. R.; Nazeeruddin, M. K., Dimensionality engineering of hybrid halide perovskite light absorbers. *Nat. Commun.* **2018,** *9*, 5028.

15. Cao, D. H.; Stoumpos, C. C.; Farha, O. K.; Hupp, J. T.;

Kanatzidis, M. G., 2D Homologous Perovskites as Light-Absorbing Materials for Solar Cell Applications. *J. Am. Chem. Soc.* **2015,** *137*, 7843-7850.

16. Ogomi, Y.; Morita, A.; Tsukamoto, S.; Saitho, T.; Fujikawa, N.; Shen, Q.; Toyoda, T.; Yoshino, K.; Pandey, S. S.; Ma, T.; Hayase, S., $CH_3NH_3Sn_xPb_{(1-x)}I_3$ Perovskite Solar Cells Covering up to 1060 nm. *J. Phys. Chem. Lett.* **2014,** *5*, 1004-1011.

17. Safdari, M.; Svensson, P. H.; Hoang, M. T.; Oh, I.; Kloo, L.; Gardner, J. M., Layered 2D alkyldiammonium lead iodide perovskites: synthesis, characterization, and use in solar cells. *J. Mater. Chem. A* **2016,** *4*, 15638-15646.

18. Lorenzon, M.; Sortino, L.; Akkerman, Q.; Accornero, S.; Pedrini, J.; Prato, M.; Pinchetti, V.; Meinardi, F.; Manna, L.; Brovelli, S., Role of Nonradiative Defects and Environmental Oxygen on Exciton Recombination Processes in $CsPbBr_3$ Perovskite Nanocrystals. *Nano Lett.* **2017,** *17*, 3844-3853.

19. Zhou, J. M.; Shi, W.; Xu, N.; Cheng, P., Highly Selective Luminescent Sensing of Fluoride and Organic Small-Molecule Pollutants Based on Novel Lanthanide Metal-Organic Frameworks. *Inorg. Chem.* **2013,** *52*, 8082-8090.

20. Waldeck, D. H., Photoisomerization Dynamics of Stilbenes. *Chem. Rev.* **1991,** *91*, 415-436.

21. Jack Saltiel, S. G., and Constance Werking, The AH for Thermal irans-Stilbene/c/s-Stllbene Isomerization. Do S_0 and T_1 Potential Energy Curves Cross? *J. Phys. Chem. C* **1986,** *91*, 2755-2758.

22. de Wergifosse, M.; Houk, A. L.; Krylov, A. I.; Elles, C. G., Two-photon absorption spectroscopy of trans-stilbene, cis-stilbene, and phenanthrene: Theory and experiment. *J. Chem. Phys.* **2017,** *146*,

144305.

23. Alvaro, M.; Aprile, C.; Ferrer, B.; Garcia, H., Functional Molecules from Single Wall Carbon Nanotubes. Photoinduced Solubility of Short Single Wall Carbon Nanotube Residues by Covalent Anchoring of 2,4,6-Triarylpyrylium Units. *J. Am. Chem. Soc.* **2007,** *129*, 5647-5655.

Chapter 4 Surface Silylation of Hybrid Benzidinium Lead Perovskite and Its Influence on the Photocatalytic Activity

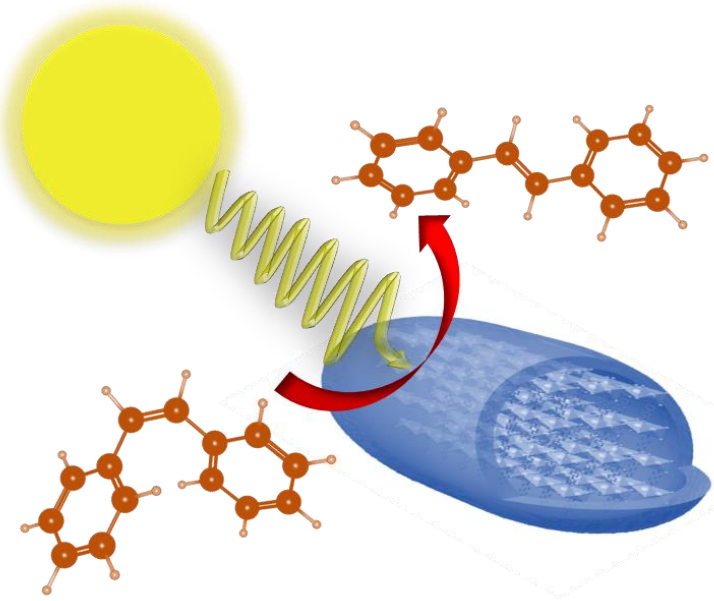

4.1 Introduction

As it has been commented in previous Chapters, hybrid organic lead perovskites have drastically modified the landscape of photovoltaic cells by reaching very high efficiencies over 20 %,[1] overcoming the values that were achieved with dye sensitized solar cells over decades.[2] One of the hypotheses of the present Doctoral Thesis is that the operation mechanism of photovoltaic cells has several common fundamental steps with photocatalytic transformations, including light absorption, charge separation and carrier migration to the surface.[3-5] Therefore it can be envisaged that if properly modified to increase their stability, hybrid organic perovskites could also have a large impact in photocatalysis.[6, 7]

In an attempt to develop and explore optoelectronic properties of hybrid lead organic perovskites in photocatalysis, we have shown in the previous Chapter the preparation of 1D benzidinium lead iodide perovskite (**BHP-3.1**), the rationale for the preparation of this hybrid perovskite was to show the possibility to modulate optoelectronic properties of the material by proper selection of the organic ammonium cation, as reported previously.[8-10] In particular, biphenyls have interesting properties since they have been widely used in photoinduced electron transfer reactions due to the stability of the corresponding radical ions that can act as electron transfer mediators.[11, 12]

It was expected, therefore, that benzidinium dications should favor charge separation in the hybrid perovskite. After the synthesis single crystal characterization of novel **BHP-3.1** showed that the material was constituted by PbI_6 octahedra sharing the faces, forming an array of parallel PbI_6 chains, that are held by Coulombic and hydrogen bridge interactions with the diammonium organic cations (Scheme 4.1). The empty space between the chains is occupied in the single crystal material by DMF molecules. Although **BHP-3.1** exhibited some range of stability in apolar organic solvents, the material was still instable in the presence of moisture and other polar solvents.

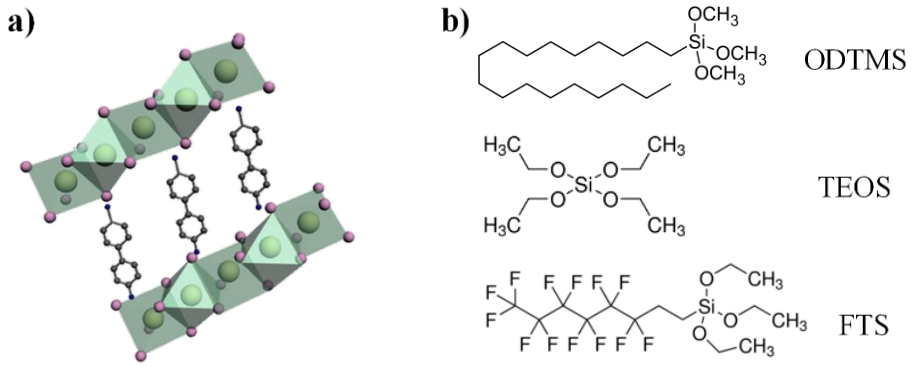

Scheme 4.1. (a) Structure of **BHP-3.1** perovskite synthesized in Chapter 3 with red and green spheres indicating I and Pb atoms, respectively, and (b) chemical structure of the three silylating reagents employed in this study (ODTMS, TEOS and FTS).

Continuing with this research line aimed at implementing hybrid perovskites in photocatalysis, in the present Chapter, the surface modification of **BHP-3.1** by coating with silylating reagents will be disclosed. There are sufficient data in the literature showing that surface silylation can protect materials by modifying the hydrophobic-hydrophilic properties of the surface.[13-15] For instance, the surface silica coating of inorganic lead halide perovskites ($CsPbX_3$; X= Cl, Br, I) has been reported not only to improve the perovskite stability, but also to enhance the quantum efficiency and to narrow the photoluminescence linewidth in light emitting devices.[16] It will be shown in the present Chapter that, while silylation of the most common $MAPBI_3$ was unsuccessful, coating of **BHP-3.1** particles can be successfully achieved by using different conventional trialkoxysilane agents. It will be presented that the photocatalytic activity of the silica-coated samples is still maintained after coating the hybrid perovskite surface with the thin silica layer. The photocatalytic activity of the silica-coated material is maintained for 3 consecutive runs.

4.2 Results and Discussion

4.2.1 Materials synthesis and characterization

Surface modification by silylating reagents is based on the presence of hydroxyl or amino groups on the surface.[17] Although ideally organic hybrid perovskites should not contain hydroxyl groups, contacting these materials with the ambient moisture results in a strong water adsorption that eventually has been proposed to replace I^- ions by hydroxyl groups with concomitant evolution of HI. In fact, the presence of adsorbed water has been proposed as the main cause for the observed deterioration of photovoltaic efficiency in perovskite solar cells upon exposure to ambient moist.[18, 19]

The leading hypothesis of the present study is that also for **BHP-3.1** some hydroxyl or amino groups could be present on the perovskite surface due to environmental humidity,[20] when the samples are exposed to the ambient. These hydroxyl groups would react with the silylating reagents forming a thin silica coating on the hybrid perovskite crystals. In addition, the possible free amino groups can also be silylated.

In order to confirm the presence of surface hydroxy groups on **BHP-3.1**, high resolution XP spectrum of O 1s peak of **BHP-3.1** sample and the best deconvolution into individual components was recorded. The results are presented in Fig. 4.1. The presence of -OH groups bonded to Pb on the **BHP-3.1** surface cannot be clearly distinguished in the Pb 4f 7/2 spectrum because of the overlap of the Pb^{2+} bonded to I^- signal at 138.1 eV. However, the Pb 4f 5/2 shows two components related to Pb-I_3^- and Pb-$(OH)_2$ at 142.88 eV and 144.03 eV, respectively.[21] Additionally, the O 1s spectrum shows the presence of four different components centered at 533.39 eV, 531.65 eV, 529.9 eV and 528.20 eV. The components at higher binding energies (533.39 and 531.65 eV) have been previously attributed to weakly bound oxygen species, such as OH^- and H_2O, as consequence of the interaction with water in outer regions.[22, 23] The components at lower binding energies have been assigned to strongly bounded lattice oxygen (-COO- and Pb-OH).[24]

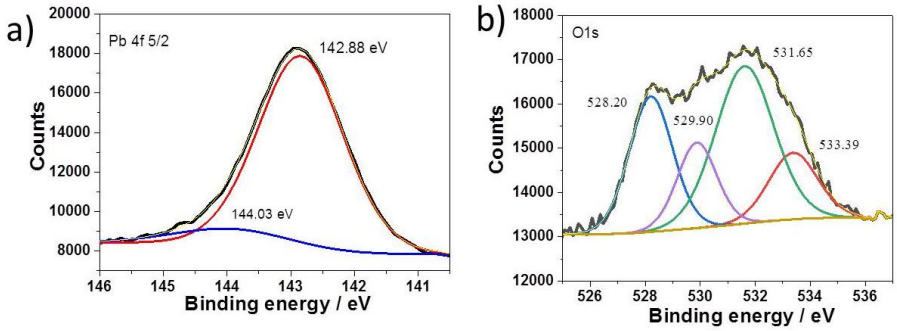

Fig. 4.1. XP spectrum of Pb 4f 5/2 and O $_{1s}$ from **BHP-3.1** sample. The best deconvolution into individual components is also shown.

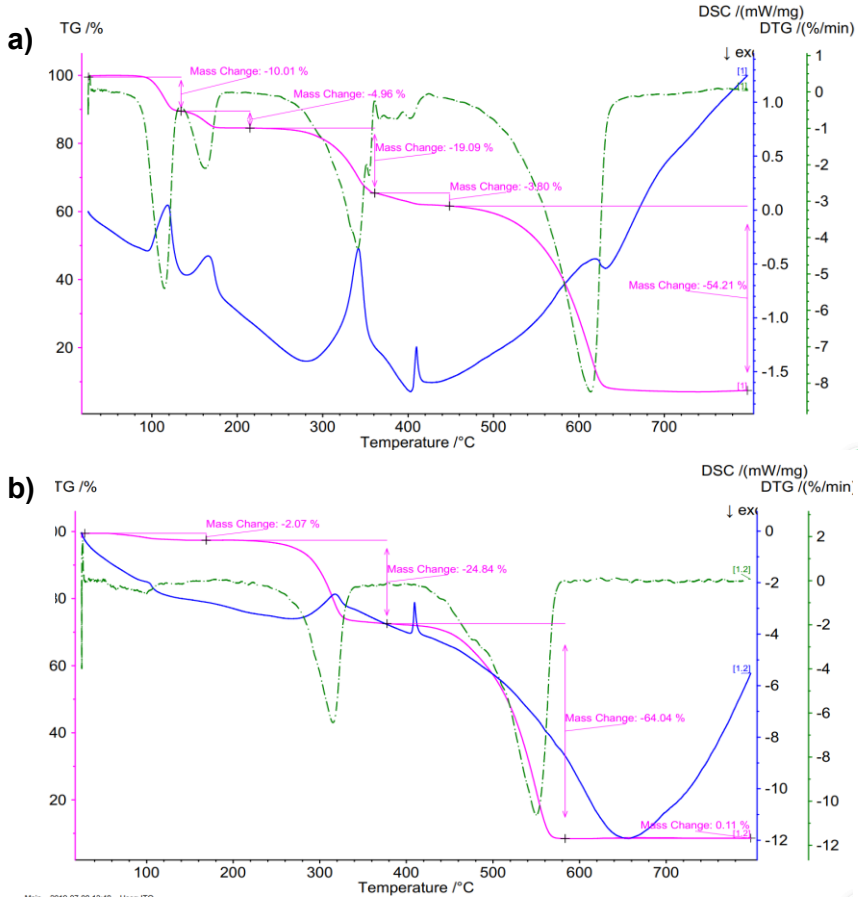

Fig. 4.2. Thermogravimetric analysis of **BHP-3.1** (a) and **SHP-4.1** (b).

Herein, perovskite silylation was carried out using trimethoxy(octadecyl)silane (ODTMS, material named as **SHP-4.1**), as well as tetraethylorthosilacate (TEOS, materials named as **SHP-4.2**) and triethoxy perfluorodecyl silane (FTS, material named as **SHP-4.3**). The structures of the silylating agents are illustrated in Scheme 4.1(b). The reaction was carried out under inert atmosphere by suspending the hybrid perovskite in a toluene solution at 50 ºC containing the desired silylating reagent. These conditions are compatible with the preservation of the structure of the hybrid perovskite as determined by powder XRD.

According to the thermogravimetric analysis presented in Fig. 4.2 and in situ XRD patterns, monitoring the crystalline structure at different temperatures (Fig. 4.3), the initial hybrid perovskite crystallinity is maintained during the coating process. On the contrary, higher temperatures or the use of other solvents can cause change of the crystal phase or even decomposition of the hybrid perovskite. It was observed, however, that the XRD pattern of pristine hybrid perovskite **BHP-3.1** changes after the silylation step.

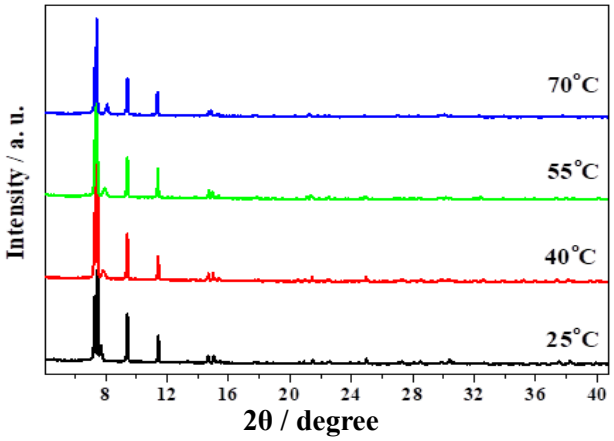

Fig. 4.3. Thermostability characterization of **BHP-3.1** monitored by in-situ XRD.

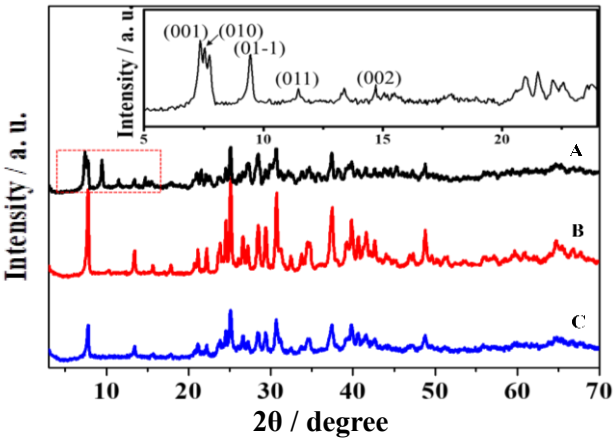

Fig. 4.4. X-ray diffraction patterns of **BHP-3.1** (A), **BHP-3.1** after dispersion in hexane for 7 h (B) and **SHP-4.1** (C). Inset: enlargement XRD pattern corresponding to the red dash frame.

Fig. 4.4 shows a comparison between the XRD patterns of the hybrid benzidinium perovskite before (**BHP-3.1**) and after silylation (material **SHP-4.1**), together with the XRD pattern of **BHP-3.1** exposed to hexane for 7 h. The change in the XRD pattern observed in Fig. 4.4 was already observed in Chapter 3, and it was attributed to the change in the 1D structure of hybrid perovskite crystals caused by the removal of DMF molecules out the intracrystalline space due to the dissolution of DMF in organic solvents, such as hexane or toluene.[25] The same hypothesis can be assumed here, since the material after silylation is still a crystalline solid and the XRD patterns exactly match with the patterns derived from sample that presumably has lost the DMF molecules. It should be commented that the quality of the crystals after silylation is not enough to perform structural elucidation by single crystal XRD.

Preservation of the optoelectronic properties of the three silica-coated hybrid perovskites was assessed by diffuse reflectance UV-vis absorption spectroscopy presented in Fig. 4.5. Only minor changes in the absorption onset of the hybrid perovskite were recorded after silylation. Specifically, the absorption onset showed a small red-shift

after silylation from 431 nm to 434 nm. Accordingly, the Tauc plots showed a minor bandgap change from 2.78 to 2.76 eV. The small shift means that after silylation, the hybrid perovskite holds the optical properties of the parent material and that the negligible changes in the absorption profile may arise from the organic-inorganic interaction at the interlayer.

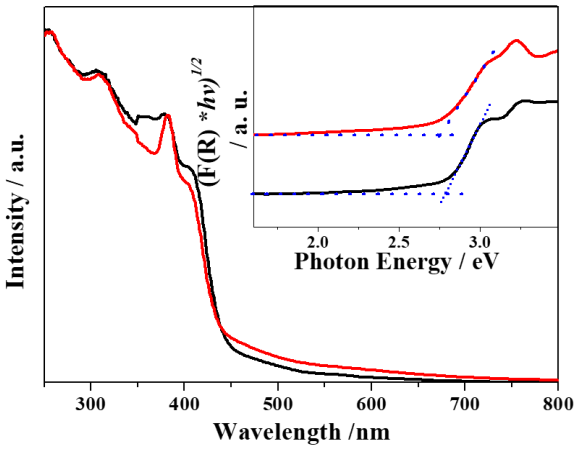

Fig. 4.5 Diffuse reflectance UV-vis spectra absorption of **BHP-3.1** (black) and **SHP-4.1** (red). Inset: Tauc plot of the corresponding **BHP-3.1** (black) and **SHP-4.1** (red) with intercept used to calculate E_g (dashed blue lines).

FTIR spectroscopy allows following the changes in the functional groups of the hybrid perovskite after silylation. Fig. 4.6 shows the FTIR spectra of the samples prepared in this study. Initially, the FTIR spectrum of **BHP-3.1** shows a very broad vibration band from 3250 till 2250 cm^{-1} due to the acid -X-H (X: N and O) bonds present in the organic cation. Upon silylation, the presence of new vibration corresponding to Si-OH silanol groups at 3500 cm^{-1} as well as C-H stretching vibrations at 2950 cm^{-1} and 2916 cm^{-1} were clearly visible, as well as the characteristic Si-O at about 1050 cm^{-1}. The position and shape of the Si-OH band indicates the occurrence of hydrogen bridges, since isolated silanol groups appear at higher frequency. It is likely that ambient moisture is responsible for the hydrolysis of alkoxy silyl groups.

The weak intensity Si-O-Si vibration band also indicates that condensation of silanol groups is not taking place in a large extent.

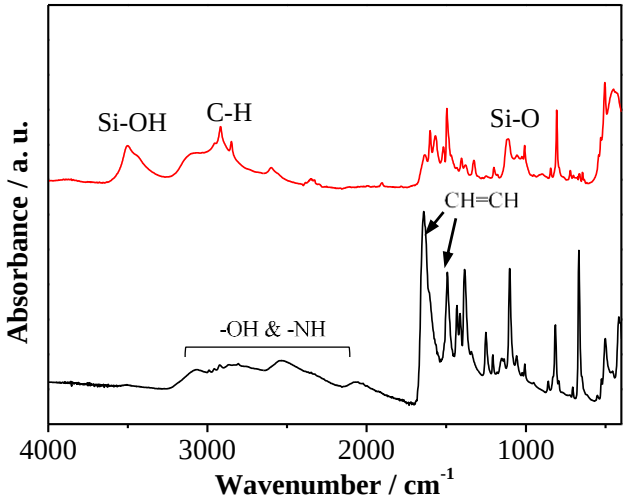

Fig. 4.6. FTIR spectra of **BHP-3.1** (black) and **SHP-4.1** (red).

High resolution XP spectra of C1s, O1s, Si2p and Pb 4f peaks and the best deconvolution into individual components of **SHP-4.1** are shown in Fig. 4.7. As it can be observed there, the XPS C1s peak (Fig. 4.7 a) shows the presence of three main components attributed to C=C (78 %) (284.6 eV, blue), C-O (19 %) (285.6 eV, orange) and C-Si (3 %) (283.1 eV, green). The O1s spectrum (Fig. 4.7 b) presents a main component attributed to O atoms single bonded to aliphatic C appearing at 532.2 eV (85.2 %), as well as two smaller components related to O double bonded to sp^2 C (9.9 %) and Si-O (4.9 %) bonds at 527.9 and 529.5 eV, respectively. The Si 2p spectrum (Fig. 4.7 c) shows a main component related to the Si-C bond from silane groups located at 102.2 eV (86.9 %), although a second component centered at 103.8 eV (13.1 %) assigned to Si-O can be also seen. The presence of –OH groups on the surface of the hybrid benzidinium perovskite cannot be clearly distinguished in the Pb4f 7/2 spectrum (Fig. 4.7 d) because of the overlap of the Pb^{2+} bonded to I^- signal at 138.1 eV.

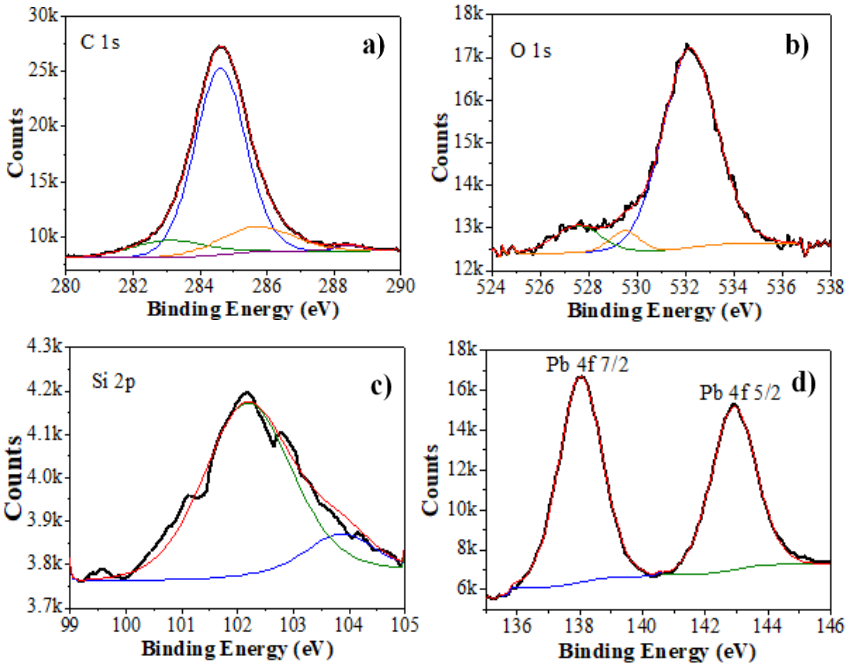

Fig. 4.7. High resolution XPS peaks for C1s (a), O1s (b), Si2p (c) and Pb4f (d) recorded for **SHP-4.1**. The best deconvolution into individual components for each peak is also shown.

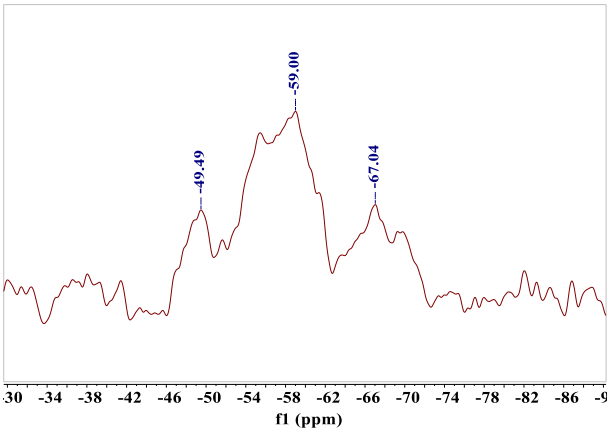

Fig. 4.8. Solid-state ^{29}Si NMR spectrum of **SHP-4.1**.

Solid-state ^{29}Si NMR spectroscopy was recorded for the **SHP-4.1** sample. The spectrum is presented as Fig. 4.8. Peaks at -49, -59 and -67 ppm were recorded and attributed to T3, T2 and T1 Si atoms in the silane groups, confirming the presence of these moieties in the hybrid perovskite in agreement with the success of surface silylation. Thus, all the available spectroscopic data are in agreement with the presence of a silica coating on the material surface.

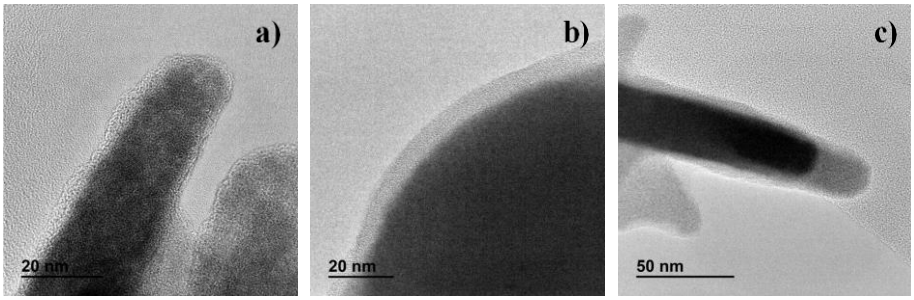

Fig. 4.9. HRTEM image of **SHP-4.1** with 1:0.5 (a and b) and 1:5 (c) ODTMS/perovskite mass ratio.

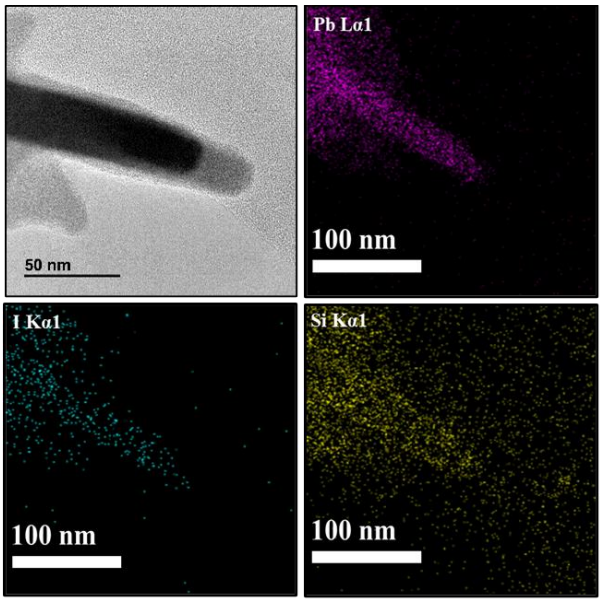

Fig. 4.10. EDS mapping of **SHP-4.1** sample.

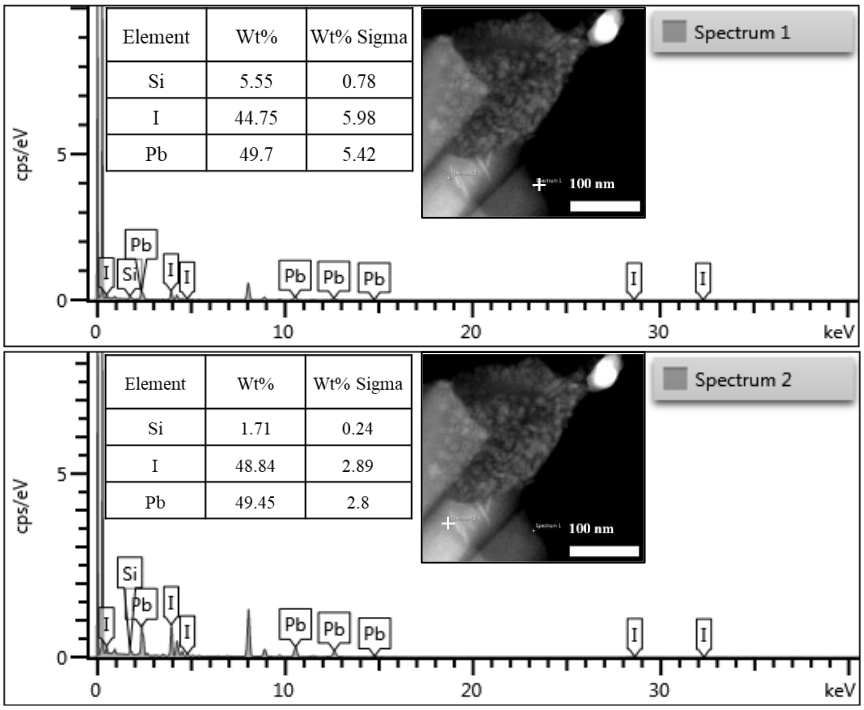

Fig. 4.11. EDX results of Si proportion at the edge (spectrum 1) and center (Spectrum 2) of **SHP-4.1**.

In fact, the presence of the silica coating on the hybrid perovskite crystals could be clearly observed in HRTEM, which also allowed us determining the thickness of the silica layer. Samples with different average thickness were prepared in the case of silica-coated **BHP-3.1** perovskite by performing the silylation step using different ODTMS to perovskite mass ratios in the silylation step. Fig. 4.9 shows representative HRTEM images of **SHP-4.1** with different thickness. Elemental mapping by EDS (see Fig. 4.10) confirmed the presence of Si completely coating the perovskite crystals surface. EDX analysis on the surface and at the center of a sample revealed that the Si proportion at the edges is much higher than the amount at the center for the silica capped perovskite (Fig. 4.11). This location of the silica layer agrees with the lighter contrast of the thin layers on the crystals observed in TEM compared to the darker contrast of the interior of the

particles due to the presence of heavy Pb element. It should be noted that HRTEM images show that the thickness of the layers is not constant throughout the particle and changes depending on the area monitored were observed. Fig. 4.12 shows the silica thickness average determined by measuring a statistical relevant number of samples as a function of the concentration of ODTMS used in the preparation of these samples.

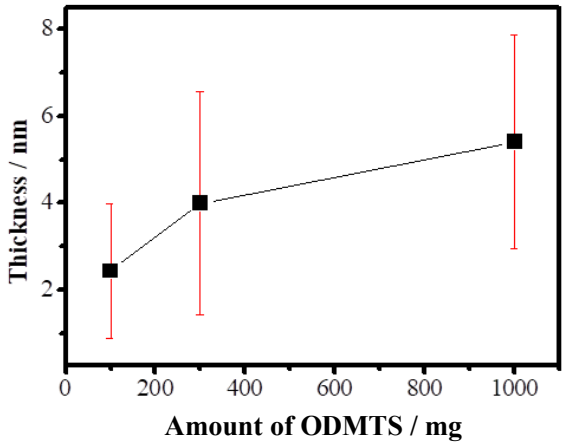

Fig. 4.12. Thicknesses statistic of the silica shell for **SHP-4.1** using different amount of ODMTS.

It should be commented that we tried to perform also surface silylation for the most common methylammonium lead perovskite with iodine or bromine ions using ODTMS as silylating agent, but the silylation failed in all cases as revealed by HRTEM (Fig. 4.13). This failure to silylate the surface of PbX_3MA solids could be attributed to lack of a sufficient density of hydroxyl groups on the surface of these hybrid methylammonium perovskites. On the contrary, **BHP-3.1** perovskite was successfully coated not only with ODTMS, but also with TEOS and FTS (Fig. 4.14), pointing out to a general methodology for coating hybrid perovskites, particularly the one containing benzidinium organic ligands considered here. The contrasting behavior between PbX_3MA and **BHP-3.1** could also be due to the different structure (3D vs. 1D), surface area and/or the presence of amino groups.

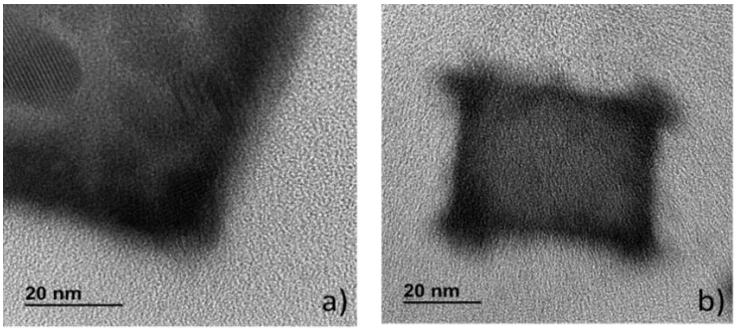

Fig. 4.13. HRTEM images of ODTMS coated (a) $MAPbI_3$ and (b) $MAPbBr_3$.

It is worth commenting that the obtained silica-coated **SHP-4.n** hybrid perovskites exhibit enhanced hydrophobic character as can be observed in Fig. 4.14. The photographs of the materials **SHP-4.1**, **SHP-4.2**, **SHP-4.3** and $PbI_3Bz_{0.5}$ placed on pure water show that while **SHP-4.1** and **SHP-4.3** materials were floating in water for long periods (days), **SHP-4.2** exhibited only partial stability in water, presenting some material precipitation. The parent **BHP-3.1** precipitated immediately in contact with the water. Additionally, the Z-potential values of the parent benzidine lead iodide perovskite, **SHP-4.1**, **SHP-4.2** and **SHP-4.3** were measured, obtaining values of -11.3, 44.1, 40.2 and 47.8 mV, respectively. These values indicate that while the parent perovskite exhibits a slightly negative surface, after coating the surface Coulombic charge is reversed and becomes positive, independently of the silica precursor employed.

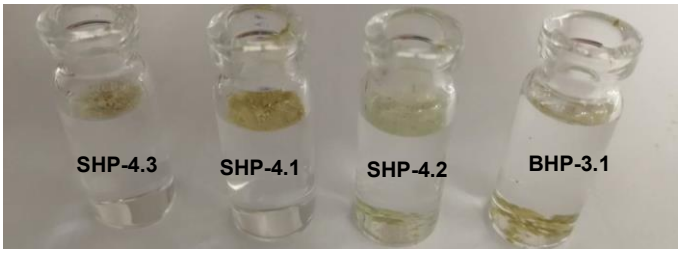

Fig. 4.14. Digital photograph of **SHP-4.1**, **SHP-4.2**, **SHP-4.3** and **BHP-3.1** placed in pure water.

4.2.2 Photocatalytic activity.

Regarding the photocatalytic activity of **BHP-3.1**, it was shown in the previous Chapter that this hybrid perovskite can promote the photocatalytic cis-to-trans isomerization of stilbene (Scheme 4.2).[25] It was, therefore, of interest to determine if after capping with the silica layer the hybrid **SHP-4.n** perovskites are still active to promote this photocatalytic reaction.

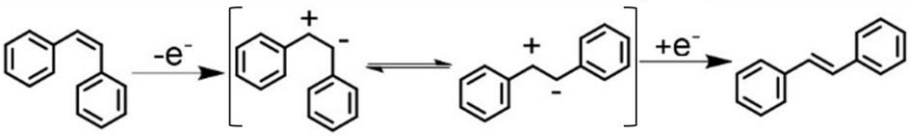

Scheme 4.2. Proposed mechanism for the photocatalytic cis-to-trans stilbene isomerization through the intermediacy of the corresponding equilibrated radical cations.

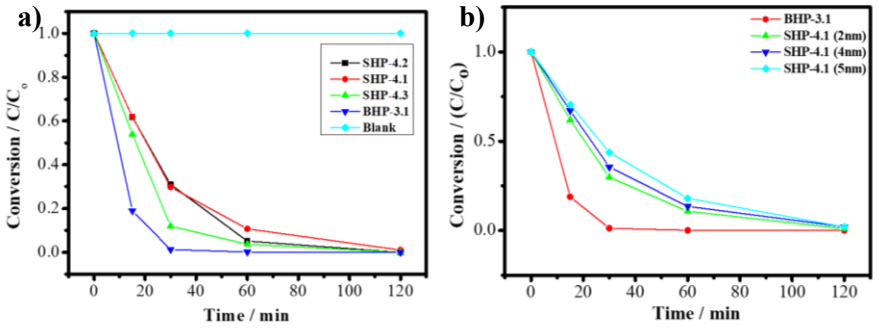

Fig. 4.15. a) Photocatalytic cis-to-trans isomerization of stilbene using as photocatalysts the parent **BHP-3.1** (blue triangles) or **SHP-4.1** (red dots), **SHP-4.2** (black squares), **SHP-4.3** (green triangles) and in the absence of photocatalysts (cyan dots). b) Influence of the thickness on the photocatalytic cis-to-trans stilbene isomerization using parent **BHP-3.1** (red dots) or 2 nm (green triangles), 4 nm (blue triangles) and 5 nm (cyan triangles) thick **SHP-4.1** samples Reaction conditions: 0.25 mmol of cis-stilbene dissolved in 1.5 mL of toluene using 2 wt% (4.1 mg) photocatalyst. Prior to irradiation, the reactor was purged with argon. The visible light irradiation (λ > 450 nm) was carried out using a 300 W Xe lamp output adapted with 450 nm filter.

Fig. 4.15 (a) shows the temporal evolution of the photocatalytic cis-to-trans isomerization as function of the different silylating agents (TEOS, ODTMS and FTS). As it can be seen there, cis-to-trans isomerization occurs in the presence of the silica-capped perovskites, independently of the silylating reagent used to form the coating. It was, however, observed that the photocatalytic activity of silylated materials decreased respect to the uncoated material. An example of GC plot recorded during the photocatalytic cis-to-trans stilbene isomerization using **SHP-4.1** is presented in Fig. 4.16 to illustrate the difference in retention time for the two stereoisomers.

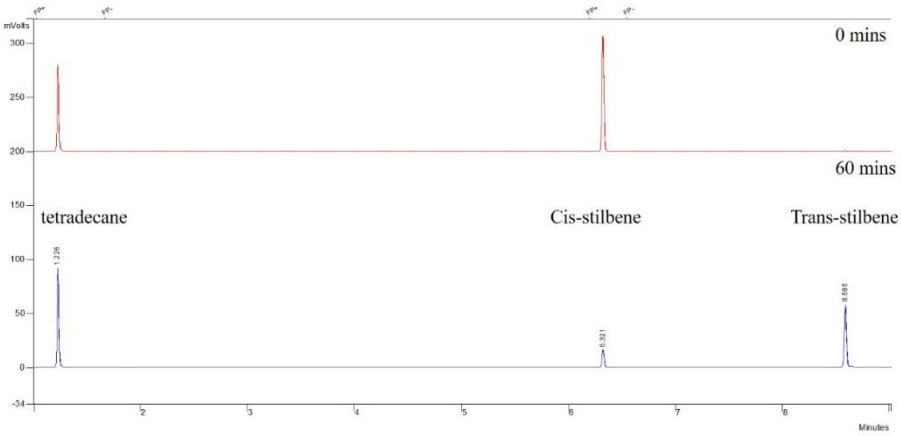

Fig. 4.16. GC plot of the photocatalytic cis-to-trans isomerization using **SHP-4.1** The top graph (red) corresponds to the cis-stilbene at reaction time 0, while bottom spectrum (blue) corresponds to the products in the reaction media after 1 h reaction. Tetradecane was using as internal pattern.

A control experiment in the absence of any photocatalyst was carried out, and the result is presented in Fig. 4.15 a. As can be observed, the photocatalytic reaction did not take place in the absence of photocatalysts or in their presence in the dark.

These results can be easily interpreted assuming that the surface of parent perovskite is free to interact with cis-stilbene, which undergoes photoinduced electron transfer isomerization. The presence of the

porous silica layer introduces some diffusing limitations to the access of cis-stilbene to the active sites of the material and, for this reason, the photocatalytic reaction becomes slower. It is worth noticing that the photocatalytic activity of the different coated perovskites did not present drastic differences among them under the present reaction conditions. This could indicate either that the porosity of the silica layers is similar or that the photocatalytic isomerization occurs on the external surface and electrons and holes are tunneling through this interface.

In order to further investigate the influence of the silica coating thickness in the photocatalytic reaction the temporal evolution of the photocatalytic, cis-to-trans isomerization of stilbene was studied for **SHP-4.n** exhibiting different average thickness. The results are presented in Fig. 4.15 b. It seems however that the thickness of the layer in the range from 2 to 5 nm screened in the present study do not make additional influence on the activity.

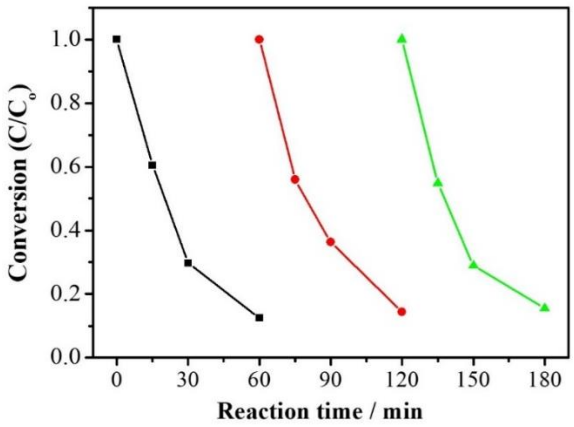

Fig. 4.17. Photocatalytic cis-to-trans isomerization of stilbene using as photocatalysts **SHP-4.1** for three successive runs. Reaction conditions: 0.25 mmol of cis-stilbene dissolved in 1.5 mL of toluene using 2 wt% (4 mg) photocatalyst. Prior irradiation, the reactor was Ar purged. The visible light irradiation (λ > 450 nm) corresponded to the output of a 300 W Xe lamp adapted with 450 nm filter.

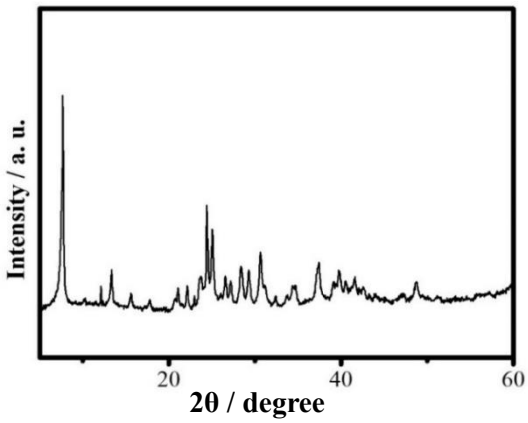

Fig. 4.18. XRD of **SHP-4.1** after 3 consecutive reuses as photocatalyst in the cis-to-trans stilbene isomerization reaction.

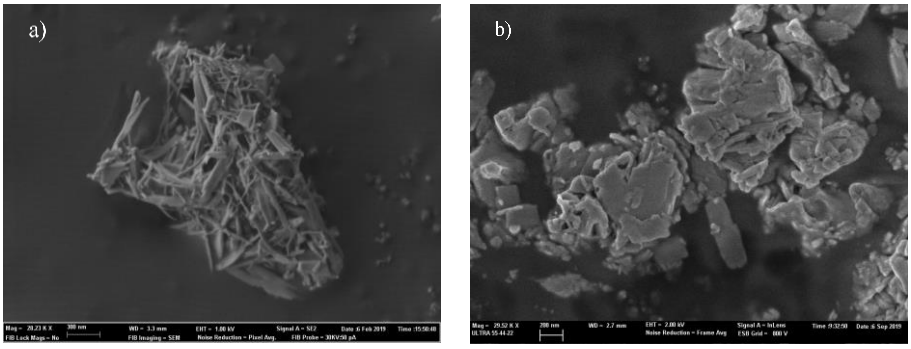

Fig. 4.19. SEM images of **BHP-3.1** (a) and **SHP-4.1** after three successive cycles of photocatalytic cis-to-trans isomerization reaction.

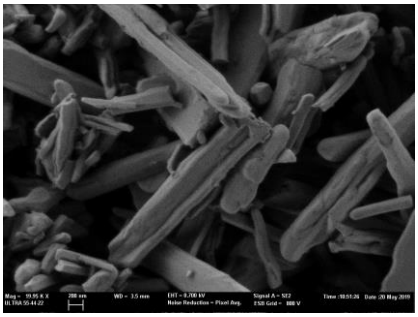

Fig. 20. SEM image of as-obtained **SHP-4.1**.

Finally, **SHP-4.1** was reused three times as photocatalyst for the cis-to-trans isomerization of stilbene in order to check its stability. The results of the successive reuses as well as the structure and morphological characterization of the used **SHP-4.1** sample after reaction are presented as Figs. 4.17, 4.18 and 4.19. As can be seen in Fig. 4.18, the photocatalytic activity of **SHP-4.1** did not decrease significantly during three consecutive runs, exhibiting a notable stability under the reaction conditions. The XRD of the reused **SHP-4.1** photocatalysts (Fig. 4.18) shows the same peaks than the fresh sample, indicating that the crystalline structure has been preserved during the three uses. The morphology of perovskite particles decreased somewhat in size after reuse (Figs. 4.19 and 4.20). However, compared with the parent perovskite, the silica coated sample exhibited excellent stability against de-aggregation during the photocatalytic reaction (Fig. 4.19). Therefore, the silica coating has a positive effect protecting the perovskite from degradation under these reaction conditions.

4.3 Conclusions

The present Chapter has shown the possibility to coat the external surface of PbI_3(**BZN-3.1**)$_{0.5}$ perovskite by silylation with different silylating reagents obtaining layers below 6 nm. The silylation process depends on the density of hydroxyl groups on the surface of the hybrid perovskite, the structure, surface area and/or presence of amino groups. Although the reaction rate was somewhat lower using the silica coating, the photocatalytic activity of the silica-coated perovskites was still remarkable. Considering that silylation is a well-known approach to modify the surface properties of materials, the present study opens the door for the control of the photocatalytic properties of perovskites, particularly those regarding their stability in different solvents.

4.4 Reference

1. Jiang, Q.; Zhao, Y.; Zhang, X.; Yang, X.; Chen, Y.; Chu, Z.; Ye, Q.; Li, X.; Yin, Z.; You, J., Surface passivation of perovskite film

for efficient solar cells. *Nat. Photonics* **2019**.

2. Kakiage, K.; Aoyama, Y.; Yano, T.; Oya, K.; Fujisawa, J.-i.; Hanaya, M., Highly-efficient dye-sensitized solar cells with collaborative sensitization by silyl-anchor and carboxy-anchor dyes. *Chem. Commun.* **2015,** *51*, 15894-15897.

3. Saravanan, R.; Gracia, F.; Stephen, A., Basic Principles, Mechanism, and Challenges of Photocatalysis. In *Nanocomposites for Visible Light-induced Photocatalysis*, Khan, M. M.; Pradhan, D.; Sohn, Y., Eds. Springer International Publishing: Cham, 2017; pp 19-40.

4. Bisquert, J.; Cahen, D.; Hodes, G.; Rühle, S.; Zaban, A., Physical Chemical Principles of Photovoltaic Conversion with Nanoparticulate, Mesoporous Dye-Sensitized Solar Cells. *J. Phys. Chem. B* **2004,** *108*, 8106-8118.

5. Kamat, P. V., Semiconductor Surface Chemistry as Holy Grail in Photocatalysis and Photovoltaics. *Acc. Chem. Res.* **2017,** *50*, 527-531.

6. Boyd, C. C.; Cheacharoen, R.; Leijtens, T.; McGehee, M. D., Understanding Degradation Mechanisms and Improving Stability of Perovskite Photovoltaics. *Chem. Rev.* **2019,** *119*, 3418-3451.

7. Aristidou, N.; Eames, C.; Sanchez-Molina, I.; Bu, X.; Kosco, J.; Islam, M. S.; Haque, S. A., Fast oxygen diffusion and iodide defects mediate oxygen-induced degradation of perovskite solar cells. *Nat. Commun.* **2017,** *8*, 15218.

8. Cortecchia, D.; Neutzner, S.; Srimath Kandada, A. R.; Mosconi, E.; Meggiolaro, D.; De Angelis, F.; Soci, C.; Petrozza, A., Broadband Emission in Two-Dimensional Hybrid Perovskites: The Role of Structural Deformation. *J. Am. Chem. Soc.* **2017,** *139*, 39-42.

9. Kawano, N.; Koshimizu, M.; Sun, Y.; Yahaba, N.; Fujimoto, Y.; Yanagida, T.; Asai, K., Effects of Organic Moieties on

Luminescence Properties of Organic–Inorganic Layered Perovskite-Type Compounds. *J. Phys. Chem. C* **2014,** *118*, 9101-9106.

10. Albero, J.; García, H., Luminescence control in hybrid perovskites and their applications. *J. Mater. Chem. C* **2017,** *5*, 4098-4110.

11. Ronlan, A.; Coleman, J.; Hammerich, O.; Parker, V. D., Anodic oxidation of methoxybiphenyls. Effect of the biphenyl linkage on aromatic cation Radical and Dication Stability. *J. Am. Chem. Soc.* **1974,** *96*, 845-849.

12. Talipov, M. R.; Boddeda, A.; Timerghazin, Q. K.; Rathore, R., Key Role of End-Capping Groups in Optoelectronic Properties of Poly-p-phenylene Cation Radicals. *J. Phys. Chem. C* **2014,** *118*, 21400-21408.

13. Zapata, P. A.; Huang, Y.; Gonzalez-Borja, M. A.; Resasco, D. E., Silylated hydrophobic zeolites with enhanced tolerance to hot liquid water. *J. Catal.* **2013,** *308*, 82-97.

14. Bu, J.; Rhee, H.-K., Improvement in hydrophobicity of Ti-MCM-41 using a new silylation agent MSTFA. *Catal. Lett.* **2000,** *65*, 141-145.

15. Kuwahara, Y.; Maki, K.; Matsumura, Y.; Kamegawa, T.; Mori, K.; Yamashita, H., Hydrophobic Modification of a Mesoporous Silica Surface Using a Fluorine-Containing Silylation Agent and Its Application as an Advantageous Host Material for the TiO_2 Photocatalyst. *J. Phys. Chem. C* **2009,** *113*, 1552-1559.

16. Zhang, F.; Shi, Z.-F.; Ma, Z.-Z.; Li, Y.; Li, S.; Wu, D.; Xu, T.-T.; Li, X.-J.; Shan, C.-X.; Du, G.-T., Silica coating enhances the stability of inorganic perovskite nanocrystals for efficient and stable down-conversion in white light-emitting devices. *Nanoscale* **2018,** *10*, 20131-20139.

17. Yoshida, W.; Castro, R. P.; Jou, J.-D.; Cohen, Y., Multilayer

Alkoxysilane Silylation of Oxide Surfaces. *Langmuir* **2001,** *17*, 5882-5888.

18. Berhe, T. A.; Su, W.-N.; Chen, C.-H.; Pan, C.-J.; Cheng, J.-H.; Chen, H.-M.; Tsai, M.-C.; Chen, L.-Y.; Dubale, A. A.; Hwang, B.-J., Organometal halide perovskite solar cells: degradation and stability. *Energy Environ. Sci.* **2016,** *9*, 323-356.

19. Niu, G.; Guo, X.; Wang, L., Review of recent progress in chemical stability of perovskite solar cells. *J. Mater. Chem. A* **2015,** *3*, 8970-8980.

20. Cheng, B.; Li, T.-Y.; Wei, P.-C.; Yin, J.; Ho, K.-T.; Retamal, J. R. D.; Mohammed, O. F.; He, J.-H., Layer-edge device of two-dimensional hybrid perovskites. *Nat. Commun.* **2018,** *9*, 5196.

21. Rocks, C.; Svrcek, V.; Maguire, P.; Mariotti, D., Understanding surface chemistry during MAPbI3 spray deposition and its effect on photovoltaic performance. *J. Mater. Chem. C* **2017,** *5*, 902-916.

22. Velichenko, A. B.; Amadelli, R.; Baranova, E. A.; Girenko, D. V.; Danilov, F. I., Electrodeposition of Co-doped lead dioxide and its physicochemical properties. *J. Electroanal. Chem.* **2002,** *527*, 56-64.

23. Shmychkova, O.; Luk'yanenko, T.; Amadelli, R.; Velichenko, A., Physico-chemical properties of PbO2-anodes doped with Sn4+and complex ions. *J. Electroanal. Chem.* **2014,** *717-718*, 196-201.

24. Pradhan, S.; Stavrinadis, A.; Gupta, S.; Bi, Y.; Di Stasio, F.; Konstantatos, G., Trap-State Suppression and Improved Charge Transport in PbS Quantum Dot Solar Cells with Synergistic Mixed-Ligand Treatments. *Small* **2017,** *13*, 1700598.

25. Peng, Y.; Albero, J.; Álvarez, E.; García, H., Hybrid benzidinium lead iodide perovskites with a 1D structure as photoinduced electron transfer photocatalysts. *Sustain. Energy Fuels* **2019**.

Chapter 5 Synthesis, Post-synthetic Modification and Stability of 2D Styrylammonium Lead Iodide Hybrid Material

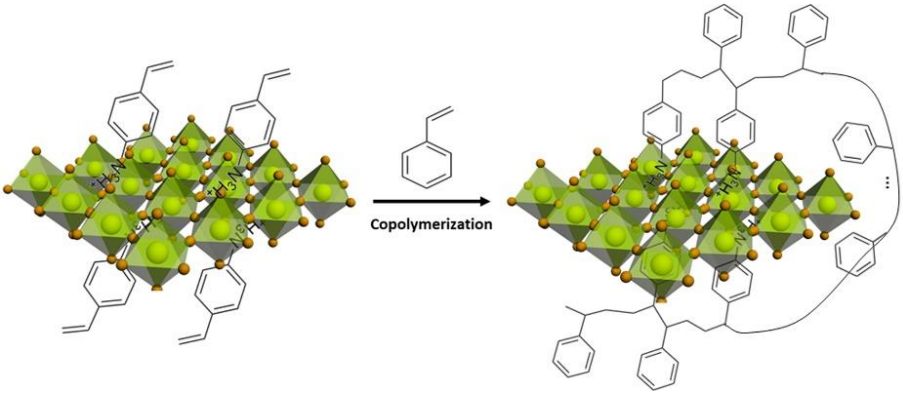

5.1 Introduction

As it is being commented since Chapter 1, the excellent optoelectronic properties of lead halide hybrid perovskites, particularly methylammonium perovskites have revolutionized in a very short time the field of photovoltaics.[1-5] Hybrid lead perovskites and related materials can absorb a considerable percentage of the solar radiation and due to their low exciton binding energy and high charge carrier mobility, exhibit high charge separation efficiency.[6-9] In comparison, with the slow pace in the increase of photovoltaic efficiency that has characterized the field of dye sensitized solar cells, hybrid perovskites solar cells have reached an impressive certified 20 % efficiency in just a few years after the initial discovery of their photovoltaic properties.[10-12]

One of the leading hypotheses of the present Doctoral Thesis is that the mechanism of operation of photovoltaic cells has common elementary steps with photocatalysis. These common steps include light harvesting, charge separation and charge migration to the particle surface. The main difference is the occurrence of surface redox reactions, transforming substrates on the particles, in the case of photocatalysis, compared to interparticle charge migration in photovoltaic devices.[13, 14] Therefore, it is somewhat surprising that in contrast to the importance of hybrid lead perovskites in photovoltaics, these hybrid materials have been almost ignored as photocatalysts.

The main reason for this scarce use of hybrid perovskites in photocatalysis is the notorious lack of stability of these materials under ambient conditions, particularly, when exposed to humidity.[15-17] It has been widely reported that exposure of these materials to the ambient moisture results in water adsorption that eventually has been proposed to cause the replacement of I^- ions by hydroxyl groups.[18, 19] Therefore, new approaches to minimize water adsorption in hybrid lead halide materials are much wanted

to improve their stability under ambient conditions, not only in the photovoltaic field, but also for their use as photocatalysts.

In the previous Chapters we have shown the possibility of synthesizing new hybrid perovskites by using organic cations different from methylammonium or formamidium, and further increased the water stability by surface silylation. However, means of surface modification in the previous Chapter rely on the surface hydroxyl group, which derived from the surface adsorbed water that degrades the perovskite structure to some extent. Thus, new strategies that avoid the dependance of ambient moisture for surface modification could be more appealing. Since hybrid perovskites allow the use of different organic cations,[14, 20-23], it leaves open the possibility of choosing proper functional organic cation allowing subsequently surface post-treatment.

In this context, it is the objective of the present Chapter to take advantage of organic reactions to modify the surface of hybrid perovskites at will. By surface modification, the properties of the resulting materials could change in such a way that they could present striking properties from the photocatalytic point of view.

Towards this objective of surface modification and in contrast to the three-dimensional (3D) structure of PbI_3MA, it has been found that accommodation of larger organic ammonia ions results in a change from 3D structure to materials with lower dimensionality, as it was the case of dication **BHP-3.1** in Chapter 3. More specifically, the hybrid lead perovskites containing benzyl ammonium cation exhibit a 2D structure that allows accommodation of the benzyl side chains within the interlayer space.[24-26] These 2D structures have shown larger hydrophobicity and, therefore, improved photo, thermal and moisture stability.[27]

Continuing in this line, the present Chapter reports the synthesis of a new 2D hybrid material having styryl ammonium as organic cation, lead as inorganic cation and iodide anions. The interest of this organic unit is that the presence of the styryl units

should allow subsequent further modification by radical polymerization under conditions compatible with the stability of the hybrid material. The data that will be presented in this Chapter shows the feasibility of a post-synthetic modification of hybrid perovskites.

5.2 Results and Discussion

5.2.1 Perovskite synthesis

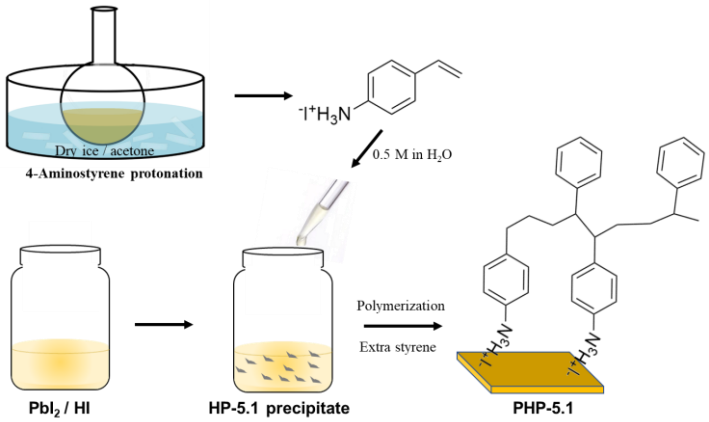

Scheme 5.1. Illustration of the synthesis of **HP-5.1** and **PHP-5.1.**

The synthesis of 4-styryl ammonium lead iodide material is illustrated in Scheme 5.1. The process starts with the protonation of commercially available 4-aminostyrene by hydroiodic acid (HI). This protonation has to be carried out carefully at low temperature (dry ice/acetone ice bath, ~ -70 °C) to avoid the occurrence of double bond polymerization and/or electrophilic additions to the C-C.[28] Protonation of the amino group results in ^{1}H NMR spectroscopy in a remarkable downfield shift of the aromatic protons at the ortho position of the amino group of about 1 ppm as well as other changes in the chemical shifts of other protons. Fig. 5.1 shows a comparison of the ^{1}H NMR spectra for 4-aminostyrene and styryl ammonium (**SA-5.1**). Importantly,

spectroscopic data confirm that under optimized protonation conditions, the vinylic $CH=CH_2$ group remains unaltered.

IR spectroscopy also shows significant changes upon protonation, the most remarkable one being the change in the position and intensity of the NH stretching vibration bands that become more intense and shifted towards smaller wavenumber upon protonation (Fig. 5.2). The hybrid styrylammonium lead iodide was finally obtained by mixing a solution of PbI_2 in aqueous HI and **SA-5.1** salt. Upon mixing, instantaneous precipitation of the hybrid material **HP-5.1** is observed, and then was separated by filtration and washed with diethyl ether.

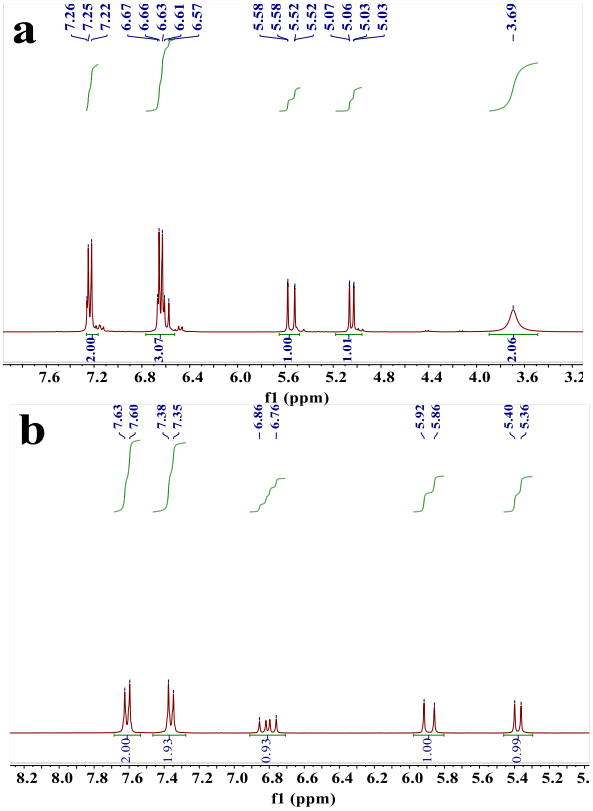

Fig. 5.1. 1H NMR spectra of 4-aminostyrene (a) and **SA-5.1** (b) solute in $CDCl_3$ and D_2O, respectively. Amino styrene 1H NMR: (300MHz, $CDCl_3$),

δ=7.25-7.22 (d, 2H; J^3=8.38, Ar), 6.66-6.63(d, 2H; J^3=8.37, Ar), 6.67-6.57 (m, H; J^3=10.894 & J^3=17.313, CH=CR), δ=5.58-5.52 (d, H; J^3=17.590, CR=CH_2), δ=5.07-5.03 (d, H; J^3=10.873, CR=CH2). **SA-5.1** ^{1}H NMR: (300MHz, D_2O) δ=7.50-7.53 (d, 2H; J^3=8.52, Ar), 7.35-7.38(d, 2H; J^3=8.56, Ar), 6.75-6.86 (m, H; J^3= 17.71 & J^3=10.96, CH=CR), δ=5.86-5.92 (d, H; J^3= 17.71, CR=CH_2), δ=5.36-5.40 (d, H; J^3=10.97, CR=CH_2).

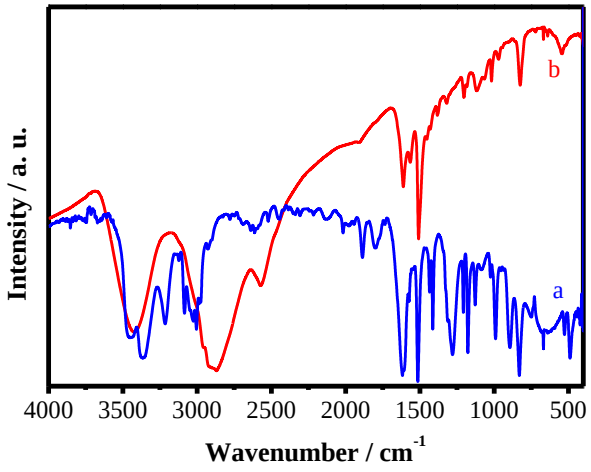

Fig. 5.2 Infrared spectra of 4-aminosyrene (a) and **SA-5.1** (b).

5.2.2 Material characterization

Powder XRD of **SA-5.1** is presented in Fig. 5.3, where comparison with the XRD patterns of the two components, i.e., PbI_2 and **SA-5.1** is presented. As can be seen there, solid **HP-5.1** is a crystalline material with a structure different than PbI_2 or **SA-5.1**. XRD analysis of **HP-5.1** confirms that the precipitated crystals correspond to a new material, whose diffraction pattern cannot be attributed to a combination of the XRD patterns of the PbI_2 and **SA-5.1** precursors. Unfortunately, all the attempts to determine the crystal structure of **HP-5.1** by single-crystal XRD analysis were unsuccessful. However, the formation of a hybrid structure, exhibiting high crystallinity, can be elucidated from the XRD pattern of **HP-5.1**. Similar diffraction pattern has been reported for a mixed 2D hybrid perovskite based on methyl and

polyethyleneimide ammonium cations.[29] In this precedent, a strong peak at 8º, indicative of a 2D hybrid structure, was recorded, very similar to the one observed in the present case.

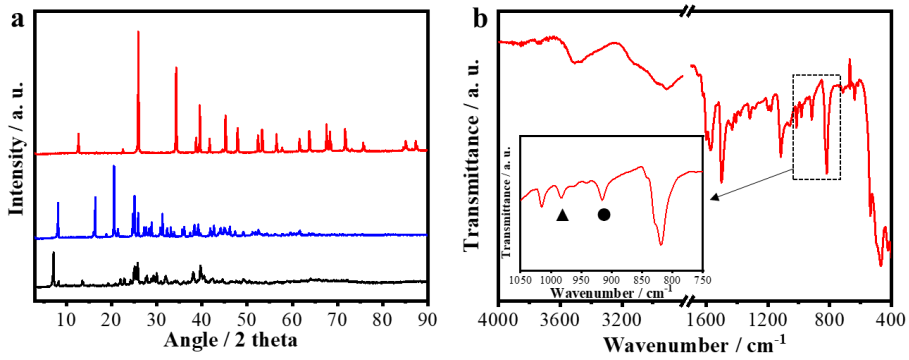

Fig. 5.3 (a) XRD patterns of **HP-5.1** (black line), **SA-5.1** (blue line) and PbI_2 (red line). (b) FT-IR spectrum of **HP-5.1**. Inset: enlarged view of the black frame. ▲Out of plane bending of the –CH=, ● out of plane vibration (wagging) of the CH_2.

FTIR of material **HP-5.1** (Fig. 5.3b) shows stretching vibration bands appearing at 3500 cm^{-1} and from 3200 to 2500 cm^{-1} corresponding to OH and NH vibrations, respectively. The IR spectrum shows also in the aromatic region, the expected peaks from 1620 to 1450 cm^{-1}. More importantly, the vibration bands showed at around 900 and 980 cm^{-1} indicate that the vinylic $HC=CH_2$ moiety of the styrylammonium cation has been preserved in the material **HP-5.1**, which allowed a further surface modification as will be elucidated later.

The morphology and composition of the **HP-5.1** particles of was observed by SEM and HRTEM accompanied with EDS analysis, which are presented in Fig. 5.4. It was observed that the material is constituted by large aggregates of about 6 μm or larger size constituted by the assembly of thin platelets. This morphology has been reported previously for 2D hybrid

materials,[30] and suggests that also in the present case, **HP-5.1** could have such 2D dimensionality in its structure.

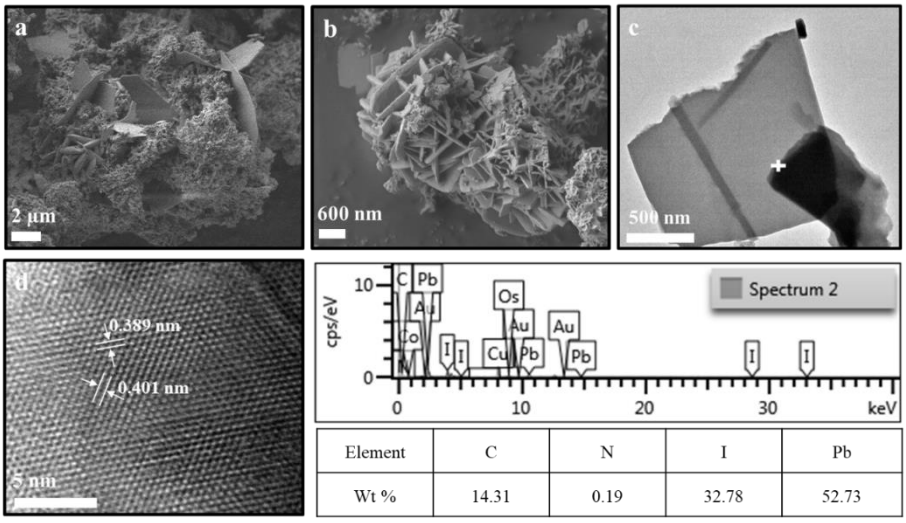

Element	C	N	I	Pb
Wt %	14.31	0.19	32.78	52.73

Fig. 5.4. Representative images of the morphology and structure of the particles corresponding to **HP-5.1** monitored by SEM (a,b) and HRTEM (c,d). Panels at the bottom show the EDS analysis of sample **HP-5.1**. Panel d shows the lattice fringes of two planes in a crystal of **HP-5.1**.

HRTEM shows that **HP-5.1** is constituted by aggregation of thin platelets with dimensions larger than 500 nm up to several micrometers. High resolution images show the presence of crystalline planes of 0.389 nm and 0.401 nm that coincide with the position of two peaks in XRD pattern ($2\theta=22.823^{o}$ and 21.975^{o}, respectively). Overall, the HRTEM images confirm the high crystallinity in accordance with powder XRD and the 2D structure of **HP-5.1**. EDS analysis of selected area corresponding to the surface of the particle shows the presence of Pb, I and C, in a relative proportion of 53, 33 and 14%, respectively, indicating that the material is constituted by these elements.

Table 5.1 Chemical composition and empirical formula of **HP-5.1** determined by combining X-ray fluorescence (XRD, Pb and I) and combustion elemental analysis (EA, N, C and H).

Item	XRF (wt%)		EA (wt%)			Rest (wt%)
	Pb	I	N	C	H	Rest
Proportion	34.758	1.16	8.47	1.04	54.189	0.383
Normalization	1	0.493	4.2	6.19	2.5	-
Formula	$PbI_{2.5}$(Amino-styrene)$_{0.5}$					

The elemental composition of **HP-5.1** was determined by combining X-ray fluorescence analysis for Pb and I, with combustion elemental analysis for C and H. The results are presented in Table 5.1. These analyses have allowed estimation of the composition $PbI_{2.5}$(Aminostyrene)$_{0.5}$ for **HP-5.1**. This composition does not agree with the expected formula for 3D, 2D or 1D hybrid lead perovskites that should be PbI_3X,[31, 32] PbI_4X_2,[33, 34] and PbI_3X (facet-sharing),[35, 36] respectively (in which X represents the organic ammonium cation). It could be that the defects on the structure are responsible for the deviation of the empirical formula from the ideal composition expected for these 2D materials. In this regard, it has to be commented that EDS analysis by electron microscopy shows that the surface of **HP-5.1** is enriched of Pb and has a low average content of I. The presence of O on the surface of **HP-5.1** is also detectable by EDS.

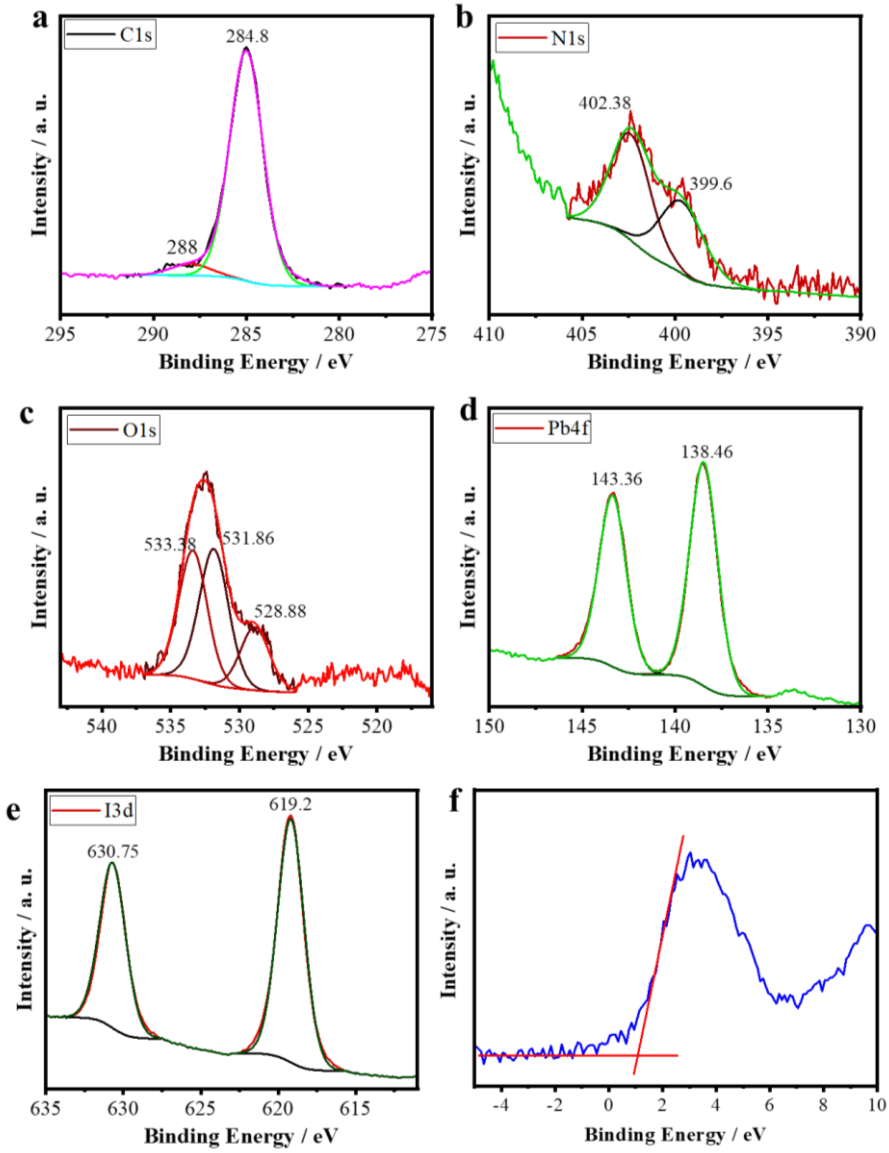

Fig. 5.5 High resolution XPS peaks for C1s (a), N1s (b), O1s (c), Pb4f (d) and I3d obtained from **HP-5.1** (e). Valence band edge of **HP-5.1** determined by low energy XPS analyses (f).

Analytic data of **HP-5.1** by XRF and combustion elemental analysis or EDS was complemented by XPS. Survey XPS analysis detected the expected elements according to the empirical formula plus the presence of oxygen. High resolution peaks for C1s, N1s, O1s, Pb4f and I3d are shown in Fig. 5.5. C1s, Pb4f and I3d are mainly composed by a single component, corresponding to sp^2 carbons, Pb^{2+} and I^-, respectively.[37] In contrast, N1s peak shows two components at 399.5 and 402.5 in a proportion of 44 and 56 %, attributable to $-NH_2$ and $-NH_3^+$.[38] This distribution of N atoms could indicate that styryl ammonium ligand is deprotonated in a significant proportion. This is compatible with the fact that XPS analysis also detects the presence of oxygen atoms in the outermost part of the particles. The deconvolution of the high resolution O1s peak indicates that there are three main components at 529.0 (25 %), 532.0 (39 %), and 533.5 eV (36 %), that can be attributed to Pb-O, Pb-OH and adsorbed H_2O, respectively.[39] According to this analysis, part of the positive charges on the external surface of the solid **HP-5.1**, resulting from the exposed Pb^{2+}, should be compensated by hydroxyl and oxide groups.

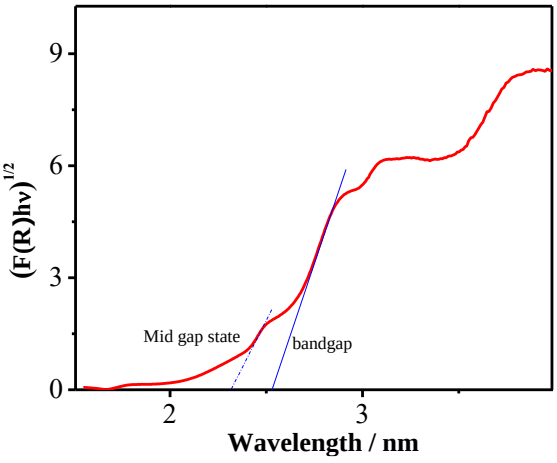

Fig. 5.6. Tauc plot of **HP-5.1** sample calculated from the diffuse reflection spectrum (see in Fig. 5.7).

XPS also allows determining the energy of the valence band edge by extrapolating the first electron emission peak at lower energy (see the description of the calculation in section 8.4 of Chapter 8). According to this measurement, the valence band energy of **HP-5.1** was determined at -5.34 eV referred to vacuum. Assuming that the obtained material presents a direct bandgap, the optical bandgap of **HP-5.1** was estimated by the Tauc plot (Fig. 5.6), and was determined of 2.53 eV.

It is worth noticing that a small band can be distinguished in the Tauc plot at lower energy. We have attributed this band to mid-gap states created as consequence of structural defects. The energy gap of this transition was determined to 2.32 eV.

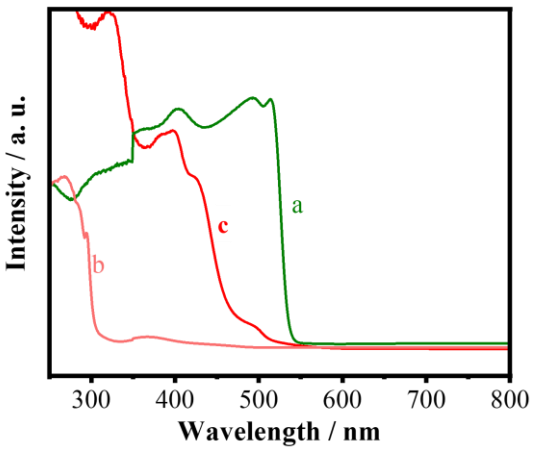

Fig. 5.7 Diffuse reflectance UV-Vis spectroscopy of commercial PbI_2 (a), **SA-5.1** (b) and **HP-5.1**(c).

The band gap value together with the valence band position allow us to calculate the energy of the conduction band energy, which is about -2.71 eV. The diffuse reflectance spectrum from which the optical bandgap was estimated is presented in Fig. 5.7. As it can be seen there, the absorption band presents a shoulder of the main absorption band at 490 nm, attributed to mid-gap states. The spectrum of **HP-5.1** presents relative maxima at 425,

400 and 310 nm, which can be attributed to excitonic peaks related with the 2D morphology.[40] This absorption spectrum corresponding to **HP-5.1** is different from the styryl ammonium iodide that has a weak absorption band at 360 nm and an intense absorption at 290 nm. The absorption spectrum of **HP-5.1** is also different from that of PbI_2 that has a very step absorption at 550 nm.

It is worth commenting that the UV-Vis spectrum recorded for **HP-5.1** presents different features than those of PbI_2 and compound **SA-5.1** precursors, indicating that the solid **HP-5.1** cannot be considered a mixture of PbI_2 and the organic precursor.

5.2.3 Post-synthetic modification

After characterization of **HP-5.1**, post-synthetic modification was performed by carrying out radical polymerization of the styryl moieties with an additional amount of styrene. As commented at the beginning of this Chapter, the objective was the preparation of a semiconductor material with an organic ligand that allows surface modification by an organic reaction under mild conditions. Styryl ammonium was selected for this purpose since it was considered that the styryl moiety of the ammonium ligand should allow copolymerization with styrene molecules.

The key point is to find a reaction compatible with the structural stability of the hybrid material. In this sense, styrene polymerization initiated by radicals can be carried out under inert atmosphere at moderate temperature (50 °C), and in non-polar organic solvent (hexane). This post-synthetic modification of **HP-5.1** allows us the control of the properties of the particle surface without altering the optoelectronic properties of the hybrid material.

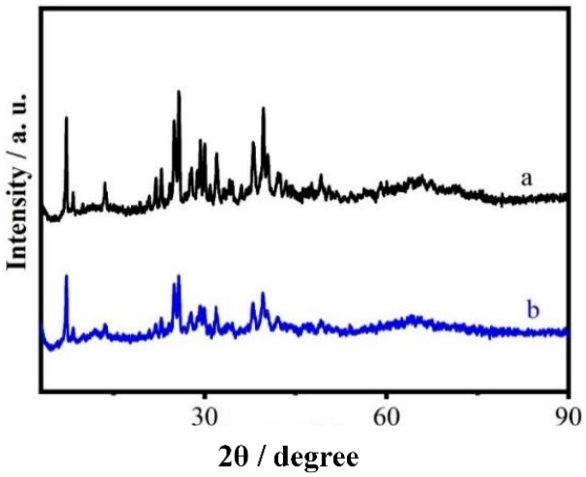

Fig. 5.8 XRD patterns of **HP-5.1** (a) and **PHP-5.1**(b).

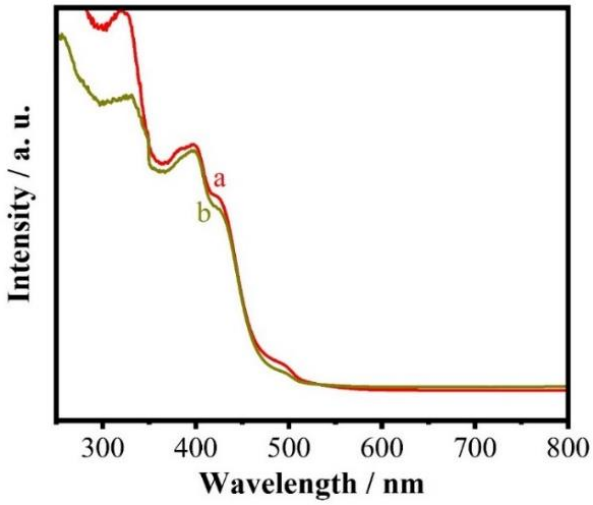

Fig. 5.9 UV-vis diffuse reflection spectroscopy of **HP-5.1** (a) and **PHP-5.1** (b).

The success of the polymerization and the preparation of surface polymerized hybrid perovskite (**PHP-5.1**) was confirmed by FTIR and ^{1}H NMR spectroscopy. Additionally, the crystallinity and optoelectronic properties of **HP-5.1** were preserved after this

post-synthetic modification, as can be deduced from XRD and diffuse reflectance UV-Vis spectroscopy in Figs. 5.8 and 5.9, respectively.

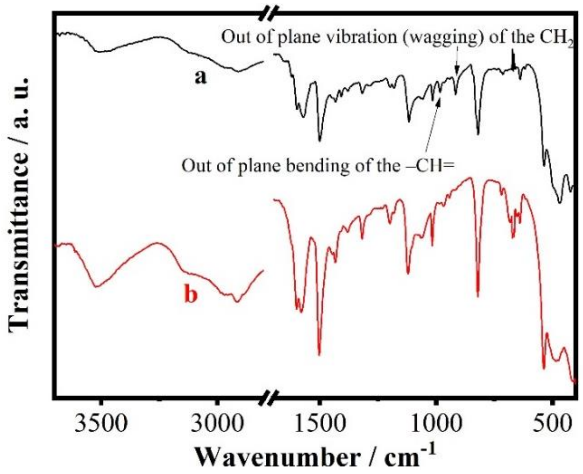

Fig. 5.10. FTIR spectroscopy of **HP-5.1** (a) and **PHP-5.1** (b). The disappearance of peaks at 980 and 915 cm^{-1} indicates the occurrence of double bond polymerization of styrylammonium ligand.

As can be observed in these Figures, the crystallinity, phase and optoelectronic properties of **HP-5.1** have been preserved after polymerization, indicating that the **HP-5.1** has not suffered any change under these reaction conditions. FTIR spectroscopy reveals the disappearance of the characteristic out of plane vibration bands corresponding to the vinylic moiety (915 and 980 cm^{-1}), which indicates the occurrence of double bond polymerization of styryl ammonium (see Fig. 5.10).

To obtain additional evidence of the occurrence of polymerization involving the styryl units, **HP-5.1** and **PHP-5.1** samples were dispersed in deuterated D_2O and the obtained liquid supernatants, containing organic ammonium moieties extracted from **HP-5.1** or **PHP-5.1**, were analyzed by ^1H NMR spectroscopy. The results are presented in Fig. 5.11. As can be seen there, in the case of **HP-5.1**, the ^1H NMR spectrum

corresponding to styryl ammonium ligand was recorded. Specifically, signals corresponding to the three vinylic hydrogens appearing at 6.75 (d-d, 1H, J^3=10.59 Hz and J^3=17.94 Hz), 5.0 (d-d, 1H, J^3=17.94 Hz) and 5.35 (d-d, 1H, J^3= 10.59 Hz), were recorded.

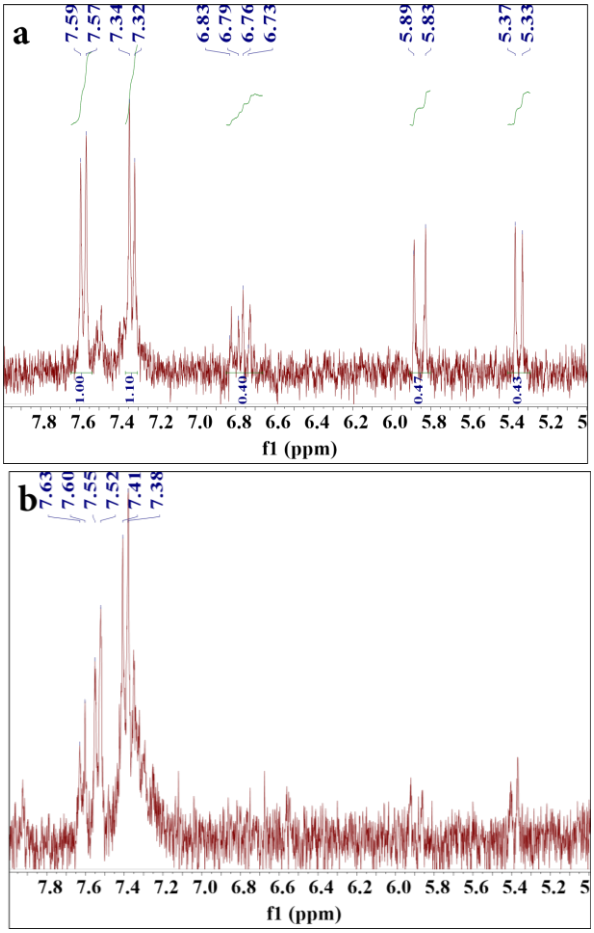

Fig. 5.11. 1H NMR spectra of organic ammonium samples extracted from **HP-5.1** (a) and **PHP-5.1** (b) using D_2O.

In contrast, a similar experiment for material **PHP-5.1** exhibits a barely detectable signal for these vinyl protons and the more

complex aromatic region was accompanied by aliphatic signals indicating the success of polymer formation.

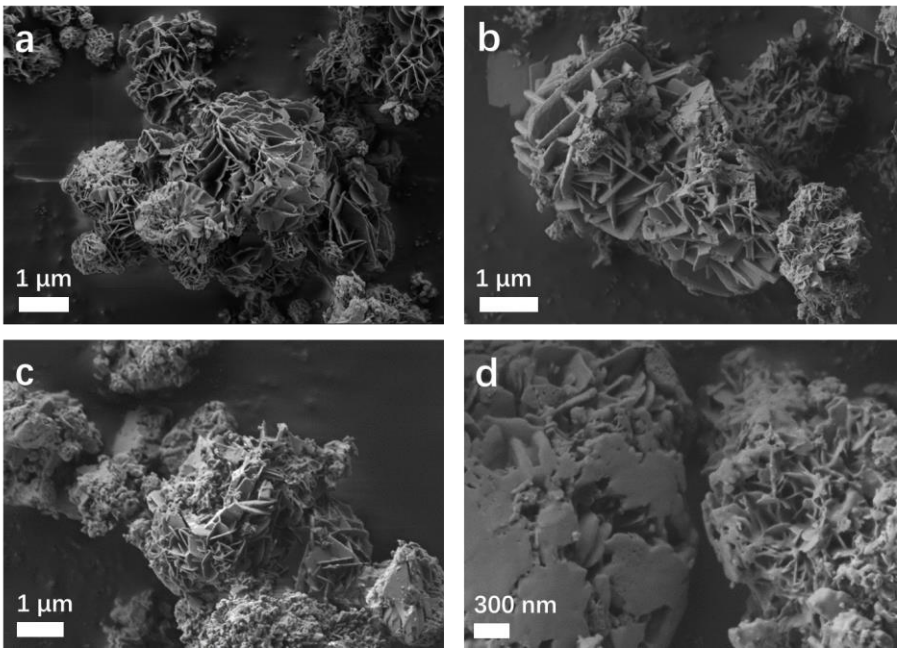

Fig. 5.12. Representative SEM images of **HP-5.1** (a), (b) and **PHP-5.1** (c), (d).

Copolymerization of **HP-5.1** with styrene results in clear morphologic change of the **PHP-5.1** particles respect to the parent material **HP-5.1**. Some representative images are provided in Fig. 5.12. As can be seen there, copolymerization results in the formation of smooth surfaces in SEM images reflecting the coating of the original flower-like particle by polystyrene.

As it could have been expected, considering the hydrophobic properties of polystyrene, **PHP-5.1** exhibits a remarkable hydrophobicity that is visually observed by solid **PHP-5.1** particles floating in water. Nevertheless, as commented before, material **PHP-5.1** becomes eventually decomposed upon stirring. In contrast, **HP-5.1** undergoes instantaneous decomposition under

the same conditions. Fig. 5.13 shows some photographs to illustrate the distinctive behavior of materials **HP-5.1** and **PHP-5.1** in water.

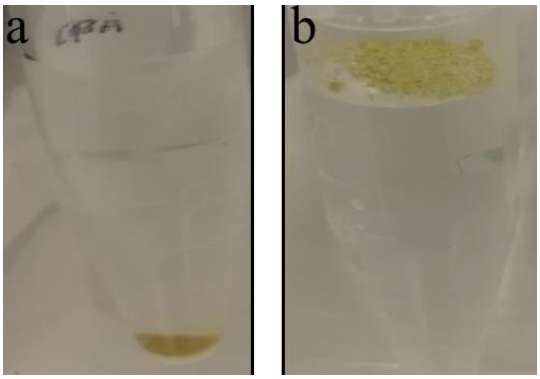

Fig. 5.13. Hydrophobicity tests of **HP-5.1** (a) and **PHP-5.1** (b) by dispersing in water. It can be seen that **HP-5.1** precipitates, while **PHP-5.1** is floating on the water surface.

5.2.4 Photostability tests

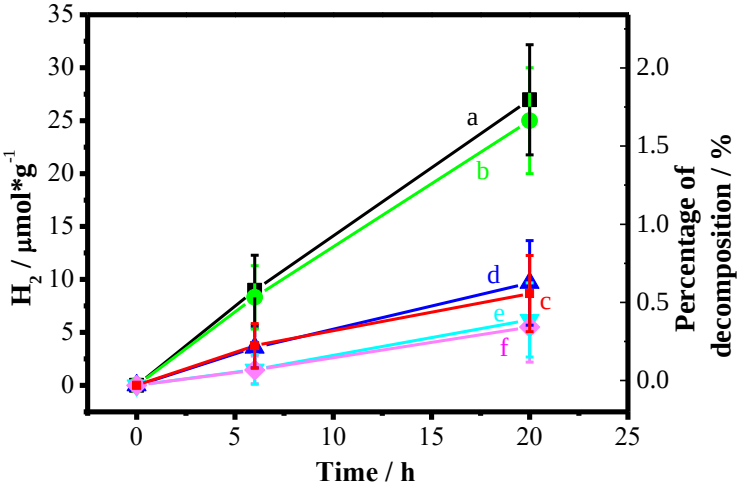

Fig. 5.14. Hydrogen evolution under different conditions: **a** (black squares): material **HP-5.1** under light and O_2; **b** (green triangles): **PHP-5.1** under light and O_2; **c** (red dots): material **PHP-5.1** under light and Ar; **d** (blue inverse triangles): material **HP-5.1** under light and Ar; **e** (cyan

diamonds) material **HP-5.1** under dark and O_2; and **f** (pink triangles): material **PHP-5.1** under dark and O_2.

As also commented at the beginning of this Chapter, the final goal of this research would be the development of hybrid materials that could be used as photocatalysts, exhibiting photostability. For this reason, it was of interest to determine the relative stability of materials **HP-5.1** and **PHP-5.1**, both in the dark, and, under visible light illumination ($\lambda > 400$ nm). It was observed that upon standing at room temperature in the absence and presence of oxygen, H_2 evolution occurs for both **HP-5.1** and **PHP-5.1** in the dark. This hydrogen evolution increases in **HP-5.1** and **PHP-5.1** samples upon visible light irradiation in the absence of oxygen, but H_2 evolution significantly enhance when **HP-5.1** and **PHP-5.1** are irradiated in the presence of oxygen. Fig. 5.14 shows the temporal H_2 evolution for the two samples under the conditions tested. As can be seen there, the differences in the H_2 evolution for materials **HP-5.1** and **PHP-5.1** are very minor, indicating that coating of the particles by polystyrene does not alter the stability of the hybrid perovskite against light or oxygen.

Quantification of the amount of hydrogen evolved indicates, however, that it corresponds to a minor percentage of the estimated amount of the total organic ligand in the material. Overall, the detection of hydrogen in these samples indicates that materials **HP-5.1** and **PHP-5.1** are instable, although the amount of hydrogen corresponds to a minor percentage of the theoretical amount for a complete decomposition of the organic ammonium cations in these materials.

It is proposed that hydrogen formation is a secondary process that derives from the initial formation of HI. It has been proposed that evolution of HI is the main cause of decomposition of methyl ammonium perovskite and the same could happen in the present case.[41, 42] From HI, hydrogen will be formed by splitting and the process could be assisted by the presence of oxygen.

Scheme 5.2 illustrates the proposed pathways resulting in hydrogen evolution.

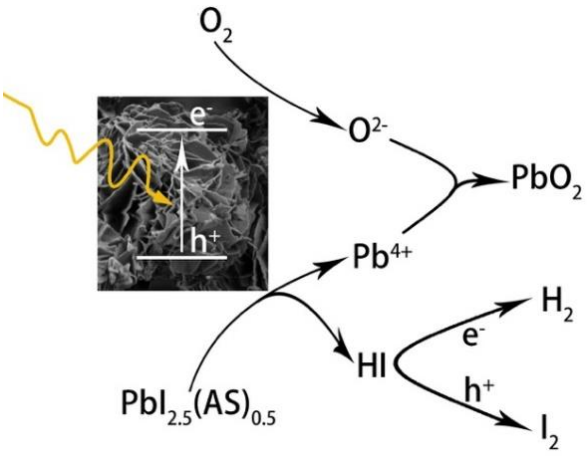

Scheme 5.2. Proposed mechanism of decomposition of materials **HP-5.1** and **PHP-5.1** and pathways resulting in H_2 evolution. (**AS** corresponds to aminostyrene).

The photocatalytic mechanism involves photogeneration of e^-/h^+ pairs upon light absorption. Then, e^- are efficiently quenched in the presence of O_2, generating superoxide radicals ($O_2^{\cdot-}$). The photogenerated h^+ could promote Pb^{2+} oxidation to Pb^{4+}, which in the presence of O^{2-} forms PbO_2. The later oxidation should induce HI evolution, and, in the presence of e^-/h^+ pairs, I_2 and H_2 are eventually produced. It appears that surface modification does not influence this decomposition mechanism and the behaviour of materials **HP-5.1** and **PHP-5.1** is similar.

In support of the proposal to explain hydrogen evolution from hybrid perovskites, XPS analysis of the samples after light irradiation shows an increase of the percentage of NH_2 with respect to NH_3^+ in the high resolution N1s peak of the irradiated sample. This indicates that deprotonation has occurred. Also, analysis of the Pb4f peak shows the appearance of a component of 15 % corresponding to Pb^{4+} in the sample. These changes were

also detectable after material **HP-5.1** was submitted to light irradiation in the absence of O_2 (Fig. 5.15).

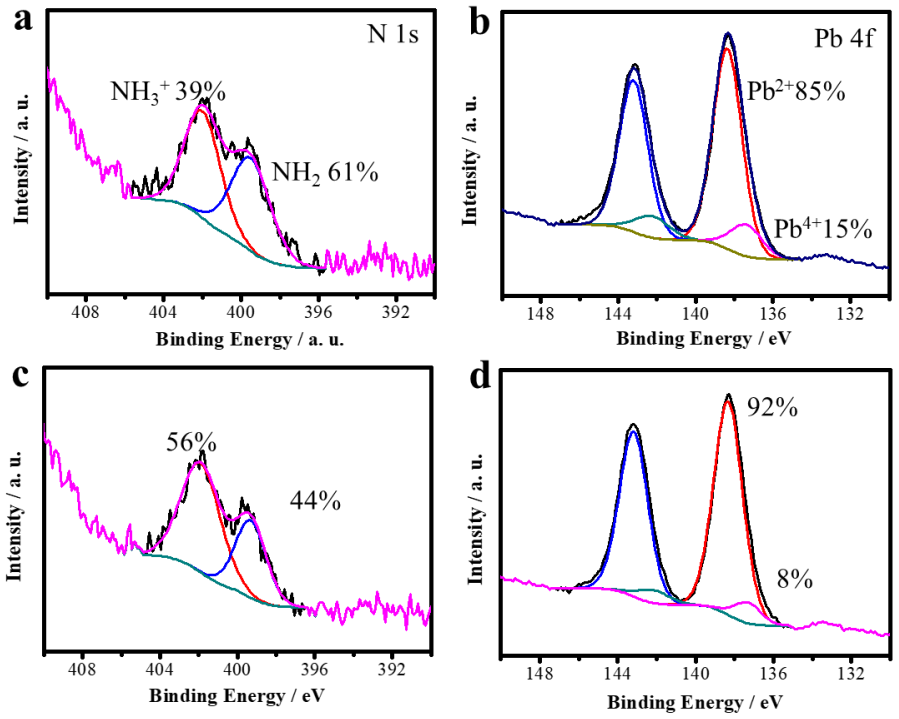

Fig. 5.15. N1s and Pb4f XPS spectra obtained from material **HP-5.1** samples: after illumination (λ > 400 nm) with O_2 (a and b) or with the absence of O_2 (c and d) for 20 hrs.

5.3 Conclusions

This Chapter has shown the preparation of a new 2D hybrid lead halide material and its post-synthetic modification based on the post-synthetic modification of the material with an organic reaction on the ammonium ligand. This strategy has been illustrated in the present case by the synthesis of a new hybrid lead halide material with styryl ammonium ligand that, after the synthesis, is submitted to cross-polymerization with styrene.

Although spectroscopic evidences confirm the success of the cross polymerization with subsequent increase in the hydrophobicity of the modified hybrid perovskite, the stability of this material in water is still not sufficient and can become dissolved.

Photostability tests show the evolution of hydrogen upon irradiation or even upon standing in the dark. It is proposed that hydrogen evolution derives from the deprotonation of the ammonium ligand, followed by the evolution of HI acid and subsequent splitting. XPS analysis provides evidence in support of this proposal, also showing the formation of some Pb^{4+} species on the surface. The decomposition of materials **HP-5.1** and **PHP-5.1** is facilitated by the presence of O_2.

Although the objective of the present research has not been achieved, the present study illustrates the potential that a proper selection of the organic ligand can have not only for the tuning of the electronic properties and structure of hybrid lead perovskites, but also to perform further modification of the material.

References

1. Lee, M. M.; Teuscher, J.; Miyasaka, T.; Murakami, T. N.; Snaith, H. J., Efficient Hybrid Solar Cells Based on Meso-Superstructured Organometal Halide Perovskites. *Science* **2012,** *338*, 643-647.

2. Boix, P. P.; Agarwala, S.; Koh, T. M.; Mathews, N.; Mhaisalkar, S. G., Perovskite Solar Cells: Beyond Methylammonium Lead Iodide. *J. Phys. Chem. Lett.* **2015,** *6*, 898-907.

3. Eames, C.; Frost, J. M.; Barnes, P. R. F.; O'Regan, B. C.; Walsh, A.; Islam, M. S., Ionic transport in hybrid lead iodide perovskite solar cells. *Nat. Commun.* **2015,** *6*, 7497.

4. Kato, Y.; Ono, L. K.; Lee, M. V.; Wang, S.; Raga, S. R.; Qi, Y., Silver Iodide Formation in Methyl Ammonium Lead Iodide Perovskite Solar Cells with Silver Top Electrodes. *Adv. Mater. Interfaces* **2015,** *2*, 1500195.

5. Malinkiewicz, O.; Yella, A.; Lee, Y. H.; Espallargas, G. M.; Graetzel, M.; Nazeeruddin, M. K.; Bolink, H. J., Perovskite solar cells employing organic charge-transport layers. *Nat. Photonics* **2013,** *8*, 128.

6. Christians, J. A.; Manser, J. S.; Kamat, P. V., Multifaceted Excited State of $CH_3NH_3PbI_3$. Charge Separation, Recombination, and Trapping. *J. Phys. Chem. Lett.* **2015,** *6*, 2086-2095.

7. Stranks, S. D.; Eperon, G. E.; Grancini, G.; Menelaou, C.; Alcocer, M. J. P.; Leijtens, T.; Herz, L. M.; Petrozza, A.; Snaith, H. J., Electron-Hole Diffusion Lengths Exceeding 1 Micrometer in an Organometal Trihalide Perovskite Absorber. *Science* **2013,** *342*, 341-344.

8. Xing, G.; Mathews, N.; Sun, S.; Lim, S. S.; Lam, Y. M.; Grätzel, M.; Mhaisalkar, S.; Sum, T. C., Long-Range Balanced Electron- and Hole-Transport Lengths in Organic-Inorganic $CH_3NH_3PbI_3$. *Science* **2013,** *342*, 344-347.

9. Albero, J.; García, H., Luminescence control in hybrid perovskites and their applications. *J. Mater. Chem. C* **2017,** *5*, 4098-4110.

10. Correa-Baena, J.-P.; Abate, A.; Saliba, M.; Tress, W.; Jesper Jacobsson, T.; Grätzel, M.; Hagfeldt, A., The rapid evolution of highly efficient perovskite solar cells. *Energy Environ. Sci.* **2017,** *10*, 710-727.

11. Jeon, N. J.; Na, H.; Jung, E. H.; Yang, T.-Y.; Lee, Y. G.; Kim, G.; Shin, H.-W.; Il Seok, S.; Lee, J.; Seo, J., A fluorene-

terminated hole-transporting material for highly efficient and stable perovskite solar cells. *Nat. Energy* **2018,** *3*, 682-689.

12. Sahli, F.; Werner, J.; Kamino, B. A.; Bräuninger, M.; Monnard, R.; Paviet-Salomon, B.; Barraud, L.; Ding, L.; Diaz Leon, J. J.; Sacchetto, D.; Cattaneo, G.; Despeisse, M.; Boccard, M.; Nicolay, S.; Jeangros, Q.; Niesen, B.; Ballif, C., Fully textured monolithic perovskite/silicon tandem solar cells with 25.2% power conversion efficiency. *Nat. Mater.* **2018,** *17*, 820-826.

13. Dhakshinamoorthy, A.; Navalon, S.; Corma, A.; Garcia, H., Photocatalytic CO_2 reduction by TiO_2 and related titanium containing solids. *Energy Environ. Sci.* **2012,** *5*, 9217-9233.

14. Albero, J.; Asiri, A. M.; García, H., Influence of the composition of hybrid perovskites on their performance in solar cells. *J. Mater. Chem. A* **2016,** *4*, 4353-4364.

15. Park, S.; Chang, W. J.; Lee, C. W.; Park, S.; Ahn, H.-Y.; Nam, K. T., Photocatalytic hydrogen generation from hydriodic acid using methylammonium lead iodide in dynamic equilibrium with aqueous solution. *Nat. Energy* **2016,** *2*, 16185.

16. Niu, G.; Guo, X.; Wang, L., Review of recent progress in chemical stability of perovskite solar cells. *J. Mater. Chem. A* **2015,** *3*, 8970-8980.

17. Sharma, S. K.; Phadnis, C.; Das, T. K.; Kumar, A.; Kavaipatti, B.; Chowdhury, A.; Yella, A., Reversible Dimensionality Tuning of Hybrid Perovskites with Humidity: Visualization and Application to Stable Solar Cells. *Chem. Mater.* **2019,** *31*, 3111-3117.

18. Berhe, T. A.; Su, W.-N.; Chen, C.-H.; Pan, C.-J.; Cheng, J.-H.; Chen, H.-M.; Tsai, M.-C.; Chen, L.-Y.; Dubale, A. A.; Hwang, B.-J., Organometal halide perovskite solar cells: degradation and

stability. *Energy Environ. Sci.* **2016,** *9*, 323-356.

19. Wang, R.; Mujahid, M.; Duan, Y.; Wang, Z.-K.; Xue, J.; Yang, Y., A Review of Perovskites Solar Cell Stability. *Adv. Funct. Mater. 0*, 1808843.

20. Ma, J.; Fang, C.; Chen, C.; Jin, L.; Wang, J.; Wang, S.; Tang, J.; Li, D., Chiral 2D Perovskites with a High Degree of Circularly Polarized Photoluminescence. *ACS Nano* **2019,** *13*, 3659-3665.

21. Tremblay, M. H.; Thouin, F.; Leisen, J.; Bacsa, J.; Srimath Kandada, A. R.; Hoffman, J. M.; Kanatzidis, M. G.; Mohite, A. D.; Silva, C.; Barlow, S.; Marder, S. R., $(4NPEA)_2PBI_4$ (4NPEA = 4-Nitrophenylethylammonium): Structural, NMR, and Optical Properties of a 3 × 3 Corrugated 2D Hybrid Perovskite. *J. Am. Chem. Soc.* **2019,** *141*, 4521-4525.

22. Spanopoulos, I.; Hadar, I.; Ke, W.; Tu, Q.; Chen, M.; Tsai, H.; He, Y.; Shekhawat, G.; Dravid, V. P.; Wasielewski, M. R.; Mohite, A. D.; Stoumpos, C. C.; Kanatzidis, M. G., Uniaxial Expansion of the 2D Ruddlesden-Popper Perovskite Family for Improved Environmental Stability. *J. Am. Chem. Soc.* **2019,** *141*, 5518-5534.

23. Febriansyah, B.; Koh, T. M.; John, R. A.; Ganguly, R.; Li, Y.; Bruno, A.; Mhaisalkar, S. G.; England, J., Inducing Panchromatic Absorption and Photoconductivity in Polycrystalline Molecular 1D Lead-Iodide Perovskites through π-Stacked Viologens. *Chemistry of Materials* **2018,** *30*, 5827-5830.

24. Zhao, Y.-Q.; Ma, Q.-R.; Liu, B.; Yu, Z.-L.; Yang, J.; Cai, M.-Q., Layer-dependent transport and optoelectronic property in two-dimensional perovskite: $(PEA)_2PbI_4$. *Nanoscale* **2018,** *10*, 8677-8688.

25. Byun, J.; Cho, H.; Wolf, C.; Jang, M.; Sadhanala, A.;

Friend, R. H.; Yang, H.; Lee, T.-W., Efficient Visible Quasi-2D Perovskite Light-Emitting Diodes. *Adv. Mater.* **2016,** *28*, 7515-7520.

26. Li, N.; Zhu, Z.; Chueh, C.-C.; Liu, H.; Peng, B.; Petrone, A.; Li, X.; Wang, L.; Jen, A. K.-Y., Mixed Cation $FA_xPEA_{1-x}PbI_3$ with Enhanced Phase and Ambient Stability toward High-Performance Perovskite Solar Cells. *Adv. Energy Mater.* **2017,** *7*, 1601307.

27. Arabpour Roghabadi, F.; Alidaei, M.; Mousavi, S. M.; Ashjari, T.; Tehrani, A. S.; Ahmadi, V.; Sadrameli, S. M., Stability progress of perovskite solar cells dependent on the crystalline structure: From 3D ABX3 to 2D Ruddlesden–Popper perovskite absorbers. *J. Mater. Chem. A* **2019,** *7*, 5898-5933.

28. Khuong, K. S.; Jones, W. H.; Pryor, W. A.; Houk, K. N., The Mechanism of the Self-Initiated Thermal Polymerization of Styrene. Theoretical Solution of a Classic Problem. *J. Am. Chem. Soc.* **2005,** *127*, 1265-1277.

29. Yao, K.; Wang, X.; Li, F.; Zhou, L., Mixed perovskite based on methyl-ammonium and polymeric-ammonium for stable and reproducible solar cells. *Chem. Commun.* **2015,** *51*, 15430-15433.

30. Bubnova, O., 2D materials: Hybrid interfaces. *Nat. Nanotechnol.* **2016**.

31. Saidaminov, M. I.; Abdelhady, A. L.; Murali, B.; Alarousu, E.; Burlakov, V. M.; Peng, W.; Dursun, I.; Wang, L.; He, Y.; Maculan, G.; Goriely, A.; Wu, T.; Mohammed, O. F.; Bakr, O. M., High-quality bulk hybrid perovskite single crystals within minutes by inverse temperature crystallization. *Nat. Commun.* **2015,** *6*, 7586.

32. Baikie, T.; Fang, Y.; Kadro, J. M.; Schreyer, M.; Wei, F.; Mhaisalkar, S. G.; Graetzel, M.; White, T. J., Synthesis and crystal chemistry of the hybrid perovskite $(CH_3NH_3)PbI_3$ for solid-state

sensitised solar cell applications. *J. Mater. Chem. A* **2013,** *1*, 5628-5641.

33. Dou, L.; Wong, A. B.; Yu, Y.; Lai, M.; Kornienko, N.; Eaton, S. W.; Fu, A.; Bischak, C. G.; Ma, J.; Ding, T.; Ginsberg, N. S.; Wang, L.-W.; Alivisatos, A. P.; Yang, P., Atomically thin two-dimensional organic-inorganic hybrid perovskites. *Science* **2015,** *349*, 1518-1521.

34. Milot, R. L.; Sutton, R. J.; Eperon, G. E.; Haghighirad, A. A.; Martinez Hardigree, J.; Miranda, L.; Snaith, H. J.; Johnston, M. B.; Herz, L. M., Charge-Carrier Dynamics in 2D Hybrid Metal–Halide Perovskites. *Nano Lett.* **2016,** *16*, 7001-7007.

35. Véron, A. C.; Linden, A.; Leclaire, N. A.; Roedern, E.; Hu, S.; Ren, W.; Rentsch, D.; Nüesch, F. A., One-Dimensional Organic–Inorganic Hybrid Perovskite Incorporating Near-Infrared-Absorbing Cyanine Cations. *J. Phys. Chem. Lett.* **2018,** *9*, 2438-2442.

36. Peng, Y.; Albero, J.; Álvarez, E.; García, H., Hybrid benzidinium lead iodide perovskites with a 1D structure as photoinduced electron transfer photocatalysts. *Sustain. Energy Fuels* **2019,** *3*, 2356-2360.

37. Wang, S.; Ono, L. K.; Leyden, M. R.; Kato, Y.; Raga, S. R.; Lee, M. V.; Qi, Y., Smooth perovskite thin films and efficient perovskite solar cells prepared by the hybrid deposition method. *J. Mater. Chem. A* **2015,** *3*, 14631-14641.

38. Zhang, F.; Srinivasan, M. P., Multilayered Gold-Nanoparticle/Polyimide Composite Thin Film through Layer-by-Layer Assembly. *Langmuir* **2007,** *23*, 10102-10108.

39. Singh, T.; Öz, S.; Sasinska, A.; Frohnhoven, R.; Mathur, S.; Miyasaka, T., Sulfate-Assisted Interfacial Engineering for High Yield and Efficiency of Triple Cation Perovskite Solar Cells with Alkali-Doped

TiO_2 Electron-Transporting Layers. *Adv. Funct. Mater.* **2018,** *28*, 1706287.

40. Jung, M.-H., Exploration of two-dimensional perovskites incorporating methylammonium for high performance solar cells. *CrystEngComm* **2021,** *23*, 1181-1200.

41. Yang, J.; Kelly, T. L., Decomposition and Cell Failure Mechanisms in Lead Halide Perovskite Solar Cells. *Inorg. Chem.* **2017,** *56*, 92-101.

42. Huang, W.; Manser, J. S.; Kamat, P. V.; Ptasinska, S., Evolution of Chemical Composition, Morphology, and Photovoltaic Efficiency of $CH_3NH_3PbI_3$ Perovskite under Ambient Conditions. *Chem. Mater.* **2016,** *28*, 303-311.

Chapter 6 Photo-Assisted N_2 Reduction by H_2 Using Cs-Promoted Ru/$SrTiO_3$ as Efficient Photocatalyst

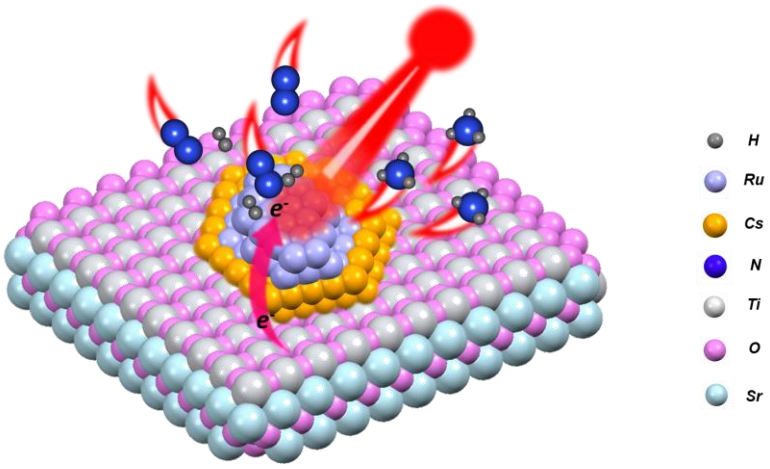

6.1 Introduction

The previous Chapters have been focused on the modification of the properties of hybrid lead perovskites to apply them as photocatalysts. Continuing with the objective of the present Doctoral Thesis, this Chapter and the following one are focused on the photocatalytic N_2 fixation, one of the reactions carried out at the largest scale in industry together with oil refining and petrochemistry.

The Haber-Bosch synthesis of ammonia allows atmospheric N_2 fixation as ammonia that is vastly used in the preparation of nitrogenated fertilizers.[1] In spite that N_2 hydrogenation is an exothermic reaction, the kinetics have so large activation barrier that requires high temperatures, pressure and convenient catalysts to occur at appreciable rates. Due to this slow reaction rate, the Haber-Bosch synthesis is an energy intensive process that it is responsible for between 1 and 2 % of the total current anthropogenic CO_2 emissions.[2] Due to N_2 chemical inertness, there is a continuous interest in developing more efficient catalysts, beyond the current Ru-modified Fe catalyst.[3]

There is a considerable number of examples showing that light can increase the reaction rates of thermal processes, including hydrogenations,[4, 5] oxidations,[6, 7] couplings,[8, 9] rearrangements[10] and others[11, 12]. Upon active metal nanoparticle (NP) light absorption, very high local temperatures at the nanoscale, which are not measurable by conventional macroscopic methods, can be reached[13] and this can result in a much enhanced catalytic activity of the active metal NP.[14, 15] This mechanism is generally termed as photothermal and causes the selective heating of the light harvester, particularly when the thermal conductivity of the support is low, since heat dissipation becomes slower.[16] Photothermal effects can occur concurrently with other photocatalytic mechanisms, such as photoinduced charge separation with the generation of electron and holes.[17, 18]

One clear example of photo-assisted hydrogenation of an inert molecule is the reverse water gas shift conversion of CO_2 into CO.[19]

Although the reaction can occur catalytically at higher temperatures, light irradiation increases CO formation rate at lower temperatures and milder conditions.

In spite of the numerous studies proving the advantages in terms of lower temperatures and higher reaction rates of photo-assisted CO_2 hydrogenation,[20, 21] to the best of our knowledge, there are no related studies regarding N_2 hydrogenation to ammonia.

The present Chapter reports the operation of a photothermal effect on the N_2 hydrogenation by Cs-promoted Ru NPs supported on strontium titanate perovskite (**STO**), enhancing the NH_3 formation rate about 50 % at 1080 W m^{-2} and reaching values that are probably the highest reported so far at the temperature and conditions used in the study.

6.2 Results and Discussion.

The synthesis and characterization of the Cs-modified **STO**-supported Ru NPs are first described, before its photothermal activity commented and data provided supporting the operation mechanism.

6.2.1 Ru(x)-STO preparation and characterization

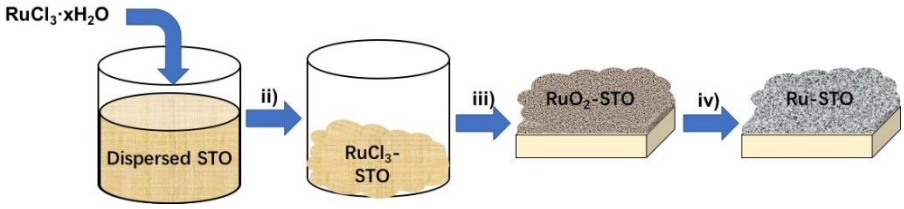

Scheme 6.1 Ru-STO photocatalyst preparation. (i) $RuCl_3 \cdot xH_2O$ is added to aqueous **STO** dispersion, (ii) the resulting slurry is dried at 70 ºC, (iii) after drying, the obtained powders are calcined at 250 ºC for 2 h, finally, (iv) the samples are thermally reduced in H_2 atmosphere at 350 ºC for 2 h.

Ru(x)-STO photocatalyst was prepared starting from commercial $SrTiO_3$ particles (**STO**) that were modified by deposition of Ru NPs by wet impregnation. Then, the resulting $RuCl_3$-impregnated **STO** powder was calcined at 250 ºC for 2 h and, subsequently, thermally reduced

under H_2 atmosphere at 350 ºC for 2 h, obtaining the final **Ru(x)-STO** samples. The preparation procedure is illustrated in Scheme 6.1.

Three Ru-**STO** samples with different Ru loading were prepared by changing the amount of the Ru precursor employed in the preparation method. X-ray fluorescence (XRF) analysis of the samples determined that the Ru content of the three **Ru(x)-STO** photocatalysts (x = 1, 2 and 4) was 0.94, 2.58, and 4.59 wt.%, respectively. X-ray diffraction (XRD) of **STO** and **Ru(4)-STO** samples (Fig. 6.1) showed the characteristic diffraction peaks corresponding to **STO**. The absence of metal Ru or RuO_2 signals in the XRD patterns could be justified by the small particle size of the Ru NPs at the loadings under study.

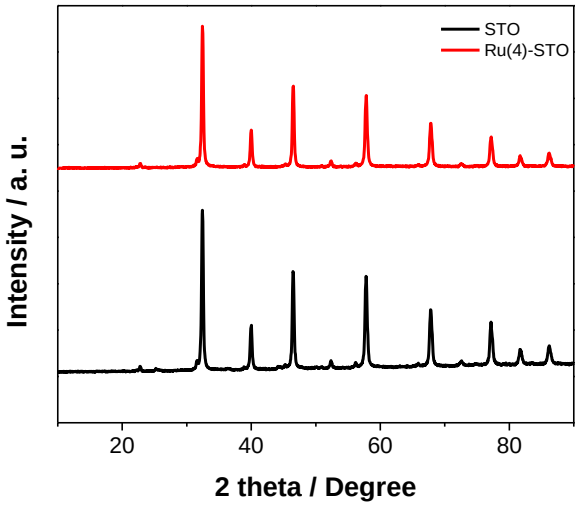

Fig. 6.1 XRD patterns of **STO** (black) and **Ru(4)-STO** (Red).

The successful formation of Ru NPs on **STO** was determined by HRTEM (Fig. 6.2). HRTEM images show small Ru NPs homogeneously distributed on larger particles. Despite their small size, the HRTEM images show that Ru NPs are crystalline, being possible to measure an interplanar distance that agrees well with the (002) interplanar distance of Ru (0) (Fig. 6.2 (b)). EDX analysis at the NPs confirmed they are constituted by Ru (Fig. 6.2 (c)). It is worth noticing that the EDS signal of Ru is always accompanied by those from Sr and

Ti of the **STO** support, in agreement with the small Ru particle size and its homogeneous distribution.

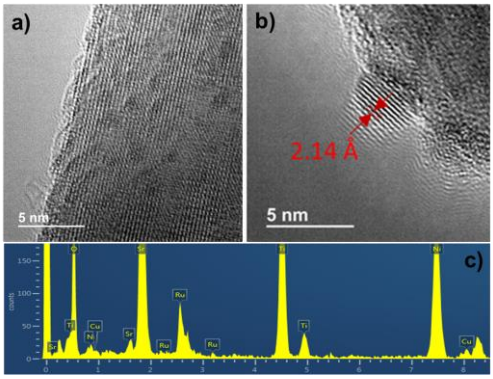

Fig. 6.2 Representative HRTEM images of **Ru(2)-STO** photocatalyst (a), highlighting in red lines the interplanar distance corresponding to Ru metal (b), and EDS analysis corresponding to Ru NPs supported on **STO**. Scale bar, 5 nm.

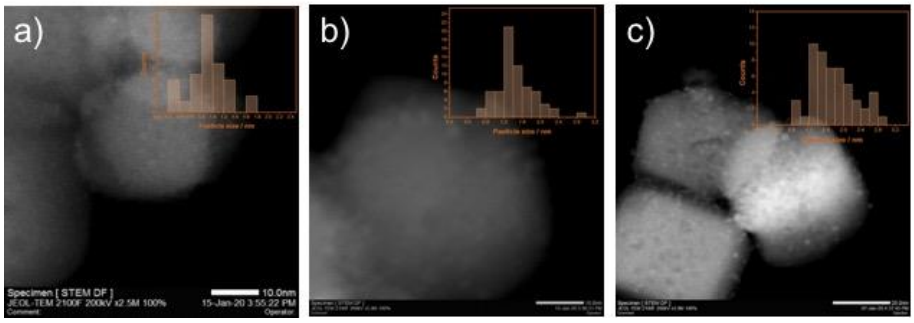

Fig. 6.3 ADF-STEM images of **Ru(1)-STO** (a), **Ru(2)-STO** (b) and **Ru(4)-STO**. The insets show the Ru NPs size distribution hi**STO**gram of each sample. Scale bars 10 nm in (a) and (b), and 20 nm in (c).

Angular dark-field (ADF) scanning transmission electron microscopy (STEM) images (Fig. 6.3) allowed estimation of the Ru NPs average size in **Ru(x)-STO** samples after measurement of a statistically relevant number of Ru NPs. Values of 0.9 ± 0.3 nm, 1.4 ± 0.4 nm and 1.8 ± 0.5 nm were obtained for **Ru(1)-STO**, **Ru(2)-STO** and

Ru(4)-STO, respectively. The slight increase of the average particle size is in agreement with the increase of Ru loading.

6.2.2 Photo-assisted NH_3 production

Photo-assisted NH_3 production was carried out in gas phase under continuous flow in a customized fixed bed borosilicate glass photoreactor equipped with a heating ribbon and a thermocouple in contact with the reactor walls controlling the temperature (see Chapter 8.2.3 and Fig. 8.1 for further details of the experimental photoreactor set up). Illumination of the system was carried out from the top of the reactor with the output of a 300 W UV-Vis Xe lamp through a quartz tube, where an optical fiber was placed at a distance of 6 cm from photocatalyst.

All photocatalysts were *in situ* activated with H_2 at 350 ºC for 2 h before testing. Activation ensures that Ru species are fully reduced to the metallic state. The ammonia production was quantified by the indophenol method and confirmed by isotopic $^{15}N_2$ experiments (see details in Chapter 8.2.4 and 8.4.1).

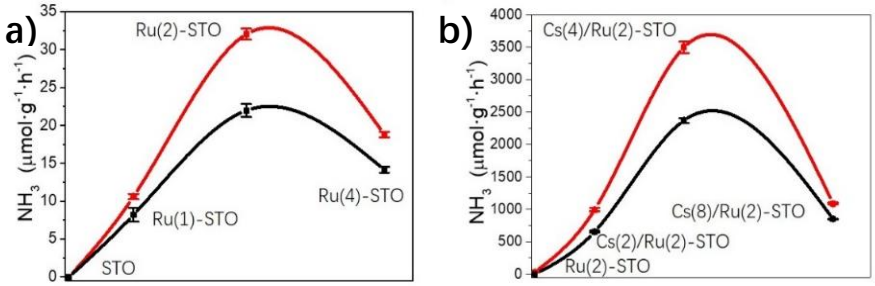

Fig. 6.4 (a) NH_3 production rate from **STO**, **Ru(1)-STO**, **Ru(2)-STO** and **Ru(4)-STO** in dark (black) and light irradiation (red) (1080 W m^{-2}). (b) NH_3 production rate from **Ru(2)-STO**, **Cs(2)/Ru(2)-STO**, **Cs(4)/Ru(2)-STO** and **Cs(8)/Ru(2)-STO** in dark (black) and light irradiation (red) (1080 W m^{-2}). Lines only indicate the experimental data trend. Condition: 60 mg catalyst; N_2 : H_2=10: 30 mL ; 350ºC; 0.1 Mpa.

The NH_3 production at 350 ºC obtained under irradiation (full Xe lamp emission spectrum, 1080 W/m^2) of the **Ru(x)-STO** samples containing different Ru loadings is presented in Fig. 6.4 (a). As can be

seen, there is an optimal amount of Ru (**Ru(2)-STO**) to obtain the highest photocatalytic activity (32 $\mu mol_{NH3}\ g_{catalyst}^{-1}\ h^{-1}$). This optimal Ru loading can be rationalized as derived from the operation of two opposite effects upon increasing the Ru loading in the photocatalysts. On one hand, the photocatalytic activity should increase with the Ru content, since this metal has the role of active site. On the other hand, excessive Ru loading increases the average particle size and, therefore, lesser percentage of exposed Ru metal.

The reaction was also carried out in the presence of the same catalysts under dark conditions at 350 ºC. As can be seen in Fig. 6.4 a, the NH_3 production rate followed the same trend as for the light assisted hydrogenation, being **Ru(2)-STO** the most efficient photocatalyst, although the NH_3 evolution increased by 50 % approximately upon light assistance. To the best of our knowledge, this is the first report on photo-assisted N_2 reduction by H_2. It is worth noticing that the system is working at atmospheric pressure in continuous flow and the reaction temperature employed is much lower than the typical values used in the Haber-Bosch process above 400 ºC.[3]

6.2.3 Cs-promotion

In order to further increase the photo-assisted NH_3 production rate, and based on previous reports on the use of alkali or alkali-earth metals as promotors to enhance the activity of some catalysts in different reactions,[22-26] we have studied the use of Cs salt as promotor in this photo-assisted reaction. Thus, **Ru(2)-STO** photocatalyst was further modified by deposition of Cs promoter (Cs_2CO_3) by wet impregnation (see Chapter 8 for the experimental details), obtaining the final **Cs(n)/Ru(2)-STO** (n: Cs/Ru atomic ratio) photocatalysts. Three different Cs promoter amounts were added, obtaining Cs:Ru atomic ratios of 1.6, 4.0 and 8.0 for **Cs(2)/Ru(2)-STO**, **Cs(4)/Ru(2)-STO** and **Cs(8)/Ru(2)-STO**, respectively, as determined by XRF analyses. As can be seen in Fig. 6.5, the XRD pattern of as-prepared **Cs(4)/Ru(2)-STO** photocatalysts does not show any new feature, neither as prepared nor after activation at 350 ºC under H_2 for 2 h, exhibiting only

the **STO** characteristic peaks. This could be due to the small amount of Cs_2CO_3 employed and its high dispersion on **STO**.

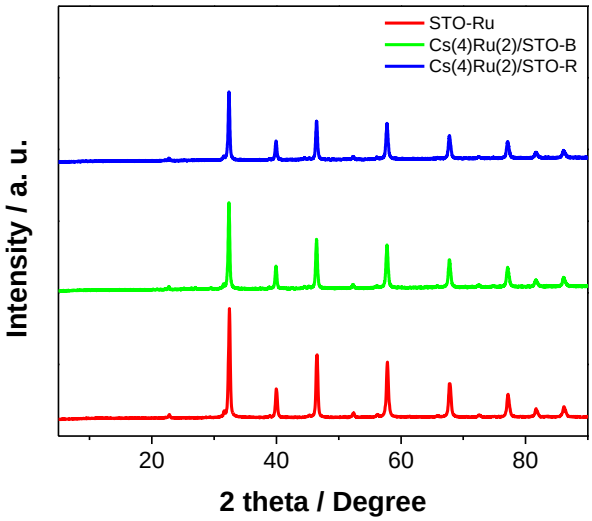

Fig. 6.5 XRD patterns collected from **Ru(2)-STO** (red), **Cs(4)Ru(2)-STO** as-synthesized and **Cs(4)Ru(2)-STO** after H_2 activation.

The photo-assisted NH_3 production at 350 ºC obtained under irradiation (full Xe lamp emission, 1080 W/m^2) promoted by **Cs(n)/Ru(2)-STO** samples containing different Cs:Ru molar ratios is presented in Fig. 6.4 (b). It is worth noticing that, in this case, the activation treatment under H_2 atmosphere at 350 ºC for 2 h could not be only responsible for Ru oxidized species reduction, but also promoting Cs salt decomposition, as reported before for other alkaline or alkaline-earth metal salts used as reaction promotors.[24] To address the nature of the Cs_2CO_3 after H_2 activation at 350 ºC, an *in situ* X-ray photoemission spectroscopy (XPS) measurement was carried out, monitoring the high resolution XPS Ru 3d + C 1s + Sr 3p peaks after *in situ* 2 h heating at 350 ºC in H_2 atmosphere inside the prechamber of the XPS instrument, thus avoiding subsequent exposure to the ambient. The results confirm the presence of the component related to carbonate species (~290 eV) after the activation treatment, as can be seen in Fig. 6.6. In the same plot, components related to Ru^0 were also recorded at 280.4 and 284.6 eV for Ru^0 $3d_{5/2}$ and Ru^0 $3d_{3/2}$, respectively.

These data not only confirm that Ru has been reduced to metal Ru during the activation, but also that Cs_2CO_3 has not suffered decomposition during the activation procedure at 350 ºC. Therefore, it is considered that Cs_2CO_3 is the actual promoting species in the photo-assisted N_2 hydrogenation reaction.

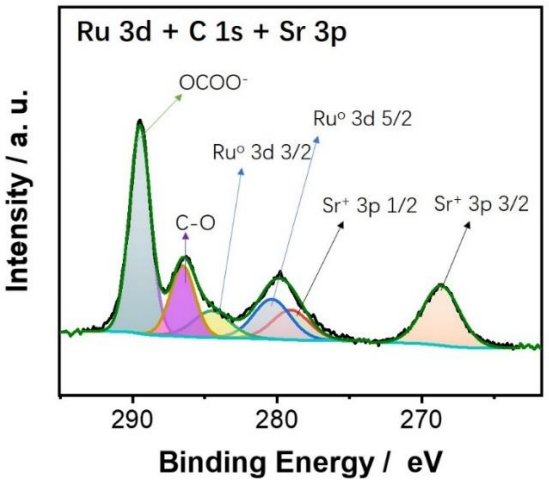

Fig. 6.6 High resolution Ru 3d + C 1s + Sr 3p XPS spectra and the best deconvolution to individual components of **Cs(4)/Ru(2)-STO** after activation.

After confirming the successful loading of Cs promoter on **Ru(2)-STO** catalyst, the N_2 reduction reactions were then performed. As can be seen in Fig. 6.4 (b), the **Cs(n)/Ru(2)-STO** photocatalysts also exhibit an optimal Cs:Ru atomic ratio to exhibit the highest photo-assisted NH_3 production. Also, the addition of the Cs_2CO_3 onto the **Ru(2)-STO** photocatalysts promotes a drastic enhancement in NH_3 production from 32.0 ± 0.7 $\mu mol_{NH3} \cdot g_{catalyst}^{-1} \cdot h^{-1}$, in the absence of Cs promoter, up to 3499.4 ± 88.2 $\mu mol_{NH3} \cdot g^{-1}_{catalyst} \cdot h^{-1}$ for a Cs : Ru molar ratio of 4 in the **Cs(4)/Ru(2)-STO** photocatalyst. This optimal Cs proportion indicates also the operation of two opposite effects upon increasing the Cs:Ru mol ratio on the photocatalyst. On one hand, the photocatalytic activity is enhanced due to the surface basicity introduced by the Cs species as confirmed by comparison of the isothermal CO_2 adsorption on **Cs(4)/Ru(2)-STO** and **Ru(2)-STO** (see Fig. 6.7), that should increase with Cs^+ loading. However, excessive

Cs^+ amounts can result in the coverage of Ru NPs, as observed by electron microscopy, and therefore, in less exposed Ru atoms.

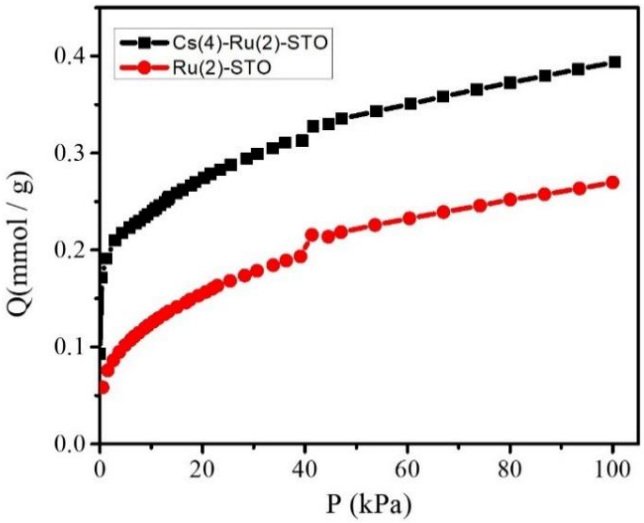

Fig. 6.7 The CO_2 adsorption plots of **Cs(4)Ru(2)-STO** and **Ru(2)-STO**.

It has been reported that the alkali or alkaline earth transition metal promoters facilitate catalytic reactions by two possible ways, one being that the promoter act as the structure or morphology re-constructor during the catalysis.[26] For example, the alkali metals can facilitate the formation of iron carbide when use Fe_2O_3/Graphene as the catalyst for the Fischer-Topsch process and the iron carbide can thereafter enhance the overall catalytic activity.[27, 28] It was found that the ammonia formation was structure sensitive, being faster on the Fe(111) surface than on Fe(110) or Fe(100) surface,[29] and the addition of promoter can direct the formation of Fe(111), thus increase the catalytic activity.[30] The aforementioned examples indicate the role of promoter favoring structure reconstruction. Another possible influence of promoters is tuning of the electron density. Deposition of alkali or alkaline earth transition metals on the surface of the support can change the basicity/acidity of the support, thus affecting the reactants/products adsorption or desorption. Also, promoters can donate electrons to the metal particles in close proximity, thus increasing the electron density

of the metal center.[26] Yet, in this specific system for ammonia synthesis, the role of Cs promoter is still unclear and in the following part a series of techniques were applied to reveal the underlying mechanism, as well as the role of light.

CO chemisorption measurements in **Ru(2)-STO** and **Cs(4)/Ru(2)-STO** samples revealed that, according to the models the Ru average crystallite size in **Ru(2)-STO** is approximately 1.4 nm, in good agreement with estimation based on STEM images. These measurements indicate that Ru dispersion decreases upon addition of Cs promoter from 6.7 $m^2 \cdot g^{-1}$ to 2.5 $m^2 \cdot g^{-1}$ for **Ru(2)-STO** and **Cs(4)/Ru(2)-STO** samples, respectively, corresponding according to the models to a Ru dispersion drop from 90 to 26 % for **Ru(2)-STO** and **Cs(4)/Ru(2)-STO** samples, respectively. These CO adsorption measurements indicate that Cs promotor at this molar ratio (n=4) is partially covering the Ru NPs, leading to a lesser 30 % percentage of accessible the Ru active sites. Fig. 6.8 and 6.9 presented the CO chemisorption spectra of the corresponding samples.

CO adsorption data are in agreement with STEM images of **Cs(4)/Ru(2)-STO**. These images show small bright NPs homogeneously distributed on the surface of larger **STO** particles (Fig. 6.9). EDS analysis in one of these bright NPs (spectrum 1 in Fig. 6.10) reveal the presence of Ru and Cs elements, as well as Sr and Ti from the support. However, EDS analyses carried out in a low contrast area (spectrum 4 in Fig. 6.10), where no Ru NPs are deposited, show undetectable signals from Ru and Cs. These results support the proposal that Cs promotor is mainly located near the Ru NPs and that at a Cs:Ru atomic ratio of 4 the Ru NPs are covered in a significant proportion (70 % according to CO adsorption data), but not totally, by Cs

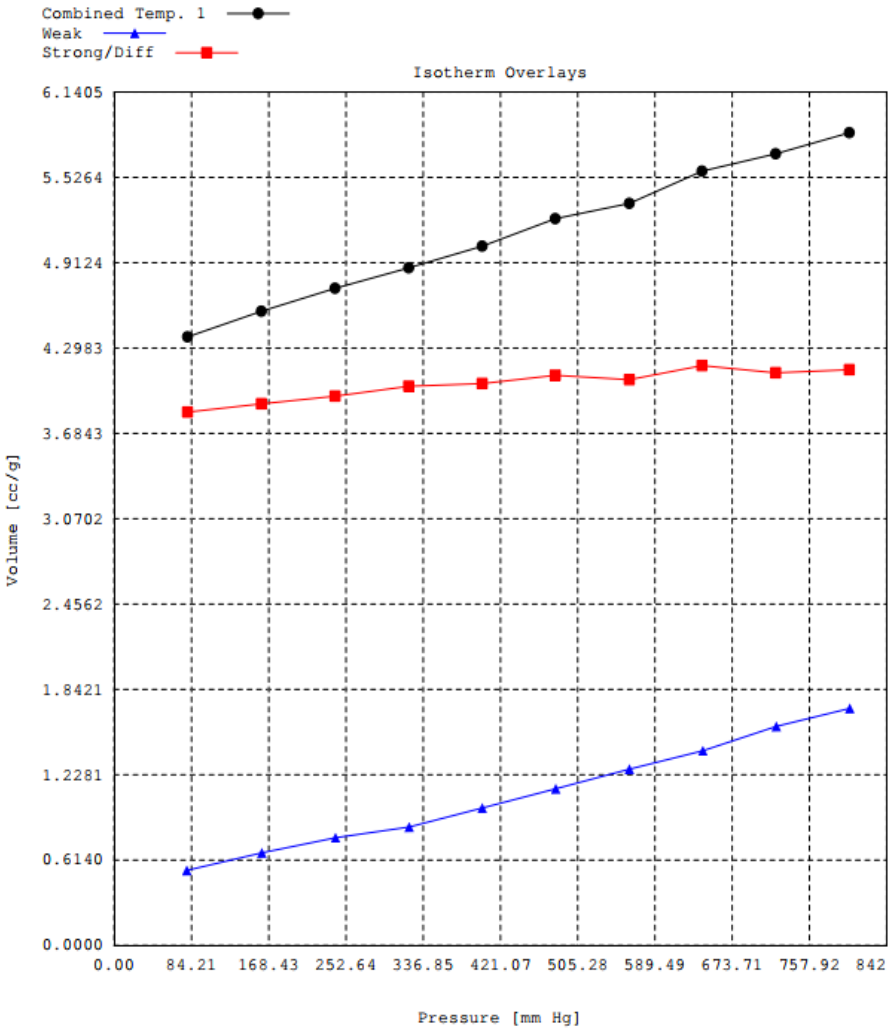

Fig. 6.8 CO chemisorption plots of **Ru(2)-STO**.

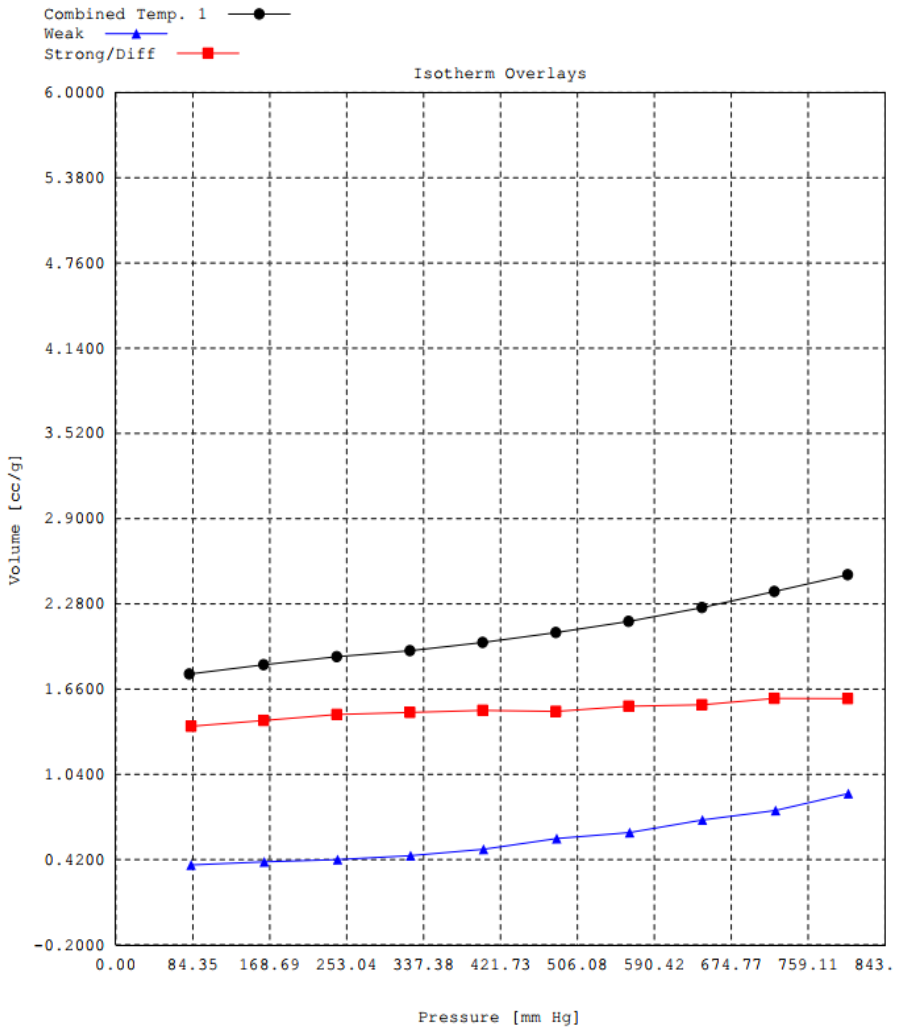

Fig. 6.9 CO chemisorption plots **Cs(4)Ru(2)-STO**.

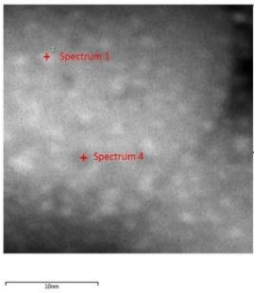

Spectrum 1	Line Type	K factor	Wt%	Wt% Sigma
O	K Series	0	24.67	2
Ti	K Series	1.09	22	0.87
Sr	L Series	1.726	47.61	1.4
Ru	L Series	1.816	5.26	0.92
Cs	L Series	2.015	0.47	0.64
Total			100	

Spectrum 4	Line Type	K factor	Wt%	Wt% Sigma
O	K Series	2.02	39.79	1.84
Ti	K Series	1.09	24.48	1.32
Sr	K Series	2.544	35.73	1.95
Ru	K Series	6,418	0	0
Cs	K Series	47.34	0	0
Total			100	

Fig. 6.10 STEM image of **Cs(4)/Ru(2)-STO** and EDS analysis results from the labelled regions as spectrum 1 and spectrum 4.

The improvement of the catalytic activity for the thermal NH_3 production of Ru NPs partially covered by Cs promotor has been previously reported by Aika et al. [26] In that report, chemisorption studies also observed that Cs promotor partially covered the Ru surface, although it had a weak interaction with the support (MgO) due to its basic character. The Cs role was ascribed to the tuning of the electron density on the Ru NP surface. It is proposed that a similar charge transfer density from the Cs promoter to the Ru NPs is taking place here in the Cs(x)/**Ru(2)-STO** samples.

In order to gain further information on the role of Cs in the present case, CO adsorption on **Cs(4)/Ru(2)-STO** and **Ru(2)-STO** samples was monitored by Fourier Transformed Infrared Spectroscopy (FTIR) (see Fig. 6. 11). CO adsorbed on **Ru(2)-STO** sample presents a vibrational peak at 2065 cm^{-1} assigned to CO adsorbed on Ru atoms.[31] However, **Cs(4)/Ru(2)-STO** shows 55 cm^{-1} shift towards lower frequency. The shift in CO stretching frequency has been previously related to an increase in the surface electron density of metal NPs, in the direction of lower frequency for electron-rich metal NPs and

towards higher frequency for electron-deficient metal NPs.[31, 32] Thus, the spectral shift is indicating that Cs increase the electron density on the Ru NPs supported on **STO**.

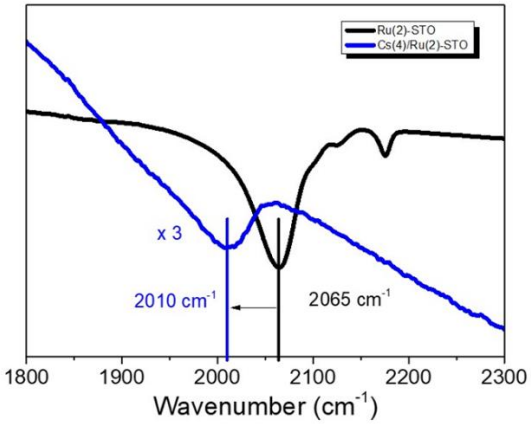

Fig. 6.11 IR spectrum of CO adsorbed on **Cs(4)Ru(2)-STO** and **Ru(2)-STO**.

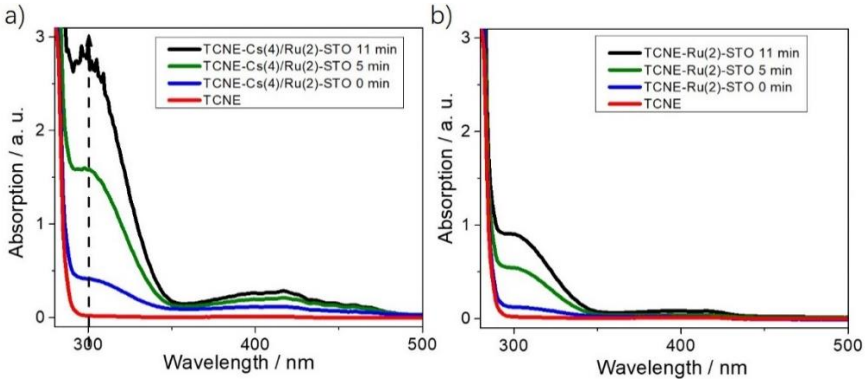

Fig. 6.12 UV-vis absorption spectrum recorded at different times collected from TCNE/CH_3CN solution in contact with **Cs(4)Ru(2)-STO** or **Ru(2)-STO**.

Further confirmation of this proposal was obtained by introducing tetracyanoethylene (TCNE) as electron acceptor probe molecule. It is well-known that TCNE is a good electron acceptor molecule forming charge-transfer complexes which can be detected and characterized by UV-Vis absorption band centred at 300 nm, observation of this UV band can be taken as a signature of the formation of the charge transfer

complex between TCNE and electron-rich Ru NPs.[33] Fig. 6.12 shows the UV-Vis spectra of TCNE in acetonitrile suspension of **Cs(4)/Ru(2)-STO** or **Ru(2)-STO** for different time periods. As can be seen there, UV-Vis spectra of **Cs(4)/Ru(2)-STO** suspensions in the TCNE solution exhibits an intense absorption peak characteristic of the charge transfer TCNE complex, while in the case of the **Ru(2)-STO** suspension the formation of this complex is much less favoured. Thus, all the available data point out to an increase in the electron density of Ru NPs due to the effect of Cs promotor in **Cs(4)/Ru(2)-STO**. It is proposed that the electron density enrichment on the active Ru NPs can favour N_2 activation, boosting, therefore, the NH_3 production.

It is worth noticing that the high NH_3 production rate obtained for the photo-assisted N_2 hydrogenation under the conditions of the present study is among the highest values ever reported in the literature for the photocatalytic N_2 fixation with H_2. Table 6.1 summarizes some of the most efficient catalysts reported so far for N_2 hydrogenation to NH_3. As can be seen there, the NH_3 production from **Cs(4)/Ru(2)-STO** in the dark, but otherwise similar conditions (temperature and pressure) is comparable with the one obtained recently by Hosono et al., using Ni@LaN NPs and only 19 % lower than that previously reported by the same author using Cs-Ru-MgO as catalyst. However, upon light-assistance **Cs(4)/Ru(2)-STO** exhibits even larger NH_3 production that any of the previous systems, demonstrating for the first time that photo-thermal process is an efficient approach to perform N_2 hydrogenation under mild conditions, with positive implications for industry.

Table 6.1. Summary of some of the most efficient catalysts for N_2 hydrogenation reported in the literature, including metal loading, conditions and reaction rate.

Entry	Catalyst	Metal Loading (wt%)	Conditions	Reaction rate ($mol \cdot g^{-1} \cdot h^{-1}$)	Referen-ce
1	**Cs-Ru@$SrTiO_3$**	Ru:2.6, Cs: 13	350 °C 0.1Mpa dark	2600	***This work***

2	**Cs-Ru@$SrTiO_3$**	Ru:2.6, Cs: 13	350°C 0.1Mpa Light	3580	***This work***
3	**Ni@LaN NPs**	Ni: 12.5	400°C 0.1Mpa	5543	34
4	**Ni@LaN NPs**	Ni: 12.5	340°C 0.1Mpa	2665	34
5	**Cs-Co_3Mo_3N**	Cs: 36.9	400°C 0.1Mpa	986	**35**
6	**Ru/C12A7:e^-_e**	Ru: 1.8	340°C 0.1Mpa	2021	**36**
7	**Cs-Ru/MgO**	Ru: 2.0	340°C 0.1Mpa	3200	36
8	**Ru/$SrTiO_3$**	Ru: 2.0	400°C 0.1Mpa	774	37
9	**Co/C12A7:e**	Co: 2.6	400°C 0.1Mpa	912	38
10	**LaRuSi**	-	400°C 0.1Mpa	1760	39
11	**LaCoSi**	-	400°C 0.1Mpa	1250	40

Control experiments using isotopically labeled $^{15}N_2$, monitoring $^{15}NH_3$ formation by ^1H NMR spectroscopy, were carried out (See in Fig.6.13). The doublet splitting for $^{15}NH_3$ protons (^{15}N nuclear spin ½) in comparison with the triplet splitting for $^{14}NH_3$ protons (^{14}N nuclear spin 1) recorded in the ^1H NMR spectra of NH_3 conclusively confirmed

$^{15}N_2$ gas as the main source of NH_3 by at least 82%. Therefore, all the available data indicate that for the experiments using **Cs(4)/Ru(2)-STO** as photocatalyst the origin of NH_3 is N_2.

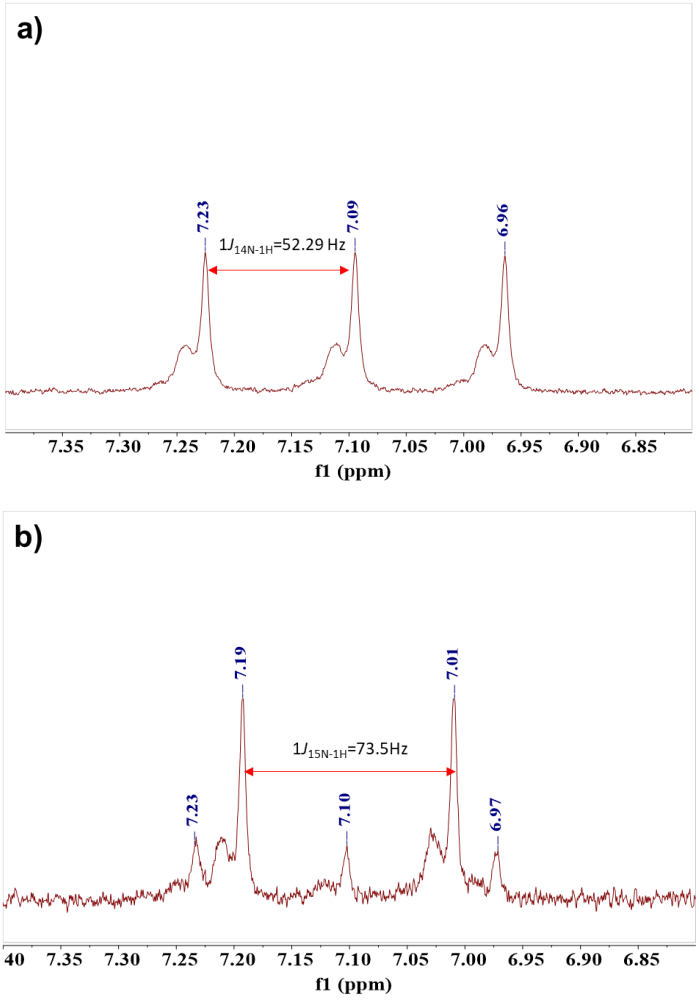

Fig. 6.13 ^{1}H NMR spectra of NH_3 obtained from $^{14}N_2$ (a) and $^{15}N_2$ (b) gas at 350 ^{o}C under illumination (1080 W m^{-2}) with H_2 using **Cs(4)/Ru(2)-STO** as photocatalyst.

The contribution of the light-assisted NH_3 production to the total amount of NH_3 was confirmed switching the light on and off during reaction. The results are presented in Fig. 6.14. After an initial period

feeding the reaction system with pure H_2 (t = 0 h), N_2 was added to the H_2 flow and a production rate of 3520 $\mu mol \cdot g^{-1} \cdot h^{-1}$ of NH_3 was obtained at 350 ºC under light irradiation (t =1 h). Then, the light was switched off and the NH_3 production rate decreased in the dark up to 1986 $\mu mol \cdot g^{-1} \cdot h^{-1}$ (t = 2 h). Then, light was turned on again and the NH_3 production rate increased up to 3423 $\mu mol \cdot g^{-1} \cdot h^{-1}$ (t = 3 h). It should be noted that the measured temperature of the (photo)catalyst bed in the cycle was constantly 350 ºC. These results confirm that photons are assisting NH_3 production on **Cs(4)/Ru(2)-STO** catalyst with a rate increase percentage of 52 % approximately at 1080 W m^{-2} light power.

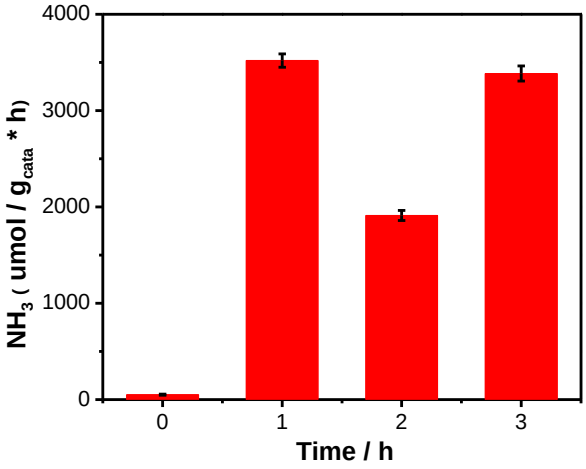

Fig. 6.14 NH_3 production rate from **Cs(4)/Ru(2)-STO** upon alternating 1 h periods in the dark (black) and light irradiation (red) (1080 W · m^{-2}). Reaction conditions: t=0: Only H_2 gas feeding to rule out the possible system contamination, 60 mg catalyst; 10 mL min^{-1} N_2 + 30 mL min^{-1} H_2; 350 ºC; 0.1 Mpa. Periods of light irradiation using the output of a 300 W Xe lamp.

6.2.4 Mechanism of the photo-assisted NH_3 production.

The influence of the reaction temperature on the photo-assisted NH_3 production using the **Cs(4)/Ru(2)-STO** photocatalyst was established by carrying out the reaction at different temperatures from 200 to 350 ºC upon light irradiation (1080 W m^{-2}) and studying the NH_3 evolution (Fig. 6.15 (a)). The photo-assisted NH_3 production did not take place under illumination at room temperature. At 260 ºC the production rate

was only 5.9 % of the observed value at 350 °C under light irradiation. The NH_3 production rate increased exponentially with the temperature following the Arrhenius equation (Equation 6.1), both in light and dark conditions (Fig. 6.15 (a)).

$$K(T) = A \cdot e^{-\frac{E_A}{RT}} \qquad \textbf{Equation 6.1}$$

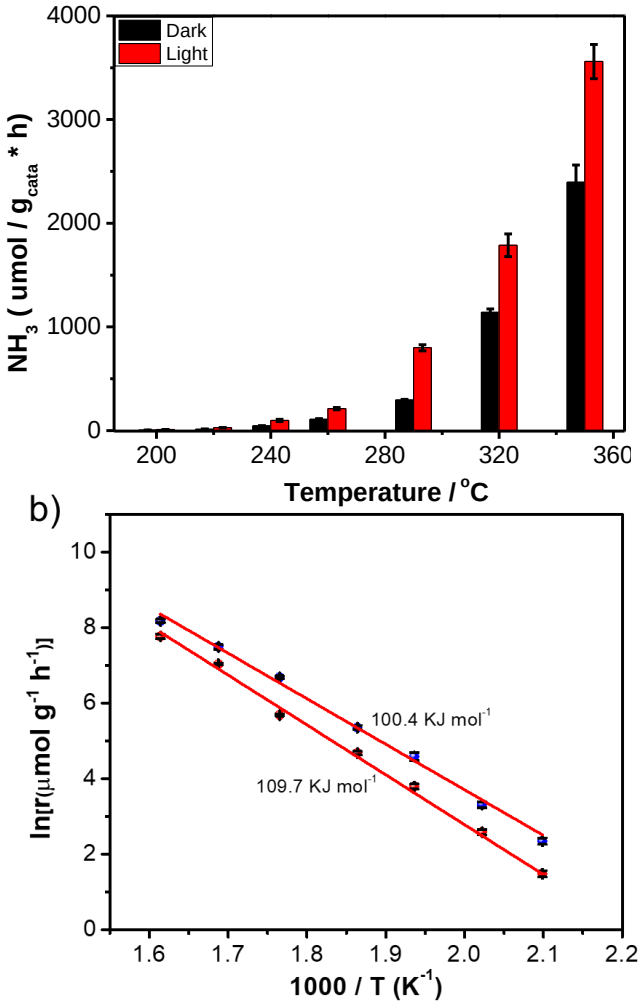

Fig. 6.15 (a) NH_3 production rate using **Cs(4)/Ru(2)-STO** in the dark (black) and under irradiation (red) (1080 W m^{-2}) at different temperatures. (b) NH_3 rate constant vs temperature under illumination (red) and in the dark (black)

conditions. The experimental data were fitted to the Arrhenius equation (Equation 6.1). The activation energy values upon irradiation and in the dark are indicated in the plot. Error bars indicate standard deviation based on independent experiments. Conditions: 60 mg catalyst; 10 mL min^{-1} N_2 + 30 mL min^{-1} H_2; 0.1 Mpa.

The activation energy (E_A) values for the NH_3 production determined from the Arrhenius plots in the temperature range from 200 to 350 ºC were 100.4 and 109.7 KJ mol^{-1} for the photo-assisted and dark processes, respectively. The calculated E_A values were, therefore, very similar both in light and dark conditions. This coincidence suggests that the reaction mechanism in both cases, thermal and photo-assisted, would have the same rate determining step. This similarity in E_A values would be against the typical photocatalytic mechanism involving photo-induced electron/hole charge separation.

The influence of the irradiation wavelength on NH_3 production was then investigated. NH_3 evolution at 350 ºC was studied upon illumination in different spectral regions (Fig. 6.16 (a)). Thus, N_2 hydrogenation reaction was carried out initially with the full spectrum of the Xe lamp (FL). Then, a pass band filter was placed in between the light source and the **Cs(4)/Ru(2)-STO** sample bed, allowing only UV light irradiation (UV). Subsequently, a UV cut-off filter was used to irradiate the sample with light in the visible and near-infrared region (Vis-NIR). Finally, the reaction was carried out in the dark (Dark), and the experiment was repeated using the same sequence. As can be seen in Fig. 6.16 (a), the NH_3 evolution under UV irradiation and in the dark was identical, while the NH_3 production under FL or Vis-NIR was higher and very similar. This is indicating that UV light is not contributing to the NH_3 formation, and only wavelengths in the visible and NIR regions are assisting NH_3 production with the **Cs(4)/Ru(2)-STO** catalyst under the present conditions.

In order to further investigate which frequencies of the electromagnetic spectrum are contributing in the catalytic activity of NH_3 generation, additional cut-off filters of different wavelengths were employed carrying out the reaction at 350 ºC and 1080 W m^{-2} power

for the full outcome of the Xe lamp. The results are presented in Fig. 616 (b). As can be seen there, 54 % of NH_3 evolution achieved with the FL irradiation is still observed at wavelengths longer than 830 nm. This data indicates that while the UV does not contribute to NH_3 formation, the Vis region is responsible for approximately 30 % of the observed NH_3 evolution under light assistance, while the other 70 % corresponds to the NIR region. Of note is that in all the set of experiments the macroscopic temperature measured for the thermocouple was constantly 350 ºC

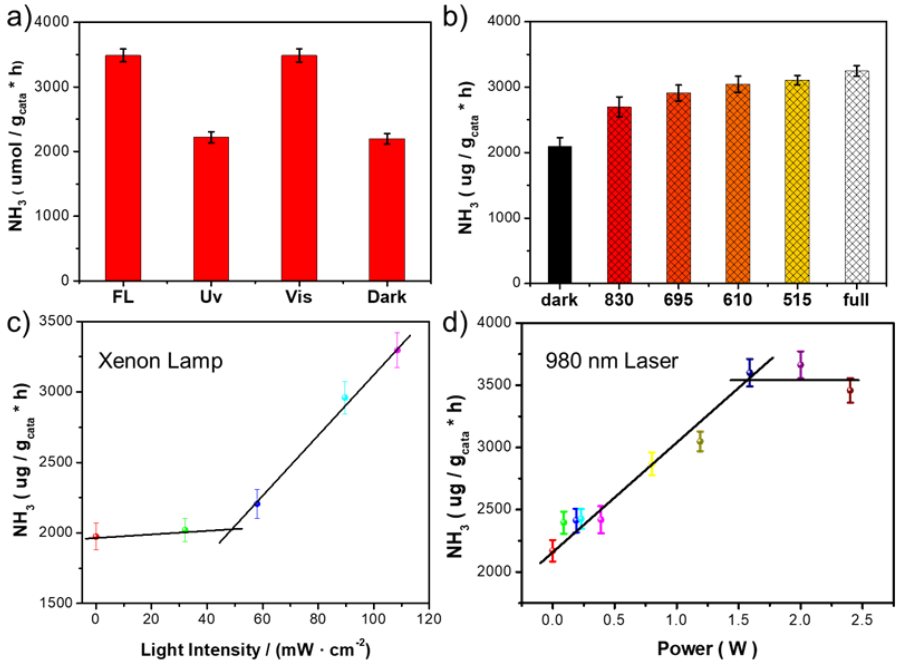

Fig. 6.16 (a) NH_3 production rate measured for **Cs(4)/Ru(2)-STO** upon alternating illumination with the full light spectrum (FL) (1080 W m^{-2}), UV light (UV), visible and NIR light (Vis) and in the dark (Dark). (b) NH_3 production rate obtained from **Cs(4)/Ru(2)-STO** in the dark, and upon illumination with filtered light at different cut-off wavelengths and with full lamp outcome. (c) NH_3 production rate achieved by **Cs(4)/Ru(2)-STO** under 300 W Xe lamp irradiation at different light intensities. (d) NH_3 production rate observed for **Cs(4)/Ru(2)-STO** under 980 nm monochromatic laser diode irradiation at different laser power. The lines in plots c and d are guides for the eyes. Error

bars indicate standard deviation from independent measurements. Conditions: 60 mg catalyst; 10 mL min^{-1} N_2 + 30 mL min^{-1} H_2; 350ºC; 0.1 Mpa.

Photo-assisted processes should depend on the light intensity. The influence of the light intensity in the photo-assisted NH_3 production was therefore investigated. Thus, a series of experiments measuring the NH_3 production at 350 ºC and varying the Xe lamp light intensity from 0 to maximum 1080 W/m^2 power was carried out. As can be observed in Fig. 6.16 c, beyond an apparent threshold of 50 mW cm^{-2}, the NH_3 production increased linearly. In a similar way, to confirm the photo-assistance in the NIR region, a monochromatic 980 nm diode laser was used as light source and the NH_3 evolution measured at different power irradiation. As can be observed in Fig. 6.16 d, the NH_3 production rate grew linearly in the power range from 0.5 to 1.5 W. Similar to the results with the Xe lamp, a minimum light intensity is needed to significantly enhance the NH_3 production, while beyond 1.5 W laser power a plateau in the NH_3 production rate was reached. This plateau would indicate saturation of photoresponsive sites and indicates again that the observed photo-assisted N_2 hydrogenation is not due to conventional thermal heating, since otherwise the higher the laser power, the higher is expected to be the temperature increase. Again, worth noting is that the thermocouple temperature was meaning constantly 350ºC at the photocatalyst bed.

Similar measurements but using a monochromatic 532 nm laser diode, instead of 980 nm, as light source was also performed (Fig. 6.17). No influence of the laser power on the NH_3 production rate was observed at this wavelength. This result can be rationalized based on the UV-Vis and the NIR absorption spectra of **Cs(4)/Ru(2)-STO** presented as Fig. 6.18. As can be seen there, the UV-Vis-NIR spectrum of **Cs(4)/Ru(2)-STO** presents a prominent absorption band in the UV region (λ < 350 nm) attributable to the absorption of **STO**. In most of the visible range the **Cs(4)/Ru(2)-STO** photocatalyst presents minor absorbance, while a broad band with onset at 600 nm and maximum in the NIR region, attributable to the Ru NPs, can be observed. Accordingly, the lack of observation of the photo-assistance effect at

532 nm, while polychromatic visible light increases NH_3 production rate by about 30%, indicates that Ru NPs are the photoresponsive component and light absorption by Ru NPs is a prerequisite. This result is again against heating as the cause of the photo-assistance, since it implies light absorption by a chromophore, Ru NPs in the present case.

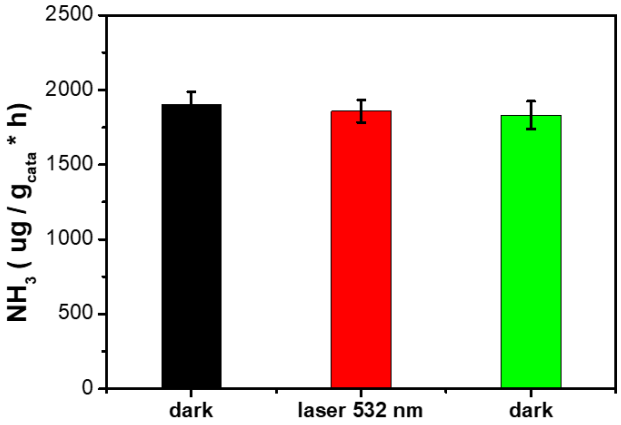

Fig. 6.17. NH_3 production rate at 350 °C under dark and light irradiation using a monochromatic 532 nm laser diode as light source. The catalysts is **Cs(4)/Ru(2)-STO**.

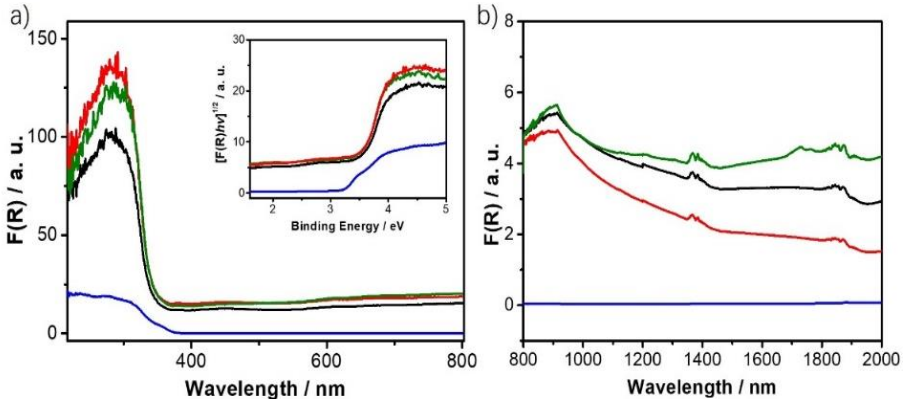

Fig. 6.18 Diffuse reflectance UV-Vis (a) and NIR (b) spectra, plotted as the Kubelka-Munk function of the reflectance (R) of **STO** (blue), **Ru(2)-STO** (black), **Cs(4)/Ru(2)-STO** (red) and **Cs(4)/Ru(2)-STO** after 20 h reaction (green). Panel a) inset shows the samples Tauc plot.

Overall, these experiments demonstrate that the light-induced activity rises mainly from the Ru NPs due mainly to their absorption in the NIR region of the electromagnetic spectrum. In view of these results, it is proposed that the high NH_3 production obtained with **Cs(4)/Ru(2)-STO** under illumination follows the so-called "*photothermal"* mechanism in which light is absorbed by the Ru NPs, increasing the local temperature of these NPs at the nanoscale, and boosting the NH_3 production in the active sites. This temperature increase at the nanometric Ru active site cannot be detectable at the macroscopic level by a conventional thermocouple measuring the catalyst bed temperature. This phenomenon has been descried elsewhere for the photo-assisted hydrogenation of unsaturated C-C multiple bonds and CO_2.[41-44]

Since the major part of the photoresponse rises from the NIR region, with negligible activity from the UV, where the main absorption is attributed to **STO**, it was of interest to elucidate whether **STO** is acting as inert support or it has any role in the NH_3 evolution. In other precedents it has been proposed that **STO** can play a role in photothermal reactions due to its low thermal conductivity.[45] With the aim to determine any possible role of **STO**, Ru NPs and Cs promoter were deposited at the optimum loadings on commercial TiO_2 P25, Al_2O_3 and aluminosilicate, and the NH_3 evolution measured at 350 ºC under 1080 W m^{-2} irradiation (Fig. 6.19). As can be seen there, the NH_3 production using **STO** as support was approximately two orders of magnitude higher than that of the catalysts in which Cs(4)/Ru(2) NPs were deposited on different supports. The higher photocatalytic activity of **Cs(4)/Ru(2)-STO** does not follow the order of the specific BET surface area, since **STO** (46 m^2 g^{-1}) is the support with the lowest specific surface area in the series of supports (71, 275 and 900 m^2 g^{-1} for P25, Al_2O_3 and aluminosilicate, respectively).

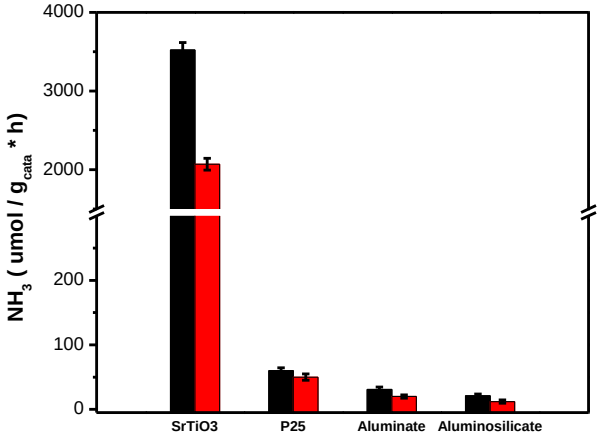

Fig. 6.19. NH_3 production rate as function of the support on which Cs-Ru NPs are deposited.

Therefore, it can be concluded that **STO** is not acting as innocent support, but it is also contributing to the photothermal activity of Cs/Ru NPs. In this regard, **STO** has been previously reported to present a basic surface together with a low thermal conductivity (12 W m^{-1} K^{-1}).[45] The basic surface makes Cs promoter interact weakly with **STO**, enhancing its interaction with the Ru NPs, as reported for other basic supports such as MgO.[26] On the other hand, the low **STO** thermal conductivity should be responsible for achieving a higher local temperature at Ru NPs upon NIR irradiation, therefore, being an ideal support for this photothermal reaction.[46]

In order to further investigate the reaction mechanism in the photo-assisted N_2 hydrogenation reaction, a set of additional experiments were carried out. First, **Cs(4)/Ru(2)-STO** photocatalyst was submitted to activation and subsequent Ar flow at 350 ºC for 15 min. Then, pure H_2 was flushed again at 350 ºC under irradiation for 30 min in order to generate any possible hydride species. After 15 min purge with Ar, a flow of pure N_2 was passed through the photocatalyst under the same conditions in order to determine if N_2 is able to react with the previously produced hydrides. 0.5 μg of NH_3 were collected after 30 min of N_2 flow under the typical reaction conditions. Subsequently, an analogous

experiment was performed exchanging the order of the gases. Thus, after activation and Ar purging at 350 ºC, pure N_2 was flushed under irradiation with the aim to form any possible nitride species on the surface of Ru NPs. Then, the reactor was purged with Ar for 15 min before, finally, introducing H_2 to consume any possible nitrides formed in the previous step. In this case, 7.1 µg of NH_3 were collected after 30 min of H_2 flow at the operating conditions. These results suggest that Ru nitrides are the key species reacting with H_2.

Similarly, the same experiments with consecutive independent exposure to N_2 and H_2 were carried out monitoring the photocatalyst surface by *in situ* FTIR spectroscopy. Thus, **Cs(4)/Ru(2)-STO** was *in situ* activated at 350 ºC under H_2 flux for 2 h. Then, after Ar purge for 15 min, the sample was submitted to N_2 flux and the FTIR spectrum acquired. The spectra are presented in Fig. 6.19 (a). Then, the sample was purged with Ar for 15 min and a H_2 flow was passed for 30 min. As can be seen in Fig. 6.20 (a), a signal located at approximately 1970 cm^{-1} was recorded under these conditions. This band can be attributed to NH- intermediate species adsorbed in the Ru active sites. Simultaneously, measurement of the FTIR chamber gas phase (Fig. 6.20 (b)) under the previous conditions revealed the presence of peaks at 3332, 1630, 965 and 929 cm^{-1}, which can be safely attributed to NH_3 in the gas phase. On the contrary, if H_2 is flushed prior N_2, no detectable signals in **Cs(4)/Ru(2)-STO** at 1970 cm^{-1} or NH_3 in the gas phase could be recorded. In a similar way, the vibrational band attributed to NH-species was not detected in **Ru(2)-STO** when N_2 was fluxed prior H_2, and neither NH_3 was detected in these conditions.

These results support the formation of nitride species on the Ru NPs characterized by the 1970 cm^{-1} vibration peak as the prevalent intermediate responsible for the NH_3 evolution, only when Cs promotor is present.

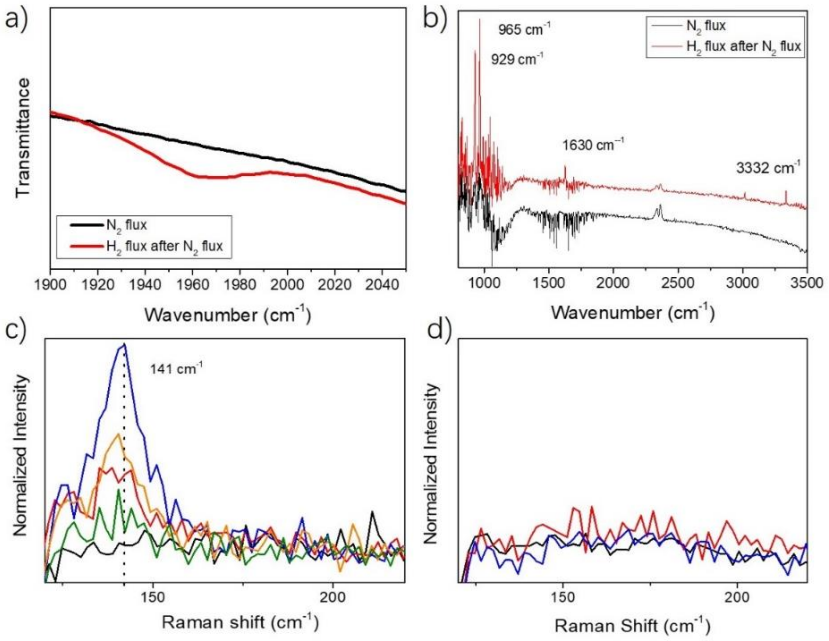

Fig. 6.20 (a) *In situ* FTIR spectra of **Cs(4)/Ru(2)-STO** at 350 ºC after activation, Ar purge and 30 min of N_2 flux (black) and subsequent H_2 flux for 30 min (red) and (b) *In situ* FTIR spectra of the gas phase simultaneously to recording the red spectrum in panel (a). Raman spectra of **Cs(4)/Ru(2)-STO** (c) and **Ru(2)-STO** (d) upon activation under H_2 flow for 2 h and Ar purge (black), N_2 flow for 10 (red) and 20 min (blue), and H_2 flow for 10 (orange) and 20 min (green). The sample temperature was constant at 350 ºC in all experiments.

Further evidence of Ru-nitride species formation on the **Cs(4)/Ru(2)-STO** is provided by complementing *in situ* Raman spectroscopy experiments. In this study, **Cs(4)/Ru(2)-STO** and **Ru(2)-STO** samples were *in situ* activated under H_2 flow at 350 ºC for 2 h, and, after Ar purging, N_2 flow was flushed and the Raman spectrum recorded at different times. The *in situ* Raman measurements are shown in Fig. 6.20c and d. They show the growth along time under N_2 atmosphere in the **Cs(4)/Ru(2)-STO** of a band centered at 141 cm^{-1}, attributed to Ru-nitride species. On the contrary, no bands at this Raman shift were detected in **Ru(2)-STO** sample (Fig. 6.20 (d)). Moreover, if gas flow is turned to pure H_2, the previously formed 141

cm^{-1} band in **Cs(4)/Ru(2)-STO** decreased with time until complete disappearance. Overall, these experiments confirm that N_2 is activated in the Ru surface only when Cs is present, probably due to the enhancement of the electron density in the Ru NPs, while no evidence of the role of Ru-H could be obtained.

6.2.5 Stability.

The stability of **Cs(4)/Ru(2)-STO** photocatalyst was determined by performing a long-run continuous N_2 hydrogenation reaction during 120 h at 350 ^{0}C under irradiation (1080 W m^{-2}). The temporal evolution of the NH_3 production rate is presented in Fig. 6.21.

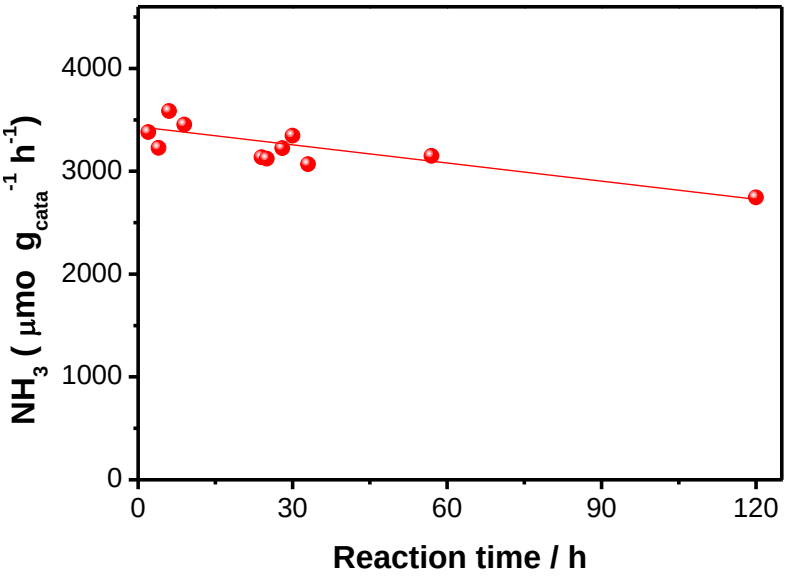

Fig. 6.21 (a) NH_3 production rate from **Cs(4)/Ru(2)-STO** at 350 ^{o}C under light irradiation (1080 W m^{-2}) for 120 h. Conditions: 60 mg catalyst; 10 mL min^{-1} N_2 + 30 mL min^{-1} H_2; 350^{o}C; 0.1 Mpa. The red line is a linear fitting of the experimental points.

As can be seen there, the NH_3 production decays slowly during the 120 h experiment, indicating a high photocatalyst stability. Thus, the NH_3 activity decayed 10 % during the first 60 h, while a 20 % decrease from the initial activity was found after 120 h of continuous reaction.

HRTEM images of **Cs(4)/Ru(2)-STO** photocatalyst after this long-run experiment show no evidence of Ru NPs agglomeration, remaining homogeneously distributed, and exhibiting very similar average particle size (Fig. 6.22). Thus, this photocatalyst demonstrates to be very stable under these reaction conditions. The slow photocatalytic activity decrease is probably due to deposition on the Ru NP surface of nitrogenated poisons.

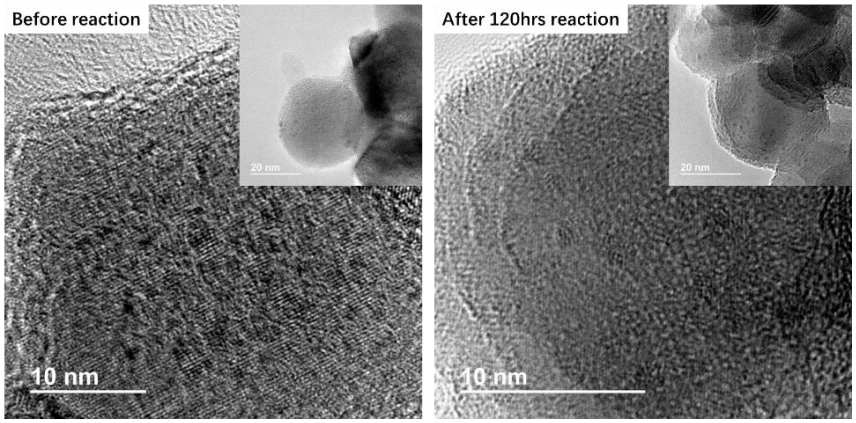

Fig. 6.22 HRTEM images of **Cs(4)/Ru(2)-STO** photocatalysts before the reaction and after 120 h reaction at 350 ^{o}C under light irradiation (1080 W m ^{2}).

6.3 Conclusions

The present Chapter has shown the influence of light increasing the rate of N_2 hydrogenation to NH_3 for the Cs-promoted Ru NPs supported on **STO**. Isotopic ^{15}N labelling confirms N_2 as the origin of NH_3. The photo-assistance increases with the light intensity, being about 50 % increase for 1080 W m^{-2}, and depends on the wavelength, NIR radiations being more efficient than visible wavelengths, while UV light does not increase the NH_3 production rate. Mechanistic data indicate that the reaction occurs upon light absorption by Ru NPs causing a localized temperature increase and that **STO** plays a role due to its low thermal conductivity and basicity favoring the promotional effect of Cs on Ru NPs.

Considering that upon illumination the **Cs(4)/Ru(2)-STO** photocatalyst disclosed here is among the most efficient catalysts reported so far for NH_3 formation, the present finding opens the door for further exploration of light assistance to ammonia synthesis.

6.4 References

1. Humphreys, J.; Lan, R.; Tao, S., Development and Recent Progress on Ammonia Synthesis Catalysts for Haber–Bosch Process. *Advanced Energy and Sustainability Research* **2021,** *2*, 2000043.

2. MacFarlane, D. R.; Cherepanov, P. V.; Choi, J.; Suryanto, B. H.; Hodgetts, R. Y.; Bakker, J. M.; Vallana, F. M. F.; Simonov, A. N., A roadmap to the ammonia economy. *Joule* **2020**.

3. Vojvodic, A.; Medford, A. J.; Studt, F.; Abild-Pedersen, F.; Khan, T. S.; Bligaard, T.; Nørskov, J., Exploring the limits: A low-pressure, low-temperature Haber–Bosch process. *Chem. Phys. Lett.* **2014,** *598*, 108-112.

4. Liu, L.; Puga, A. V.; Cored, J.; Concepción, P.; Pérez-Dieste, V.; García, H.; Corma, A., Sunlight-assisted hydrogenation of CO2 into ethanol and C2+ hydrocarbons by sodium-promoted Co@ C nanocomposites. *Applied Catalysis B: Environmental* **2018,** *235*, 186-196.

5. Mateo, D.; De Masi, D.; Albero, J.; Lacroix, L.-M.; Fazzini, P.-F.; Chaudret, B.; García, H., Synergism of Au and Ru Nanoparticles in Low-Temperature Photoassisted CO_2 Methanation. *Chem. Eur. J.* **2018,** *24*, 18436-18443.

6. Espinosa, J. C.; Catalá, C.; Navalón, S.; Ferrer, B.; Álvaro, M.; García, H., Iron oxide nanoparticles supported on diamond nanoparticles as efficient and stable catalyst for the visible light assisted Fenton reaction. *Appl. Catal. B* **2018,** *226*, 242-251.

7. Sun, Z.; Fang, S.; Lin, Y.; Hu, Y. H., Photo-assisted methanol steam reforming on solid solution of Cu-Zn-Ti oxide. *Chem. Eng. J.* **2019,** *375*, 121909.

8. Prajapati, P. K.; Saini, S.; Jain, S. L., Nickel mediated palladium free photocatalytic Suzuki-coupling reaction under visible light irradiation. *J. Mater. Chem. A* **2020,** *8*, 5246-5254.

9. Mori, K.; Kawashima, M.; Yamashita, H., Visible-light-enhanced Suzuki–Miyaura coupling reaction by cooperative photocatalysis with an Ru–Pd bimetallic complex. *Chem. Commun.* **2014,** *50*, 14501-14503.

10. Wrighton, M.; Hammond, G. S.; Gray, H. B., Group VI metal carbonyl photoassisted isomerization of olefins. *J. Organomet. Chem.* **1974,** *70*, 283-301.

11. Kim, C.; Lee, H., Light-assisted surface reactions on metal nanoparticles. *Catal. Sci. Technol.* **2018,** *8*, 3718-3727.

12. Cheng, G.; Tan, X.; Song, X.; Chen, X.; Dai, W.; Yuan, R.; Fu, X., Visible light assisted thermocatalytic reaction of CO+ NO over Pd/$LaFeO_3$. *Appl. Catal. B* **2019,** *251*, 130-142.

13. Hogan, N. J.; Urban, A. S.; Ayala-Orozco, C.; Pimpinelli, A.; Nordlander, P.; Halas, N. J., Nanoparticles heat through light localization. *Nano Lett.* **2014,** *14*, 4640-4645.

14. Fuku, K.; Hayashi, R.; Takakura, S.; Kamegawa, T.; Mori, K.; Yamashita, H., The synthesis of size‐and color‐controlled silver nanoparticles by using microwave heating and their enhanced catalytic activity by localized surface plasmon resonance. *Angew. Chem.* **2013,** *125*, 7594-7598.

15. Zhang, X.; Li, X.; Reish, M. E.; Zhang, D.; Su, N. Q.; Gutiérrez, Y.; Moreno, F.; Yang, W.; Everitt, H. O.; Liu, J.,

Plasmon-enhanced catalysis: Distinguishing thermal and nonthermal effects. *Nano Lett.* **2018,** *18*, 1714-1723.

16. Ghoussoub, M.; Xia, M.; Duchesne, P. N.; Segal, D.; Ozin, G., Principles of photothermal gas-phase heterogeneous CO_2 catalysis. *Energy Environ. Sci.* **2019,** *12*, 1122-1142.

17. Gan, Z.; Wu, X.; Meng, M.; Zhu, X.; Yang, L.; Chu, P. K., Photothermal contribution to enhanced photocatalytic performance of graphene-based nanocomposites. *ACS nano* **2014,** *8*, 9304-9310.

18. Lu, S.; Liu, F.; Qiu, P.; Qiao, M.; Li, Y.; Cheng, Z.; Xue, N.; Hou, X.; Xu, C.; Xiang, Y., Photothermal-assisted photocatalytic degradation with ultrahigh solar utilization: Towards practical application. *Chem. Eng. J.* **2020,** *379*, 122382.

19. Yang, Z.; Qi, Y.; Wang, F.; Han, Z.; Jiang, Y.; Han, H.; Liu, J.; Zhang, X.; Ong, W.-J., State-of-the-art Advancements on Photo-Assisted CO_2 Hydrogenation: Recent Progress in Catalyst Development and Reaction Mechanism. *J. Mater. Chem. A* **2020**.

20. Mateo, D.; Albero, J.; García, H., Photoassisted methanation using Cu_2O nanoparticles supported on graphene as a photocatalyst. *Energy Environ. Sci.* **2017,** *10*, 2392-2400.

21. Barrio, J.; Mateo, D.; Albero, J.; García, H.; Shalom, M., A Heterogeneous Carbon Nitride–Nickel Photocatalyst for Efficient Low‐Temperature CO_2 Methanation. *Adv. Energy Mater.* **2019,** *9*, 1902738.

22. Rossetti, I.; Pernicone, N.; Forni, L., Promoters effect in Ru/C ammonia synthesis catalyst. *Appl. Catal. A-GEN* **2001,** *208*, 271-278.

23. Liu, L.; Puga, A. V.; Cored, J.; Concepción, P.; Pérez-Dieste, V.; García, H.; Corma, A., Sunlight-assisted hydrogenation of CO_2 into ethanol and C2+ hydrocarbons by sodium-promoted Co@C

nanocomposites. *Appl. Catal. B* **2018,** *235*, 186-196.

24. Aika, K.-i., Role of alkali promoter in ammonia synthesis over ruthenium catalysts—Effect on reaction mechanism. *Catal. Today* **2017,** *286*, 14-20.

25. Lin, B.; Wei, K.; Ma, X.; Lin, J.; Ni, J., Study of potassium promoter effect for Ru/AC catalysts for ammonia synthesis. *Catal. Sci. Technol.* **2013,** *3*, 1367-1374.

26. Aika, K.-i.; Takano, T.; Murata, S., Preparation and characterization of chlorine-free ruthenium catalysts and the promoter effect in ammonia synthesis: 3. A magnesia-supported ruthenium catalyst. *J. Catal.* **1992,** *136*, 126-140.

27. Tian, Z.; Wang, C.; Yue, J.; Zhang, X.; Ma, L., Effect of a potassium promoter on the Fischer–Tropsch synthesis of light olefins over iron carbide catalysts encapsulated in graphene-like carbon. *Catal. Sci. Technol.* **2019,** *9*, 2728-2741.

28. Chernavskii, P. A.; Kazak, V. O.; Pankina, G. V.; Perfiliev, Y. D.; Li, T.; Virginie, M.; Khodakov, A. Y., Influence of copper and potassium on the structure and carbidisation of supported iron catalysts for Fischer–Tropsch synthesis. *Catal. Sci. Technol.* **2017,** *7*, 2325-2334.

29. Connor, G. P.; Holland, P. L., Coordination chemistry insights into the role of alkali metal promoters in dinitrogen reduction. *Catal. Today* **2017,** *286*, 21-40.

30. Strongin, D.; Somorjai, G. J. P. P. C., Catalytic ammonia synthesis: fundamentals and practice. **1991**.

31. Kita, Y.; Kuwabara, M.; Yamadera, S.; Kamata, K.; Hara, M., Effects of ruthenium hydride species on primary amine synthesis by direct amination of alcohols over a heterogeneous Ru catalyst. *Chem.*

Sci. **2020,** *11*, 9884-9890.

32. Yang, K.; Zhang, Y.; Li, Y.; Huang, P.; Chen, X.; Dai, W.; Fu, X. J. A. C. B. E., Insight into the function of alkaline earth metal oxides as electron promoters for Au/TiO_2 catalysts used in CO oxidation. *Appl. Catal. B* **2016,** *183*, 206-215.

33. Wang, F.; Ueda, W.; Xu, J., Detection and Measurement of Surface Electron Transfer on Reduced Molybdenum Oxides (MoOx) and Catalytic Activities of Au/MoOx. *Angew. Chem. Int. Ed.* **2012,** *51*, 3883-3887.

34. Ye, T.-N.; Park, S.-W.; Lu, Y.; Li, J.; Sasase, M.; Kitano, M.; Tada, T.; Hosono, H., Vacancy-enabled N_2 activation for ammonia synthesis on an Ni-loaded catalyst. *Nature* **2020,** *583*, 391-395.

35. Kojima, R.; Aika, K.-i., Cobalt molybdenum bimetallic nitride catalysts for ammonia synthesis: Part 2. Kinetic study. *Appl. Catal. A-GEN* **2001,** *218*, 121-128.

36. Kitano, M.; Inoue, Y.; Ishikawa, H.; Yamagata, K.; Nakao, T.; Tada, T.; Matsuishi, S.; Yokoyama, T.; Hara, M.; Hosono, H., Essential role of hydride ion in ruthenium-based ammonia synthesis catalysts. *Chem. Sci.* **2016,** *7*, 4036-4043.

37. Horiuchi, Y.; Kamei, G.; Saito, M.; Matsuoka, M., Development of Ruthenium-loaded Alkaline-earth Titanates as Catalysts for Ammonia Synthesis. *Chem. Lett.* **2013,** *42*, 1282-1284.

38. Inoue, Y.; Kitano, M.; Tokunari, M.; Taniguchi, T.; Ooya, K.; Abe, H.; Niwa, Y.; Sasase, M.; Hara, M.; Hosono, H., Direct Activation of Cobalt Catalyst by $12CaO{\cdot}7Al_2O_3$ Electride for Ammonia Synthesis. *ACS Catal.* **2019,** *9*, 1670-1679.

39. Wu, J.; Li, J.; Gong, Y.; Kitano, M.; Inoshita, T.; Hosono, H., Intermetallic Electride Catalyst as a Platform for Ammonia Synthesis.

Angew. Chem. Int. Ed. **2019,** *58*, 825-829.

40. Gong, Y.; Wu, J.; Kitano, M.; Wang, J.; Ye, T.-N.; Li, J.; Kobayashi, Y.; Kishida, K.; Abe, H.; Niwa, Y.; Yang, H.; Tada, T.; Hosono, H., Ternary intermetallic LaCoSi as a catalyst for N_2 activation. *Nat. Catal.* **2018,** *1*, 178-185.

41. Jia, J.; O'Brien, P. G.; He, L.; Qiao, Q.; Fei, T.; Reyes, L. M.; Burrow, T. E.; Dong, Y.; Liao, K.; Varela, M., Visible and Near‐Infrared Photothermal Catalyzed Hydrogenation of Gaseous CO_2 over Nanostructured Pd@ Nb_2O_5. *Adv. Sci.* **2016,** *3*, 1600189.

42. Zhou, S.; Shang, L.; Zhao, Y.; Shi, R.; Waterhouse, G. I.; Huang, Y. C.; Zheng, L.; Zhang, T., Pd Single‐Atom Catalysts on Nitrogen‐Doped Graphene for the Highly Selective Photothermal Hydrogenation of Acetylene to Ethylene. *Adv. Mater.* **2019,** *31*, 1900509.

43. Jia, J.; Wang, H.; Lu, Z.; O'Brien, P. G.; Ghoussoub, M.; Duchesne, P.; Zheng, Z.; Li, P.; Qiao, Q.; Wang, L., Photothermal catalyst engineering: hydrogenation of gaseous CO_2 with high activity and tailored selectivity. *Adv. Sci.* **2017,** *4*, 1700252.

44. Chen, G.; Gao, R.; Zhao, Y.; Li, Z.; Waterhouse, G. I.; Shi, R.; Zhao, J.; Zhang, M.; Shang, L.; Sheng, G., Alumina‐Supported CoFe Alloy Catalysts Derived from Layered‐Double‐Hydroxide Nanosheets for Efficient Photothermal CO_2 Hydrogenation to Hydrocarbons. *Adv. Mater.* **2018,** *30*, 1704663.

45. Mateo, D.; Albero, J.; García, H., Titanium-perovskite-supported RuO_2 nanoparticles for photocatalytic CO_2 methanation. *Joule* **2019,** *3*, 1949-1962.

46. Ulmer, U.; Dingle, T.; Duchesne, P. N.; Morris, R. H.; Tavasoli, A.; Wood, T.; Ozin, G. A., Fundamentals and applications of

photocatalytic CO_2 methanation. *Nat. Commun.* **2019,** *10*, 1-12.

Chapter 7 Nitrogen Reduction to Ammonia by Using Transition Metal Tris(3-tert-butyl-5-methyl-1pyrazolyl)borate Complex as the Catalyst

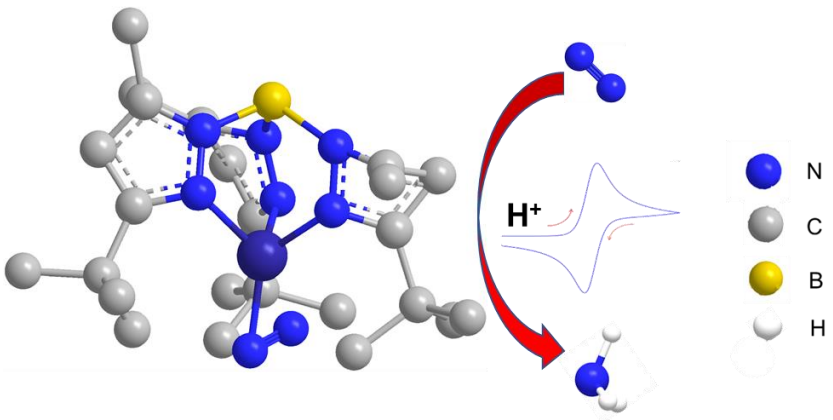

7.1 Introduction

As it has been commented in Chapter 6, ammonia is one of the essential chemicals to sustain human daily activities and currently it is mainly obtained from the Haber-Bosch process, which accounts for almost 96% of the total ammonia production. However, the requirements of high energy input and harsh reaction conditions motivate the researchers to find new available approaches to synthesize the ammonia at milder conditions. With the aim of performing N_2 hydrogenation under mild conditions, considerable research efforts are focused on photocatalysis,[1] electrocatalysis[2] and homogeneous catalysis[3]. Among those research areas, the homogeneous catalysis for the nitrogen reduction reaction has been inspired by the natural azotobacter which can convert atmospheric dinitrogen to nitrogen-contained organic compounds under mild conditions by means of its nitrogenase enzymatic system.

The synthesis of ammonia using metal-complexes as homogeneous catalyst can be dated back to the last century, yet the reported turnover numbers (TON) of ammonia formed were less than 1.[4-6] That means the ammonia formation via those processes was not really catalytic. Even so, a large variety of metal complexes have been screened out for the purpose of nitrogen activation,[7] and a key milestone was reported by Chatt, describing the protonation and reduction of coordinated dinitrogen to ammonia and predicting the mechanism of nitrogenase cycle in Nature, (Scheme 7.1a).[8] It was not until the year 2003 that the first example of catalytic nitrogen reduction to ammonia was reported by Schrock and co-workers, exhibiting TON values larger than 8 using molybdenum catalyst containing tetradentate triamidoamine ligands. In addition, almost all the proposed intermediates by Chatt were isolated in Schrock's work, further manifesting the validity of the Chatt cycle.[9] Later from that one, Nishibayashi and Peter and so on have contributed to this exciting unchartered field with new and efficient nitrogen coordinated dimolybdenum pincer ligand[10] (Scheme 7.1b) and nitrido-iron-triphosphino[11] (Scheme 7.1c) with remarkable selectivity to nitrogen

reduction instead of proton reduction. Especially, a recent work by Nishibayashi and co-works reported a system with TON for ammonia formation over 4000,[12] which is a truly remarkable value depicting the potential for industrialization of such systems.

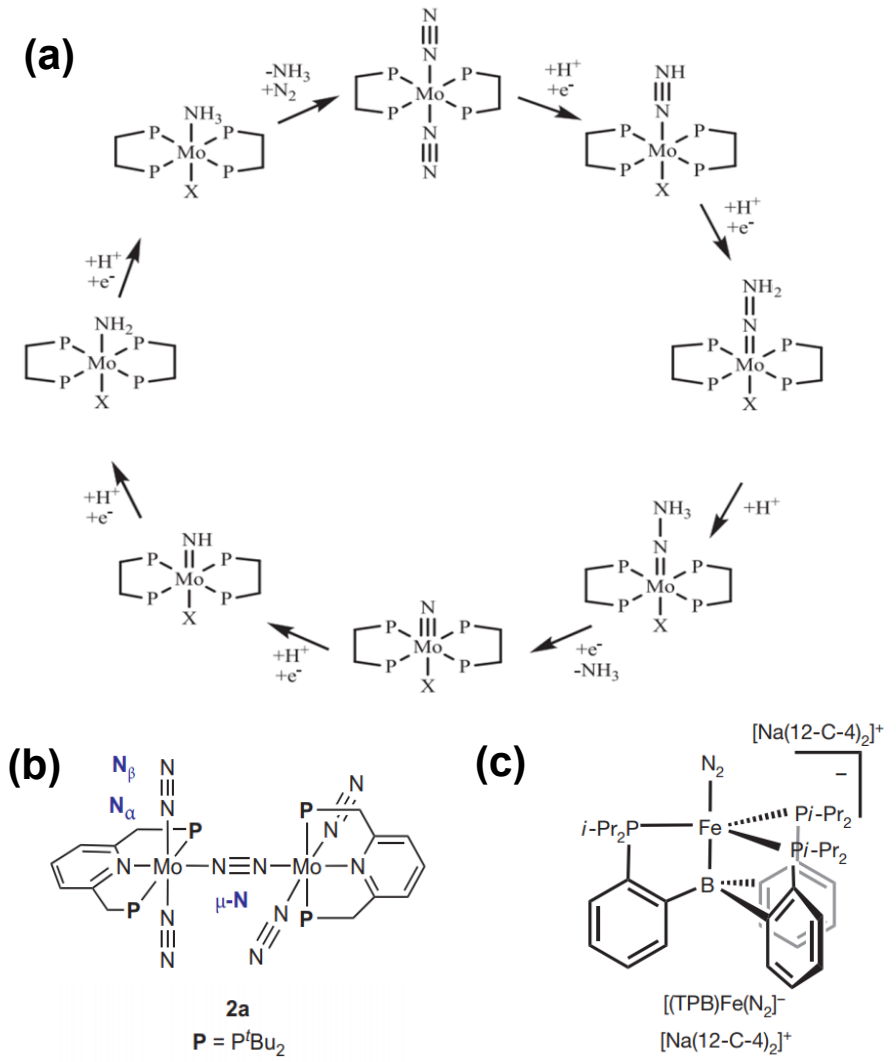

Scheme 7.1. (a) Chatt cycle for N_2 reduction at a mononuclear Mo metal complex, (b) Dimolybdenum–dinitrogen complex bearing PNP (PNP, 2,6-bis(di-tert-butylphosphinomethyl)pyridine) pincer ligands developed by

Nishibayshi and coworkers, (c) $[(TPB)Fe(N_2)][Na(12\text{-crown-}4)_2]$ (TPB, tris(phosphine)borane) complex reported by Peter and co-workers.

It has been reported in the literature that the Co^{+} complex with a derivative of trispyrazolylborate with 3-methyl and 5-tert-butyl substituents in each pyrazolyl unit can bind molecular N_2. Upon complexation with dinitrogen as ligand, a stable mononuclear complex in which a N_2 molecule is bound Co^{2+} is formed.[13] The structure of these cobalt complex with a N_2 molecule could be resolved by single crystal X-ray crystallography, meaning that this species is sufficiently stable to crystallize and also suitable to be manipulated at the ambient.

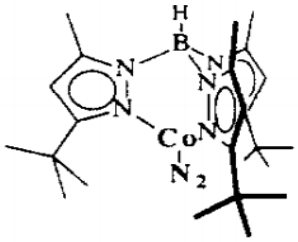

Fig. 7.1 Structure of the dinitrogen coordinated Co-tpzB complex. (tpzB: trispyrazolylborate).

Considering the poor coordinating ability of N_2, the number of complexes containing N_2 as ligand that have been isolated as pure compounds and crystallized is very limited. This is the reason why the structure of the complex tpb-Co-N_2 is so unique.

In homogeneous catalysis by metal complexes, coordination of the substrate to the metal ion of a complex is generally the first step in the reaction mechanism, before undergoing subsequent reactions. Scheme 7.1 presented one of these general reaction mechanisms.

For this reason, it occurred to us that the formation of the N_2 complex of trispyrazolyl Co^{+} under appropriate conditions could be somehow exploited to develop a catalytic cycle as the one indicated in Scheme 7.2, in which the binding with the Co^{2+} ion is the first step to undergo N_2 reduction.

The aim of the present Chapter is to explore the possibility of using the tris(3-methyl-5-*tert*-butyl)pyrazolyl borate as a tridentate ligand in combination with a first-raw transition metal to develop a photo- or electrocatalytic N_2 reduction reaction. The results presented here, even though still preliminary and needing to be completed, show that tris(3-methyl-5-*tert*-butyl)pyrazolyl borate as a ligand of first raw transition metals promotes the electrocatalytic N_2 fixation to NH_3.

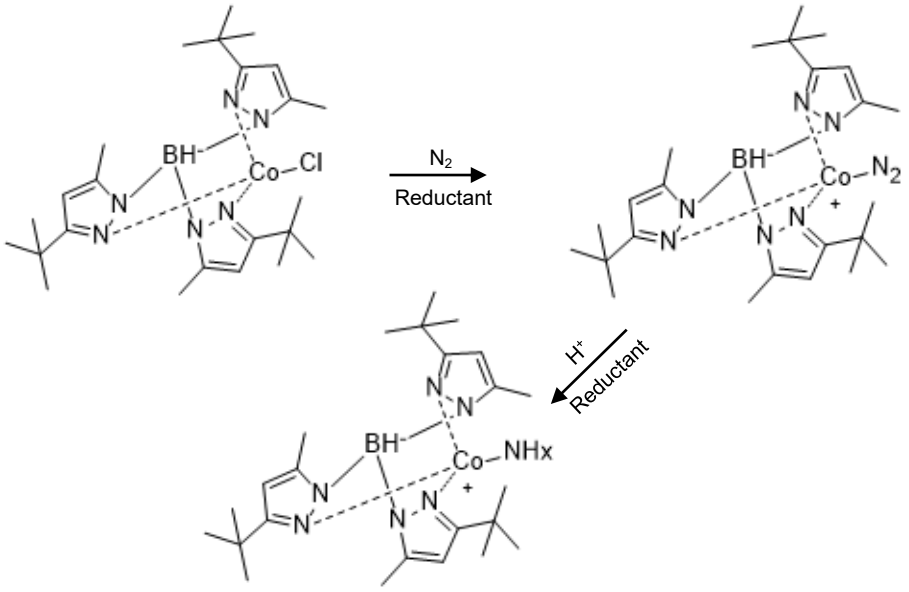

Scheme 7.2. proposed nitrogen coordination and protonation process on a Co-tpzB complex.

7.2 Results and Discussion.

7.2.1 Materials synthesis and characterization

Preliminary studies were performed using commercially available tris(3,5-dimethyl-pyrazolyl) borate ($tpz^{Me}B$) as ligand of Co^{2+} ions. However, due to the small steric hinderance of the less bulk methyl group, Co^{2+} was coordinated with two ligands, forming $Co(tpz^{Me}B)_2$. It seems that in this case, it is very hard to break the Co-hexadentate

coordination by the inert nitrogen molecular, and the cobalt dinitrogen complex could not be formed under the conditions reported in ref. 13.

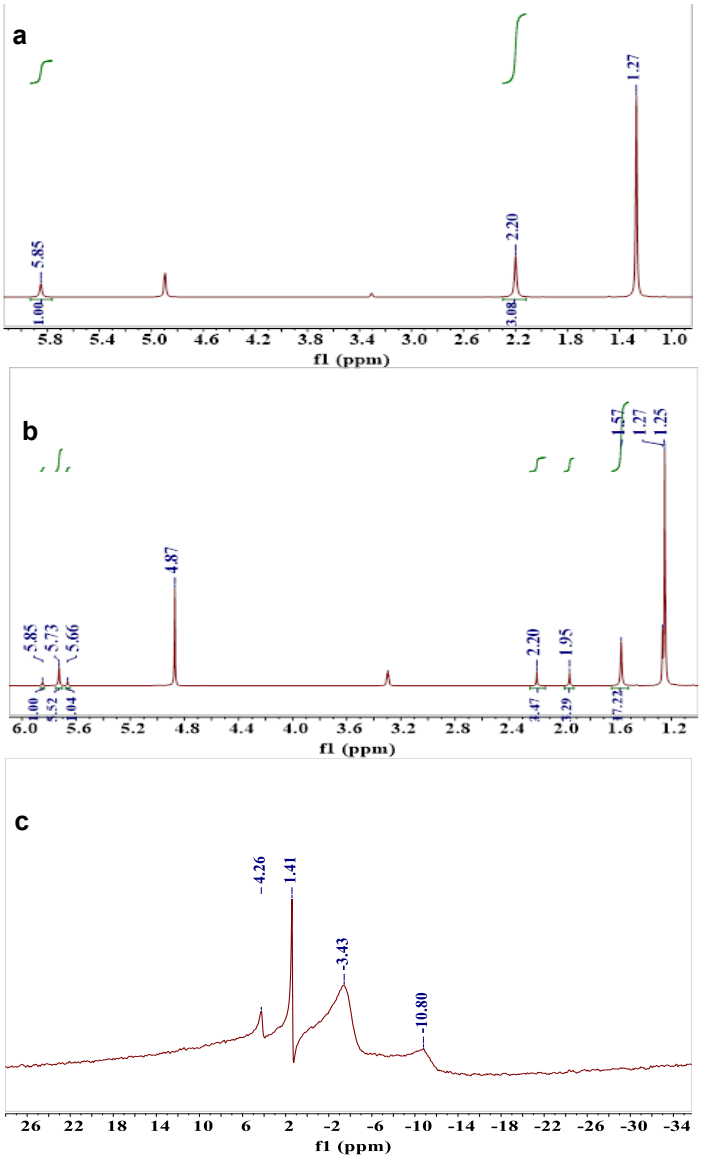

Fig. 7.2. ^{1}H NMR spectra of 3-methyl-5-*tert*-butyl pyrazole (a) and Me^{t}Bu-tpzB (b), and ^{11}B NMR spectrum of Me^{t}Bu-tpzB (c). Solute in MeOD. 3-methyl-5-tert-butyl pyrazole ^{1}H NMR: (300MHz, MeOD), δ=5.85 (s, H, -CH), δ=2.20 (s,

-CH_3), δ=1.27 (s, -$(CH_3)_3$); Me^{t}Bu-tpzB ^{1}H NMR: (300MHz, MeOD): δ=5.73 (s, -CH), δ=1.57 (s, -CH_3), δ=1.25 (s, -$(CH_3)_3$).

As consequence of this failure and based on the study of N_2 complexation with the Co complexes, where it has been suggested that substituents on the pyrazolyl rings play a positive role in increasing the bulkiness of the resulting tpzB ligand, as well as stabilizing the nitrogen coordination by the butyl group electron donating effect, the preparation of tris(3-methyl-5-*tert*-butyl)pyrazolylborate (Me^{t}Bu-tpzB) was undertaken by reaction of 5,5-dimethyl-2,4-hexanedione with hydrazine followed by formation of the B-N bonds as indicated in Equation 7.2. This figure also shows the corresponding ^{1}H NMR spectra of 3-methyl-5-*tert*-butylpyrazole and Me^{t}Bu-tpzB. Figure 7.2 includes the ^{11}B NMR spectrum of Me^{t}Bu-tpzB and the detailed synthesis procedures to obtain Me^{t}Bu-tpb can be found in Chapter 8.

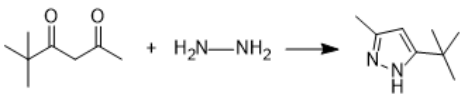

Equation 7.1

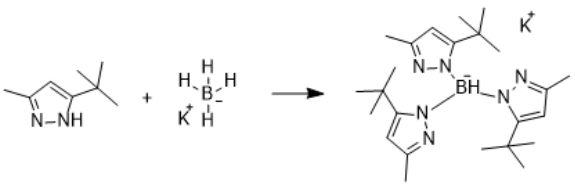

Equation 7.2

Formation of the complex between $CoCl_2$ and Me^{t}Bu-tpzB was firmly supported by by mass spectrometry, where a peak at 552 Da, corresponding to the Me^{t}Bu-tpzB-Co complex with an excellent match between the theoretical and the experimental isotopic distribution pattern for the Me^{t}Bu-tpzB-CoCl complex. ^{1}H NMR spectrum of Me^{t}Bu-tpzbCoCl could also be recorded, confirming the formation of the complex by the dramatic shift to lower fields of the protons corresponding to the C-4 proton of the pyrazolyl ring from 5.85 to 13.18 ppm, and the C-5 tert-Butyl from 1.57 to 8.82 ppm. Fig. 7.3 and Fig. 7.4, respectively, present the corresponding mass and ^{1}H NMR spectra of Me^{t}Bu-tpzB-CoCl.

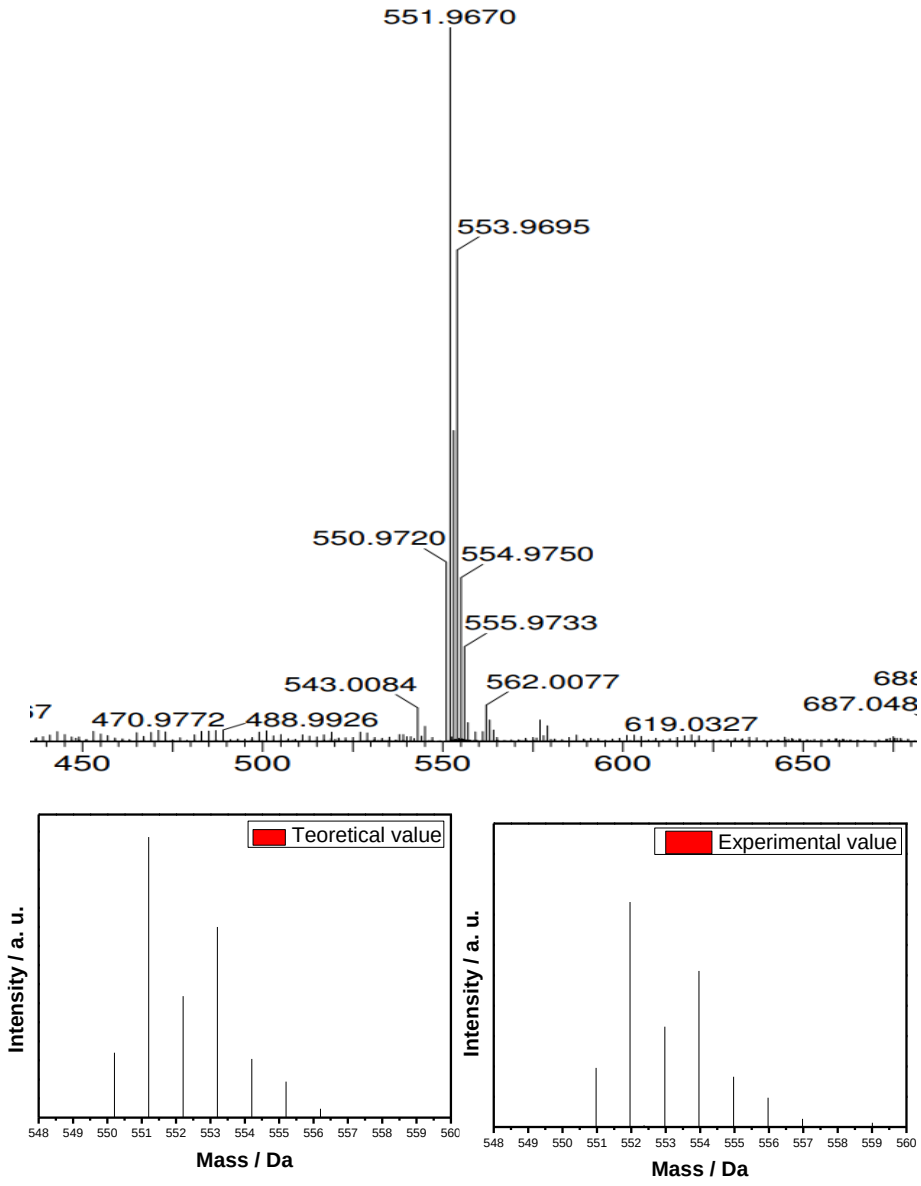

Fig. 7.3 UPLC-Mass spectra of tpzB-$CoCl_2$ and the corresponding theoretical isotopic mass distribution pattern.

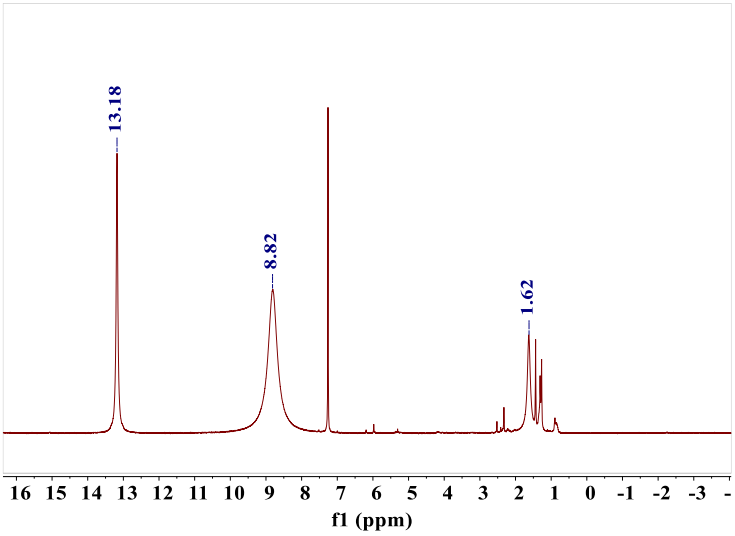

Fig. 7.4 ^{1}H NMR spectrum of tpzB-CoCl in $CDCl_3$. ^{1}H NMR (300MHz, $CDCl_3$, δ=13.18 (s, H, Ar-H), δ=8.82 (s, -$(CH_3)_3$), δ=1.62 (s, -CH_3).

7.2.2 Nitrogen reduction by conventional homogeneous catalysis

Following also a report on the stoichiometric N_2 reduction to NH_3 promoted by molybdenum complexes and using a cocktail of cobaltocene as reducing organometallic agent and lutidinium as proton source,[14] a series of experiments were carried out with the Me^{t}Bu-tpzB-CoCl complex replacing the Mo phosphine pincer complex initially reported. The system is presented in Fig. 7.5, in which also the amount of H_2 and NH_3 formed in the experiments is also indicated. Although some NH_3 (0.21 μmol) was detected at 24 h of reaction time, the major product observed was H_2 (77 μmol) from the direct reduction of H^+ by cobaltocene and further studies were not pursued.

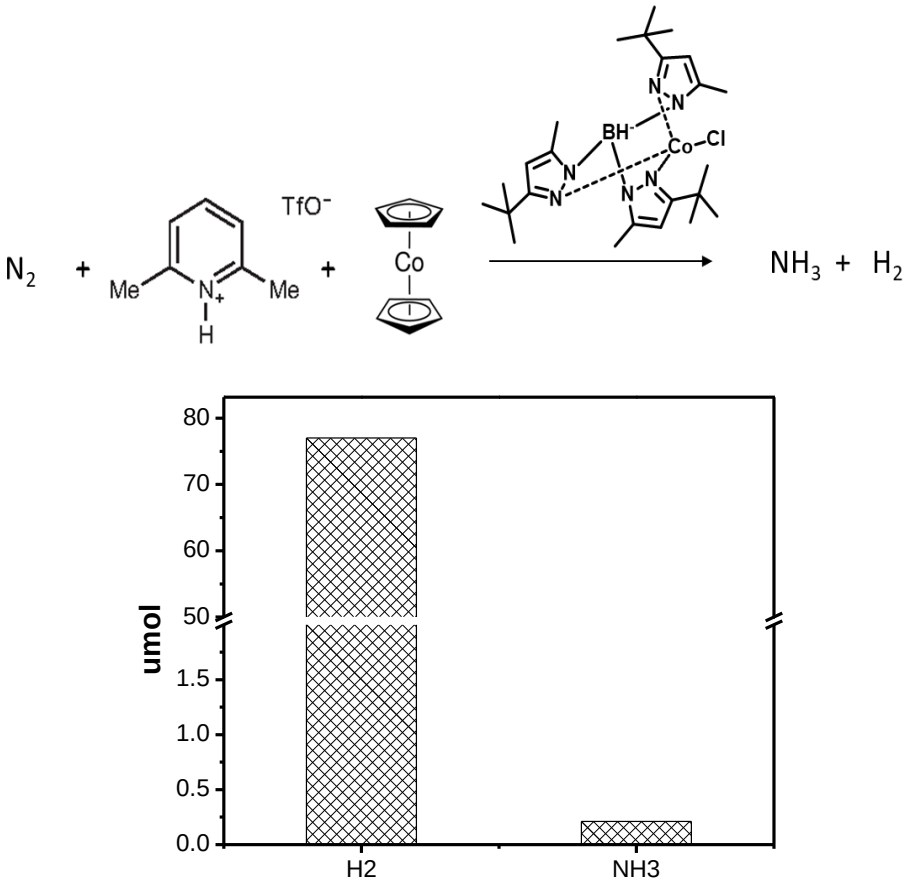

Fig. 7.5 Heterogeneous nitrogen fixation system using tpzB-CoCl as the catalyst and the consequent products evolved.

7.2.3 Nitrogen fixation by photocatalysis

Attempts to promote photocatalytic NH_3 by N_2 reduction using Me^{t}Bu-tpzB-CoCl complex as photocatalyst were performed using N,N,N',N'-tetramethyl-*p*-phenylenediamine as sacrificial electron donor in THF or THF-MeOH as solvent. Evolution of H_2 in a significant amount was observed and although formation of NH_3 was detected, it was in negligible amounts. The results are presented in Figure 7.6.

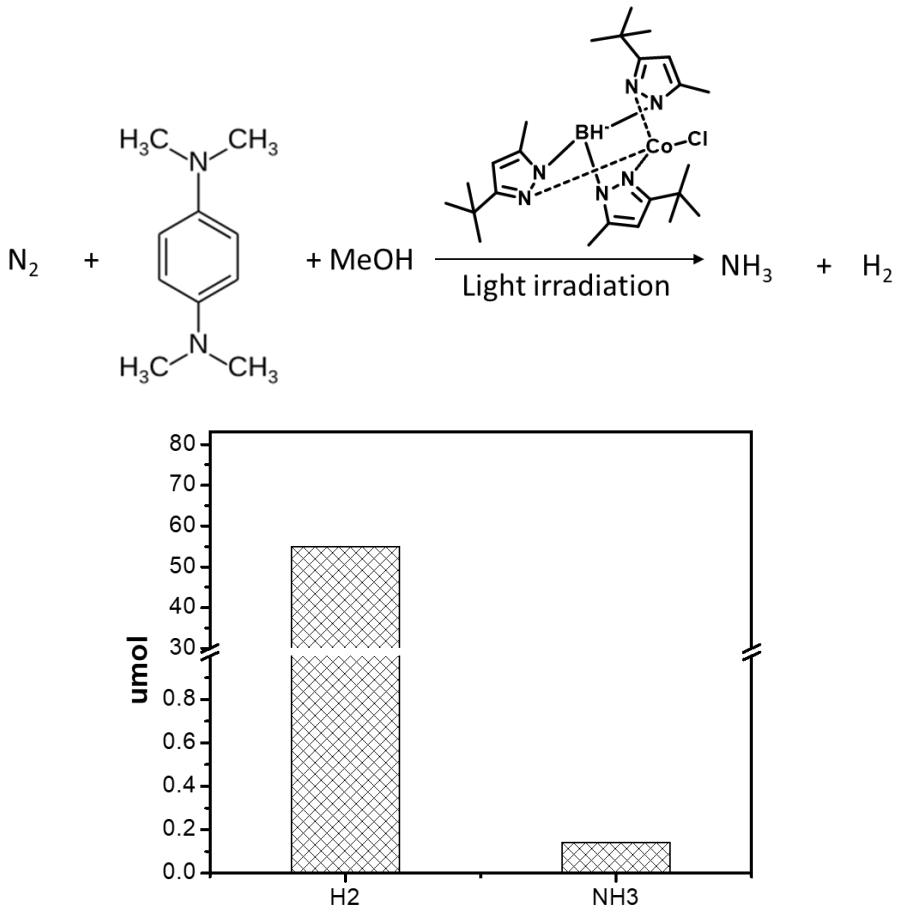

Fig. 7.6 Results of the photocatalytic nitrogen fixation using Me^{t}ButpzB-CoCl as the catalyst and the photosensitizer.

Similar photocatalytic experiments adding $Ru(bpy)_3^{2+}$ as photosensitizer to increase light harvesting and replacing the tetramethyl-p-phenylenediamine by cobaltocene as electron donor agent also form considerably higher amounts of hydrogen in comparison with ammonia. The system and results are indicated in Figure 7.7.

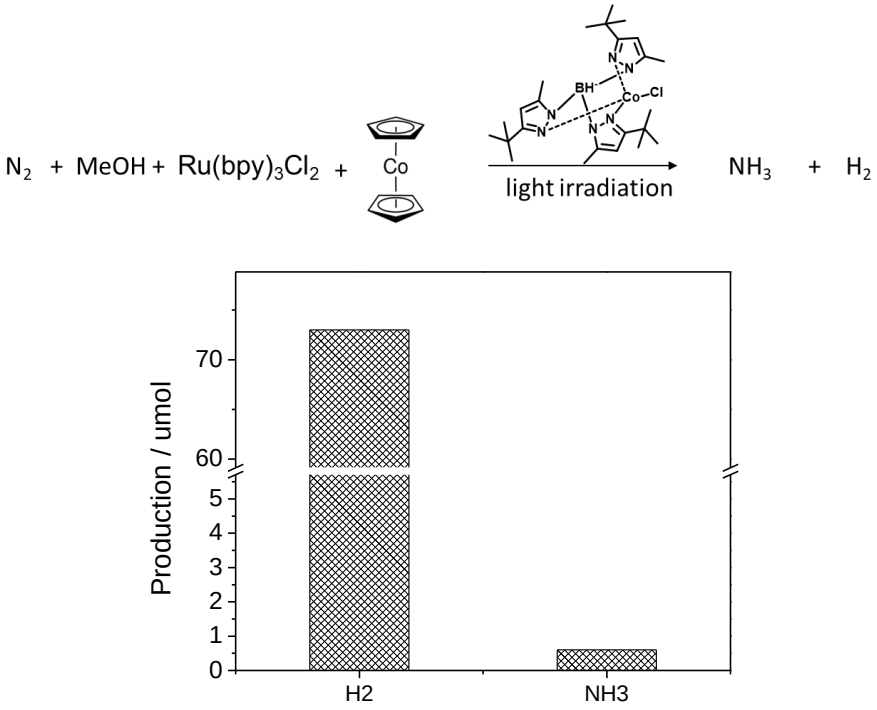

Fig. 7.7 Results of the attempted photocatalytic nitrogen fixation system using tpzB-CoCl as the catalyst and $Ru(bpy)_3^{2+}$ as the photosensitizer, and the consequent products evolved.

The above results clearly show that using conventional catalysis or photocatalysis using Me^{t}Bu-tpzB-CoCl as photocatalyst, the main product is hydrogen and only trace amounts of ammonia can be detected. Based on those results, it is reasonable to hypothesize that to optimize the selectivity towards dinitrogen reduction instead of hydrogen evolution, it is better to rationally adjust reduction potential in the reaction system. Thus, electrochemical nitrogen reduction using the Me^{t}Bu-tpzB-$CoCl_2$ was studied.

7.2.4 Nitrogen reduction by electrocatalysis

Electrochemical measurements were carried out in THF as solvent using $LiClO_4$ as electrolyte. Formation of NH_3 with a Faradaic efficiency

of 9.9 % and 6.8 % at a bias voltage of -1.3 or -1.8 V vs Fc/Fc^+, respectively, was determined, being able to detect in trace amounts the ammonia after 2 h reaction (1.6 µg and 4.0 µg under -1.3 and -1.8 V, respectively). Cyclic voltammetry measurements also agree with the conclusion of the electrochemical reduction of N_2 in the presence of Me^{t}Bu-tpzB-CoCl complex by comparing the voltammograms under Ar or under N_2 atmosphere. A summary of this electrochemical study is provided in Fig. 7.8.

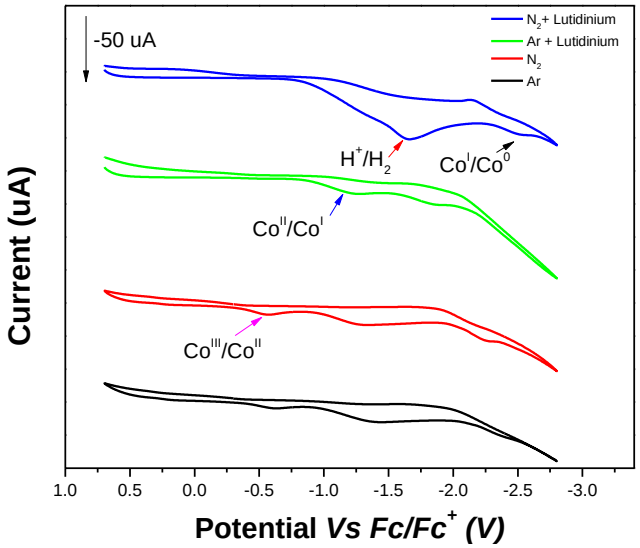

Fig. 7.8. Cyclic voltammograms of Me^{t}Bu-tpzB-$CoCl_2$ complex under different conditions as indicated in the plot. Conditions: 0.1M $LiCO_4$ in THF; Scan rate, 0.1 V/s.

Thus Me^{t}Bu-tpzB-CoCl complex exhibit in the cathodic reduction region the presence of three peaks that can be attributed to the Co^{3+} reduction to Co^{2+} at -0.57 V, Co^{2+} to Co^+ at -1.40 V and Co^+ to Co(0) at -2.27 V (*Vs* Fc^+/Fc). Upon addition of lutidinium as proton source under Ar atmosphere observation of a peak at -1.75 V attributable to H_2 evolution was observed. Under N_2 atmosphere, the intensity of this peak H_2 evolution increased considerably and overlaps with that of Co^{2+}/Co^+, a fact that can be attributed to the interaction with dinitrogen as previously indicated in Scheme 7.2.

In an attempt to further promote the electrocatalytic N_2 reduction using Me^{t}Bu-tpzB as ligand, other first raw transition metals were also screened.

Using Me^{t}Bu-tpzB-FeCl complex as electrocatalyst, higher NH_3 evolution was determined by the indophenol colorimetric titration. In an electrolytic experiment at -1.8 V vs. Fc/Fc^+ in a two-compartment cell and using Pt wire as anode, a production of 8.3 μmol NH_3 was reached.

Table 7.1 Ammonia production results using Me^{t}Bu-tpzB ligand coordinated with different transition metal center under given conditions.

Catalyst	Co-Tp			V-Tp	Cr-Tp	Fe-Tp	Ni-Tp
Condition	-1.8 V	Cobalto-cene	Photo-catalysis	-1.8 V	-1.8 V	- 1.8 V	-1.8 V
Amount of ammonia	4 ug (2h)	3 ug (24h)	2.5 ug (24h)	463 ug (2h)	7.4 ug (2h)	142 ug (2h)	1ug (2h)

Encouraged by these results, analogous electrtocatalytic measurements were carried out in the two-compartment cell using Me^{t}Bu-tpzB metal complexes of V^{3+}, Cr^{3+} and Ni^{2+}. The results are summarized in Table 7.1. This Table also contains data of the photocatalytic experiments previously commented. As it can be seen there, the production of NH_3 varied depending on the metal, the best results being obtained with Me^{t}Bu-tpzB-V complex for which a notable NH_3 production was reached. This production after 2 h using Me^{t}Bu-tpzB-VCl_2 complex as catalysts at -1.8 V vs. Fc/Fc^+ was large enough to be detectable by 1H NMR spectroscopy as shown in Figure 7.9.

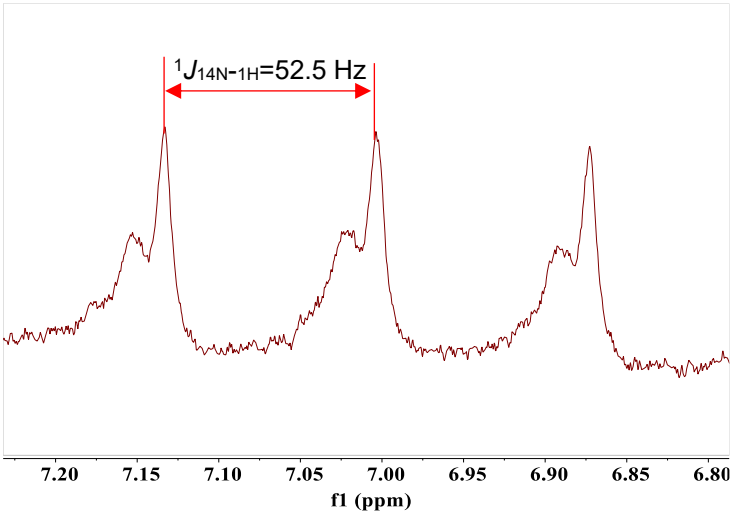

Fig. 7.9 ^{1}H NMR spectrum of ammonia produced using Me^{t}Bu-tpzB-V complex as the catalyst (reaction condition: 0.1 M $LiClO_4$ as electrolyte under -1.8 V *vs* Fc^{2+}/Fc). The triplet peak with coupling constant of 52.5 Hz indicates the formation of NH_3.

7.3 Conclusions.

It has been demonstrated that that first raw transition metals of Me^{t}Bu-tpzB ligand are suitable electrocatalysts for N_2 reduction to NH_3. The process is highly dependent on the nature of the metal, being V^{3+} the most efficient catalyst. Future experiments to study the active center and the intermediates, as well as confirming the ammonia nitrogen source are necessary to complete the work.

In contrast to the electrocatalytic N_2 fixation, photocatalysis using these Me^{t}Bu-tpzB metal complexes and an electron donor tends to promote the generation of H_2, rather than N_2 reduction. Combination with a dye to increase visible light absorption increases somewhat the activity, but the selectivity still favors largely H_2 formation. It would be necessary to find a suitable medium and conditions that disfavors H_2 evolution.

7.4 References

1. Zhang, G.; Sewell, C. D.; Zhang, P.; Mi, H.; Lin, Z., Nanostructured photocatalysts for nitrogen fixation. *Nano Energy* **2020,** *71*, 104645.

2. Zhang, L.; Chen, G.-F.; Ding, L.-X.; Wang, H., Advanced Non-metallic Catalysts for Electrochemical Nitrogen Reduction under Ambient Conditions. *Chem. Eur. J.* **2019,** *25*, 12464-12485.

3. Chalkley, M. J.; Drover, M. W.; Peters, J. C., Catalytic N_2-to-NH_3 (or -N2H4) Conversion by Well-Defined Molecular Coordination Complexes. *Chem. Rev.* **2020,** *120*, 5582-5636.

4. Chatt, J.; Pearman, A.; Richards, R. J. N., The reduction of mono-coordinated molecular nitrogen to ammonia in a protic environment. **1975,** *253*, 39-40.

5. Takahashi, T.; Mizobe, Y.; Sato, M.; Uchida, Y.; Hidai, M., Preparation and properties of molybdenum- and tungsten-dinitrogen complexes. 10. Conversion of ligating dinitrogen into hydrazine with hydrazido(1-) complexes as intermediates. *J. Am. Chem. Soc.* **1979,** *101*, 3405-3407.

6. Takahashi, T.; Mizobe, Y.; Sato, M.; Uchida, Y.; Hidai, M., Protonation reactions of molybdenum and tungsten dinitrogen complexes with halogen acids. Hydride hydrazido(2-) and diazenido complexes as intermediate stages of reduction. *J. Am. Chem. Soc.* **1980,** *102*, 7461-7467.

7. Fryzuk, M. D.; Johnson, S. A., The continuing story of dinitrogen activation. *Coord. Chem. Rev.* **2000,** *200-202*, 379-409.

8. Chatt, J.; Dilworth, J. R.; Richards, R. L., Recent advances in the chemistry of nitrogen fixation. *Chem. Rev.* **1978,** *78*, 589-625.

9. Yandulov, D. V.; Schrock, R. R., Catalytic Reduction of Dinitrogen

to Ammonia at a Single Molybdenum Center. *Science* **2003,** *301*, 76-78.

10. Arashiba, K.; Miyake, Y.; Nishibayashi, Y., A molybdenum complex bearing PNP-type pincer ligands leads to the catalytic reduction of dinitrogen into ammonia. *Nat. Chem.* **2011,** *3*, 120-125.

11. Anderson, J. S.; Rittle, J.; Peters, J. C., Catalytic conversion of nitrogen to ammonia by an iron model complex. *Nature* **2013,** *501*, 84-87.

12. Nakajima, K.; Toda, H.; Sakata, K.; Nishibayashi, Y., Ruthenium-catalysed oxidative conversion of ammonia into dinitrogen. *Nat. Chem.* **2020,** *12*, 424-424.

13. Egan, J. W.; Haggerty, B. S.; Rheingold, A. L.; Sendlinger, S. C.; Theopold, K. H., Crystal structure of a side-on superoxo complex of cobalt and hydrogen abstraction by a reactive terminal oxo ligand. *J. Am. Chem. Soc.* **1990,** *112*, 2445-2446.

14. Tanabe, Y.; Nishibayashi, Y., Comprehensive insights into synthetic nitrogen fixation assisted by molecular catalysts under ambient or mild conditions. *Chem. Soc. Rev.* **2021**.

Chapter 8 Experimental Section

8.1 Material Synthesis

8.1.1 Chemicals

All solvents and reagents were used without further purification. MilliQ water was obtained using a IQ 7000 purifying system. Ethanol Absolute (analytical grade), anhydrous tetrahydrofurane 99.99 % (THF), diethyl ether (puriss. p.a. ACS reagent dried 00.5 % GC 0.0075 % water), hexane (HPLC grade), toluene (chromasolvr for HPLC 99.9 %), N,N-dimethylformamide anhydrous 99.8 % (DMF) and acetone were purchased from Scharlau. Hydrazobenzene (< 10 % azobenzene), tetradecane (≥ 99 %), aqueous hydriodic acid (HI, 55 wt%), aqueous hydrochloric acid (HCl, 37 wt%), lead iodide (99.999 % trace metals basis) (PbI2), cis-stilbene (96 %), tetraethyl orthosilicate (TEOS, reagent grade 98%), *cis*-stilbene (96 %), *trans*-stilbene (96 %), benzoyl peroxide (75%), lead bromide (99.999 % trace metals basis, $PbBr_2$), potassium iodide (99.5%, KI), deuterium oxide (D_2O), ruthenium chloride hydrate ($RuCl_3 \cdot xH_2O$, 98%), strontium titanate ($SrTiO_3$), sodium nitroprusside dihydrate ($Na_2[Fe(CN)_5NO] \cdot 2H_2O$, 99%), phenol (99.9%), sulfuric acid (95-98%, ACS REAGENT), potassium nitrate (KNO_3, 99%), cesium carbonate (Cs_2CO_3, 99%), sodium citrate tribasic ($HOC(COONa)(CH_2COONa)_2$, 99%) and trans-stilbene (96 %) were purchased from Sigma Aldrich. NaOH micro pearls (98 %) were purchased from ACROS. Octadecyl trimethoxy silane (ODTMS, 97%) and perfluoro decyl triethoxy silane ((FTS, 98%) were purchased from ABCR. Sodium hypochlorite solution (NaClO, 11-14wt%) was purchased from Fisher Chemical™. Nitrogen gas (N_2, 99.99%) and hydrogen gas (H_2, 99.99%) were purchased from Abello Linde SA.

8.1.1 Synthesis of BZ-3.1

Commercial hydrazobenzene (1 g) was dissolved in ethanol/water (60 mL/40 mL) solution with stirring, followed by adding 10 mL concentrated HCl (~37 wt%). After 10 mins reaction, the solution was concentrated under reduced pressure evaporation by about one third of the initial volume and benzidine precipitate was obtained by

neutralizing the solution with 1 M NaOH. The final obtained product was isolated by filtration and washed with H_2O/EtOH. The purity of benzidine was confirmed by ^1H NMR and IR spectroscopy.

8.1.2 Synthesis of BZI-3.1

Benzidinium diiodide (**BZI-3.1**) was obtained by protonation of benzidine. Specifically, 0.92 g of benzidine (5 mmol) was dissolved in 20 mL THF under stirring at 0 ^oC (ice bath), then 1.6 mL concentrated hydroiodic acid aqueous solution (55 wt%) was added to the solution drop by drop. After 2 h of reaction, **BZI-3.1** was precipitated by adding 20 mL of cold diethyl ether into the solution. The final product was filtered, washed with diethyl ether and characterized by IR spectroscopy and combustion elemental analysis.

8.1.3 Synthesis of BHP-3.1

BHP-3.1 either as a fine powder or as single macro crystal was synthesized. The preparation method for fine powder is as follows. PbI_2 (184 mg, 0.4 mmol) and **BZI-3.1** (88 mg, 0.2 mmol) were dissolved in 4 mL DMF under stirring. Then 10 mL of toluene were added to the precursors solution to precipitate the perovskite. The as-obtained **BHP-3.1** fine powder was isolated by filtration and washed with diethyl ether, and finally, dried under vacuum.

Single crystals of **BHP-3.1** were obtained by slow diffusion of toluene vapor into the perovskite precursor solution. Specifically, the afore mentioned perovskite precursor solution was diluted to 0.05 M in a vial, and then put into a sealed bottle which was filled with some amount of toluene. The single crystal can be formed in the vial within 1 day.

8.1.4 Surface silylation of BHP-3.1

Surface silylation was performed in toluene under argon atmosphere. Specifically, **BHP-3.1** (200 mg) was dispersed in toluene (20 ml) by sonication in a 50 ml flask, followed by adding a desired

amount of silylating reagent. Then, the dispersion was kept stirring overnight at 50 ^{o}C under inert atmosphere. The final product was isolated by centrifugation and dried in air for further use.

8.1.5 Synthesis of SA-5.1

Styryl ammonium (**SA-5.1**) was obtained by low protonation of the amino group. To avoid polymerization of double bond during protonation process, acetone/dry ice bath was applied to cool the solution. Typically, 1 g amino-styrene was added to 20 mL THF under stirring and the insoluble impurities were removed by filtration. Then, 1.35 mL concentrated hydriodic acid was added to the solution dropwise. **SA-5.1** was precipitated by adding diethyl ether after 2 h reaction under acetone/dry ice bath, and finally washed with 400 ml cold diethyl ether. The product was characterized by IR and ^{1}H NMR spectroscopy after dry under vacuum overnight.

8.1.6 Synthesis of HP-5.1

For the synthesis of **HP-5.1**, 230.5 mg (0.5 mmol) of PbI_2 was added to 1 mL concentrated hydriodic acid aqueous solution (55 wt%) under stirring until all the solid was dissolved, then 1 mL of **SA-5.1** solution (0.5 M) was added to the previous solution dropwise. The desired perovskite appeared as precipitate immidiately. The solid was collected and washed with diethyl ether and dried under vacuum for overnight.

8.1.7 Synthesis of material PHP-5.1 from HP-5.1

PHP-5.1 was obtained by radical-assisted copolymerization with extra addition of styrene. Specifically, material **HP-5.1** (100 mg) was dispersed in 20 mL hexane, followed by adding 9 mg (~ $2*10^{-6}$ M) of benzoyl peroxide and 0.02 mmol of styrene. After 5 h reaction at 50^{o}C under argon atmosphere, the **PHP-5.1** production was washed with diethyl ether and dried under vacuum for overnight.

8.1.8 Synthesis of Ru(x)-STO

Ru(x)-STO samples were prepared by impregnation of $SrTiO_3$ and $RuCl_3$ precursors. Specifically, commercial $SrTiO_3$ (1 g) was dispersed in 20 mL MilliQ water by strong sonication for 30 min, followed by adding desired amounts of ruthenium chloride precursor in the slurry (The sample adding 1 wt %, 2.5 wt% and 5 wt% of ruthenium content). Then, the slurry was subjected to heating at 70 ºC under gently stirring to evaporate water and further dried at 100 ºC overnight. Afterwards, the samples were calcinated at 250 ºC for 2 h (5 ºC/min) and subsequently reduced with H_2 at 350 ºC for 2 h (5 ºC/min). Finally, the samples were thoroughly washed with MilliQ water until no chloride ions were detected in the filtrate (by using $AgNO_3$ solution as the indicator). Finally, dried in oven the solid overnight.

8.1.9 Synthesis of Cs(y)Ru(x)-STO

Cs(y)Ru(x)-STO samples were prepared by the impregnation method. 500 mg **Ru(x)-STO** sample were dispersed in MilliQ water by sonication. Then, the wanted amount of Cs_2CO_3 to obtain the required Cs/Ru ratio was added to the dispersion. Water was slowly evaporated at 70ºC under gently stirring. Then, the as-obtained catalysts were dried in oven overnight.

8.1.10 Synthesis of 3-methyl-5-tert-butyl-pyrazole

3-Methyl-5-tert-butyl-pyrazole was synthesized by reacting an excess of hydrazine with 2,2-dimethyl-3,5-hexanedione in methanol. The process is known as Knorr pyrazole synthesis. The solid product was isolated from the solvent by methanol reduced pressure evaporation, and then purified by sublimation.

8.1.11 Synthesis of potassium hydridotris(3-methyl-5-tert-butyl)pyrazolyl borate (Me^{t}Bu-tpzB)

Me^{t}Bu-tpzB was prepared by heating a mixture of potassium borohydride and 3-methyl-5-tert-butyl-pyrazole at a mole ratio 1:5.4 at 200 ºC. The extent of reaction was monitored by the volume of

hydrogen evolved and the reaction ceased when 3 equivalent H_2 from potassium borohydride were produced. Excess of unreacted pyrazole species was removed by sublimation.

8.1.12 Synthesis of Me^{t}Bu-tpzB transition metal complexes (Metal=Co, Fe, Cr and Ni)

A solution of Me^{t}Bu-tpzB in methanol (0.2 M, 5 mL) was added to a solution of MCl_2 in methanol (0.4 M, 5 mL) under stirring. The immediately formed precipitate was isolated by filtration and washed with methanol, then dried under vacuum.

8.1.13 Synthesis of vanadium Me^{t}Bu-tpzB complex

Vanadium MetBu-tpzB complex was synthesized using a standard Schlenk line. Typically, 70 mg VCl_3 was refluxed in THF at 70 °C for 24 hrs, followed by addition of 300 mg Me^{t}Bu-tpzB and the mixture was kept under heating for another 14 h. The product was collected by removing the solvent under vacuum.

8.2 Reaction Procedure

8.2.1 Photoinduced cis-to-trans-isomerization of stilbene

The photoinduced isomerization reactions were performed under visible light irradiation using a 300 W Xe lamp equipped with 450 nm filter. Specifically, cis-stilbene (0.25 mmol) was dissolved in 1.5 mL of toluene and 0.15 mL tetradecane was added to the above solution as the internal standard to quantify the amount of cis-stilbene. The amount of catalyst used was 2 wt% (4.1 mg). Prior to irradiation, the reactor was purged with argon to remove ambient oxygen. The course of cis-stilbene conversion was followed periodically by injecting aliquots of the reaction mixture in the GC. The final products were isolated and characterized by 1H NMR spectroscopy.

8.2.2 Photocatalytic H_2 evolution for the stability test of material HP-5.1 and PHP-5.1

Evaluation of light and oxygen stability of **HP-5.1** and **PHP-5.1** was conducted by measuring the amount of hydrogen evolution in the course of the irradiation time. The photo reactor was a cubic aluminium sealed reactor (total volume 100 mL) with a quartz cover allowing light pass through and inlet/outlet bearing independent valves that were adapted to a manometer to determine pressure. 20 mg of perovskite was first placed in the reactor. Then the system was purged with argon or filled with a certain amount of oxygen until reach a final pressure of 1.3 atmosphere. A Hamamatsu Xenon lamp (235 - 850 nm) with a focused intensity on the flask of 1080 mW/cm^2 was used as a UV-vis light source. A UV cut-off filter (>400 nm) was employed to carry out the experiments with UV filtered light.

A 0.25 mL sample of the generated gas was collected periodically and the hydrogen content was analyzed by gas chromatography (GS-MOL 15 m column ID 0.55 mm TCD from J&W Scientific).

8.2.3 Photo-assisted nitrogen fixation with hydrogen for ammonia

All the catalysts before test were activated with H_2 at 350 ^oC for 2 h to fully reduce ruthenium species. Photothermal ammonia synthesis was performed in a customized fixed bed borosilicate glass reactor mounted with K-type thermocouple and heating mantle (as shown in Scheme 8.1). Light irradiation was introduced from the top of the reactor through a quartz tube, in which the optical fiber can be placed. The feeding gases were purified by passing in sequence through sulfuric acid, water and $CaCl_2$, and then passed through a spiral preheater before introducing to the reactor. Produced ammonia were collected by using 5 mM sulfuric acid (reservoir 1) and protected from ambient ammonia contamination by reservoir 2. A control experiment with only H_2 feeding was performed before each batch of ammonia synthesis reaction to eliminate any ammonia contamination from the system.

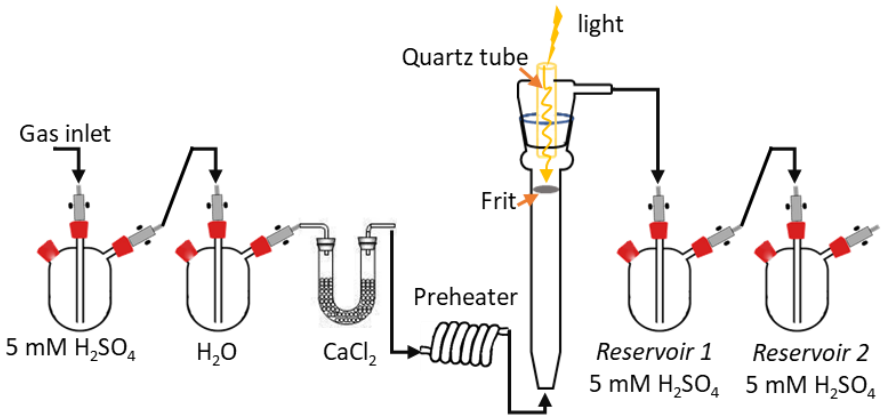

Scheme 8.1. Schematic diagram of photothermal ammonia synthesis system.

8.2.4 ^{15}N isotopic experiments

$^{15}N_2$ isotopic experiments for photocatalytic nitrogen hydrogenation by H_2 were performed in a closed circulation system modified from set-up shown in Fig 8.1 by joint the reservoir 2 and gas inlet with a Richardson rubber pear. Before charging H_2 and $^{15}N_2$, the system was thoroughly purged with argon. The formation of $^{15}NH_3$ product in reservoir 1 was confirmed by ^1H NMR spectroscopy.

8.2.5 Photocatalytic/conventional N_2 reduction by using metal Me^{t}Bu-tpzB as the catalyst

The reaction was performed using a customized cylindrical quartz reactor mounted with a manometer that determines the pressure inside the reactor, and an inlet/outlet bearing valves (see in Fig. 8.1). Specifically, 20 mg of metal complex catalyst was dispersed in 18 mL THF, followed by adding 120 mg of lutidinium triflate as the proton source and 2 mL methanol as the hole scavenger. Before being subjected to the Xenon lamp irradiation, the reactor was thoroughly purged with argon. After the reaction, the gas phase was quantified by MicroGC. The produced ammonia was separated from the solution by distillation and trapped by 5 mM H_2SO_4 solution (see Scheme 8.2).

The conventional homogeneous catalysis for nitrogen reduction reaction was performed using the same set-up as that for the photocatalytic reactions. Instead of using a combo of light and scavenger, cobaltocene was adopted as the reductive reagent.

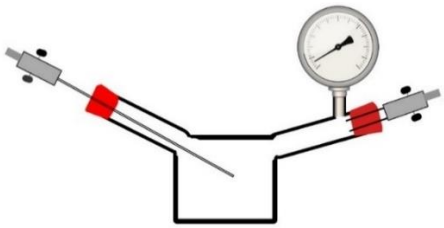

Fig. 8.1 Drawing of the photoreactor used for photocatalytic nitrogen reduction reaction.

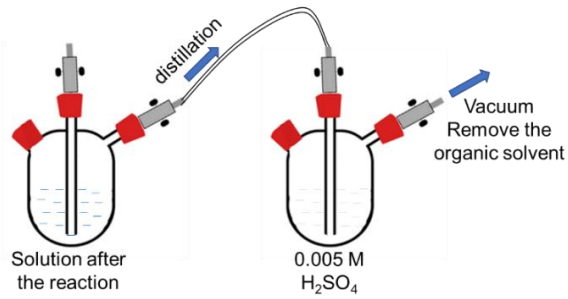

Scheme 8.2 Illustration the distillation process for trapping ammonia in acid solution after the reaction

8.2.6 Electrochemical nitrogen reduction by using Me^{t}Bu-tpzB as electrocatalyst

The electrochemical nitrogen reduction was performed in a H cell having a porous frit to separate the cathode and anode parts, using Pt wire, carbon paper and silver wire as the counter, working electrode and pseudo-reference, respectively. 40 mL of $LiClO_4$ (0.1 M) solution in acetonitrile/tetrahydrofuran (mole ration1:1) containing also 10 mg of catalyst and 400 mg lutidinium triflate as the proton source was used as the electrolyte. Before the reaction, the reference electrode was calibrated by measuring the ferrocene redox potential (as shown in Fig.

8.3). For the ammonia formation test, -1.8 V *vs* Fc^{+}/Fc bias potential was applied and the reaction was kept for 2 h before subjecting to the distillation process, as described in Scheme 8.2.

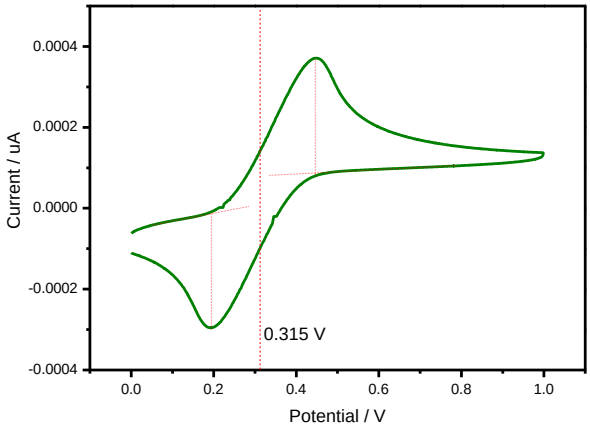

Fig. 8.2 Cyclic voltammetry of ferrocene in CH_3CN/THF with 0.1 M $LiClO_4$ as the electrolyte with indication of the corresponding redox potential.

8.3 Characterization Techniques

8.3.1 Transmission Electron Microscopy (TEM)

TEM images were made with a Philips CM300 FEG microscope operating at 200 kV, coupled with an X-Max 80 energy dispersive X-ray detector (EDX) (Oxford instruments). The microscope is equipped with the STEM unit, the dark-field and high-angle field image detectors (HAADF) that facilitate the observation of phase contrast with different atomic number

For the sample preparation, after bath sonication, a drop of well-dispersed solid of the sample in dichloromethane was deposited on copper or nickel grid coated with a carbon film, and then dried in vacuum before implement the characterization.

8.3.2 Scanning Electron Microscopy (SEM)

SEM images was collected with a JEOL JSM 6300 apparatus equipped with an X-MAX detector of OXFORD INSTRUMENTS. The

elemental analysis by EDX was performed with an Oxford instruments detector coupled to these microscopes.

The samples for SEM were prepared by adhering the specimens on a sample holder that is covered with a double-sided conductive tape.

8.3.3 X-Ray Diffraction (XRD)

XRD patterns were collected with a Shimadzu XRD-7000 diffractometer by using Cu Kα radiation (λ=1.5418 Å), operating at 40 kV and 40 mA at a scanning speed of 10^{o} per min in the 2–90^{o} 2θ range

8.3.4 X-Ray Photoemission Spectroscopy (XPS)

XPS were measured on a SPECS spectrometer equipped with a Phoibos 1509MCD detector using a nonmonochromatic X-ray source (Al and Mg) operating at 200 W. The samples were evacuated in the prechamber of the spectrometer at 1×10^{-9} mbar. The measured intensity ratios of the components were obtained from the area of the corresponding peaks after nonlinear Shirley-type background subtraction and corrected by the transition function of the spectrometer. The work function of the apparatus was calibrated with Ag and Au with a value 4.2440 eV.

8.3.5 UV-Vis Absorption Spectroscopy

UV-VIS measurements in solution were carried out in a Cary 50 spectrometer of Varian, with Xenon lamp in the range of 200-800 nm..

8.3.6 Inductively Coupled Plasma Optical Emission Spectrometry (ICP-OES)

Metal content was determined by inductively coupled plasma-optical emission spectrometry (ICP-OES, Varian 715-ES, CA, USA) vector.

8.3.7 Diffuse Reflectance UV-Vis Spectroscopy (DRS)

UV-Vis-NIR diffuse reflectance spectroscopy measurements of solid samples are performed on a Cary 5000 Varian spectrophotometer. The study by diffuse reflectance of the opaque solids was performed using

an integrating sphere, obtaining spectra whose intensity is expressed in reflectance units (R) as a percentage, taking as 100% reflectance of $BaSO_4$ over the entire wavelength range. The absorption spectrum is obtained by representing 1/R, or the Kubelka-Munk function ($F(R) = (1-R)^2/2R$), against the wavelength.

8.3.8 Single Crystal X-Ray structure Analysis

Single crystal X-ray structure analysis was conducted collaboratively by Dr. Eleuterio Álvarez from *Departamento de Química Inorgánica, Instituto de Investigaciones Químicas CSIC-US.*

One crystal of **BHP-3.1** of suitable size for X-ray diffraction analysis was coated with dry perfluoropolyether and mounted on glass fibers and fixed in a cold nitrogen stream (T = 193 K) to the goniometer head. Data collection was performed on a Bruker-Nonius X8Apex-II CCD diffractometer, using monochromatic radiation λ(Mo K_α) = 0.71073 Å, by means of ω and φ scans with a width of 0.50 degree. The data were reduced (SAINT) [1] and corrected for absorption effects by the multi-scan method (SADABS) [2]. The structures were solved by direct methods (SIR-2002) [3] and refined against all F_2 data by full-matrix least-squares techniques (SHELXTL-6.12) [4] minimizing $w[F_{o2}-F_{c2}]_2$. All the non-hydrogen atoms were refined anisotropically, while C-H hydrogen atoms were placed in geometrically calculated positions using a riding model. The asymmetric unit of the structure of **BHP-3.1** contains a set of independent PbI_3, formed in turn by two independent half lead-atoms that match an inversion center, both metals being separated by half of crystallographic *a*-axis, i.e. 4.041(2) Å. By symmetry and translation of the unit cell this motif forms a chain link of the 1D anionic polymer that develops along the crystallographic *a*-axis. In addition, the asymmetric unit has half a molecule of dication [1,1'-biphenyl-4,4'-diyl] diammonium, which appear positionally disordered in two halves with the same occupancy factors. These halves are close to an inversion center at the end of the phenyl group in such a way that by symmetry the entire molecule of the dication is generated. Two DMF crystallization molecules complete the asymmetric unit, one of which

appears disordered with the ratio of occupancy factors of 57:43. Some geometric restraints (DFIX command), the ADP restraint SIMU and the rigid bond restraint DELU were used to make the geometric and ADP values of the disordered atoms more reasonable. A summary of cell parameters, data collection, structure solution, and the refinement of this crystal structure is provided below (Table 8.1, Fig. 8.3 and Fig. 8.4). The corresponding crystallographic data were deposited on the Cambridge Crystallographic Data Centre as supplementary publications. CCDC 1902819. The data can be obtained at:https://www.ccdc.cam.ac.uk/structures/

Table 8.1: Crystal data and structure refining for BHP-3.1.

Empirical formula	$C_{12}H_{21}I_3N_3O_2Pb$
	$[I_3Pb, C_6H_7N, 2(C_3H_7NO)]$
Formula weight	827.21
Temperature	193(2) K
Wavelength	0.71073 Å
Crystal system	Triclinic
Space group	$P\bar{1}$
Unit cell dimensions	a = 8.0816(8) Å = 97.876(4)°.
	b = 12.3906(12) Å = 106.389(4)°.
	c = 12.9013(11) Å = 104.083(4)°.
Volume 1	172.40(19) Å3
Z	2
Density (calculated)	2.343 Mg/m^3
Absorption coefficient	11.151 mm^{-1}

F(000)	742
Crystal size	0.400 x 0.100 x 0.050 mm3
Theta range for data collection	2.676 to 25.248°.
Index ranges	-9<=h<=9, -14<=k<=14, -15<=l<=15
Reflections collected	15886
Independent reflections	4246 [R(int) = 0.0306]
Completeness to theta = 25.242°	99.8 %
Absorption correction	Semi-empirical from equivalents
Max. and min. transmission	0.7461 and 0.4715
Refinement method	Full-matrix least-squares on F^2
Data / restraints / parameters	4246 / 352 / 307
Goodness-of-fit on F^2	1.070
Final R indices [I>2sigma(I)]	R1 = 0.0374, wR2 = 0.1253
R indices (all data)	R1 = 0.0415, wR2 = 0.1303
Extinction coefficient	n/a
Largest diff. peak and hole	2.484 and -1.683 e.$Å^{-3}$

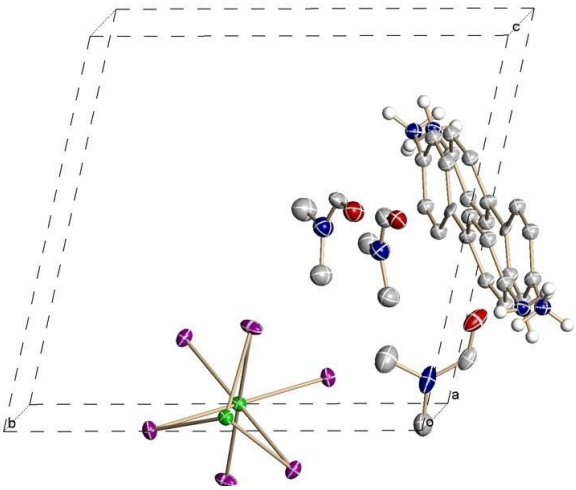

Fig. 8.3 ORTEP drawing of the crystal asymmetric unit of **BHP-3.1** view along a-axis with thermal ellipsoids set at a 30% probability level, hydrogen atoms and one part of modelling of a disordered DMF solvent molecule are omitted for clarity.

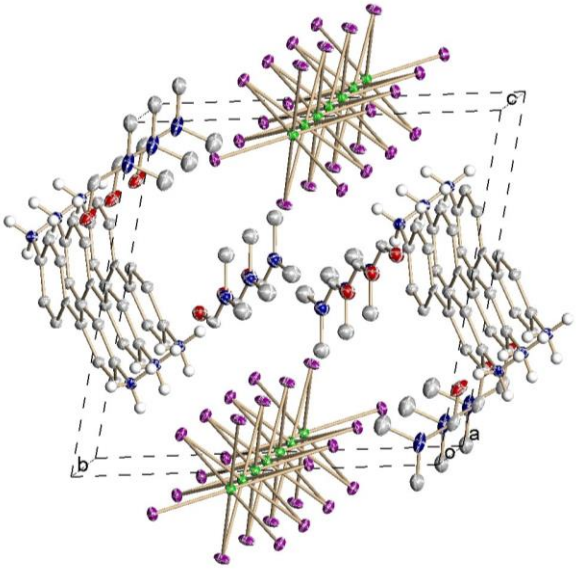

Fig. 8.4 Partial packing diagram of **BHP-3.1** view along a-axis with thermal ellipsoids set at a 30% probability level, hydrogen atoms are omitted for clarity.

8.3.9 Fourier Transformed Infrared Spectroscopy (FTIR)

FTIR spectra were recorded in the 4000 to 400 cm^{-1} range using a Thermo Nicolet 6700 FTIR with ATR accessory instrument (Thermo scientific, USA).

8.3.10 Proton Nuclear Magnetic Resonance (^{1}H NMR)

^{1}H NMR spectra were recorded on a Bruker AV300 (300 MHz) spectrometer, Chemical shifts of ^{1}H signals are reported in ppm using the solvent peak as internal standard. Data are reported as follows: chemical shift, multiplicity (s = singlet, br = broad, d = doublet, t = triplet, sept = septuplet, m = multiplet), integral, coupling constants (Hz) and assignment.

8.3.11 X-Ray Fluorescence Spectroscopy (XRF)

X-ray fluorescence spectroscopy were collected on a Philips MiniPal 25 fm instrument. The calibration of the target elements was done by preparing and measuring a series of known concentration standard sample.

8.3.12 Gas Chromatography (GC)

ESI-MS were acquired on an Agilent Esquire 6000 instrument

Cis-stilbene and trans-stilbene were quantified on a Varian CP-3800 apparatus equipped with an Carbowax column (15m x 0.32 mm x 0.25 µm).

Hydrogen content was analysed by gas chromatography (GS-MOL 15 meters column ID 0.55 mm TCD from J&W Scientific).

8.3.13 Optical Microscopy

Optical microscopy images were obtained with a Leica DM4000 microscope coupled with an Avantes AvaSpec-2048 Fiber Optic Spectrometer.

8.3.14 Time-Resolved Fluorescence Spectroscopy

Time-resolved fluorescence measurements were performed with an Easylife X Filter Fluorescence Lifetime Fluorometer (PTI, Canada) using a 380 nm filter.

8.3.15 In-situ IR Spectroscopy Measurements

The in-situ FTIR spectra were collected with a Bruker “vertex 70” and a Thermo Nicolet 8700 spectrometer equipped with a DTGS detector (4 cm^{-1}resolution, 32 scans). An IR cell allowing in situ treatments under controlled atmospheres and temperatures from 25 ºC to 500 ºC has been connected to a vacuum system with gas dosing facility. Self-supporting pellets (ca. 10 mg cm^{-2}) were prepared from the sample powders and treated in hydrogen flow (40 ml min^{-1}) at 350 ºC for 2 h before the test.

8.3.16 CO Chemisorption

The dispersion of ruthenium in **Cs(x)Ru(y)-STO** was estimated from CO monolayer Chemisorbed volume (V_m) using the double isotherm method on a Quantachrome Autosorb-1C equipment. Prior to adsorption, the samples were reduced in situ by flowing pure hydrogen (30 ml/min) at the same reduction temperature applied before catalysis (350 ºC) for 2 h (10 ºC/min rate). After reduction the samples were degassed at $1333x10^{-3}$ Pa for 2 h at the reduction temperature. Then, pure CO was admitted and the first adsorption isotherm (i.e. the total CO uptake) was measured. After evacuation at the same temperature of 350 ºC, the second isotherm (i.e. the reversible CO uptake) was taken. The volume of chemisorbed CO (V_m) was then obtained by subtracting the two isotherms. Thus, the monolayer uptake (N_m) can be obtained through the following equation:

$$N_m = 44.61\, V_m \qquad \textbf{Equation 8.1}$$

Where, N_m is in µmol / g and V_m is in cc / g.

The exposed active sites (or Active Surface Area, ASA) can be estimated through equation 8. 2.

$$ASA = \frac{N_m S A_m}{166}$$ **Equation 8.2**

Where, S is the number of surface atoms covered by each chemisorbed gas molecule (assuming a stoichiometry of Ru/CO=1.in our study), and A_m is the cross-sectional area occupied by each active surface atoms. ASA is in m^2 per gram of sample.

The percent metal dispersion (D) is calculated from equation 8.3.

$$D = \frac{N_m S M}{100 L}$$ **Equation 8.3**

Where M and L are the molecular weight and percent loading of the supported metal.

The pressure range studied was 0.5-11 x 10^4 Pa. The mean Ru^0 diameter (d) was determined from chemisorption data assuming spherical geometry for the metal particle according to the procedure described by Anderson.[5]

8.3.17 CO_2 Adsorption

The adsorption isotherms in the low-pressure range were measured by using a Micromeritics ASAP 2010 instrument with approximately 200 mg of solid placed in a sample holder, which was immersed into a liquid circulation thermostatic bath for precise temperature control. Before each measurement, the sample was treated overnight at 350 °C under vacuum. CO_2 adsorption isotherms were then acquired at 0 °C.

8.3.18 Ultra Performance Liquid Chromatography - Tandem Mass Spectrometer (UPLC-MS/MS)

The metal complex mass was analyzed by using Xevo Q ToF UPLC-MS/MS.

8.4 Other Procedures

8.4.1 Detailed calculation process for experimental formula of BHP-3.1 material

The Atomic proportion of each element Atom% = Weight proportion / Molecular weight, then,

Pb (Atom %) = 0.137, N (Atom %) = 0.184, C (Atom %) = 0.947, H (Atom %) = 1.453

Normalizing the number of Pb to be 1, then,

n(Pb)= 1, n(N) = 1.343, n(C) = 6.9, n (H) = 10.6

Assuming each **BHP-3.1** contains half benzidinium, having the empirical formula C_6H_7N, the ratio of the rest carbon ($C_{0.9}$) and nitrogen ($N_{0.343}$) is ~2.6 : 1, which is coincidence with the C, N ratio of DMF. So, the number of DMF in this molecular is ~0.3, and the weight proportion of oxygen in **BHP-3.1** could then be obtained as 0.66 %. After taking out of the weight proportion of O and Pb, the rest weight proportion is from iodine, and its value is 55.5 %. Based on that value and repeating the calculation process we can get the number of I in the formula is ~3. So, the experimental formula of **BHP-3.1** is PbI_3(Benzidnium)$_{0.5}$ $DMF_{0.3}$.

8.4.2. Calculation of valence band edge of material HP-5.1

All the XPS spectra were obtained with Al as the X-ray source. The valence band spectrum was first calibrated by C1s (284.8 eV), The valence band edge position was determined by intersection of tangent line and baseline of the valence band lowest energy peak, giving a value of 1.11 eV. The obtained value refers to the valence band energy versus to Fermi level, E_{BF}. The valence band edge to vacuum EBV can be calculated according to the following formula:

$$E_{VB} = E_{BF} + \phi_{sp} \qquad \textbf{Equation 8.4}$$

in which ϕsp is the work function of the XPS apparatus (4.244 eV). So, the valence band position (versus vacuum) can be obtained as follow:

E_{VB} = – (1.11 + 4.244) eV = - 5.344 eV

8.4.3 Quantification of ammonia

The amount of ammonia was quantitatively determined by the indophenol blue method.[6] Typically, in 5 mL diluted reservoir 1 (Scheme 8.1) solution, added firstly 0.2 mL phenol solution (100 mg/mL in ethanol), followed by adding 0.2 mL 0.5 wt% sodium nitroprusside solution. Then added 0.5 mL oxidation reagent (0.25 M NaOH solution containing 20 wt% sodium citrate and 1wt % sodium hypochlorite). After 3 h, UV-vis spectrum of the resulted solution was measured. The formation of indophenol blue was determined by the absorption at λ= 640 nm (diluting the reservoir 1 solution to a concentration that the resulted indophenol blue absorption value is below 1). The relationship between absorption and ammonia concentration was established by using different concentration of standard NH_4Cl solution (0, 0.02, 0.1, 0.5 and 1 ug/mL), as seen in Fig 8.5.

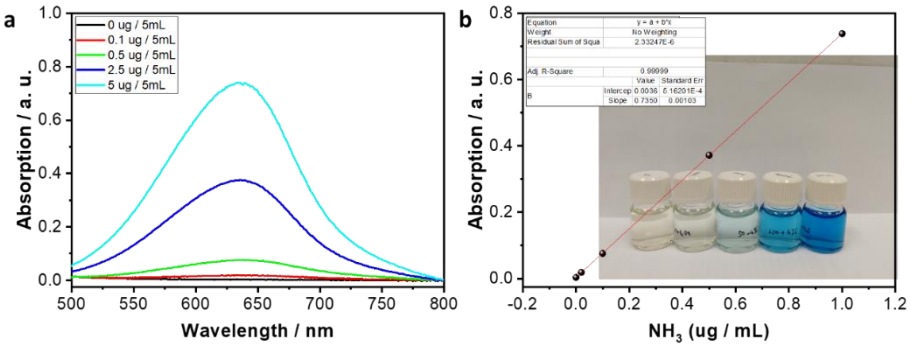

Fig. 8.5. UV-vis absorption spectra (a) and calibration curve (b) from standard NH_4Cl solution.

8.5 References

1 Bruker (**2007**). *APEX2*. Bruker AXS Inc., Madison, Wisconsin, USA.
2 Bruker (**2001**). *APEX2*. Bruker AXS Inc., Madison, Wisconsin, USA.
3 C. M. Burla, M. Camalli, B. Carrozzini, G. L. Cascarano, C. Giacovazzo, G. Poliori, R. Spagna, *SIR2002*: the program; (**2003**). *J. Appl. Cryst.* **36**, 1103–1103.

4 G. M. Sheldrick, Acta Crystallogr., Sect. A: Found. *Crystallogr.*, **2008**, 64, 112-122
5 J.R. Anderson “Structure of Metallic Catalysts”. *Academic Press*, London, 1975.
6. N. M. Tzollas, G. A. Zachariadis, A. N. Anthemidis and J. A. Stratis, *International Journal of Environmental Analytical Chemistry*, **2010**, 90, 115-126.

Chapter 9 Conclusions

The previous Chapters have illustrated with the case of benzidinium diammonium that it should be possible to prepare a vast variety of hybrid lead perovskites with different organic ammonium cations. By selecting the organic (di-/poly) ammonium cation it could be possible to modify and control the photocatalytic properties of the hybrid perovskite. It has also been shown that post-synthetic modifications can serve to coat and modify the surface properties of the perovskites.

Regarding N_2 fixation, the extremely high photothermal activity of Cs-modified Ru nanoparticles supported on strontium titanate has been disclosed. The activity of this material compares favorably with the most efficient systems for N_2 fixation at low temperature and atmospheric pressure and, therefore, this is probably the most significant results achieved in the Thesis. In addition, the electrocatalytic activity of transition metal complexes of tris-(3-methy-5-tert-butylpyrarolyl) borate has been determined, although additional work is still necessary to optimize the results.

Thus, the specific conclusions of the present Doctoral Thesis are the following:

1. It has been possible to synthesize and characterize by single-crystal XRD the hybrid organic lead perovskite of benzidinium diammonium. The material is not stable in water and many organic solvents. However, the material can be used as photocatalyst in hexane exhibiting activity to promote the electron transfer induced cis-to-trans stilbene isomerization. The changes observed in the XRD pattern have been attributed to the restructuration derived from the removal of a DMF solvent molecule.
2. Surface silanation of the hybrid benzidinium diammonium lead perovskite results in some increase in the surface hydrophobicity, as well the stability against disaggregation during reactions in hexane. However, this silica layer is not efficient to protect the material against water. By using the *cis-to-trans* isomerization of stilbene it has been found that the efficiency of the photoinduced electron transfer

decreases with the thickness of the silica layer, although the photoinduced isomerization still takes place in a considerable rate.

3. A hybrid styryl ammonium lead perovskite has been prepared and characterized as a 1D perovskite. The C=C double bond remains intact during the synthesis and can be used subsequently to perform a radical polymerization or even cross-polymerization with additional styrene. However, none of these materials is photo stable and they undergo decomposition with observation of H_2 evolution. It is proposed that the observed H_2 derives from the splitting of volatile HI evolved in the photochemical reaction.

4. Upon Cs modification, the resulting Ru nanoparticles supported on strontium titanate is an extremely efficient photocatalyst for N_2 hydrogenation to ammonia at atmospheric pressure. The performance of the photocatalytic process compares favorably with those previously reported in the literature. Based on the influence of the irradiating wavelength, it is proposed that the active sites are the Ru nanoparticles through photothermal mechanism, in which the photon energy is converted into local heat. Since no photoresponse to the UV light is observed, it is proposed that the role of strontium titanate is as a support of low heat transmission allowing the energy of the photon to be localized on the Ru nanoparticles that reached highest temperature. The role of Cs as promoter is to increase basicity on the Ru nanoparticles by charge transfer.

5. It has been found to tris-(3,5-disubstitutedpyrazolyl) borate is a suitable ligand to bind transition metal ions to form complexes exhibiting electrocatalytic activity for the reduction of N_2 to ammonia.

Although the studies on hybrid perovskites have open new methodologies to modify these materials, it has not been yet possible to prepare one of such materials stable in water or in organic solvents. The approach of surface coating has not been successful. However, the most remarkable results of the present Doctoral Thesis is the very high photocatalytic activity of Cs-modified Ru nanoparticles for N_2 fixation that is one of the most efficient photocatalysts known so far.

This is a step forward in the direction of implement photocatalysis for the direct use of solar light for the synthesis of chemicals and fuels.

Abstract

Solar energy to chemicals conversion is regarded to be one of the most plausible strategies addressing the issues of fossil fuel crisis and excessive anthropogenic CO_2 emission. For photo-assisted catalysis, including photocatalysis and photothermal catalysis, the key point is the development of efficient and robust photocatalysts that can efficiently utilize the solar energy as well as they are stable enough that meets the requirements for commercialization. Hybrid organic-inorganic perovskites have revolutionized the photovoltaic field in the last decade, reaching a certified sunlight conversion efficiency of 20 %. Since photocatalysis and photovoltaics share common processes, the application of these materials in photocatalysis would be possible. In this Doctoral Thesis, novel hybrid perovskite materials have been synthesized with the aim to improve their stability against moisture by taking advantage large variety of the available organic ligand, which can promote surface modifications capable to adjust the hydrophilic/hydrophobic properties. Additionally, the photocatalytic activity of these novel perovskite materials has been studied in model reactions in order to confirm their stability under reaction conditions.

On the other hand, the photo-assisted nitrogen fixation reaction has been also studied in detail in this Doctoral Thesis. on one hand, new organometallic complexes have been synthetized, characterized and tested as homogeneous photo and electrocatalysts for this reaction. They have been demonstrated to be able to activate dinitrogen molecule under electrochemical cathodic potentials to form ammonia. On the other hand, ruthenium nanoparticles deposited on a titanate-based perovskite material have been prepared and tested as heterogeneous photocatalyst for ammonia production in continuous flow. Moreover, it has been demonstrated that the addition of alkali metals to this photocatalyst can boost the photocatalytic activity of this reaction. Thus, this composite material has demonstrated to be among the most efficient photocatalysts in the current state-of-the art for this reaction, as well as very stable under reaction conditions. Considering the large industrial importance of N_2 fixation and the mild conditions of pressure and temperature used in the present study, the results of the

photo-assisted N_2 hydrogenation to ammonia can have a large impact in the area.

Key words: photocatalysis, organic-inorganic hybrid perovskite, surface modification, moisture stability, hydrophobicity, nitrogen reduction, ammonia.

La conversión de energía solar a productos químicos se considera una de las estrategias más viables para abordar los problemas derivados del uso masivo de combustibles fósiles y la excesiva emisión antropogénica de CO_2. En catálisis asistida con luz, incluida la fotocatálisis y la catálisis fototérmica, el punto clave es el desarrollo de fotocatalizadores eficientes y robustos que puedan utilizar al máximo la energía solar y que sean lo suficientemente estables como para su comercialización. Los materiales basados en perovskitas híbridas orgánicas-inorgánicas han revolucionado el campo de la fotovoltaica en la última década, alcanzando una eficiencia de conversión de luz solar del 23%. Dado que los campos de la fotocatálisis y la fotovoltaica comparten procesos comunes, se abre la posibilidad de aplicación de estos materiales en fotocatálisis. Con el objetivo de confirmar esta posible aplicación de las perovskitas híbridas en fotocatálisis, en esta Tesis Doctoral, se han sintetizado nuevos materiales híbridos de perovskita con el objetivo de mejorar su estabilidad frente a la humedad aprovechando la gran variedad de ligandos orgánicos disponibles, que además pueden ser usados para promover modificaciones superficiales capaces de ajustar las propiedades hidrofílicas / hidrofóbicas. La actividad fotocatalítica de estos nuevos materiales de perovskita se ha estudiado en reacciones modelo para confirmar su estabilidad en las condiciones de reacción.

Por otro lado, la reacción de fijación de nitrógeno fotoasistida también ha sido estudiada en detalle en esta Tesis Doctoral. Por un lado, se han sintetizado, caracterizado y testado nuevos complejos organometálicos como foto- y electrocatalizadores homogéneos para esta reacción. Estos han demostrado ser capaces de activar la molécula de dinitrógeno bajo un potencial electroquímico de reducción para formar amoníaco. Por otro lado, se han preparado nanopartículas de rutenio depositadas sobre un material de perovskita a base de titanato como fotocatalizador heterogéneo para la producción de amoniaco en flujo continuo. Además, se ha demostrado que la incorporación de metales alcalinos a este fotocatalizador puede potenciar su actividad fotocatalítica en esta reacción. Así, este material

compuesto ha demostrado estar entre los fotocatalizadores más eficientes del estado del arte en la actualidad para esta reacción demonstrando además una su elevada estabilidad en las condiciones de reacción.

Palabra Clave: fotocatalisis, perovskite híbrida orgánica/inorgánica, modificación de la superficie, estabilidad al aire, hidrofobicidad, reducción de nitrogeno, amoniaco.

La conversió d'energia solar en productes químics es considera una de les estratègies més viables per abordar els problemes derivats de l'ús massiu de combustibles fòssils i l'excessiva emissió antropogènica de CO_2. En catàlisi assistida amb llum, inclosa la fotocatàlisi i la catàlisi fototèrmica, el punt clau és el desenvolupament de fotocatalitzadors eficients i robustos que puguen utilitzar al màxim l'energia solar i que siguen prou estables com per a la seva comercialització. Els materials basats en perovskites híbrides orgàniques-inorgàniques han revolucionat el camp de la fotovoltaica en l'última dècada, aconseguint una eficiència de conversió de llum solar del 23%. Atès que els camps de la fotocatàlisi i la fotovoltaica comparteixen processos comuns, s'obre la possibilitat d'aplicació d'aquests materials en fotocatàlisi. Amb l'objectiu de confirmar aquesta possible aplicació de les perovskites híbrides en fotocatàlisi, en aquesta tesi doctoral, s'han sintetitzat nous materials híbrids de perovskita amb l'objectiu de millorar la seva estabilitat enfront de la humitat aprofitant la gran varietat de lligands orgànics disponibles, que amés poden ser usats per a promoure modificacions superficials capaços d'ajustar les propietats hidrofíliques / hidrofòbiques. L'activitat fotocatalítica d'aquests nous materials de perovskita s'ha estudiat en reaccions model per confirmar la seva estabilitat en les condicions de reacció.

D'altra banda, la reacció de fixació de nitrogen fotoassistida també ha sigut estudiada en detall en aquesta tesi doctoral. D'una banda, s'han sintetitzat, caracteritzat i testat nous complexos organometàl·lics com foto- i electrocatalitzadors homogenis per a aquesta reacció. Aquests han demostrat ser capaços d'activar la molècula de dinitrogen sota un potencial electroquímic de reducció per formar amoníac. D'altra banda, s'han preparat nanopartícules de ruteni depositades sobre un material de perovskita a força de titanat com fotocatalitzador heterogeni per a la producció d'amoníac en flux continu. A més, s'ha demostrat que la incorporació de metalls alcalins a aquest fotocatalitzador pot potenciar la seva activitat fotocatalítica en aquesta reacció. Així, aquest material compost ha demostrat estar entre els fotocatalitzadors més eficients de l'estat de l'art actualment per a

aquesta reacció seva demostrant amés una elevada estabilitat en les condicions de reacció.

Paraula Clau: fotocatàlisi, perovskite híbrida orgànica / inorgànica, modificació de la superfície, estabilitat a l'aire, hidrofobicitat, reducció de nitrogen, amoníac.

List of publications

The following publications form part of the present Doctoral thesis:

Chapter 3

Hybrid benzidinium lead iodide perovskites with a 1D structure as photoinduced electron transfer photocatalysts.

Yong Peng, Josep Albero, Eleuterio Álvarez, Hermenegildo García

Published in: *Sustainable Energy Fuels*, 2019,**3**, 2356-2360

Chapter 4

Surface silylation of hybrid benzidinium lead perovskite and its influence on the photocatalytic activity.

Yong Peng, Josep Albero, Hermenegildo García

Published in: *ChemCatChem*, **2019**,*11*, 6384

Chapter 5

Synthesis, post-synthetic modification and stability of a 2D styryl ammonium lead iodide hybrid material.

Yong Peng, Josep Albero, Hermenegildo Garcia

Chapter 6

Photo-assisted N_2 reduction by H_2 using Cs-promoted $Ru/SrTiO_3$ as efficient photocatalyst.

Yong Peng, Patricia Concepción, Antonio Franconeti, Josep Alberoand Hermenegildo García; **Manuscript preparation**

Other publications:

Photocatalytic Overall Water Splitting Activity of Templateless Structured Graphitic Nanoparticles Obtained from Cyclodextrins.

Yong Peng, Alejandra Rendón-Patiño, Antonio Franconetti, Josep Albero, Ana Primo, Hermenegildo García

Published in: *ACS Appl. Energy Mater.* 2020, 3, 7, 6623–6632

Photocatalytic CO2 Reduction to C2+ Products

Josep Albero, **Yong Peng**, Hermenegildo García

Published in: *ACS Catal*. 2020, 10, 10, 5734–5749

Porous Graphitic Carbons Containing Nitrogen by Structuration of Chitosan with Pluronic P123

Lu Peng, **Yong Peng**, Ana Primo, Hermenegildo García

Published in: *ACS Appl. Mater. Interfaces* 2021, 13, 11, 13499–13507

Effect of Linker Distribution in the Photocatalytic Activity of Multivariate Mesoporous Crystals

Belén Lerma-Berlanga, Carolina R. Ganivet, Neyvis Almora-Barrios, Sergio Tatay, **Yong Peng**, Josep Albero, Oscar Fabelo, Javier González-Platas, Hermenegildo García, Natalia M. Padial*, and Carlos Martí-Gastaldo*

Published in: *J. Am. Chem. Soc.* 2021, 143, 4, 1798–1806